NOVA SCHOOL OF SCIENCE & TECHNOLOGY

DEPARTMENT OF CHEMISTRY

NANOSERS MICROFLUIDICS PLATFORM FOR RAPID SCREENING FOR INFECTIOUS DISEASES

MARIA JOÃO QUITOLES DE OLIVEIRA

Master in Biotechnology

DOCTORATE IN BIOENGINEERING

NOVA University Lisbon
September, 2022

NOVA SCHOOL OF SCIENCE & TECHNOLOGY

DEPARTMENT OF CHEMISTRY

NANOSERS MICROFLUIDICS PLATFORM FOR RAPID SCREENING FOR INFECTIOUS DISEASES

MARIA JOÃO QUITOLES DE OLIVEIRA

Master in Biotechnology

Adviser: Hugo Manuel Brito Águas
Associate Professor, NOVA University Lisbon

Co-advisers: José Ricardo Ramos Franco Tavares
Associate Professor, NOVA University Lisbon

Hugh J. Byrne
Professor and Head of the FOCAS Research Institute, Technological University Dublin

Examination Committee

Chair: Rodrigo Ferrão de Paiva Martins
Full Professor, NOVA University Lisbon

Rapporteurs: Tito da Silva Trindade
Full Professor, University of Aveiro

Lorena Diéguez
Principal Investigator, International Iberian Nanotechnology Laboratory

Adviser: Hugo Manuel Brito Águas
Associate Professor, NOVA University Lisbon

Members: Eulália Fernanda Alves de Carvalho Pereira
Associate Professor, Faculty of Science of University of Porto

Rui Miguel Prudêncio Cunha Pignatelli
Principal Investigator, Molecular Medicine Institute of University of Lisbon

Luís Miguel Nunes Pereira
Associate Professor, NOVA University Lisbon

DOCTORATE IN BIOENGINEERING

NOVA University Lisbon
September, 2022

NanoSERS Microfluidics platform for rapid screening for infectious diseases

This document was created with the (pdf/Xe/Lua)LaTeX processor and the NOVAthesis template (v6.8.9) [0].

Para o meu avô Francisco, por me ensinar que o caminho para aprender provém de nós

Para o meu avô Zé, pela sua joie de vivre apesar das adversidades

Para os meus Pais, por tudo

Acknowledgements

So many words should be written to thank everyone who in one way or another helped me during these four years. When I look back, I see myself surrounded by wonderful and incredible people that shared with me happy (and sometimes sad) moments. You all enriched my life. Unfortunately, I cannot write 200 pages of acknowledgements so I will try to be short, but please know that I am truly grateful to everyone, more than I can express in these pages.

First of all, I would like to thank the people that stood by my side these four years, Professors Hugo Águas, Ricardo Franco and Hugh J. Byrne.

To my adviser Professor Hugo Águas, for accepting me as his MSc student and then PhD student, for giving me all conditions for my work and for all the support with much calm, patience, and perseverance.

To my adviser Professor Ricardo Franco, for the opportunity of becoming part of the research group at the BionanoLab, for always encouraging the discussion of ideas for my work, and for always asking for more and better.

To my co-adviser Professor Hugh J. Byrne, thank you for always sharing your knowledge with such enthusiasm, for your patience and encouragement, and for your helpful suggestions and good mood always at the distance of an email.

Thank you for helping me to give a sense of direction to my project, for allowing me to broaden my horizons and largely contributed to my professional and personal growth, and more importantly, to show me that there is always room to learn much more.

To Professor Elvira Fortunato and Professor Rodrigo Martins, for the unquestionable perseverance and relentless efforts towards the success of Centro de Investigação de Materiais (CENIMAT) and Centre of Excellence in Microelectronics, Optoelectronics and Processes (CEMOP) research centres. Your devotion to constant improvement allowed me to develop my work and for that, I thank you for the trust you deposited in me and my project.

To Fundação para a Ciência e Tecnologia for the financial support, without it, this work would not have been possible (SFRH/BD/132057/2017).

To the Doctoral Program in Bioengineering Systems from Massachusetts Institute of Technology (MIT)|Portugal and all the Professors, from who I learnt so much. A special thanks to Dr. Fátima Lopes and Dr. José Silva Lopes for managing the whole bureaucratic issues of the PhD at MIT|Portugal and for having given me all the assistance I needed to conclude this journey.

To Professor Eulália Pereira, for all the discussions and helpful suggestions, and to Miguel Peixoto de Almeida, for teaching me how to synthesise gold nanostars.

To PhD Miguel Prudêncio and PhD Soraia Caetano from the Instituto de Medicina Molecular (IMM), for providing the red blood cells samples and help needed to bring this work to closure.

A special thank you to all the contributors to this LaTeX template, in particular, to Professor João Lourenço without him, this Thesis wouldn't be so good-looking and organised. The hours spent on this template (and thus spared to all that use this template!) are undoubtedly appreciated and never forgotten! I also want to thank Professors José Alferes, and João Leitão e Ricardo Dias that taught me LaTeXduring the course "Scientific Text Processing- LaTeX". I would also like to take this opportunity to thank the dedication of the other Professors who teach the courses at the NOVA Doctoral School.

To Professor Ludwig Kripphal, one of the best Professors I had during my academic path. For the eReuss software used throughout this Thesis and so many others, and also, for introducing me to Python - so important in this work.

To everyone in the Department of Conservation and Restoration, for allowing me, a Master's student at the time, to work with the Raman spectrometer. Especially, to Vanessa Otero, for teaching me, for the laughs, and for the continuous support.

To my colleagues from the PhD program, Pedro Silva, Rita Oliveira, Carolina Peixoto, Manuel Almeida, and everybody else, for the laughing moments despite all the stress and deadlines.

To Professor Luís Pereira, for allowing me to steal one of his best students and for all the insightful discussions. Also to Professor Pedro Barquinha and Professor Rui Igreja, that always had time for sharing their knowledge even with a person from a completely different area.

To all my colleagues at CENIMAT for the help and support that I received from you over these years, Alexandra Gonçalves and Sónia Pereira (the help ever there), Tomás Calmeiro (for all the AFM measurements), Daniela Nunes (for all the pretty SEM images), Ana Pimentel, Joana Pinto, Paul Grey (for introducing me into the amazing world of Blender!), Emanuel Carlos, Sofia Ferreira, Carolina Marques, Rita Branquinho (thank you for all the FTIR/Raman sessions), Ana Rovisco, Jorge Martins, Diana Salgueiro, Jonas Duermeier, Asal Kiazadeh, Ricardo Ferreira, Tiago Mateus, Diana Gaspar, Tiago Carvalho, Raquel Barras, Manuel Mendes, Sumita Goswami, Suman Nandy, Maria Morais (the new generation!) and everybody else.

To Paulo Manteigas, Susana Mendes, Lúcia Mendes, Mafalda Gonçalves, and Valéria Gomes for the help with administrative issues. For the incredible help from Bárbara Costa and Isabel Rodrigues with everything related to the submission of this Thesis. Also, I would like to thank Idalina Martins, Conceição Luís, Elsa Gonçalves, and Ermelinda Borges, for all the laboratory assistance.

To Joana Neto and André Moura, thank you for all the support and insights in microfluidics and especially for the contagious good mood!

To Beatriz Coelho, for all the support and understanding, and for all the conversations that will lead to a book of PhD stories! And a heartily thank you, because of you, I have a new member in my family.

To everyone from the Bionano lab, people that started as colleagues and became so much more! Diego Carvalho (for all the Whatsapp audios monologues - may they never end!), Mónica Ferreira (one of the dearest persons I've ever met), David Peitinho (for all the conversations, help with Python, and boosting my mood!). To Carlos Costa (for all the curiosities about the world!), Bruno Guerreiro (the unofficial member), Karolina Socha, Maria Enea, André Dias, Mafalda Pinto and Marta Giza. Thank you all for brainstorming, for lunches, for sharing the joy of successful experiments and for cheering after the worse ones.

To all my students who let me disorient them. To Sara Margarida Jorge, Patrícia Ferreira, Marina Bento, Rafaela Martins, Tiago Roquito, Maria Cardoso and Filipe Sabino. Thank you for your patience and for all the questions that you had as it only helped me to increase my knowledge and to evolve. Sometimes people come into our lives at a time when we wouldn't choose to, and I'm glad they do. A very big thank you to Ana Dalot, my right and left arm that supported me in such a stressful time. It was a pleasure to pass on my little knowledge to someone like you.

Specjalne podziękowania dla Kamil Filipczak (przepraszam za błędy gramatyczne). Jestem bardzo szczęśliwy, że cię poznałem i że byliśmy przyjaciółmi przez lata. Dziękuję za całe życzliwe i motywujące wsparcie, którego udzieliłeś mi przez cały ten czas. Wiele dla mnie znaczyły.

Una persona che non potrei mai dimenticare di menzionare è Rosaceleste! So che non ho bisogno di parole perché c'è stata complicità tra noi da quando abbiamo iniziato a sintetizzare le stelle insieme! Tuttavia, sono grata che siate venuti in Portogallo, per tutte le storie che abbiamo condiviso ridendo e per tutte quelle che condivideremo ancora! Grazie per tutto il sostegno, le parole e i saluti.... E, siccome so che vuoi leggere questo: sei perfetto!

Gracias a Rocìo, por escucharme y tener siempre una palabra de apoyo y por estar siempre dispuesta ayudar. Ya sabes que te admiro muchísimo, como persona y científico. Eres un científico fuera del camino, y debería haber mucho más como tú. Gracias por tus bailes y locuras que hizo que el día fuera siempre mejor.

To Raquel Borda d'Água, Diogo Lima, and Miguel Xavier for being the energetic people that you are, for all the travels and "field trips" (hoping to do much more in the

future). A special thanks to Inês Cunha, an energy that cannot be contained. It was our passion for science that led to a collaboration, so important for this Thesis.

To Marisa, Tatiana and Ana, is hard to believe that you have been part of my life for all these years. I cannot imagine my life without you in it. Thank you from the bottom of my heart. For all the laughs, crying, love and support you have been giving me, every day, even in the distance. I honestly could not have done this without you.

Por último, quero agradecer a todos os membros da minha família (incluindo os de 4 patas!).

Aos meus sogros e família que me adoptou. Obrigada pelo carinho com que me receberam e por terem trazido ao mundo uma pessoa incrível para partilhar a minha vida.

Obrigada ao meu avô Francisco, avô Zé e avó Soledade, embora não vos veja, vocês vivem no meu coração e através dos ensinamentos que me deram.

À minha Piglet, pelo apoio, por todas discussões, gargalhadas e complicidade que existe entre nós mesmo quando mais ninguém nos percebe. Apesar de já seres adulta, continuas a ser a minha maninha e todos os dias sinto-me grata por te ter. Aproveito também para agradecer ao Marco por toda a paciência que tem para responder a todas as perguntas que faço, e sobretudo, por aturar a minha irmã!

Ao David, por tudo. Não há muito que consiga dizer o quão agradecida estou por te ter conhecido. Obrigada pelo apoio incondicional e paciência imensurável que tens demonstrado ao longo destes 14 anos juntos. Obrigada pelo carinho e amor mais do que alguma vez sonhei. Obrigada por seres a minha luz quando me sinto às escuras. Por me fazeres inexplicavelmente feliz. Obrigada por me amares.

Aos meu pais e avó Bina, não existem palavras em qualquer língua que demonstrem a gratidão que sinto por tudo o que fizeram e continuam a fazer por mim. Obrigada pela força, motivação e amor que me deram para ultrapassar todos os obstáculos e chegar a "white shores, and beyond, a far green country under a swift sunrise" - J.R.R. Tolkien.

"Science can only flower out when there is an internal urge. It cannot thrive under external pressure." (C.V. Raman)

"I have been bent and broken, but - I hope - into a better shape." (Charles Dickens, Great Expectations)

Abstract

Early and accurate disease detection is critical for clinical diagnosis and ultimately determining patient outcomes. Point-of-care testing (POCT) platforms are needed in low-resource settings and also to help the decentralisation of healthcare centres. Immunoassays using Surface-Enhanced Raman Spectroscopy (SERS) are especially interesting for their increased sensitivity and specificity. Additionally, SERS can be easily translated into POCT formats with microfluidics. In this work, a sensitive, selective, capable of multiplexing, and reusable SERS-based biosensor was developed. The SERS immunoassay relies on a sandwich format, whereby a capture platform and SERS immunotags can capture and detect a specific antigen, respectively. The SERS immunotags consisted of gold nanostars, allowing exceptionally intense SERS signals from attached Raman reporters, and the covalent attachment of antibodies provided a stable antigen-antibody binding activity. As a capture platform, a regenerated cellulose-based hydrogel provided a robust design and the added advantage of environmental friendliness. Besides being a transparent material with low background fluorescence and Raman signal, its high-water retention capacity was particularly suited for preserving the high activity of covalently bound antibodies, improving the assay time-stability. This SERS-based immunoassay was then integrated into a microfluidic device, allowing high-throughput sample screening allied with the high sensitivity and multiplexing features of the developed assay. The device was fabricated in less than 30 minutes by exploring direct patterning on shrinkable polystyrene sheets for the construction of adaptable complex three-dimensional microfluidic chips. Finally, to validate the microfluidic system, *Plasmodium falciparum* infected red blood cell culture samples were tested for malaria biomarker detection. The discrimination of SERS immunotags signals from the background was made through the direct classical least squares method. As a result, better data fitting was achieved, compared to the commonly used peak integral method. Considering these features, the proposed

SERS-based immunoassay notably improved the detection limits of traditional enzyme-linked immunosorbent assay approaches. Its performance was better or comparable to existing SERS-based immunosensors. Moreover, this approach successfully overcame the main challenges for application at POCT, including increasing reproducibility, sensitivity, and specificity. Hence, the microfluidic SERS system represents a powerful technology which can contribute to early diagnosis of infectious diseases, a decisive step towards lowering their still substantial burden on health systems worldwide.

Keywords: Disease detection, Immunoassay, Surface-Enhanced Raman Spectroscopy, Microfluidics.

Resumo

A detecção precoce e precisa de doenças é fundamental para o diagnóstico clínico determinando frequentemente o prognóstico do paciente. Desta forma, plataformas de teste de rastreio (conhecidos pelo acrónimo de POCT) são extremamente necessárias, não só em locais com poucos recursos, mas também para ajudar à descentralização dos cuidados de saúde. Os ensaios imunológicos que utilizam a espectroscopia de Raman aumentada pela superfície (conhecida pelo acrónimo de SERS) são particularmente interessantes pela sua elevada sensibilidade. Além disso, os ensaios em SERS podem ser facilmente convertidos para formatos POCT quando combinados com microfluídica. Este trabalho consistiu no desenvolvimento de um biosensor sensível, selectivo, capaz de múltipla detecção e reutilizável baseado no fenómeno de SERS. O ensaio imunológico em SERS foi realizado num formato em sanduíche onde um antigénio específico é apreendido por uma plataforma de captura e reconhecido por imunosondas activas em SERS. Estas sondas consistem em nanopartículas de ouro em forma de estrela, que proporcionam um sinal de SERS intenso proveniente das moléculas repórter de Raman ligadas às nanopartículas. As sondas adquirem a especificidade necessária para o antigénio de anticorpos a elas ligados de forma covalente, e, por conseguinte, permitem uma ligação estável antigénio-anticorpo. O hidrogel regenerado à base de celulose forneceu uma plataforma de captura de design robusto e ecológico. Além de ser um material transparente com baixa fluorescência e, portanto, de baixa interferência no sinal de Raman, é um material com uma elevada capacidade de retenção de água tornando-o particularmente adequado para preservar a actividade dos anticorpos ligados covalentemente. Deste modo, o hidrogel proporciona uma plataforma de captura estável ao longo do tempo. O immunoensaio baseado em SERS desenvolvido foi posteriormente integrado num dispositivo de microfluídica, permitindo analisar um grande número de amostras sendo simultaneamente sensível e passível para aplicações de análise de múltiplos antigénios. O dispositivo foi fabricado em menos de 30 minutos devido à padronização directa em folhas de poliestireno contrácteis possibilitando a

construção tridimensional de um dispositivo de microfluídica. Finalmente, para validar o sistema de microfluídica, amostras de cultura de eritrócitos infectados com *Plasmodium falciparum* foram testadas para detecção de biomarcadores de malária. A discriminação dos sinais das immunosondas activas em SERS, relativamente a sinais interferentes, foi feita através do método clássico de quadrados mínimos. Como resultado, foi conseguido um melhor ajuste de dados em comparação com o método de cálculo do integral das áreas das bandas habitualmente utilizado. Assim, o ensaio imunológico baseado em SERS proposto neste trabalho permitiu obter um limite de detecção mais baixo do que o obtido pelas abordagens tradicionais como o ensaio de imunoabsorção enzimática (conhecido pelo acrónimo de ELISA), além de exibir um desempenho melhor ou comparável a outros sensores baseados em SERS já existentes na literatura. Adicionalmente, o sistema desenvolvido neste trabalho permite ultrapassar desafios que impedem a utilização deste tipo de sensores em locais de poucos recursos, apresentando valores elevados de reprodutibilidade, sensibilidade e especificidade. Por conseguinte, um sistema que combina SERS e microfluídica representa uma tecnologia potencialmente importante na detecção precoce, na esperança de que, num futuro próximo, as consequências das doenças infecciosas que ainda impõem um fardo substancial ao sistema de saúde a nível mundial, sejam minoradas.

Palavras-chave: Detecção de doenças, Ensaios imunológicos,
Espectroscopia de Raman aumentada pela superfície, Microfluídica.

Contents

List of Figures

List of Tables

List of Listings

Acronyms

ABTS	2,2'-azino-bis(3-ethylbenzthiazoline-6-sulfonic acid)
AFM	atomic force microscopy
AGE	agarose gel electrophoresis
AIDS	acquired immunodeficiency syndrome
ANOVA	analysis of variance
ASSURED	affordable, sensitive, specific, user-friendly, rapid and robust, equipment-free, and deliverable to end-users
ATR	attenuated total reflectance
AuNP	spherical gold nanoparticle
AuNS	gold nanostar
BCA	bicinchoninic acid
BSA	bovine serum albumin
CCD	charge-coupled-device
CEMOP	Centre of Excellence in Microelectronics, Optoelectronics and Processes
CENIMAT	Centro de Investigação de Materiais
CHEM	chemical enhancement
DCLS	direct classical least squares
DLS	dynamic light scattering
DNA	deoxyribonucleic acid
DSC	differential scanning calorimetry
DTNB	5,5-dithio-bis-(2-nitrobenzoic acid)

EDC	1-ethyl-3-(3-(dimethylamino)propyl)carbodiimide
EDS	energy-dispersive spectroscopy
EDTA	ethylenediamine tetra-acetic acid
EF	enhancement factor
ELISA	enzyme-linked immunosorbent assay
EM	electromagnetic enhancement
Fab	fragment antigen-binding
Fc	fragment crystallisable region
FIB	focused ion beam
FTIR	Fourier-transform infrared spectroscopy
FWHM	full width at half-maximum
GERS	graphene-based enhanced Raman scattering
HEPES	4-(2-hydroxyethyl)-1-piperazineethanesulfonic acid
HIV	Human immunodeficiency virus
HOMO	highest occupied molecular orbital
HRP	horseradish peroxidase
Ig	immunoglobin
IMM	Instituto de Medicina Molecular
IPTG	isopropyl β-d-1-thiogalactopyranoside
IR	infrared
iRBC	*P. falciparum* infected red blood cell
IUPAC	International Union of Pure and Applied Chemistry
LAMP	loop-mediated isothermal amplification
LASER	light amplification by stimulated emission of radiation
LCA	life cycle assessment
LOD	limit of detection
LOQ	limit of quantification
LSPR	localised surface plasmon resonance
LUMO	lowest unoccupied molecular orbital
MBA	4-mercaptobenzoic acid
MCR	multivariate curve resolution
MES	2-ethanesulfonic acid
MIT	Massachusetts Institute of Technology
ML	machine learning

MUA 11-mercaptoundecanoic acid
MVA multivariate analysis

Ni-NTA nickel-nitrilotriacetic acid
NP nanoparticle

PAGE polyacrylamide gel electrophoresis
PBS phosphate-buffered saline
PCA principal components analysis
PCR polymerase chain reaction
PDMS polydimethylsiloxane
PEG polyethylene glycol
***Pf*ALD** *Plasmodium falciparum* aldolase
***Pf*HGPRT** *Plasmodium falciparum* hypoxanthine guanine phosphoribosyl transferase
***Pf*HRP2** *Plasmodium falciparum* histidine rich protein 2
***Pf*HRP3** *Plasmodium falciparum* histidine rich protein 3
***Pf*LDH** *Plasmodium falciparum* lactate dehydrogenase
***P*GluDH** *Plasmodium* glutamate dehydrogenase
pI isoelectric point
PLS partial least squares
PMMA poly(methyl methacrylate)
POCT point-of-care testing
PS polystyrene

QD quantum dot

RBC red blood cell
RCH regenerated cellulose hydrogel
RDT rapid diagnostic test
REASSURED real-time connectivity, ease of specimen collection and environmental friendliness, affordable, sensitive, specific, user-friendly, rapid and robust, equipment-free, and deliverable to end-users
RNA ribonucleic acid
RPMI Roswell Park Memorial Institute
RR Raman reporter
RSD relative standard-deviation

SAM self-assembled monolayers
SARS-CoV-2 severe acute respiratory syndrome Human coronavirus

SDS	sodium dodecyl sulphate
SEM	scanning electron microscopy
SERRS	surface-enhanced resonance Raman scattering
SERS	surface-enhanced Raman scattering
SNHS	N-hydroxysulfosuccinimide
TEM	transmitance electron microscopy
TEMPO	2,2,6,6,-tetramethylpipelidine-1-oxyl radical
TGA	thermogravimetric analysis
TO	TEMPO-oxidised
UV-Vis	ultraviolet-visible
WHO	World Health Organization
XRD	X-ray powder diffraction

Symbols

A	Enhancement factor
α	Polarisability
c_p	specific heat of the material
D	Diffusion coefficient
$\Delta\mu_e$	Electrophoretic mobility normalised relative to the maximum mobility band
$\Delta\mu_{e,max}$	Maximum electrophoretic mobility normalised relative to the maximum mobility band
E	Electromagnetic field
E_e	Electric field
η	Liquid viscosity
F	Body force
G	Bulk reaction rate
h	Planck's constant
I	Excitation laser intensity
k	Thermal conductivity of the material
k_B	Boltzmann's constant
K_D	Dissociation constant

k_a	Antigen-antibody adsorption rate
k_d	Antigen-antibody desorption rate
μ	Fluid viscosity
μ_e	Electrophoretic mobility
μ_{inc}	Induced dipole moment
n	Hill factor, cooperativity parameter
N_S	Number of molecules
v_e	observed rate of migration of a component
P	Pressure
P^{SERS}	Power of the SERS signal
Pe	Peclet number
q	Internuclear separation at any instant
r	Radius of a molecule
Re	Reynolds number
ρ	Density
$\sigma^{R}_{adsorbed}$	Raman scattering cross section of the adsorbed molecule
$\sigma^{SERS}_{effective}$	SERS scattering cross section of the adsorbed molecule
T	Temperature
t	Time
T_R	Response time of the biosensor
U	Fluid velocity
v	Bulk velocity of the flow
ω_{inc}	Frequency of an incident monochromatic laser beam
ω_s	Frequency of the Stokes Raman scattering
ω_v	Frequency of a molecular vibration
W_c	Microchannel width
W_s	Reaction surface width
ζ	ζ-Potential

Chapter

1 Introduction

1.1 Motivation

As the severe acute respiratory syndrome Human coronavirus (SARS-CoV-2) pandemic has proven, accurate and timely diagnosis of infection is imperative for efficient disease management and vigilance.

Every year infectious diseases are responsible for approximately 7.8 million deaths. For instance, in 2020, malaria alone caused an estimated 241 million new clinical episodes, increasing from 229 million in 2019, mainly because of disruptions to services during the SARS-CoV-2 pandemic [1–3]. From 241 million cases, 627 000 resulted in death (69 000 more than in 2019), of which 77% were children under 5 years old [1–3]. In other words, for every 10 people dying of malaria, 8 are children. Additionally, 3.2 billion (nearly half of the people in the world) are at risk of catching malaria. Unquestionably, a higher percentage of all infectious illness-related deaths occurs in low- and middle-income countries, which are poorly equipped to deal with the escalation of infectious disease numbers. Ninety-six percent of deaths caused by malaria in 2020 occurred in Africa. Nevertheless, 8,641 malaria cases were reported in the European Union/European economic area in 2019 [3]. This represents a loss of 10 billion € per year, considering only the direct costs (*e.g.* illness, treatment, premature death) [2]. Thus, if surveillance is not well-managed, even the highest-income countries will strive to manage the spiralling costs of treatment and care [4, 5].

Infectious diseases are caused by parasites, viruses, bacteria, and fungi, transmitted through animals (people or insect bites), the environment (contaminated food or water), or objects. Some of the most common infectious diseases are Human immunodeficiency virus (HIV) infection/acquired immunodeficiency syndrome (AIDS), influenza, malaria, tuberculosis, and hepatitis. Mosquito-borne and bacterial infectious diseases are classified as neglected tropical diseases by the World Health Organization (WHO) and need to be controlled by 2030 [3].

Early diagnosis is crucial in infectious disease management and enhances the clinical outcome. Current conventional diagnostic techniques such as the enzyme-linked immunosorbent assay (ELISA) and polymerase chain reaction (PCR), provide reliable and sensitive detection and are capable of treatment monitoring [6]. These highly accurate diagnostic tests are available for most infectious diseases of public health importance in the developed world, but these methods are technically challenging and expensive for implementation in resource-limited settings. When suitable, most detection procedures rely on light microscopy-based cytological examination. However, the low sensitivity and the requirement for specialised equipment and personnel make this technique unfeasible in low- to middle-income countries [4].

This has driven a strong interest in diagnostic platforms applicable for widespread implementation at point-of-care testing (POCT) sites. The ideal diagnostic platform adheres to several criteria defined by WHO as affordable, sensitive, specific, user-friendly, rapid and robust, equipment-free, and deliverable to end-users (ASSURED) [4]. A redefinition of this acronym to REASSURED was proposed to include real-time connectivity, and ease of specimen collection and environmental friendliness, due to the development in digital technology and mobile health [4]. Thus, the development of detection methods has been focused on technologies applicable in all types of healthcare systems to guide treatment and clinical management decisions.

Biosensors are especially suited for the fulfilment of these criteria. These integrated receptor-transducer devices as defined by International Union of Pure and Applied Chemistry (IUPAC) offer analytical information that can be translated into a qualification and quantification of an analyte of interest [7]. Although previously a biological recognition element (*e.g.* antibodies, enzymes or nucleic acids) was required for capturing the analyte, nowadays, the receptor can be inorganic or synthetic mimicking a bioreceptor of biological nature (*e.g.* molecular imprinted polymers) with higher stability than their natural counterparts.

Due to the myriad of possible target molecules, a multitude of biomimetic structures and transduction principles have been developed leading to an evolving field of biosensors. The rapid advancement in the nanotechnology industry is one of the leading factors that drove biosensors worth's market to be valued at ≈25 billion euros in 2021 and is excepted grow at a compound annual growth rate of 7.3% from 2022 to 2028 [8].

Rapid diagnostic tests (RDTs), such as lateral flow assays and paper-based devices, are the most promising way for early detection of infectious diseases, and just in 2020, 419 million RDTs were sold for malaria detection [1]. They are rapid, inexpensive and of easy fabrication. However, these tests also present low sensitivity, selectivity and reliability [4] and do not eliminate the need for malaria test microscopy.

Hence, the continuous progress of science has been directed to address the challenges of the current methods and create the next generation of diagnostics platforms to lessen the burden of infectious diseases in the world.

Recently, surface-enhanced Raman scattering (SERS) spectroscopy has come to be considered as the ideal candidate to extract most of information in a sample [5, 9, 10]. SERS spectroscopy is known to provide highly sensitive detection of molecular species, of interest to a diverse range of areas such as environmental, biomedicine, analytical or material chemistry [5]. The chemical information offered by the multitude of narrow vibrational bands in a Raman spectrum, and the sensitivity accomplished by SERS substrates, competes with more traditional methods such as fluorescence. In addition, the combination of SERS spectroscopy with other techniques such as microfluidics allows to bring the high sensitivity and multiplex capability to a high throughput analysis system [5].

To this end, SERS-microfluidics systems have been extensively investigated in biomedical applications [11]. These systems are an attractive choice due to the potential impact of early detection of diseases as infections. Microfluidics consolidate sample preparation, manipulation and separation, and *in situ* detection into one working unit without impairing reliable and consistent performance [11]. Hundreds of research papers about the design and possible applications of SERS spectroscopy and microfluidics have been published, as the steady growth shows in Figure 1.1. Nevertheless, the number of publications in microfluidic SERS-related research indicates that much development is still required. Curiously, 2020 was the first year that research output in the research field suffered a small drop, probably due to the SARS-CoV-2 pandemic situation.

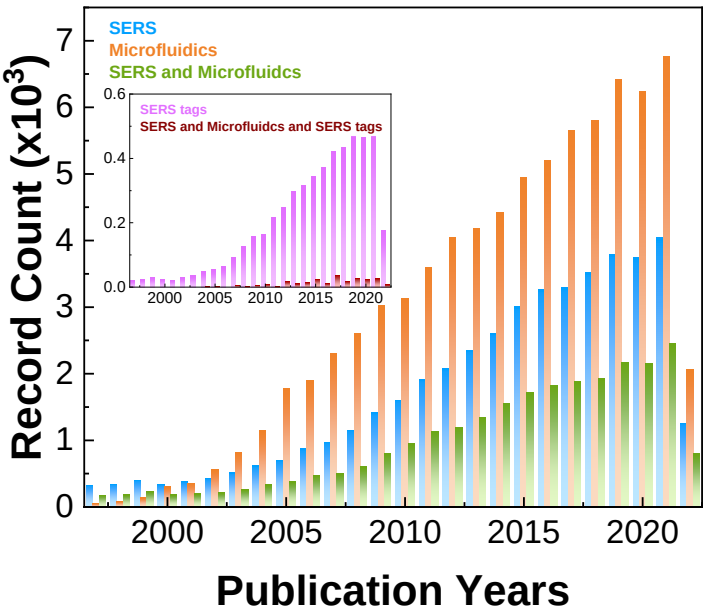

Figure 1.1: Number of publications search in Web of Science, as SERS: "TOPIC: (surface enhanced raman) OR TOPIC: (sers)"; microfluidics: "TOPIC: (microfluidc*)"; SERS tags: "TOPIC: (surface enhanced raman) OR TOPIC: (sers) AND TOPIC: SERS tag, OR TOPIC: SERS label OR TOPIC: SERS probe". This search is as of June 2022[12].

This project aims to develop a new biosensor for low-abundance biomarker detection (Figure 1.2). The platform will be based on a microfluidic-SERS system to combine the

sensitivity and multiplexing ability from SERS spectroscopy with the high throughput and multiparametric screening offered by microfluidics. Figure 1.2 shows the advantages that the combination of these two fields might bring to diagnostic platforms and therefore the objectives to pursue in this Thesis. This type of system can potentially significantly improve the timely identification of pathogens which could increase the sensitivity of diagnosis.

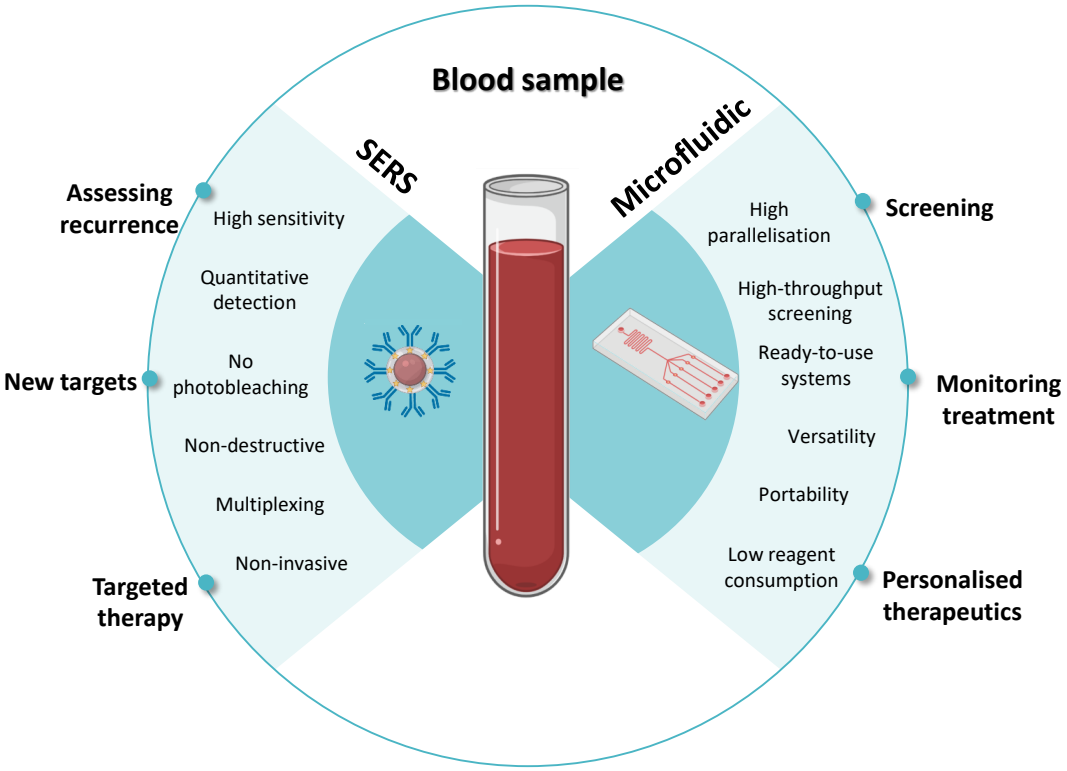

Figure 1.2: Advantages of a strategy using SERS spectroscopy combined with microfluidics for blood sample analysis.

1.2 Research aims and objectives

The main aim of this project was to develop a microfluidic SERS immunoassay system capable of disease diagnosis through capturing spectra of single SERS tags attached to analytes for the reliable identification [11, 13, 14].

To develop the immunoassay SERS-based microfluidic biosensor, two objectives were established: (1) the development of a SERS-based immunoassay and (2) the fabrication of a microfluidic device suitable for the SERS-based assay (Figure 1.3). Thus, five tasks were designed as follows:

i. *Development and characterisation of SERS tags:* SERS detection uses SERS tags as labels for recognition in sample analysis. Since sharp tips can lead to highly intense electromagnetic field enhancements and hence represent hotspots, the objective was to synthesise anisotropic nanoparticles (NPs) [15]. The strategy for the SERS tags involved the functionalisation of the metal NPs with a Raman reporter (RR), followed by coating and conjugation with a molecular recognition element for disease specific receptors. Physicochemical characterisation of the SERS tags was performed by determination of polydispersity index, diameter and morphology [16].

ii. *Proof-of-concept SERS assay:* These SERS tags were used to discriminate samples expressing low levels of biomarkers, from those expressing none, so this phase had the objective of estimating the sensitivity and robustness of the SERS tags. For this, a simulated immunophenotyping scenario was developed [17]. The various contributions of SERS tags were evaluated by performing analysis to resolve individual components in mixed spectra using multivariate statistical analysis [18].

iii. *Design and simulation of the microfluidics system for SERS analysis:* To design an efficient biosensor, is important to consider the process related to the transport of the targeted molecules to the capture surface of the biosensor. Thus, this task is dedicated to design a robust simulation to understand what parameters most influence the biosensor's performance.

iv. *Fabrication and performance analysis of the microfluidics system:* Microfluidic device fabrication and characterisation included the design of detection chambers to concentrate the analyte in the interrogation point [11, 13, 14]. The designs were validated by simulation before fabrication.

v. *Proof-of-concept of the developed microfluidic system with clinical samples:* After microfluidic device optimisation, proof-of-concept studies were carried out on multiple biomarkers to analyse groups such as malaria infected samples versus normal samples.

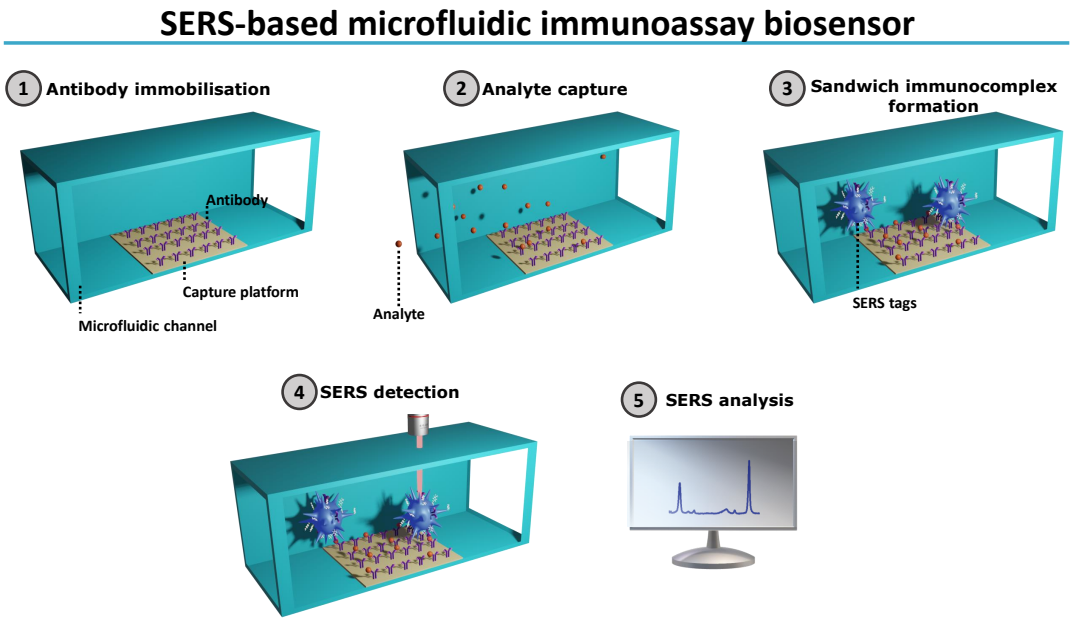

Figure 1.3: Proposed immunoassay SERS-based microfluidic device. (1) The microfluidic channel includes a capture platform with the antibody (the bioreceptor) immobilised to (2) capture the antigen (the analyte) in an unknown sample which is (3) identified by the SERS tags attached to the antigen forming the sandwich immunocomplex. The SERS tags give a fingerprint signal (4) detected by the Raman spectrometer (the transduction mechanism) that is able to transform the physical-chemical interaction of the sandwich immunocomplex into a (5) measurable signal.

1.3 Overview of work and structure of the Thesis

The work carried out for this Thesis focused on the development of a robust and sensitive POCT immuno-platform using SERS as readout system and microfluidics for process automation. The biosensor development started with the construction of SERS-immunotags based on gold nanostars, allowing exceptionally intense SERS signals from attached Raman labels and covalent attachment of antibodies by a simple chemical method providing high antigen binding activity. Then, a capture platform was prepared, resulting in a regenerated cellulose hydrogel (RCH), a transparent material, ideal for microfluidics applications, with low background fluorescence and Raman signal, particularly suited for preserving the high activity of the covalently bound antibodies. The sandwich SERS immunoassay was analysed by direct classical least squares (DCLS), resulting in superior discrimination of SERS signals from the background and much better data fitting. Then, the sandwich SERS immunoassay was incorporated into a microfluidic system and proof-of-concept studies were carried out on multiple biomarkers to analyse groups such as malaria infected blood samples versus healthy blood samples.

This PhD Thesis comprises of a brief introductory chapter 1, this chapter, to present the motivation and context of the PhD project, followed by chapter 2, which provides the fundamental background to various aspects involved within this Thesis and a state-of-the-art section on malaria SERS-based microfluidic biosensors is also given. Part of the

chapter 2 has been published in Journal Materials Chemical C with the title "Multifunctional cellulose-paper for light harvesting and smart sensing applications". The following chapters are based on manuscripts already published or in preparation which have been edited and/or merged for consistency of the Thesis and reading flow.

Chapter 3 is based on a publication entitled “Design and Simple Assembly of Gold Nanostar Bioconjugates for Surface-Enhanced Raman Spectroscopy Immunoassays” and partly on a second publication entitled “Reusable and highly sensitive SERS immunoassay utilising gold nanostars and a cellulose hydrogel-based platform”. This chapter 3 describes the development and characterisation of SERS tags with a single reporter, while chapter 4 demonstrates the functionality of the SERS tags by a proof-of-concept immunoassay created on a RCH as capture immuno-platform. The results obtained were published in Journal Materials Chemical B with the title “Reusable and highly sensitive SERS immunoassay utilising gold nanostars and a cellulose hydrogel-based platform”. Chapter 5 details the design and simulation of a microfluidics system for SERS analysis to incorporate the immunoassay developed in chapter 3 and chapter 4, which enabled the establishment of a microfluidic system for SERS biosensing. The microfluidic SERS-based immunoassay was tested with samples infected with malaria to prove the applicability of this work in SERS biosensing applications and is described in detail in chapter 6. These two chapters, 5 and 6, are going to be published with the title "Polystyrene-based microfluidic device for malaria detection by SERS analysis". Finally, chapter 7 summarises the findings and presents the general conclusions of the work described herein and suggests how this work could be furthered in the future. The chapters 2 and 7 are also under review to be published in a revision paper entitled "Microfluidic SERS devices: brightening the future of bioanalysis".

1.4 List of publications

The most relevant results obtained after concluding each task resulted in the preparation of brief reports that were modified into scientific papers, developed in co-authorship research:

1. António T. Vicente, Andreia Araújo, Manuel J. Mendes, Daniela Nunes, **Maria João Oliveira**, Olalla Sanchez-Sobrado, Marta P. Ferreira, Hugo Águas, Elvira Fortunato and Rodrigo Martins. Multifunctional cellulose-paper for light harvesting and smart sensing applications. J. Mater. Chem. C 6, 3143–3181 (2018).
   This article presents the state-of-art related to the integration and optimisation of photonic structures and light harvesting technologies on cellulose-based platforms. These paper-supported technologies can then be utilised into several applications such as SERS and photovoltaic solar cells. Part of the article focuses on the basic principles of SERS detection whereby an explanation of the Raman and electromagnetic and chemical enhancement is provided. This section was used as starting point for the theoretical background presented in chapter 1.

2. **Maria João Oliveira**, Miguel P. de Almeida, Daniela Nunes, Elvira Fortunato, Rodrigo Martins, Hugh J. Byrne, Eulália Pereira, Hugo Águas, and Ricardo Franco. Design and Simple Assembly of Gold Nanostar Bioconjugates for Surface-Enhanced Raman Spectroscopy Immunoassays. Nanomaterials 9, 1561 (2019).
   All the results obtained and published in this article are included in chapter 3 regarding the development of SERS immunotags. Being an essential part of the SERS-based immunoassays, all steps needed to produce a SERS immunotag were carefully developed and optimised. The procedure and results obtained during NP synthesis, functionalisation and bioconjugation with a immunoglobin IgG antibody were fully presented and discussed. The use of a proof-of-concept antibody-antigen complex opened the possibility to other antibody-antigen systems.

3. **Maria João Oliveira**, Inês Cunha, Miguel P. de Almeida, Tomás Calmeiro, Elvira Fortunato, Rodrigo Martins, Luís Pereira, Hugh J. Byrne, Eulália Pereira, Hugo Águas, and Ricardo Franco. Reusable and highly sensitive SERS immunoassay utilising gold nanostars and a cellulose hydrogel-based platform. J. Mater. Chem. B, 9(36), 7516-7529 (2021).
   This article includes topics that were divided between two chapters – 3 and 4. The first part of the article focuses on the optimisation SERS immunotags with covalent attachment of antibodies by a simple chemical method providing exceptional antigen binding activity. Since it relates to the development of a SERS immunotag, this section of the article was moved and combined with the content of the previous article. The development of POCT platforms involves a robust and sensitive capture platform that forms the antibody-antigen complex when the antigen is

present within the sample. For that, capture platform from a RCH was developed, particularly suited for preserving high activity of the covalently bound antibodies. This hydrogel and the sandwich complexes formed between RCH-antigen-SERS-immunotag were optimised and characterised, and the results were presented and discussed throughout chapter 4 regarding the proof-of-concept SERS immunoassay. This article also includes the application of DCLS method for SERS data analysis and consequent essential features in a biosensor such as reproducibility, sensitivity, specificity, and regeneration. The discussion of all these parameters was included in chapter 4.

4. **Maria João Oliveira**, Soraia Caetano, Ana Dalot, Filipe Sabino, Elvira Fortunato, Rodrigo Martins, Miguel Prudêncio, Hugh J. Byrne, Ricardo Franco, and Hugo Águas. Polystyrene-based microfluidic device for malaria detection by SERS analysis. (under submission)
   This article includes topics that were divided between two chapters – 5 and 6. The first part of the article focuses on the optimisation of the polystyrene-based microfluidic device by laser patterning shrinkable polystyrene sheets providing a rapid and simple microfluidic fabrication method. The microfabrication parameters were optimised and characterised, and the results were presented and discussed throughout chapter 5. Then, to prove the applicability of the POCT platform, the microfluidic device with the capture platform previously developed, was tested towards malaria detection. This part of the article is dedicated to the application of DCLS method for SERS data analysis and consequent essential features in a biosensor such as reproducibility, sensitivity, specificity, and long-term and thermal stability. The discussion of all these features was included in chapter 6.

5. **Maria João Oliveira**, Hugh J. Byrne, Ricardo Franco, and Hugo Águas. Microfluidic SERS devices: brightening the future of bioanalysis. (under revision)
   This article reflects on the new avenue that microfluidic and SERS fields have opened for applications in the biomedical field. The recent and innovative advances in nanomaterial science, novel Raman labels, and emerging bioconjugation protocols have helped develop SERS tags as powerful tools for multiplex SERS-based detection and diagnosis applications. Nevertheless, for SERS platforms translate to real-world problems, some challenges, especially for clinical applications, must be overcome. Microfluidics can help to make the translation. This review presents the current understanding of the factors influencing the quality of SERS and the strategies commonly employed to improve not only spectral quality but analyte-specific target ligand interaction in a reproducible manner. It further explores some of the most common approaches which have emerged for development of microfluidic SERS devices for biomedical applications.

Initial work as background for the development of SERS-active surfaces:

6. Andreia Araújo, Ana Pimentel, **Maria João Oliveira**, Manuel J Mendes, Ricardo Franco, Elvira Fortunato, Hugo Águas and Rodrigo Martins. Direct growth of plasmonic nanorod forests on paper substrates for low-cost flexible 3D SERS platforms. Flex. Print. Electron. 2, 014001 (2017).

7. **Maria João Oliveira**, Pedro Quaresma, Miguel Peixoto de Almeida, Andreia Araújo, Eulália Pereira, Elvira Fortunato, Rodrigo Martins, Ricardo Franco and Hugo Águas. Office paper decorated with silver nanostars - an alternative cost-effective platform for trace analyte detection by SERS. Sci. Rep. 7, 2480 (2017).

8. Ana Pimentel, Andreia Araújo, Beatriz J. Coelho, Daniela Nunes, **Maria João Oliveira**, Manuel J. Mendes, Hugo Águas, Rodrigo Martins and Elvira Fortunato. 3D ZnO/Ag surface-enhanced Raman scattering on disposable and flexible cardboard platforms. Materials (Basel). 10, (2017).

Other works not included in this Thesis:

9. Ana Rovisco, Rita Branquinho, Jorge Martins, **Maria João Oliveira**, Daniela Nunes, Elvira Fortunato, Rodrigo Martins, and Pedro Barquinha. Seed-Layer Free Zinc Tin Oxide Tailored Nanostructures for Nanoelectronic Applications: Effect of Chemical Parameters. ACS Appl. Nano Mater. 1, 3986–3997 (2018).

10. Célia M. Silveira, Rosaceleste Zumpano, Miguel Moreira, Miguel Peixoto de Almeida, **Maria João Oliveira**, Marina Bento, Cláudia Montez, Inês Paixão, Ricardo Franco, Eulália Pereira, and M. Gabriela Almeida. Star-Shaped Gold Nanoparticles as Friendly Interfaces for Protein Electrochemistry: the Case Study of Cytochrome c. ChemElectroChem 6, 4696–4703 (2019).

11. Tomás Pinheiro, João Ferrão, Ana C. Marques, **Maria João Oliveira**, Nitin M. Batra, Pedro M. F. J. Costa, M. Paula Macedo, Hugo Águas, Rodrigo Martins and Elvira Fortunato. Paper-based in-situ gold nanoparticle synthesis for colorimetric, non-enzymatic glucose level determination. Nanomaterials 10, 1–20 (2020).

12. Neusmar J. A. Cordeiro, Cristina Gaspar, **Maria João de Oliveira**, Daniela Nunes, Pedro Barquinha, Luís Pereira, Elvira Fortunato, Rodrigo Martins, Edson Laureto and Sidney A. Lourenço. Fast and low-cost synthesis of MoS_2 nanostructures on paper substrates for near-infrared photo-detectors. Appl. Sci. 11, 1–15 (2021).

13. Sofia Henriques Ferreira, Maria Morais, Daniela Nunes, **Maria João Oliveira**, Ana Rovisco, Ana Pimentel, Hugo Águas, Elvira Fortunato and Rodrigo Martins. High UV and sunlight photocatalytic performance of porous ZnO nanostructures synthesized by a facile and fast microwave hydrothermal method. Materials (Basel). 14, 2385 (2021).

1.5 List of presentations

As part of PhD activities, the most relevant results obtained were presented in scientific meetings. These conferences allowed sharing and development of knowledge related to recent research in the biotechnology field. Moreover, these opportunities allowed to establish connections, exchange ideas and even suggestions to problem solving. A summary of oral and poster presentations in national and international conferences is listed in Table 1.1.

Table 1.1: List of presentations, oral and in poster, in conferences.

February, 2021	*Material Science: Characterisation and Applications of Advanced Nanophotonic Materials and Structures Virtual Conference* (February 9^{th} to 10^{th}) Poster: "Sticky Cellulose Hydrogel as a Reusable Platform for a SERS Based Immunoassay" **Maria João Oliveira**, Inês Cunha, Miguel P. De Almeida, Elvira Fortunato, Rodrigo Martins, Eulália Pereira, Luís Pereira, Hugh J. Byrne, Ricardo Franco, and Hugo Águas
September, 2020	*NanoPT Online Conference (NPTO2020)* (September 23^{rd} to 24^{th}) Oral Contribution: "Sticky Cellulose Hydrogel as a Reusable Platform for A SERS Based Immunoassay" **Maria João Oliveira**, Inês Cunha, Miguel P. De Almeida, Elvira Fortunato, Rodrigo Martins, Eulália Pereira, Luís Pereira, Hugh J. Byrne, Ricardo Franco, and Hugo Águas Poster: "Simple one-pot separation of histidine-tagged proteins through centrifugation using NTA-functionalised gold nanostars" Diego Wiechers de Carvalho, **Maria João Oliveira**, Eulália Pereira, Ricardo Franco
January, 2020	*IV^{th} International Symposium on Nanoparticles/Nanomaterials and Applications 2020 – ISN2A* (Caparica, January 19^{th} to 24^{th}) Oral presentation and poster: "Design and Assembly of Effective Gold Nanostars Immunoprobes for SERS-Based Assays" **Maria João Oliveira**, Miguel P. De Almeida, Daniela Gomes, Elvira Fortunato, Rodrigo Martins, Eulália Pereira, Hugh J. Byrne, Hugo Águas and Ricardo Franco
April, 2019	*XIX Congresso da Sociedade Portuguesa de Materiais and X International Symposium on Materials* (Lisbon, April 14^{th} to 17^{th}) Poster: "SERS-Based Bionanoplatform for Immuno-Detection of Food Toxins" **Maria João Oliveira**, Marina Bento, Miguel Peixoto De Almeida, Eulália Pereira, Elvira Fortunato, Rodrigo Martins, Hugo Águas, and Ricardo Franco Oral contribution: "Plasmonic Office Paper as An Alternative Cost-Effective Platform for Trace Analyte Detection by Surface-Enhanced Raman Spectroscopy" **Maria João Oliveira**, Pedro Quaresma, Miguel Peixoto De Almeida, Andreia Araújo, Eulália Pereira, Elvira Fortunato, Rodrigo Martins, Ricardo Franco, and Hugo Águas
August, 2018	*PhD' Meeting and Nanoanalysis Symposium from The Fraunhofer IKTS Dresden* (Dresden, August 29^{th} to 31^{st}) Oral presentation and poster: "Office paper as an alternative platform for trace analyte detection by Surface-Enhanced Raman Spectroscopy" **Maria João Oliveira**, Pedro Quaresma, Andreia Araújo, Eulália Pereira, Ricardo Franco, Elvira Fortunato, Rodrigo Martins, Hugo Águas

1.6 Participation in national projects

- NanoBE - "Innovative Gold Nanostructured Interfaces for Eletrochemical Biosensing"at REQUIMTE/UCIBIO, Chemistry Department of the Faculty of Sciences and Technology of the NOVA University of Lisbon, supported by FCT (Portuguese Foundation for Science and Technology).

- DISERSTOX - "Disposable microfluidic devices to food contaminants detection by SERS"(PTD/CTM-NAN/2912/2014) at CENIMAT|i3N in the Science Materials Department and REQUIMTE/UCIBIO, Chemistry Department of the Faculty of Sciences and Technology of the NOVA University of Lisbon, supported by FCT (Portuguese Foundation for Science and Technology).

1.7 Master and Bachelor Thesis guidance

- Master Thesis of Ana Dalot, master student in Biotechnology, FCT-NOVA University of Lisbon, "Plasmonic Nanostars for Sensitive SERS-based immunodetection" Advisors: Professor Ricardo Franco and Professor Hugo Águas.

- Master Thesis of Filipe Sabino, master student in Micro and Nanotechnology Engineering, FCT-NOVA University of Lisbon, "Immunodetection by SERS on microfluidic platform" Advisors: Professor Hugo Águas and Professor Ricardo Franco.

- Bachelor Thesis of Maria Cardoso, bachelor student in Biochemistry, FCT-NOVA University of Lisbon, "Malaria immunoassay based on anisotropic nanoparticles and detection by Surface Enhanced Raman Spectroscopy." Advisor: Professor Ricardo Franco.

- Bachelor Thesis of Tiago Roquito, bachelor student in Biochemistry, FCT-NOVA University of Lisbon, "Malaria immunoassay based on anisotropic nanoparticles and detection by Surface Enhanced Raman Spectroscopy." Advisor: Professor Ricardo Franco.

- Bachelor Thesis of Rafaela Martins, bachelor student in Biochemistry, FCT-NOVA University of Lisbon, "Malaria immunoassay based on detection by Surface Enhanced Raman Spectroscopy" Advisor: Professor Ricardo Franco.

- Master Thesis of Kamil Flipjack, master student in Nanotechnology Engineering, Faculty of Chemistry, at the Lodz University of Technology (Poland), "Ultra-sensitive biodetection and fingerprinting applications of plasmonic nanoparticles using Surface Enhanced Raman Spectroscopy" Advisors: Professor Ricardo Franco and Professor Hugo Águas.

- Master Thesis of Marina Bento, master student in Biochemistry, FCT-NOVA University of Lisbon, "Plasmonic Nanoparticles for biodetection by Raman spectroscopy" Advisors: Professor Ricardo Franco and Professor Hugo Águas.

1.8 Tutoring of Master classes

- Classes of Raman spectroscopy in "Characterisation and Non-Destructive Testing Techniques" and in "Techniques of Characterisation of Materials" courses under supervision of Professor Rita Branquinho.
- Classes of Interdigital Electrode Microfabrication Techniques in "Biosensors" course under supervision of Professor Hugo Águas.
- Classes of Detection of Glucose using Microfluidics in Paper in "Biosensors" course under supervision of Professor Hugo Águas.
- Classes of Bionanotechnology Techniques in "Biomolecular Techniques I" course under supervision of Professor Maria João Romão.
- Classes of Raman spectroscopy in "Biomolecular Spectroscopies" course under supervision of Professor Ricardo Franco.

1.9 Courses

The intensive courses granted the chance to learn about new and unexplored topics which complements the knowledge learned so far.

1. European Advanced Training Course in "Nanoscale materials - Characterisation techniques and applications", August 27^{th}-20^{th}, 2018, Fraunhofer Institute, Dresden, Germany;
2. "Research Skills Development 30^{th} edition" from NOVA Doctoral School, October 19^{th}-22^{th}, 2018, NOVA University of Lisbon, Portugal;
3. "Design Thinking 17^{th} edition" from NOVA Doctoral School, November 10^{th}-17^{th}, 2018, NOVA University of Lisbon, Portugal;
4. “A Practical Guide for the 10^{th} Hands-on course in ultrafast sample treatment for proteomics” from BIOSCOPE Research Group & PROTEOMASS Scientific Society, February 18^{th}-20^{th}, 2019, FCT-NOVA University of Lisbon, Portugal;
5. “A Practical Guide for the 9^{th} Hands-on Course in Sample Preparation Using Nanoparticles for proteomics” from BIOSCOPE Research Group & PROTEOMASS Scientific Society, February 25^{th}-27^{th}, 2019, FCT-NOVA University of Lisbon, Portugal;

6. "Project Management 16th edition" from NOVA Doctoral School, April 6th-13rd, 2019, NOVA University of Lisbon, Portugal;

7. "Scientific Text Processing with LaTeX 9th edition" from NOVA Doctoral School, May 3th-17th, 2019, NOVA University of Lisbon, Portugal (where the template used for this Thesis was presented[19]);

8. "Data Processing Automation" from NOVA Doctoral School, May 11th-25th, 2019, NOVA University of Lisbon, Portugal;

1.10 Recognition

- Excellent Shotgun Poster Presentation Prize "Design and Assembly of Effective Gold Nanostars Immunoprobes for Surface-Enhanced Raman Spectroscopy-based Assays" **Maria João Oliveira**, Miguel P. De Almeida, Daniela Gomes, Elvira Fortunato, Rodrigo Martins, Eulália Pereira, Hugh J. Byrne, Hugo Águas and Ricardo Franco in IVth International Symposium on Nanoparticles/Nanomaterials and Applications 2020 - ISN2A (Caparica, January 19th to 24th).

- Cover of Nanomaterials: "Design and Simple Assembly of Gold Nanostar Bioconjugates for Surface-Enhanced Raman Spectroscopy Immunoassays" **Maria João Oliveira**, Miguel P. de Almeida, Daniela Nunes, Elvira Fortunato, Rodrigo Martins, Hugh J. Byrne, Eulália Pereira, Hugo Águas, and Ricardo Franco. Nanomaterials. 9, 1561 (2019) (Figure 1.4).

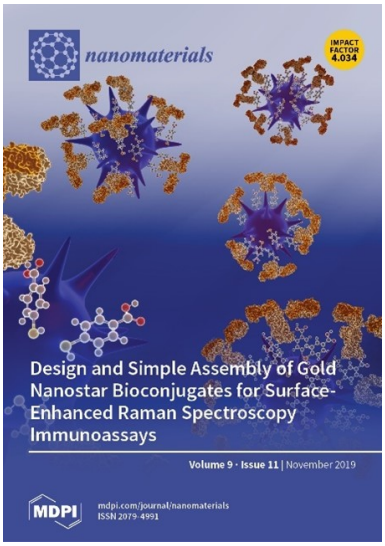

Figure 1.4: Front cover for the issue 11 of Nanomaterials where the article "Design and Simple Assembly of Effective Gold Nanostars Bioconjugates for Surface-Enhanced Raman Spectroscopy immunoassays" was published.

References for chapter 1

[1] World Health Organization. *World Malaria Report 2021*. Tech. rep. Geneva: World Health Organization, 2021, pp. 1–322.

[2] *Centers for Disease Control - Malaria - Malaria Worldwide - Impact of Malaria*. 2021. URL: https://www.cdc.gov/malaria/malaria%7B%5C_%7Dworldwide/impact.html (visited on 07/22/2021).

[3] World Health Organization. *Surveillance template protocol for pfhrp2/pfhrp3 gene deletions*. World Health Organization, 2020, pp. 1–26.

[4] K. J. Land et al. "REASSURED diagnostics to inform disease control strategies, strengthen health systems and improve patient outcomes". In: *Nature Microbiology* 4.1 (2019), pp. 46–54.

[5] J. Langer et al. "Present and Future of Surface-Enhanced Raman Scattering". In: *ACS Nano* 14.1 (2020), pp. 28–117.

[6] P. D. Howes, R. Chandrawati, and M. M. Stevens. "Colloidal nanoparticles as advanced biological sensors". In: *Science* 346.6205 (2014), pp. 53–63.

[7] M. Nič et al., eds. *IUPAC Compendium of Chemical Terminology*. Research Triagle Park, NC: IUPAC, 2009.

[8] Global Market Insights. *Biosensors Market*. Tech. rep. Delaware: Global Market Insights Inc., 2021, pp. 1–208.

[9] S. Madlener and J. Gojo. "Liquid biomarkers for pediatric brain tumors: Biological features, advantages and perspectives". In: *Journal of Personalized Medicine* 10.4 (2020), pp. 1–15.

[10] L. Hamm, A. Gee, and A. S. D. S. Indrasekara. "Recent Advancement in the Surface-Enhanced Raman Spectroscopy-Based Biosensors for Infectious Disease Diagnosis". In: *Applied Sciences* 9.7 (2019), p. 1448.

[11] J. Godin et al. "Microfluidics and photonics for Bio-System-on-a-Chip : towards a microfluidic flow cytometry chip". In: *Journal of biophotonics* 376.5 (2008), pp. 355–376.

[12] *Results from Web of Science Core Collection for: SERS: "TOPIC: (surface enhanced raman) OR TOPIC: (sers)"; microfluidics: "TOPIC: (microfluidc*)"; SERS tags: "TOPIC: (surface enhanced raman) OR TOPIC: (sers) AND TOPIC: SERS tag, OR TOPIC:SERS label OR TOP*. 2022. URL: https://www.webofscience.com/wos/woscc/summary/dcface5b-0415-4807-bc26-3a7bb18cdd51-420820d2/relevance/1 (visited on 06/01/2022).

[13] B. Dura et al. "Profiling lymphocyte interactions at the single-cell level by microfluidic cell pairing". In: *Nature Communications* 6 (2015), pp. 1–13.

[14] A. Pallaoro et al. "Rapid identification by surface-enhanced Raman spectroscopy of cancer cells at low concentrations flowing in a microfluidic channel". In: *ACS Nano* 9.4 (2015), pp. 4328–4336.

[15] F. Tian et al. "Surface enhanced Raman scattering with gold nanoparticles: effect of particle shape". In: *Anal. Methods* 6.22 (2014), pp. 9116–9123.

[16] J. P. Nolan, E. Duggan, and D. Condello. "Optimization of SERS tag intensity, binding footprint, and emittance". In: *Bioconjugate Chemistry* 25.7 (2014), pp. 1233–1242.

[17] M. R. Hoonejani et al. "Quantitative multiplexed simulated-cell identification by SERS in microfluidic devices". In: *Nanoscale* 7.40 (2015), pp. 16834–16840.

[18] H. J. Byrne et al. "Spectral pre and post processing for infrared and Raman spectroscopy of biological tissues and cells". In: *Chemical Society Reviews* 45.7 (2016), pp. 1865–1878.

[19] J. M. Lourenço. *The NOVAthesis LaTeX Template User's Manual*. NOVA University Lisbon. 2021.

Chapter

2 Theory, background and state-of-art

*Part of the literature review presented in this chapter has been published, in part, elsewhere: António T. Vicente, Andreia Araújo, Manuel J. Mendes, Daniela Nunes, **Maria João Oliveira**, Olalla Sanchez-Sobrado, Marta P. Ferreira, Hugo Águas, Elvira Fortunato and Rodrigo Martins. Multifunctional cellulose-paper for light harvesting and smart sensing applications. J. Mater. Chem. C 6, 3143–3181 (2018). Maria João Oliveira was responsible for writing the basic principles of SERS detection and review of the current literature regarding cellulose-based SERS substrates with emphasis on solution-processed SERS substrates.*

This chapter describes the fundamental theory behind the work in this Thesis relating to SERS phenomena and the basic principles of producing a SERS tag. Thus, it includes some background on nanoparticle (NP) synthesis, and functionalisation of NPs with Raman reporters and bioconjugation strategies, with emphasis on bioconjugation with antibodies. The literature review also focuses on microfluidics, and provides a short description of the state-of-the-art of microfluidic devices for immunoassay SERS-based microfluidic platforms. Due to the health burden caused by malaria, the final section included in this chapter is centred on its life cycle and current diagnostic techniques, particularly in the areas of SERS-based microfluidics biosensors. The aim of this chapter is to give a broader view for to the introduction sections given in each results chapter.

2.1 Raman spectroscopy

The Raman effect is based on a shift in frequency of a small fraction of radiation scattered by molecules, having a different frequency from that of the monochromatic incident beam [1, 2]. In Raman spectroscopy, sample molecules are illuminated with a monochromatic laser beam of energy ($h\omega_{inc}$), which results in light scattering in all

directions. The most frequent event is that the interaction of light and molecule happens without net exchange of energy ($E = 0$), so the scattered radiation has a frequency equal to the frequency of incident radiation ($E = E_0$) (Figure 2.1a). Consequently, the collisions between the photon and the molecule are said to be elastic. This process constitutes elastic or Rayleigh scattering [1, 2]. A minute fraction of the scattered radiation - 1 part in 10 million - has a different frequency from that of the incident radiation and is termed inelastic or Raman scattering [3]. This phenomenon occurs through the interaction of the radiation with vibrations of the molecules, resulting in excitation or deactivation of molecular vibrations in which either the photon loses or gains an amount of energy equal to that of the vibration $h\omega_v$. Hence, a molecule in the ground vibrational level ($\omega = 0$) can scatter a photon of energy $h\omega_{inc}$, and to produce a photon of energy $h(\omega_{inc} \pm \omega_v)$ (Figure 2.1a). In other words, the Raman shift occurs because photons (particles of light) exchange part of their energy with molecular vibrations in the material [1, 2, 4, 5].

The Raman spectrum reflects the energy differences between the incident and inelastically - scattered photons, which depend upon the chemical structure of the molecules responsible for scattering. When the interaction with the molecule causes the photon to gain vibrational energy from the molecule, then the frequency of the scattered light will be higher than that of the incident light ($E = E_0 + E_v$), known as anti-Stokes Raman scattering. However, if the molecule gains energy from the incident photon then the frequency of the scattered light will be lower than that of the incident light ($E = E_0 - E_v$), and hence, Stokes lines appear in Raman spectrum (Figure 2.1a). This provides the 'molecular fingerprint' information and consequently, the unique identification of the molecules from molecular vibrations [1, 2, 5].

Basically, Raman scattering occurs when light interacts with atoms in the molecules, causing them to change vibrational state. However, a molecule is only Raman active when there is a change in polarisability during the vibration ($\frac{\partial \alpha}{\partial q} > 0$), which means that the scattering involves a momentary distortion of the electrons distributed around the bond in a molecule, followed by re-radiation of the photon as the bond returns to its normal state. In addition, the symmetry of a molecule is also an important consideration, as the symmetric stretches are more intense in Raman spectra [1, 2].

This is similar to the more widely known infrared (IR) absorption spectroscopy, but different selection rules apply. In IR absorption, a change in a dipole moment or a change in distribution during vibration caused by the interaction between radiation and the molecule is required. This gives rise to, in simple terms, a mutual exclusion principle, *i.e.*, if the molecules have a centre symmetry, such as CO_2, no IR active transitions are in common with Raman active transitions. In the case of non-centrosymmetric molecules, many vibrational modes may be both Raman and IR active, - although the intensities of the bands are different because they reflect the probability of the transitions. However, the energy shifts observed in a Raman experiment should be identical to the energies of its IR absorption bands, provided the vibrational modes involved are both IR and Raman active. Therefore, IR spectroscopy is considered a complementary technique to Raman

spectroscopy and is discussed in many cases for completeness [1, 2].

One of the difficulties associated with Raman spectroscopy is the inherently low sensitivity, due to the small scattering cross section of many materials and, consequently, Raman signals can be weak (one scattered photon per 10 million incident), which limits its applicability [5]. Sensitivity enhancement is accomplished by SERS, a phenomenon in which the Raman scattering intensity from molecules close to the surface of nanostructures of a good conductor is enhanced [1, 2].

2.2 Surface-enhanced Raman spectroscopy

When Fleischmann, Hendra and McQuillan, in 1974, were interested in studying species adsorbed on large-area oxide catalysts, they come across an unusually strong and potential-dependent Raman signal on electrochemically roughened silver electrodes (fractal like) [6]. Since the positions and intensities of the Raman bands of pyridine ring-stretching modes were affected by the voltage applied to the electrode, the authors attributed the phenomenon to an increase of surface coverage of pyridine molecules on the electrode [6, 7]. This simple explanation, although appealing, did not explain the increased Raman scattering cross section per molecule compared to the same molecule in solution, as independently demonstrated by Jeanmire and Van Duyne [8] and Albrecht and Creighton [9] three years later, in 1977. The large intensity (enhancements factors of $10^5 - 10^6$) could not be accounted for only the increase in surface area, and consequently, Van Duyne's and Creighton's groups proposed enhancement mechanisms based on electromagnetic and chemical effects, respectively, and the acronym SERS was coined [8, 10]. Although Albrecht and Creighton [9] suggested a resonant Raman effect involving plasmon excitation based on Philpott's work [11], it was Moskovits who later provided the grounds for the understanding of electromagnetic effect in metallic surfaces by making the connection of SERS intensities to enhanced fields arising from localised surface plasmons in nanostructured metals [12].

Despite the initial enthusiasm, the irreproducibility of substrates fabricated by electrochemical roughening led to significant variability in SERS spectroscopy performance, causing a withdrawal from the SERS spectroscopy field in the mid-1980s [13–15]. Over the following years, SERS spectroscopy research reached a plateau (reviewed by Moskovits in 1985) [16], and a renewed interest was only observed in 1997, mainly in response to the two independent works of Nie and Emory [17], and Kneipp *et al.* [18]. As previously foreseen by Pettinger *et al.* in 1988 [19], who demonstrated that rhodamine 6G cross section was competitive with that of an allowed electronic transition when adsorbed on silver, both groups, demonstrated that detection of a single-molecule was possible by SERS. They isolated light emissions from a single NP aggregate, reporting SERS spectra of individual molecules under specific conditions (which was not possible due to instrumental deficiencies prior to the 1990s) [17, 18]. Revolutionary developments in Raman spectrometers, such as light amplification by stimulated emission of radiation

(LASER), background light rejection based on filters instead of gratings, and the replacement of photomultipliers by charge-coupled-device (CCD) detectors, allowed researchers to work with reduced laser excitation intensities with a high-sensitivity Raman scattering detection [20]. Allied to Raman instrumentation improvements, the advances in nanoscience contributed to catalysing an explosion of new possibilities regarding SERS substrate design and fabrication. Hence, SERS spectroscopy evolved from a curious physical phenomenon to a true multidisciplinary field, to which the development of a robust and effective analytical technique has attracted scientists from various backgrounds as such physics, chemistry, biology, engineering, among others [21, 22].

2.2.1 Fundamental theory of SERS

SERS is a nanoscale phenomenon that enhances the Raman signal of molecules adsorbed on metal nanostructured substrates [7, 23]. The origin of this observed enhancement have been long debated and it is now accepted among researchers that the overall enhancement (quantified in terms of the enhancement factor (EF) [24]) can arise from either and/or a combination of two mechanisms: so-called chemical enhancement (CHEM) [25], due to charge transfer mechanisms to or from the metal particles (commonly known as metal-molecule bond), and electromagnetic enhancement (EM) [26], associated with surface plasmon excitation in metal nanostructures.

The chemical enhancement mechanism of SERS is based on the interaction of chemisorbed molecules with the metal surface and is independent of the EM environment [27, 28]. CHEM can be attributed to two contributions: the changes in the polarisability derivative due to the transfer of charge induced by the molecule adsorbed on the metal, and the lowest unoccupied molecular orbital (LUMO) to highest occupied molecular orbital (HOMO) transition of the chemisorbed molecule. This occurs when the energy of the transition falls symmetrically with the Fermi level of the metal surface and then the excitation of half the energy can make the transition. Generally, its contribution to the EF is of the order of one to three orders of magnitude [29], and significantly smaller than the EM contribution, which is commonly considered to be the dominant mechanism for SERS [21].

Raman scattering efficiency is related to the interaction of the electromagnetic field of the incident light, of specific wavelengths (or frequency ω), with the polarisability of the scattering bond. EM enhancement is the result of the concentration of electromagnetic energy $E(\omega)$ in the vicinity of a good, nanostructured, conductor, when the incident light frequency is resonant with that of the collective oscillation of the nanostructure surface electrons. The electronic oscillation of the surface electrons causes a charge separation with respect to the ionic lattice, originating a dipole oscillation in the direction of the electric field of light, a phenomenon known as localised surface plasmon resonance (LSPR). As a result, this localised electric-field enhancement can act as an antenna, leading to highly amplified Raman scattering signals of molecules adsorbed onto, or in the vicinity

of the surface of the nanostructures [4, 5, 23, 30]. The SERS enhancement can be approximately described by $\frac{|E(\omega_{inc})|^4}{|E_0|^4}$, E_0 being the oscillating electric field of the incoming laser radiation and $|E(\omega_{inc})|^4 \approx |E(\omega_{inc})|^2|E(\omega_v)|^2$, because the Stokes Raman scattered frequency (ω_v) is much smaller than the incident $\omega_{inc} \gg \omega_v$ or $\omega_{inc} \approx \omega_{inc} - \omega_v$ [5].

Electric field enhancements have been observed for nanostructured surfaces and colloidal nanoparticles [31–33]. Enhancements depend on the size of the nanofeature [25] and are observed to be particularly strong in the neighbourhood of sharp peaks, at which so called "hotspots" are produced [31, 34–36]. Hotspots are also observed when the near-field regions between adjacent nanofeatures or particles overlap (Figure 2.1b) [37]. In NP systems, SERS performance is optimised by controlling their shape to produce sharp structures, or by NP aggregation. Other geometrical structures such as within NP junctions and flat metal surfaces that support surface plasmon resonance can generate hotspots and many reports try to maximise this feature with gap distances (ideally in the range of 2-10 nm) (see Figure 2.1b) [38, 39].

A persistent misconception regarding SERS EM is that the SERS excitation profile does not necessarily follow the extinction spectrum of the SERS substrate [21]. This is because the extinction spectrum of the SERS substrate includes absorptions and scattering contributions from the entire nanostructure and the SERS spectrum mainly depends on the resonances of the "hottest spots" [40]. In fact, works by Schatz and Van Duyne [23], showed that highest EM could be achieved away from the wavelength of maximum absorption, due to "dark" plasmon, or quadrupolar modes. These dark plasmon modes can lead to strong far-field intensities because the dipole field of the absorbed molecules can excite quadrupolar and higher-order multipolar resonances with better efficiency than light waves [23].

Ultimately, the EM depends on the nanostructure's inherent properties (*e.g.* material, size and shape) and the CHEM is determined by the chemical features of the analytes attached onto the metal surface. It should be noted that, in both cases, the SERS effect is extremely localised to the surface of the nanostructure. CHEM enhancement only applies to molecular species adsorbed to the surface, while EM enhancement decays within ≈10 nm of the surface [23]. The surface can rapidly become saturated, limiting the sensitivity of the technique, and, in the case of complex media, competitive binding can influence the selectivity. An in-depth review of the SERS mechanisms is beyond the scope of this thesis, but can be found elsewhere [23, 25, 27–29].

2.2.2 SERS in bioanalysis: Direct versus indirect detection

Whilst developments in treatment and prevention are important factors in overcoming disease, diagnostic tools are vital to provide accurate and timely diagnosis of life-threatening conditions. Early and accurate disease detection is critical for clinical diagnosis and in many situations determines the treatment success and ultimately the patient outcome[41]. The confirmation of a particular condition is commonly accomplished by

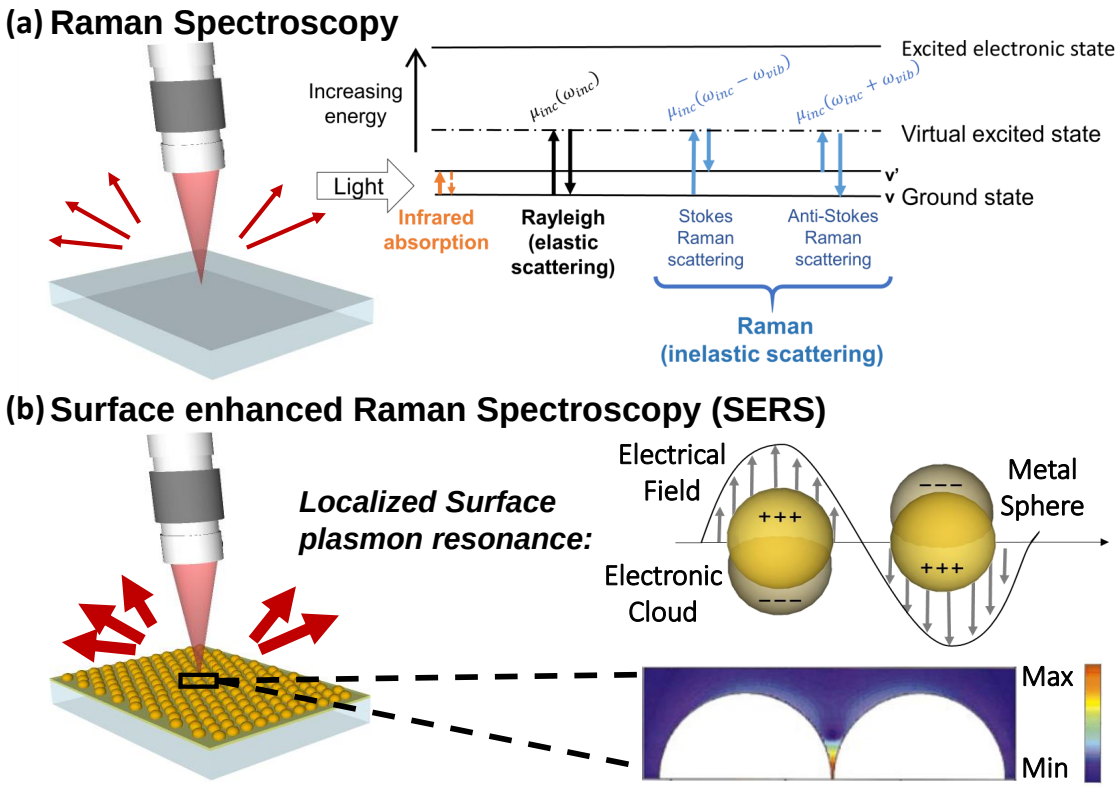

Figure 2.1: Raman versus SERS phenomenon. (a) Schematic of Raman Spectroscopy and energy diagram representing (from left to right) the infrared absorption, elastic Rayleigh scattering and the inelastic anti-Stokes (*left*) and Stokes (*right*) Raman scattering with ω_{inc}, $\omega_{inc} \pm \omega_v$ and ω_v referring to the frequencies of the incident light, the Raman scattered light, and the molecular vibration, respectively. μ_{inc} refers to the induced dipole moment, which in turn, is the product of Raman polarisability, α, and the magnitude of the incident electromagnetic field, E. (b) Illustration of SERS and of the LSPR effect. This consists of the collective oscillation of the conduction electrons in a metal NP in resonance with the frequency of the incident light. The colour plot at the bottom corresponds to the electric field intensity profile in the inter-space of a dimer with two Au nanospheres having a separation of 1 nm. The colour scale is logarithmic. Adopted from [36].

detection of molecular biomarkers. Biomarkers, individual or combined, act as biochemical indicators of a specific state, and can be used for detecting the presence or even the stage of progression of a disease. As a result, extensive efforts have been devoted to detecting and profiling techniques for early diagnosis and monitoring of diseases during the course of treatment. Traditional diagnostic tools, such as enzyme-linked immunosorbent assay (ELISA) [42–44], the gold standard for detection of proteins in physiological samples, polymerase chain reaction (PCR) [45, 46], the gold standard for detection of nucleic acids, electrophoresis [47, 48], and fluorescence methods [49, 50], among others, do not provide the limit of detection (LOD) required to detect the new, low abundance molecular biomarkers identified in recent fundamental biological studies [51]. Other techniques such as Matrix-Assisted Laser Desorption/Ionisation-Time of Flight mass spectrometer are highly specific, but the interrogation is dependent on infectious agents cultures and requires a substantial capital instrument [52].

Fundamental studies of disease have discovered that the ideal molecular profiling of disease and personalised medicine is dependent on biomarkers which are low in abundance [53, 54]. On the other hand, fundamental studies of nanomaterials have revealed new features which hold great promise towards biosensing applications [23]. This increased demand for molecular biomarker detection has instigated the development of ultrasensitive sensors based on nanotechnology.

Various nanomaterials can be used as signal transducers in biosensing systems, as they provide strong signal intensities, tuneable physicochemical properties (*e.g.* LSPR and surface chemistry) and exhibit extremely large ensemble surface areas using a very small quantity of nanomaterials [4, 5, 23]. In theory, any biomarker, identified by fundamental studies, can be correlated with suitable biorecognition ligands, which, in turn, can be coupled to any transducer. The numerous possible combinations of nanomaterials and biomarkers being integrated into miniaturised devices, present biosensor platforms a versatility that benefits tremendously diagnostic tools and can provide effective early diagnosis of life-threatening conditions [53, 55–57].

The interest in SERS spectroscopy as a bio-detection tool is due to its outstanding analytical features, such as high sensitivity, specificity, and, multiplexing and non-destructive detection abilities [4, 5, 22, 23]. Furthermore, SERS spectroscopy has evolved considerably and found application as a diagnostic tool for medical samples allowing the detection of biorelevant targets in complex biochemical matrices which is enabled due to the low interference from water resulting in minimal background signals from aqueous biological samples [56]. SERS substrates for bioanalysis applications can be fabricated via top-down approaches, involving patterned complex nanostructures on a surface, and bottom-up methods, utilising chemically synthesised NPs in suspension or assembled into well-defined arrays on a substrate [58–60].

Regarding the biosensing method, SERS spectroscopy can be explored in two ways (Figure 2.2): (i) direct or label-free intrinsic SERS and (ii) indirect or extrinsic SERS tags. The former takes profit from an enhanced Raman signal from the analyte when it is in close vicinity of a nanostructured metal surface, whereas the latter uses *a priori* knowledge of a Raman signal from a reporter molecule and utilises it as an amplified label for recognition of target analyte which is mediated by a target-specific ligand [23, 56, 61, 62]. In direct SERS sensing, if the target is within a complex medium, overlapping of vibrational modes of different molecules is inevitable which hinders interpretation. The latter offers a more universal and versatile option towards biosensing.

2.2.2.1 Immunoassays SERS-based biosensors

Biosensors are nowadays a field of high investment interest with application both in research and industry [67]. Among these, immunoassays represent a well-established affinity-based analytical test that measure a specific analyte in solution, through the binding event between antibodies and antigens [62, 68].

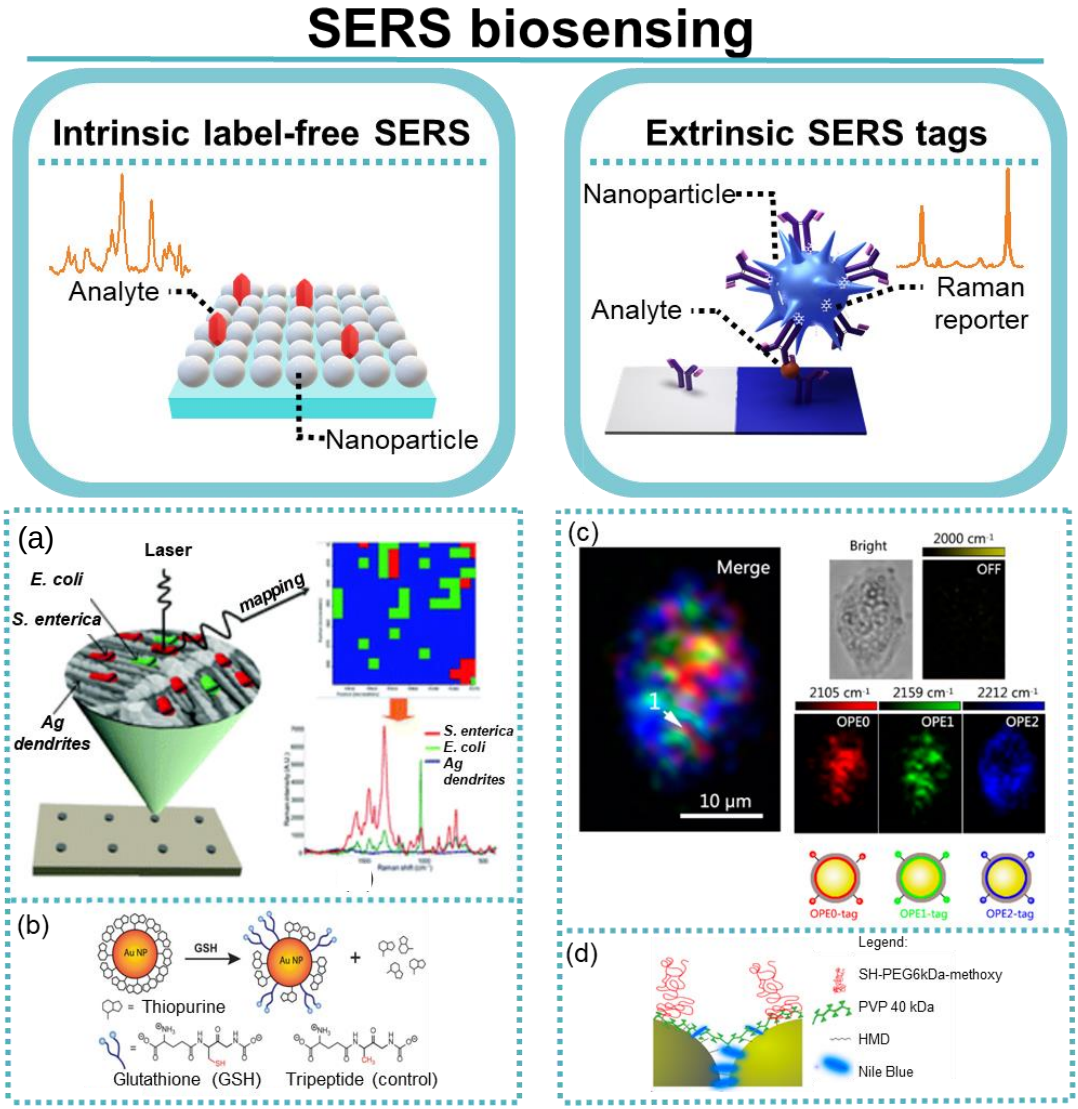

Figure 2.2: SERS spectroscopy biosensing. Left: direct or label-free intrinsic SERS. Right: indirect or extrinsic SERS tags. (a) Schematic details on the SERS-active substrate with patterned nanopillar forests and flat metal areas for self-detection. Adapted from [63]. (b) Release of thiopurine on AuNPs via glutathione. Adapted from [56, 64]. (c) Three-colour SERS spectroscopy imaging using SERS probes of alkyne SERS palette [65]. (d) Schematic of SERS-based biotags assembly process and subsequent etching of the metallic cores by hexacyanoferrate and thiosulfate. Adapted from [66].

ELISA is a powerful technique based on the antibody-antigen biding event [69]. Initially made with antibodies labelled with radioisotopes, soon were replaced by antibodies chemically linked to enzymes or fluorophores whose activities produce a measurable signal [69]. In the typical design to detect an antigen, the antigen is immobilised either by a direct adsorption or via an antibody previously adsorbed. Then, the antigen is probed with a specific antibody [69]. This antibody may be directly labelled with an enzyme or a fluorophore or it may be secondarily probed with a secondary antibody that is enzyme- or fluorophore-labelled. Several approaches derived from the original ELISA method and are represented in Figure 2.3. This method has revolutionised immunology due to its fairly good sensitivity (usually between 0.01 ng to 0.1 ng) and selectivity. However, ELISA is laborious, time-consuming, and hard to implement for point-of-care testing (POCT). SERS-based immunoassays inspired in ELISA technique represent an interesting alternative due to its high sensitivity, speed and simplicity compared to the conventional ELISA [69–73].

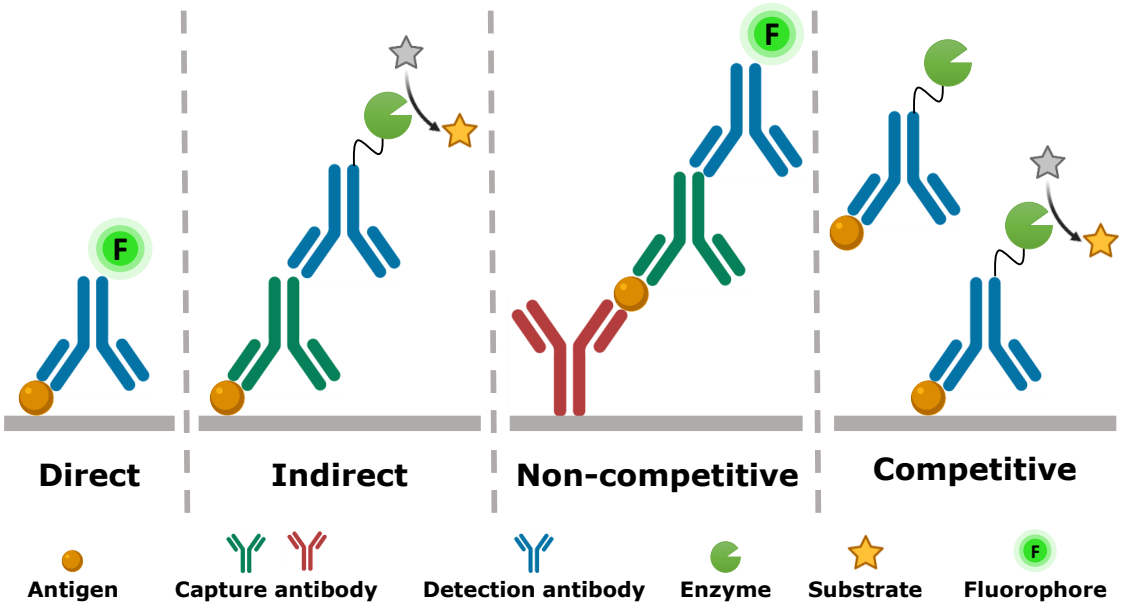

Figure 2.3: Types of ELISA test based on the antigens and antibodies bounded and detected. Direct ELISA: primary antibody binds to the antigen and has an attached enzyme or fluorophore for signal detection. Indirect ELISA: is identical to direct ELISA except that the detection antibody binds to a capture antibody previously added to bind the antigen. Non-competitive ELISA: also called sandwich whereas the antigen is captured between two antibodies followed by a detection antibody. Competitive ELISA: the substrate pre-coated with the antigen within the sample competes with the antigen added. The unbound antibody is removed, and the more antigen is in the sample, less antibody will be able to bind to the antigen in the well. The detection method might either be through an enzyme conjugated to an antibody or a fluorophore. Adapted from [69–73].

In the label-based approach, two key components are needed to form a SERS-based immunoassay: immuno-substrate and the SERS tag (also referred to as SERS immunotag) [62, 68]. Depending on binding design of the immunocomplex, SERS immunoassays

can be classified as non-competitive (widely known as sandwich) and competitive assays (Figure 2.4). In the sandwich assay, the analyte is between the capture antibody and the detection antibody. The capture antibody is immobilised on a substrate (*e.g.* surface or magnetic immunobead), whereas the detection antibody is coupled with a NP labelled with a RR (the SERS immunotag) [62, 71, 74, 75]. When the antigen binds to the antibodies present in the substrate and in the SERS immunotag, a specific SERS signal is obtained and can be correlated with detection and quantification [56, 62, 76]. Competitive SERS immunoassays use the same capture antibody, yet the signal is generated by the antigen attached to a NP labelled with a RR. As a result, the intensity of the signal is negatively correlated with concentration of the target antigen that competes for the same capture antibodies with the labelled antigens [62].

The choice between the design will rely on the type of analyte. Usually, for small analytes (*e.g.* hormones, drugs, and peptides), the competitive assays are preferred whereas, macromolecules are more suitable for the sandwich assay [62, 77]. Comparing the performances obtained by both classes, sandwich assays allow higher sensitivity, dynamic range, and reproducibility [62, 77] and are therefore used in this work. The choice of SERS tag is critical to a successful SERS immunoassay, and therefore, the following sections will focus on the properties and development of SERS tags that present the optimal features for bioanalytical assays [56, 78].

2.3 Properties of SERS tags

In optical methods, the signal generation that allows the localisation and detection of target molecules is generally provided by labelling agents. Several examples are well represented in literature, such as fluorescent dyes/quantum dots (QDs) (*e.g.*, in immunofluorescence [79, 80]), enzymes that catalyse a colourimetric reaction (*e.g.*, horseradish peroxidase in ELISA and immunohistochemistry [44, 81]) and RRs [23]. However, the detection event is entirely controlled by the noncovalent interactions of the target-specific ligands used for molecular recognition of the target. For instance, antibodies specifically recognise antigens, whereas oligonucleotide strands hybridise thanks to complementary Watson-Crick base pairing [82–84]. The target can be a metabolite or protein biomarker in blood or tissue or even a membrane protein on a specific cell. All multi-component ensembles of noble metal NPs, functionalised with RRs followed by recognition ligands, belong to a class known as SERS tags (also named as SERS nanoprobes and occasionally as SERS labels). These SERS tags provide a uniquely strong spectral signature with wide ranging applications in biological detection and imaging [84]. Table 2.1 summarises and compares the features of dyes, QDs, and RRs and Figure 2.5 shows a spectral comparison of the three types of labels, using the example of Cy5 fluorophore, 4-nitrothiobenzoic acid as RR and eight colours CdSe – ZnS core-shell QDs. To avoid confusion, the terms SERS tag and SERS probe will be used to describe a NP coated with a RR and with a target-specific ligand, whereas the term label will be used as a synonym to reporter meaning the

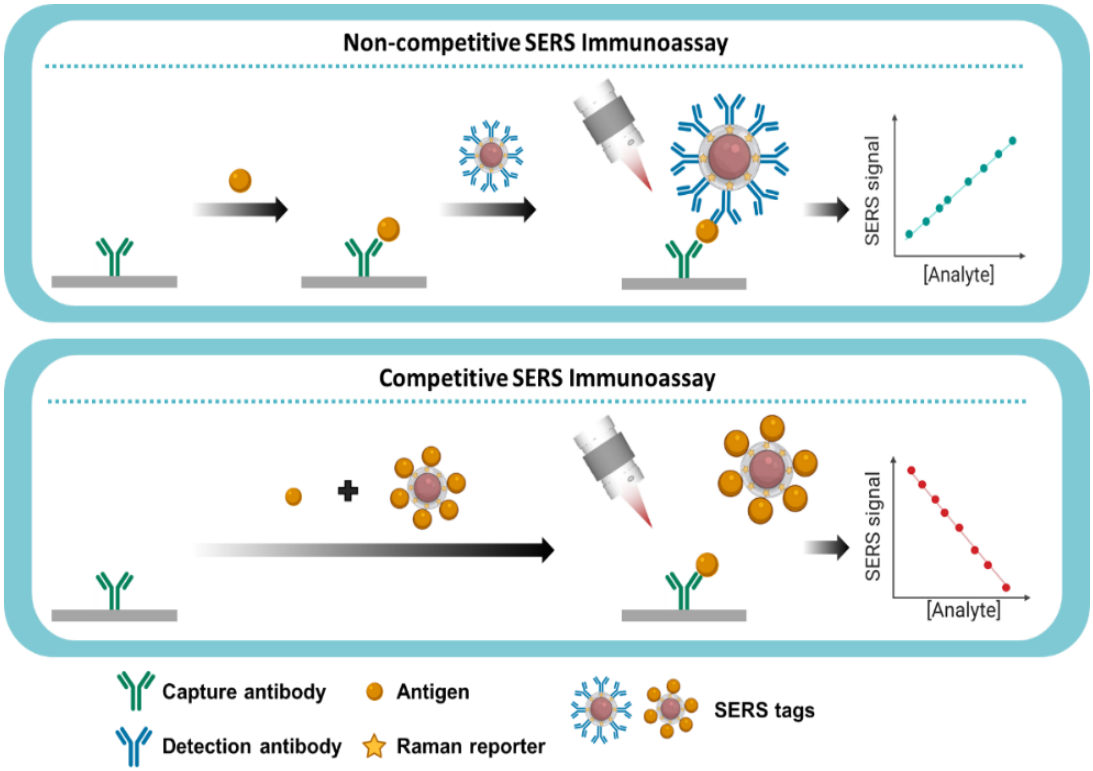

Figure 2.4: Principles of non-competitive (sandwich) and competitive SERS immunoassay. In the non-competitive SERS immunoassay, the SERS signal is generated when the RR used in the SERS tag is indirectly attached to the antigen (mediated by the respective antibody) whereas in the competitive, the signal is generated only if there is no antigen to bind the capture antibody.

specific "code" that provides the identification of the recognition event.

The advantages of SERS tags include: (i) spectral capacity for multiple detection (multiplexing) due to the narrow full width at half-maximum (FWHM) of vibrational Raman bands compared to the broad emission profiles of molecular fluorophores; (ii) quantitative ability since the SERS signal is proportional to the recognition events between analyte-ligand from the SERS tags (as exemplified in Figure 2.4); (iii) photostability, allowing repetition or long-time measurements of the SERS tag contrary to common fluorophores; (iv) possibility of addressing spectrally distinct SERS tags with a single wavelength source; and (v) sensitivity of SERS tags with plasmon resonances in red to near-IR which minimise the autofluorescence from biological tissues. Nevertheless, the size of SERS tags in studies of biological cells which require high-spatial resolution confocal microscopy might be an impairment due to steric hindrance. Other challenges are related to the bioconjugation process and the dearth of standardised protocols for quality control over the colloids in the same and different batches, as well as synthesis scalability. These are features often overlooked and are going to be addressed in this Thesis [23, 79, 84, 90–92].

Table 2.1: Comparison of SERS tags, conventional dyes, and QDs main features [85–89].

Properties	SERS tags	Dyes	QDs
Physical phenomenon	Raman scattering	Electronic absorption and Fluorescence emission	Fluorescence emission
Core composition	Noble metal NPs	Organic compounds	Semiconductor materials (*e.g.*, ZnS, ZnSe, CdS, CdSe and others)
Size	≈ 60 nm	≈ 1 nm	≈ 10 nm
Spectral FMHM[1]	2 nm	>50 nm	25–35 nm
Fingerprinting ability	Yes	No	No
Multiplexing capacity	>100 (theoretically)	≈ 20	12-15
Photostability	Strong	Weak[2]	Mid[3]
Toxicity	No	Mild	Strong
Technology maturation/ Translation to medicine	Early stage	Developed	Making the translation

[1] FMHM: full-width-at-half-maximum.
[2] Decay under weak excitation.
[3] Decay under strong excitation.

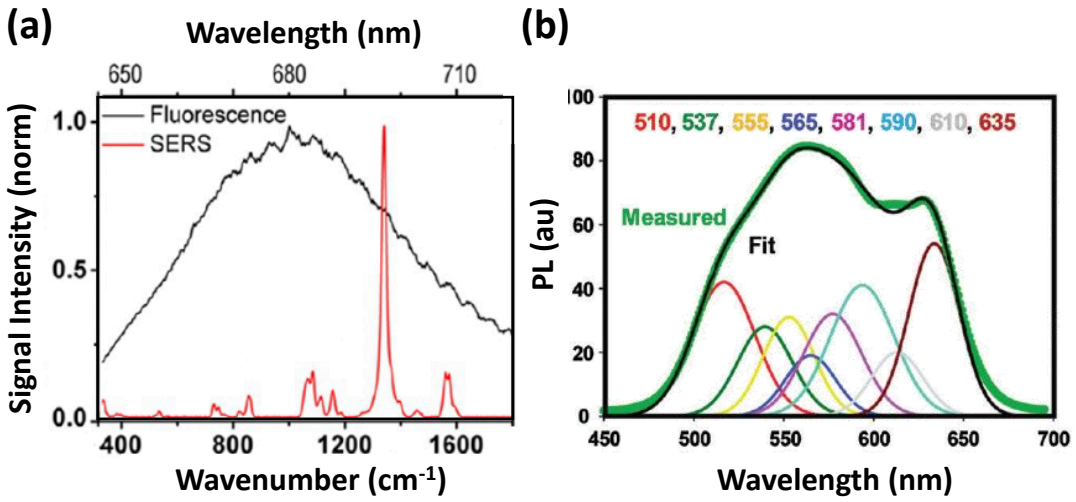

Figure 2.5: Comparison of spectral emission profiles: (a) fluorescence from Cy5 and SERS signal from 4-nitrothiobenzoic acid on gold NPs excited with 632.8 nm laser radiation. Adopted from [93]. (b) Photoluminescence spectra of QDs composite (green) with deconvolved contributions of eight different QD colours (510, 537, 555, 565, 581, 590, 610, and 635 nm QDs) and the overall model fit (black). Adopted from [94].

2.4 The building blocks of SERS tags

As depicted in Figure 2.6, a SERS tag comprises a noble metal NP core with RRs adsorbed or bounded on the metal surface, providing a Raman spectral signature and a target-specific ligand, such as an antibody or an oligonucleotide, to enable bioanalytical and biomedical applications. Between the RR and the recognition biomolecule, a biocompatible shell can be inserted to keep the RR near the NP, to maximise the SERS signal enhancement and stabilise the NPs. Each one of the components can be chosen from a large number of options, depending on the desired application: (i) the type of NP, (normally Au and Ag but other examples report the use of Cu/Mn [95], ZnO [96], $W_{18}O_{49}$ nanocrystals [97], MoO_2 [98, 99], graphene/MoS_2 nanohybrids [100] *etc.*) as well as its size and shape (nanorods and nanostars being preferred to spheres for increased signal from hotspots [31]); (ii) number of NPs: single versus clusters (assembly of NPs offers gaps which are a source of hotspots for increased signal); (iii) the type of RR (*e.g.*, fluorescent dyes or small aromatic thiols); (iv) the protective shell (*e.g.*, polymers as polyethylene glycol (PEG), biomolecules, and silica); (v) the type of bioconjugation process, depending on the functional groups available from the previous step (*e.g.* carboxylic acids, amines, thiols, *etc.*) [21, 23, 61, 82–84, 101, 102]. Figure 2.6 represents the sequential procedure for designing a SERS tag and Table A.1 in appendix A summarises the most common molecules that form a SERS tag.

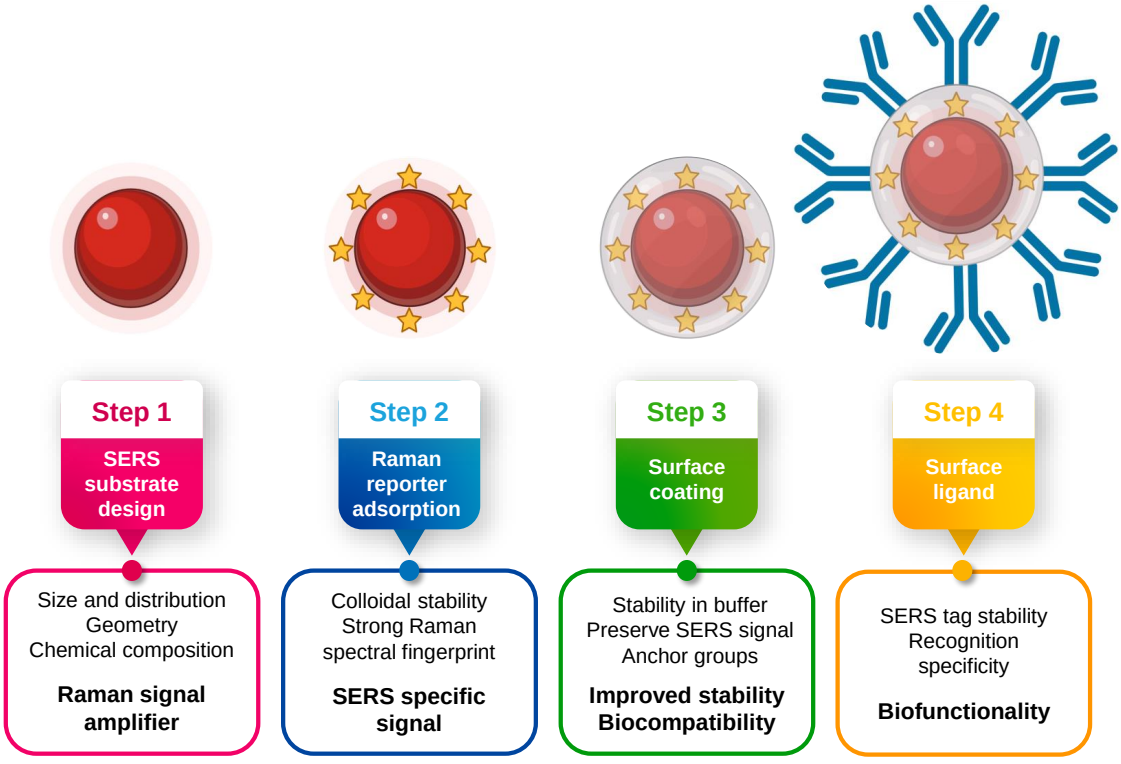

Figure 2.6: Sequential procedure for fabricating a SERS tag.

To fulfil the promise that SERS tags hold, *i.e.*, achieve specific and quantitative detection, care must be taken during the SERS tags design. The choice of each component will ultimately depend upon the application and to combine all the necessary features without compromise is not a trivial task. For instance, in biomedical applications, one has to consider the optical window of human tissue [86] and the pH of a medium, as well as phenomena such as tissue extravasation, opsonisation [103], cytotoxicity, enzymatic cleavage, cellular uptake mechanisms, the ability to avoid or resist the endolysosomal network, among others [83, 86].

2.4.1 Signal amplifiers: Inorganic nanoparticles

The metal NP of the SERS tag is essential for signal enhancement and to act as a structural scaffold. Its optical properties, in particular the position and intensity of the LSPR band, will determine the efficiency. As mentioned in section 2.2.1, the LSPR of metal NPs strongly depend on the size, shape, and composition [23]. Gold and silver are the metals most frequently used, gold being preferred in the biomedical field compared to other plasmonic NPs, due to lower toxicity and high stability [104–106], whereas silver is favoured when the SERS efficiency is the limiting factor and not the stability [104–106]. Alloys of Au and Ag combine the stability of gold and the enhancement activity of silver, giving signals 10 to 100 fold higher [33]. These types of alloys have been applied in SERS-based immunoassay [107], cell imaging [108], label-free chemical detection [109, 110], and drug delivery [111].

Having a history that dates to ancient Rome [112], ever since Faraday's work on spherical gold nanoparticles (AuNPs) [113], numerous protocols have been developed for the synthesis of nanospheres of Ag and Au [113, 114]. Chemical synthesis by the reduction of metal salts is well-known and can be performed with a diversity of reducing and capping agents. The capping agent works as a stabiliser to prevent the particles from aggregating, yielding a common and cost-effective approach to yield monodisperse metal spherical NPs of Ag and Au. The surface of the resultant Au and Ag NPs can be readily modified by thiol and disulphide stabilisers providing a simple route to surface modification [115]. Choice of the type of stabiliser is determined by the further bio-functionalisation strategies [116].

The narrow size distribution, with low or no coalescence, generates homogeneous Raman scattering cross sections. Thus, single spherical NPs give comparable SERS intensities which is essential for quantification purposes. These spherical NPs have long shelf lives, retaining their morphology, which offers quality control for downstream applications. However, the common synthesis methods produce NPs with an average diameter of 10-20 nm, which results in LSPR centred at 520 and 400 nm for Au and Ag nanospheres, respectively. This is unsuitable for the near-IR spectral region, in which the effective attenuation coefficient is lower for biological tissues [86]. Increasing the NP size results in a red-shift. Nevertheless, increasing the size results in larger radiation damping effects

which decreases the enhancement [117]. Thus, the size range of 30-100 nm obtained for spheres is not sufficient for near-IR radiation [118–120] and the sensitivity provided by a single nanosphere is low (EF $\approx 10^3$).

To increase SERS tag brightness, the NP must possess hotspots [23]. These locations, at which the near field is enhanced, occur at tight junctions between metallic NPs, edges, and vertices in non-spherical NPs [34, 36]. As result, the morphology is considered as the factor that can most influence the SERS efficiency [23].

Two different ways can be explored to increase the number of hotspots, by controlled NP assembling to form clusters (*e.g.* dimers [32, 121] and core–satellite systems [122, 123]) or by production of anisotropic NPs with intrinsic hotspots (nanorods [124–127], nanostars [23, 58, 71, 128], nanocubes [129], nanocages [130], nanotriangles [131], nanoprisms [131] and others [132–135]). The final NP shapes are tuned using agents that lead to a preferential growth starting from a specific crystal facet [136].

The advantage of using nanostars is the sharp branches emanating from a core giving several hotspots per particle [137–139] with multiple resonances – the so-called "sharp tip effect" [139]. The nanostars provide plasmonic near-field enhancements and lightning rod effect (maximised in a tip-to-tip nanostar dimer) which leads to EFs of orders of 10^9 [23, 140–142]. Although challenging, their plasmonic properties can even be controlled by modulating the morphology of their arms and consequently enhancing the SERS signal [143]. The gold nanostars are typically produced by the seed-mediated approach [142, 144] or by the 4-(2-hydroxyethyl)-1-piperazineethanesulfonic acid (HEPES)-based approach [141]. Using silver as director agent proved to be advantageous to synthetise citrate capped gold nanostars (AuNSs) that can be easily replaced by another capping agent (*e.g.* Raman reporter) [142]. Silver ions adsorbed preferentially on certain crystal facets of gold seeds block the growth of these facets forcing the newly available gold ions deposit only in the remaining crystal faces [142, 144]. Anisotropic etching can also be used to control the NP shape, achieving new NP structures with high yield and purity that cannot be attained by the conventional chemical NP synthesis [145].

It should be noted that the advantage of multiple intrinsic hotspots only applies to particles in colloidal suspensions. As demonstrated by Solís *et al.*, simpler morphologies might lead to higher enhancements when in an organised close packed array [31]. Furthermore, tips of nanostars and nanorods are dynamical evolving entities due to atom migration and facet reorganisation [126] and the modification of the tips, with time [146], can lead to the loss of SERS activity [138].

While most of the published work is based on metal nanostructures, one non-metal substrate that has been demonstrated to enhance Raman signals of adsorbed molecules in a clean and stable way is graphene. Relying on the chemical enhancement caused by charge-transfer interactions between the molecule and the monolayer substrate, graphene-based enhanced Raman scattering (GERS) presents EFs of one or two orders of magnitude [147]. This enhancement can be improved by coupling metal nanostructures, a technique known as G-SERS [148]. This resonant Raman effect was also predicted to

occur in semiconductors for charge transfer states between the molecule and the semiconducting substrate [149]. Therefore, studies on monolayer semi-conducting transition metal dichalcogenide substrates such as ZnS@GO [150] MoO_2 [99, 151], $MoS_{(2-x)}O_x$ [152], WSe_2-perylene-3,4,9,10-tetracarboxylic dianhydride [149] are now being performed and hold promising results for highly active SERS substrates [96, 149].

2.4.2 Coding: Raman reporters

Raman reporters are also called Raman labels and the terms are used in this work interchangeably. They are molecules responsible for the indirect detection of a selected analyte, a process which can be considered extrinsic labelling. The enhancement observed in SERS requires that RR molecules be bound to, or near the surface of the metal, since the EM enhancement is distance-dependent and CHEM enhancement requires chemical bonding [5]. An ideal RR exhibits the following properties: (i) high Raman scattering cross sections for high brightness; (ii) a small number of atoms and/or high symmetry, thus presenting a limited number of vibrational bands to reduce possible overlaps and improve spectral multiplexing; (iii) no photobleaching for signal stability upon illumination with laser light, and (iv) ability to bind to a metal surface, usually by possessing nitrogen- and/or sulphur- containing moieties for chemisorption onto the metal surface. If the RR does not contain any of these surface-seeking groups, it should still be strong enough to prevent desorption during the following modification steps [23, 61, 92, 102, 153].

In terms of RRs, there are two main options, chromophores and fluorophores or small aromatic thiols. Chromophores and fluorophores are excellent RRs since, under resonant Raman conditions, known as surface-enhanced resonance Raman scattering (SERRS), the enhancement can increase 10-100 fold compared to conventional SERS spectroscopy experiments with electronically non-resonant molecules. The combination of different dyes in multiplexing analysis, although promising, is difficult to accomplish due to the lack of dyes with similar absorption bands or with a broad range of excitation wavelengths [61, 62, 82, 154, 155]. Efforts have been made towards the synthesis of reporters that absorb in the near-IR spectral region through synthesis and screening members of libraries of compounds such as triphenylmethine and tricarbocyanine (Figure 2.7a,b) [156–158]. Still, this has proven a difficult task and the examples in literature are scarce [156–160]. Also, in the case of fluorophores, the tag design is especially important since the fluorescence can generate intense background [66].

Aromatic thiols, isothiocyanates and amines, on the other hand, are small, also have high Raman cross sections and are poorly fluorescent [62]. Due to their structure that contains surface-seeking moieties for chemisorption, they can form a self-assembled monolayers (SAM) on gold surfaces *e.g.* via Au-S bonds [161]. The dense packing in SAM offers a uniform orientation of RR molecules and therefore the response to an individual binding event is markedly amplified. Consequently, other molecules present in the surrounding

medium, from buffers or synthesis reagents, are not adsorbed on the metal surface and spectral interferences are minimised or complete avoided. This generates maximum SERS brightness with reproducible SERS signatures, in contrast to fluorescent dyes, for which the packing density is much lower [58, 92, 101, 153, 162–164]. A study undertaken by Schlücker's group showed an increase of 22 times in the RR SERS signal when the NPs had a complete monolayer coverage, compared to those NPs with sub-monolayer coverage (Figure 2.7c, d and e) [165]. This confirms what is illustrated by equation 2.1, that the SERS brightness of a single tag is proportional to the number of RRs attached to the NP:

$$P^{SERS}(\omega_s) = N_S \sigma^{SERS}_{effective} \cdot I(\omega_{inc}) \Longleftrightarrow P^{SERS}(\omega_s) = N_S \cdot \sigma^{R}_{adsorbed} \cdot |A(\omega_{inc})|^2 \cdot |A(\omega_s)|^2 \cdot I(\omega_{inc}) \tag{2.1}$$

The SERS brightness *i.e.*, SERS Stokes signal $P^{SERS}(\omega_s)$, depends on excitation laser intensity $I(\omega_{inc})$ and on the effective SERS cross section $\sigma^{SERS}_{effective}=\sigma^{R}_{adsorbed}\cdot|A(\omega_{inc})|^2 \cdot |A(\omega_s)|^2$, which is influenced by the Raman scattering cross section of the adsorbed molecule $\sigma^{R}_{adsorbed}$, that is enhanced due to CHEM when compared to the cross section in a "normal" Raman experiment. $A(\omega_{inc})$ and $A(\omega_s)$ are laser and Raman scattering field enhancement factors, respectively. N_S is the number of molecules that undergo the SERS process [105, 166].

Also, in this case, no or minimal photobleaching occurs, since resonant electronic excitation of the molecule is not required. Due to their smaller size and higher symmetry, aromatic thiols produce fewer vibrational bands ($3N-6$ and $3N-5$ vibrational bands for nonlinear and linear molecules, respectively, N = number of atoms). Thus, smaller Raman labels maximise multiplexing capacity, whereas overlapping contributions from different fluorophores can only be differentiated by multivariate analysis methods [2].

However, SAM of RRs is limited to a few charged molecules [165]. For instance, 4-mercaptobenzoic acid (MBA), has a thiol group for Au attachment and carboxyl group to generate negative charge in solution. It is difficult to produce these high coating densities in uncharged molecules on NPs without inducing severe aggregation.

Instead of selecting the suitable RRs and optimising the functionalisation according to the chemistry of each RR, some researchers use custom-made RRs [156, 159, 167–169]. For example, benzotriazole azo dye proved to be a suitable scaffold for excellent SERRS dyes [168]. Some groups used dyes with alkynes (C≡C) [170], nitriles (C≡N) [171, 172], azides (N_3) [75], and deuterium (C−D) [173] that show single narrow bands in the biological Raman-silent spectral window (1800–2800 cm^{-1}), avoiding background interference [169, 171] (Figure 2.7f). A remarkable approach from Fujioka and co-workers [167] enabled the synthesis of Raman labels that generate strong signals due to electronic preresonance upon reaction with enzymes in live cells [167] (Figure 2.7g). These cases illustrate the need for rational design and screening of novel reporters.

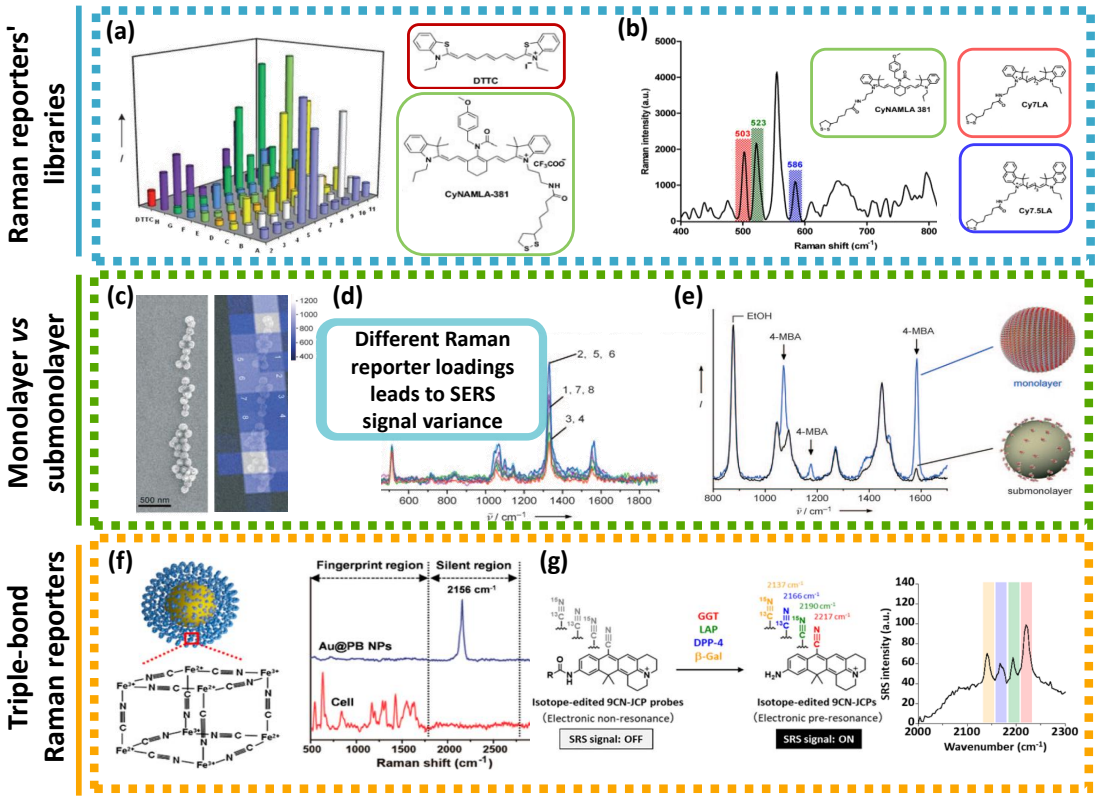

Figure 2.7: RR libraries examples, coverage influence and triple-bond RR examples. RR libraries examples. (a) Comparative SERS intensities with excitation at 785 nm of the whole 80-member of the CyNAMLA library. The molecule 3,3'-diethyl-thiatricarbocyanine (DTTC in the figure) was used as reference and is plotted (red bar) and the molecular structure is represented in the red box. The highest near-IR SERS intensity was obtained for the compound CyNAMLA-381 (green bar) and its molecular structure is represented in the green box. Adopted from [158]. (b) Demonstration of multiplex ability of SERS spectroscopy detection in the liver of SERS tags with Cy7LA (red shade and box), CyNAMLA-381 (green shade and box) and Cy7.5LA (blue shade and box) as RRs. Adopted from [159]. RR coverage influence. (c) Left: scanning electron microscopy (SEM) image of silica-encapsulated SERS reporters on a silicon wafer. Right: False-colour SERS map overlaid with the SEM image. (d) SERS spectra of 5,5'-dithiobis(2-nitrobenzoic acid) obtained from squares labelled 1–8 in (c). (e) Impact on SERS signal strength due to differences in surface coverage: complete SAM produces a stronger SERS signal compared to submonolayer coverage with RRs. Triple-bond RRs. (f) Left: Schematic illustration of the AuNP-Prussian blue: a 30 nm AuNPs treated with $K_3[Fe(CN)_6]$ followed by a CN-bridged Prussian blue (PB in the figure) shell formed by treating with $K_4[Fe(CN)_6]$ and $FeCl_3$ simultaneously. Right: Raman spectra of Prussian blue coated AuNPs and HepG2 cells. Biological species exhibit complex multiple bands in the fingerprint region, whereas the AuNPs-Prussian blue possess an intense and sharp single band (2156 cm^{-1}) in the cellular Raman-silent region throughout the whole spectrum. Adopted from [172]. (g) Development of activatable RRs for enzyme activities based on isotope-edited xanthene derivative bearing a nitrile group at position 9 (9CN-JCPs): 9CN-JCP (red), 9C15N-JCP (green), 913CN-JCP (blue), 913C15N-JCP (yellow). The Raman signals from 9CN-JCP-based reporters are activated upon reaction of the RR with the target enzyme because the absorption is shifted from the visible (electronic nonresonance conditions) to the near-IR region (electronic preresonance conditions). GGP: γ-glutamyl transpeptidase; LAP: leucine aminopeptidase; DPP-4: dipeptidyl peptidase-4; β-Gal: β-galactosidase. Stimulated Raman scattering spectra of enzyme activities obtained from H226 cells. Adopted from [174].

2.4.3 Protection and stabilisation: coating layer

At this stage, the strong and specific SERS signal from the RR is assured by the proximity to the plasmonic NP. To enclose the NP and the RR, a coating is usually employed. To guarantee the brightness stability of SERS tag, the interaction between NP and the RR should be much stronger than that between the NP and the coating protecting layer to avoid RR displacement. This protective shell prevents the displacement of RRs from the proximity of the metal surface as well as adsorption of spectrally interfering molecules which reduces the brightness of SERS tags. Also, the encapsulant improves colloidal stability, making them suitable for dispersion in biological fluids without being prone to aggregation due to high-ionic-strength media. Furthermore, the coating can improve water solubility and biocompatibility, since it prevents metal substrate exposure to the biological environment that can elicit cytotoxicity [5, 23, 61, 83, 92, 153, 175].

Simultaneously, the coat can provide a surface for subsequent bioconjugation. Biofunctional stabilisers, for instance, are used to stabilise and introduce chemical functionalities (*e.g.* thiolated-PEG molecules having carboxylic, amine, azide groups, *etc.*). A highly important aspect for the coating shell is to avoid non-specific binding, *i.e.*, the binding selectivity should only occur by the target-specific binding molecule [61, 83, 153].

The coating typically falls into four classes (Figure 2.8): (i) short spacers that provide direct hydrophilic stabilisation of SAM, (ii) biomolecules, (iii) polymers, (*e.g.* PEG), and (iv) glasses such as silica. Table 2.2 shows the main advantages and disadvantages of materials used as coating layer to protect and stabilise the final SERS tags.

2.4.4 Specificity entities: target-specific ligands

The specificity towards the target analyte is provided by the last step of the preparation of SERS tags, the bioconjugation with a target-specific entity. The most frequently used biomolecules for targeting molecules are antibodies [208], aptamers [209], oligonucleotides [177], and small-molecules ligands such as folic acid [210, 211], and toxins [23, 82, 212].

Parameters such as purity, affinity, and orientation of these elements attached to the NPs influence greatly the targeting efficiency. The bioconjugation strategy depends on the configuration of the SERS tag components chosen, which influences the stability and performance of the SERS tag. The target moiety needs to be bound in a way that ensures no exchange with other tags and the coverage should be optimised to maximise the amount of target-ligand interaction while minimising nonspecific interactions. Covalent bonds are preferred, since they do not allow "cross-talk" between different SERS tags [62, 76]. The conjugation can be done directly to unprotected SERS tags, or through the conjugation of ligands to protected SERS tags [23, 84, 153].

For unprotected SERS tags, the adsorption of the targeting entity can be performed by electrostatic interactions or covalent binding. Noncovalent methods might lead to a co-adsorption of a thiolated RR and antibody molecules, leading to a mixed monolayer [213].

Table 2.2: Comparison between the advantages and disadvantages of well-established materials used for coating SERS tags.

Coating layer	Advantages	Disadvantages	References
Short hydrophilic spacers	Colloidal stability Water solubility Controlled bioconjugation Minimum non-specific binding	High synthetic complexity Longer EG chains impairs its use *in vivo* applications No scalable	[84, 162, 176–178]
Biomolecule	Biocompatibility Availability Versatility Ability to design stimulus responsive tags Low-cost	Limited to detection *in vitro* or *ex vivo* Enzymatic cleavage when in contact with biological environment	[128, 134, 179–184]
Polymers and Biopolymers	Colloidal stability Biocompatibility Versatility Minimum non-specific binding Chemical oxidation resistance Controlled bioconjugation Suitable for *in vivo* applications Ability to design stimulus responsive tags	High-cost No scalable Batch-to-batch variability High-molecular-weight polymer: suboptimal bioconjugation Low-molecular-weight polymer: fail to provide colloidal stability Layer-by-layer polyelectrolyte coating unsuitable for *in vivo* delivery	[116, 135, 136, 185–199]
Silica	Physical and chemical stability Applicable to multiple NP morphologies Long-term storage	Labour-intensive Time-consuming Requirement for protective atmosphere (use of moisture-sensitive silane) Prone to nonspecific binding	[76, 93, 164, 200–206]

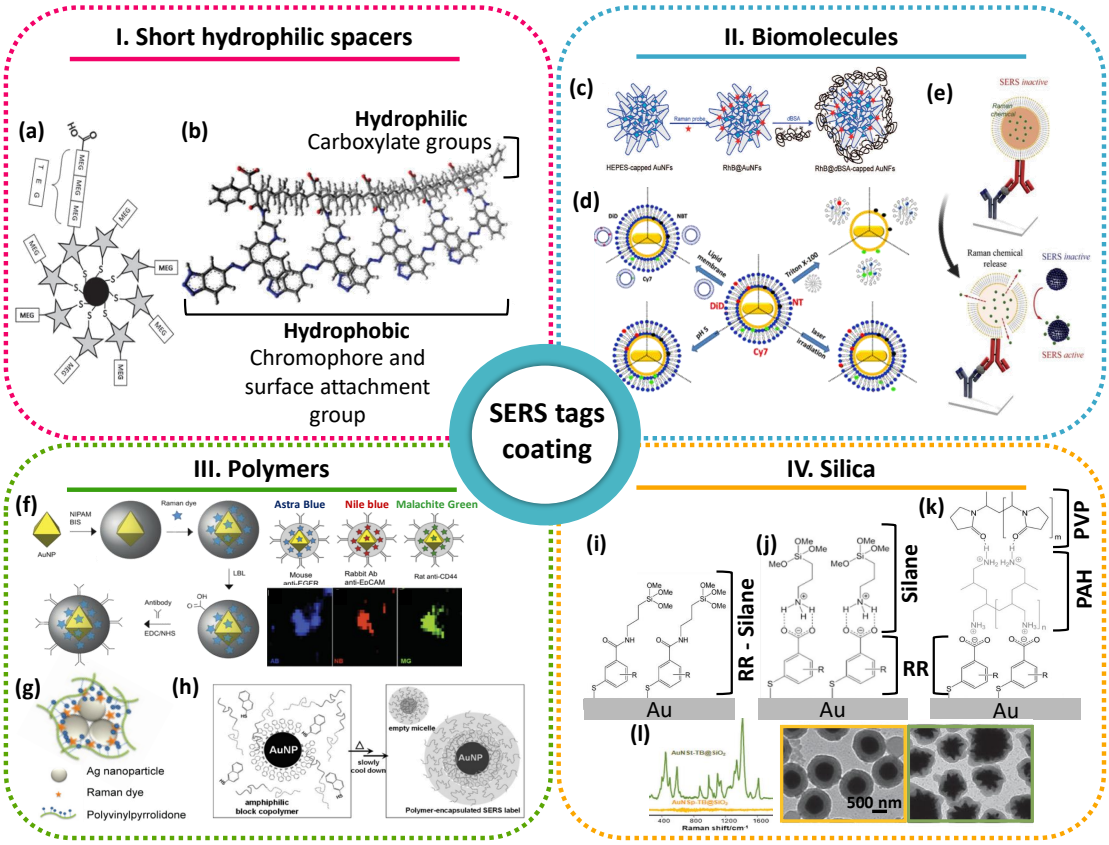

Figure 2.8: SERS tags coating approaches. (I) Hydrophilic short spacers. (a) mono- and triethylene glycols are conjugated with the RRs to stabilise the SAM and provide terminal carboxy moieties to bioconjugation of biomolecules. Adopted from [162]; (b) schematic representation of the chemical structure of the polymer dyes: oxygen atoms of the carboxylates are highlighted in red and N–N bonds in the attachment groups in blue. Adopted from [176]. (II) Biomolecules. (c) design of denature albumin protected gold nanoflowers as SERS tags. Adopted from [134]; (d) schematic illustration of the location of each RR in lipid-coated SERS tags and the lipid dissolution after: liposome fusion; addition of 10% Triton X-100; lowering the pH to 5; and photothermal treatment. The liposome SERS tag is divided in three and each part represents one kind of tag. Adopted from [207]. (e) Schematic representation of RR-encapsulated liposome-that upon stimulus release the RR and a SERS signal is generated when in contact with Au@Ag-assembled silica NPs. Adopted from [107]. (III) Polymers. (f) Left: design of Au@pNIPAM SERRS-encoded tags. Right: SERRS tags scheme and corresponding mapping using different bands for each reporter: 748 cm^{-1} band of Astra Blue in blue; 592 cm^{-1} band of Nile Blue and 420 cm^{-1} band of Malachite green. Adopted from [185]; (g) Polyvinylpyrrolidone-coated, Raman-tagged AgNPs. The aggregation is induced by adding a NaCl solution and the addition of polyvinylpyrrolidone forms a shell around the SERS tags. Adopted from [197]; (h) Preparation of polymer-encapsulated AuNPs by self-assembly by heating the AuNPs with 2-naphthalenethiol and PS154-b-PAA60 followed by gradual cooling. Adopted from [199]; (IV) Silica. Encapsulation routes for silica coating: (i) RR molecules with covalently bound terminal SiO_2 precursors; (j) silane as a noncovalently bound SiO_2 precursor bound to the RR molecule with a polar head group (*e.g.* carboxylic acid) and (k) use of two polyelectrolytes (polycyclic aromatic hydrocarbon and polyvinylpyrrolidone) to render the surface vitreophilic. Adopted from [164]. (l) Left: SERS spectra of the spheric (AuNSp-TB@SiO_2) and star-shaped (AuNSt-TB@SiO_2) SERS tags. Right: transmitance electron microscopy (TEM) images of each SERS tag. Adopted from [204].

If the thiolated RR with a functional terminal group forms a SAM, then the protein can be covalently attached through the formation of an amide linkage [214]. In this second approach, Ni *et al.* circumvented non-specific binding and "cross-talk" between different SERS reporters, but failed to avoid the steric accessibility of carboxilic groups moieties in the SAM on the Au surface for posterior bioconjugation [213, 214]. A further improvement was developed by Porter and co-workers that consists of introducing mixed thiols, one aromatic thiol for the characteristic Raman signal and a second alkylthiol with a terminal functional group (*e.g.*, succinimidyl group) for bioconjugation [214]. SERS tags can also bound directly to the NP for deoxyribonucleic acid (DNA) detection. Graham and McKenzie, for instance, conjugated thiolated DNA to SERRS labels through the strong Au–S bond for DNA detection [177]. Incubation of thiolated aptamers or oligonucleotides can partially replace the stabilising molecules from NPs (such as citrate) and still maintain colloidal stability. When the SERS tag is protected by a stabilising shell, the terminal functional groups of the protective entity most frequently end in carboxyl groups or primary amines. These groups can then form an amide bond by carbodiimide activation [215]. This type of coupling strategy has been employed to hydrophilically stabilised SAMs, polymer- and silica-encapsulated SERS nanoprobes [153]. Other chemical approaches include binding of biotin-modified tags to avidin or streptavidin-modified NPs, silane chemistry, Michael addition, click chemistry, or Diels-Alder reaction, among others [216].

The SERS tag signal generation is controlled by the interaction of recognition biomolecules towards the specific target. Consequently, parameters used in the chosen conjugation scheme, namely, chemical reactions involved, linker, anchoring groups, stoichiometry between biomolecules and NPs, and conjugation conditions, determine the effectiveness of the SERS tag and should be designed accordingly for the given target and assay. Due to its importance, the following section is dedicated to bioconjugation strategies.

2.5 Bioconjugation strategies

Bioconjugates in nanotechnology are a popular approach that have two major biomedical applications, namely therapy and diagnosis. They consist of a hybrid material involving the attachment of inorganic NPs to biomolecules allowing the NPs to interact with biological systems in a specific manner [116, 217–219]. Nanoparticle-biomolecule conjugates combine the beneficial properties of inorganic particles such as magnetic moment or LSPR, with biorecognition provided by proteins (*e.g.* enzymes or antibodies), or nucleic acids such as aptamers or complementary oligonucleotides [116, 191, 220, 221].

Depending on the application, it is necessary to choose the targeting component and the strategy to attach it on the surface of the particle considering the kinetics of the reaction and the stability during the assay. Assuring that the NPs remains stable in solution is often the biggest challenge while bioconjugation process takes place. This is a

consequence of using compounds for bioconjugation that disturb the fragile balance between attractive and repulsive forces. Besides colloidal stability, bioconjugation processes can have significant impacts on physico-chemical properties such as size, surface charge, hydrophobicity and targeting features [116, 217–219].

Due to the diversity of NPs and biomolecules reported to date, the choice of a coupling strategy is nontrivial. Depending on the nanosystem, different functional groups, biomolecules to attach, stability and hydrophobicity degrees, will dictate the bioconjugation conditions (*e.g.* pH, temperature, ionic strength, solvent choice, structure of the surfactant). As a result, there are no standardised protocols for NP bioconjugation, and each research group must balance pros and cons [116, 217–219].

Immobilisation of biomolecules can be accomplished by two main mechanisms, simple adsorption, or chemical linkages. Adsorption is very useful because takes profit from the noncovalent forces (hydrogen bonding, ionic interactions, and van der Waals forces). Chemical linkages allow immobilisation of the biomolecules on a biocompatible matrix, normally using bifunctional linkers [116, 217–219]. The strategies for the conjugation of biomolecules to NPs and a comprehensive comparison between covalent and noncovalent conjugation strategies are summarised in Table A.2 (see appendix A) and a few bioconjugation strategies are represented in Figure 2.9.

2.5.1 SERS Immunotags

Antibodies and their fragments are among the proteins which have found the widest applications in SERS tags, because the antigen-antibody region is highly specific [222]. The specificity of the antibodies towards a large variety of antigens, allied with the transducer sensitivity, provides the basis of the immunoassays [62]. Additionally, antibody purification has been a mature production and modification process for several decades [223]. However, the success of antibody-antigen interaction depends on epitope presentation and binding chemistry [222]. A non-oriented conjugation of antibodies to the surface of NPs can impair antigen binding due to the steric blocking which often leads to decrease in sensitivity of the assay. A recent study by Avvakumova *et al.* [208] showed how the selection of the conjugation strategy, including antibody orientation or the presence of a polymeric spacer or recombinant protein linker, can impact on targeting cancer cells. Also, in the presence of high complexity samples, antibodies might exhibit cross-reactivity. Other disadvantages are related to high cost and long-term stability [223].

Immunoassay performance is undoubtedly influenced by antibodies that specifically recognise foreign molecules, known as antigens and are involved in immune recognition and host defence systems. These glycoproteins from the immunoglobin (Ig) supergene family are produced in membrane-bound or secreted form by B lymphocytes and can recognise multiple epitopes or determinants by their paratopes [222]. Essentially, antibodies are glycoproteins of approximately 110 amino acids with a total molecular mass

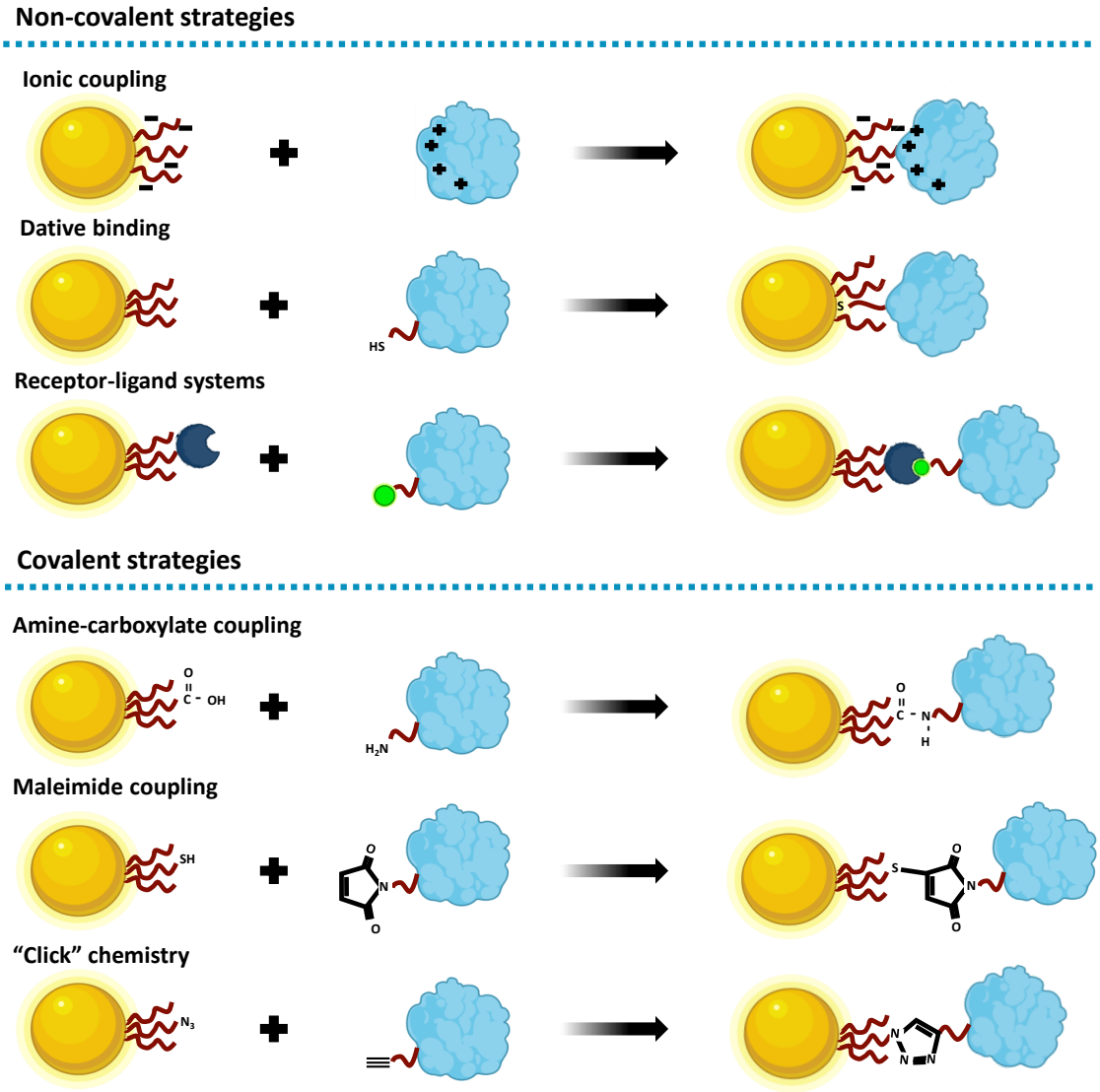

Figure 2.9: Conjugation strategies for achieving NP-biomolecules conjugates. noncovalent strategies: ionic coupling, dative binding (mainly accomplished by the affinity of sulphur atoms towards gold surface), and receptor-ligands systems such as avidin/biotin interaction with a monomer of biotin. Covalent strategies: covalent attachment to a ligand using amino-carboxylate coupling, maleimide coupling known as Michael addition, and "click" chemistry reaction using an azide tagged NP and an alkyne tagged protein.

of around 150 kDa in the flexible shape of a Y consisting of two identical 'heavy' polypeptide chains paired with two identical shorter 'light' chains, linked by a variable number of disulphide bonds (see Figure 2.10 for structural and functional detail). Their diversity, with remarkable binding affinity, allows identification of a multitude of antigens with small differences in chemical structure and thus they have been used in many applications in many diagnostics, drug delivery systems [224], affinity separation [224], and therapeutic applications [222, 225]. In fact, the ability to bioengineer an antibody to a specific antigen through hybridoma cells gives rise to the possibility of producing monoclonal antibodies, biochemically identical antibody molecules that bind to one epitope of an antigen. The monoclonal antibodies reduce variability between tests, compared to polyclonal antibodies, *i.e.*, antibodies that recognise different epitopes in the same antigen [222]. On the other hand, polyclonal antibodies have shown potential in treating many human diseases throughout the world [225].

To be mentioned that some applications might profit from the use of chemically fractionated antibody fragments such as fragment antigen-binding (Fab), which has antigen binding-activity and is obtained by removing the fragment crystallisable region (Fc), responsible for the biological activity [103, 222].

2.6 Microfluidic devices

Microfluidics as a field of study of fluidic behaviour and control within structures of micrometre dimensions has been demonstrated to be an efficient platform for integration of several laboratory processes on a single chip [227]. The miniaturisation of the conventional laboratory methods results in lower energy consumption, lower reaction times and better temperature control [227]. Their micro-scale dimensions decrease the required amounts of costly or hazardous reagents (100 nL to 10 μL), while their close architecture reduces the contamination risk. Characterised by a laminar flow and molecule diffusion as mixing method, microfluidics permits optimisation of the chemical reaction rate and enrichment of the products to obtain higher signal-to-noise ratio [228, 229].

Microchannels with complex trajectories can be designed to distinct purposes and operate subsequently or in parallel. For example, gradient formation chromatography, electrophoresis systems can be combined to perform multiple tasks and define even sites to deliver stimuli to sub-cellular compartments [228, 229]. The detection methods can vary from optics, electricity, electrochemistry, and magnetics [228, 229]. Moreover, these devices can be automated, reducing the operator error risk providing more reliable analysis results [228, 229].

Thus, the intrinsic plasticity allied with portability of the microfluidics field allows the integration of multistep procedures into one working unit without impairing reliable and consistent performance at high-throughput. Therefore, microfluidic devices represent a promising option to bring diagnostic tools that heretofore were confined to laboratories, to POCT sites [230].

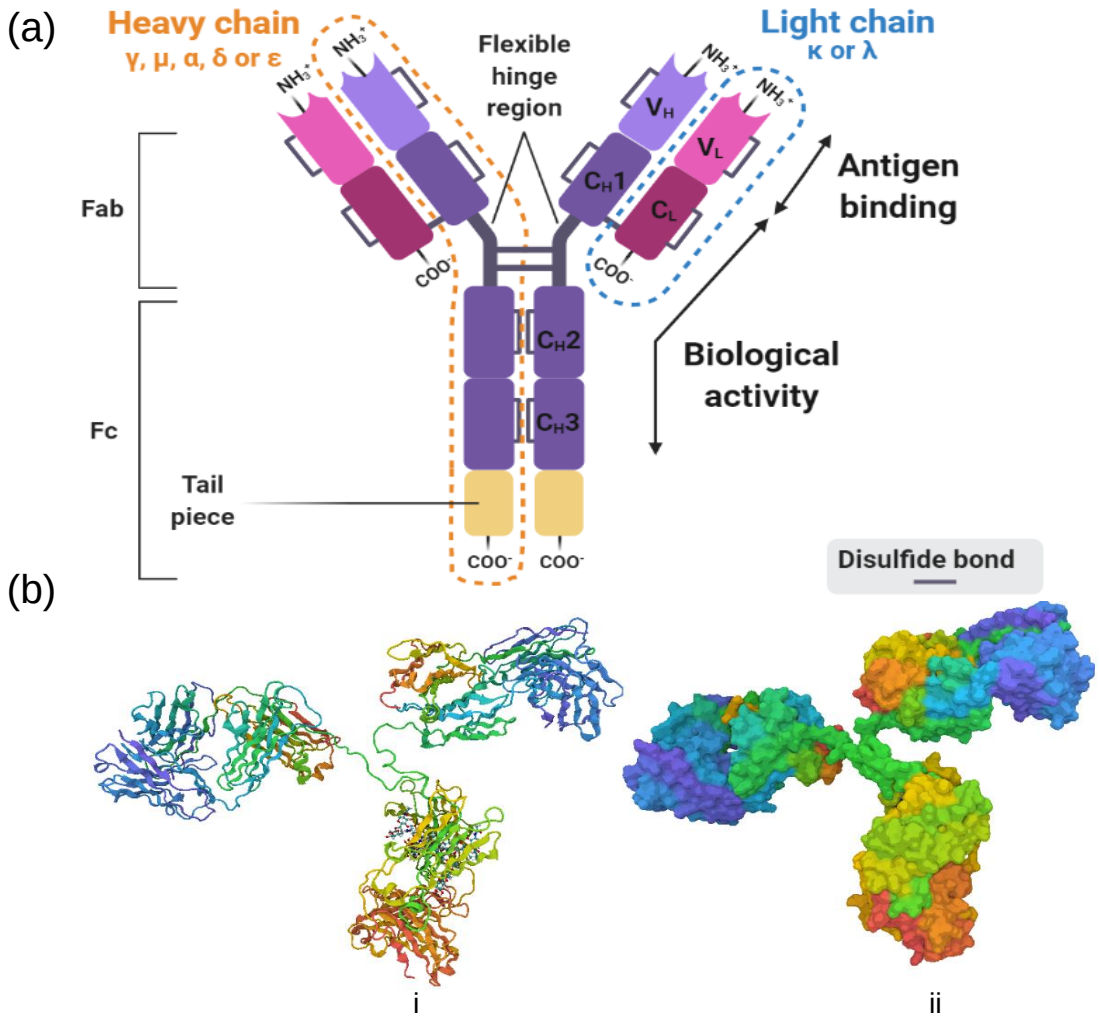

Figure 2.10: Immunoglobulin structure and function. (a) Schematic diagram of antibody structure (Human IgG) illustrating a pair of identical heavy (H) chains consisting of three constant domains (C_H1, C_H2, C_H3 in purple) and one variable domain (V_H in pink) linked to a pair of identical light chains consisting of one constant domain (C_L) and one variable domain (V_L). Each heavy and light chain contains an amino-terminal variable domain (light purple and light pink, respectively) each have three hypervariable loops complementarity-determining regions responsible for specific bind to antigen. The binding of antigens to this regions triggers the effector functions of antibodies mediated by constant domains. The constant regions have a smaller degree of variation that defines the two light chain subtypes and the five heavy-chain subclasses: γ, δ, α, μ and ε that give classifies the Ig class in IgG, IgD, IgA, IgM and IgE, respectively. These classes can even be classified in subclasses due to their heterogeneity, especially IgG, that can be divided in IgG1, IgG2, IgG3, IgG4. Chains γ, δ and α contain a proline-rich hinge region, μ and ε, lack of hinge region but contain an additional immunoglobulin domain in the Fc portion of the molecule. Adapted from [103, 222]. (b) (i) native (folded) conformation and (ii) surface ribbon three-dimensional representation of an intact secreted monoclonal IgG antibody, the identical heavy chains are coloured green and orange so clear visualisation, and the light chains are coloured in blue. Structure download from Protein Data Bank based on the work of [226]. Images created in Biorender.com.

2.6.1 Fluid behaviour at microscale

The small dimensions of microfluidics devices increases the surface area to volume ratio, leading to the fluid within the channels behaving differently [228, 229]. The understanding of the flow behaviour in a microdevice can be done though a group of dimensionless parameters such as Reynolds and Peclet numbers [228, 229]. Reynolds number describes the importance of the inertial and viscous forces in the flow. In another words, is represented by the ratio of the momentum on the fluid to the friction force imparted on the fluid by the walls [228, 229] (2.2):

$$Re = \frac{inertial}{viscous} = \frac{\rho v W_c}{\eta} \tag{2.2}$$

in which ρ is the fluid density; v is bulk velocity of the flow; W_c is the width of the microchannel and η is fluid viscosity. When the Reynolds number is high, the inertial forces dominate the system, and the flow is turbulent. Turbulence is characterised by a random variation of flow properties in time and space simultaneously. As a result, advective mass transport occurs in all directions. This type of flow behaviour is more commonly observed in daily life, such as in filling water in the sink, in a river flow or even stirring cream in our *cappuccino* [228, 229].

At low dimensions, the viscous forces dominate, and the Reynolds number decreases. As a result, the flow is smooth and ordered and known as laminar flow. In this case, the streams flow parallel to each other, with constant fluid velocity at all locations and invariant with time. The advective mass transport only occurs in the direction of the flow. Although less common, a few examples can be observed such as pouring honey, squeezing toothpaste from the tube or streams of ice in a glacier [228, 229].

The transition between turbulent to laminar flow occurs typically at Re=2000, although it might depend on channel shape, surface roughness, aspect ratio or if it is a liquid or a gas. This region is sometimes used to induce mixing in laminar flows that are characteristic of microfluidic systems where the Re is usually bellow 1. The mixing in laminar flows only occurs by diffusion (process of spreading molecules from a region of higher concentration to one of lower concentration by Brownian motion). Thus, the distance that a particle will diffuse in time t is dependent on their diffusion coefficient D in the solvent and can be given by [228, 229] (2.3):

$$x = 2\sqrt{Dt} \overset{D=\frac{k_{BT}}{6\pi\eta}}{\Longleftrightarrow} x = 2\sqrt{\frac{k_{BT}}{6\pi\eta}t} \tag{2.3}$$

being k_B the Boltzmann's constant, T the temperature, η the fluid viscosity and r the molecule radius.

Similarly to Reynolds number to describe how the fluids flow, Peclet number describes how the mass transport associated with mixing occurs. Peclet is the ratio of the advective and the diffuse mass transport contributions [228, 229] (2.4):

$$\frac{\text{advective mass transport}}{\text{diffuse mass transport}} = \frac{\frac{L^2}{D}}{\frac{L}{v}} = \frac{vL}{D} \equiv Pe \tag{2.4}$$

When $Pe < 1000$, the mixing is better accomplished by molecular diffusion than stirring. Congruently, microfluidic devices require long channels for effective mixing. To enhance the mixing, researchers recur to active mixing using additional energy source, *e.g.* ultrasounds, or passive mixing by adding geometries within the channel that increase the contact surface area, *e.g.* obstacles. Working at low Pe numbers can be very useful to control the diffusion in chemical reactions at higher rates than macroscopic reaction vessels [228, 229].

The function of a microfluidic device is greatly dependent on the material used as structure as well as the fabrication method (see chapter 5 for details). The choice of the material will depend on the application, as each material has its own advantages and disadvantages (Figure 2.11) [228, 229]. Originally, materials such as silicon and glass and technologies frequently used in the semiconductor industry were adapted to fabricate microdevices with excellent mechanical, chemical and thermal stability [228]. However, the fabrication cost and taxing processes, led to adoption of polymers, a broad class of softer materials with a wide range of material properties. The possibility of reducing the cost per unit and scalability, allied with the various properties depending on the chosen polymer, resulted in polymers becoming the most used group as microfluidic materials, displacing silicon and glass. Thus, polymers became especially important in diagnostic devices. However, due to their chemical composition and structure, polymers can be Raman active materials - *e.g.* polydimethylsiloxane (PDMS). To overcome this challenge, confocal Raman microscopy can be used to focus on the volume inside the microfluidic channel [228, 229].

The use of cellulose-based materials also contributes to the adoption of sustainable concepts, urgently needed in the new worldview of modern society [231]. The interest and increasing trend of using cellulose derives from its large abundance, renewability, biodegradability, biocompatibility, and hydrophilicity [231, 232]. Among different cellulose materials, nanofibrillated cellulose has been used as substrate material to fabricate electronic devices [232], SERS substrates [233], photoluminescent systems [232], and cell culture platforms [233]. Notably, a transparent, low-cost, easy to fabricate, and reusable material is highly desirable to better meet the requirements of POCT and possibility to integrate in microfluidics devices. Recently, Shin *et al.* demonstrated the ability of performing extrusion three-dimensional (3D) printing using cellulose nanofibre hydrogel as a matrix allowing ease of processing and freedom of design [234]. Cellulose-based hydrogels not only represent an attractive choice due to low energy consumption during fabrication and their smooth surfaces, but also as a substrate for immunoassays due to combining cellulose biocompatibility with other fascinating properties such as high-water absorption capacity, stretchability, moldability and stimuli-responsiveness from the hydrogels [235, 236]. Paper has become an increasingly popular material for biosensors

also due to its biocompatibility and fabrication cost. Table A.3 in appendix A presents overview of the main materials for microfluidic chip fabrication, comparing their fabrication processes, stability, price and main advantages and disadvantages.

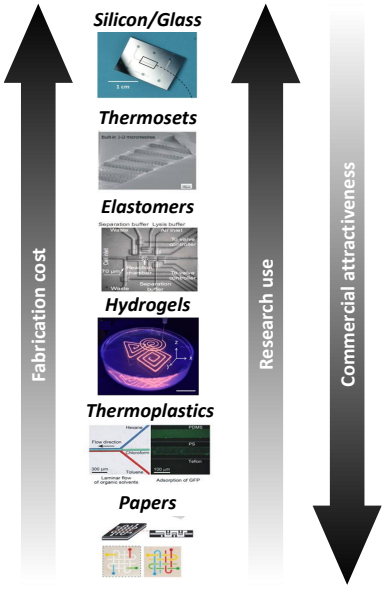

Figure 2.11: The most promising materials for microfluidic chip fabrication and comparison of the resulting devices' cost. Adapted from [228, 234]. Thermosets, inorganic materials and hydrogels have properties suitable for the research level use, while paper may constitute the most spread material in commercial microfluidics.

2.6.2 SERS-based microfluidic immunoassays biosensors

The combination of microfluidic with SERS spectroscopy allows the creation of optofluidic immuno- and cellular assays with an improved performance [23]. The high surface-to-volume ratio of the microchannels leads to an accelerated recognition event between the antibody and antigen which, in turn, allows the development of biosensors with a faster response. Furthermore, the microfluidics network provides a continuous flowing environment able to generate homogeneous mixing conditions, favourable to heat dissipation, and reduces nonspecific adsorption of SERS tags. This allows reduction of the variability inherent in SERS spectroscopy assays, caused by the lack of control over factors such as NP aggregation, size and analyte distributions on the detection surface. Consequently, the SERS-microfluidic devices have increased sensitivity and quantification accuracy [23, 62, 237, 238].

SERS-based microfluidic immunoassays platforms represent an important advance, since the microfluidic chip fabrication know-how can automate the immunoassay process. Steps of adding sample solution, wash buffer and polyclonal antibody-conjugated SERS tag suspension can be automated. Thus, not only can the microfluidic chip replace a tedious human operation and reduce the operator error, but it can also increase the high-throughput biosensing through multiple SERS spectroscopy detection channels [23, 62,

237, 238].

It should be highlighted that the miniaturisation of the optical sensing device is a crucial aspect in medical diagnostics. Thus, although microfluidics provide the ability to develop a small detection platform, most Raman spectrometers are external to the microfluidic device and comprise large optical components (LASERs, microscopes, monochromator, and detector). When microfluidic devices and portable Raman spectrometers become integrated into one single system, it will be most likely to become a powerful and robust next-generation biomedical diagnostic tool [23, 62, 237, 238].

Although the benefits of these biomedical diagnostic tools can be easily foreseen, the development and application of such devices may exhibit potential health and environmental risks which are not yet be fully understood. To address these concerns, life cycle assessment (LCA) is made to access potential environmental problems and ensure sustainability of the technology created [239, 240]. LCA is thus an approach responsible for analysing the impacts of a product throughout its entire life cycle from the raw materials acquisition and energy input in manufacturing process to the end-of-life [239, 240]. Considering the growth of health products that use nanomaterials, this LCA becomes greatly important even for those technologies that may be non-invasive allowing to balance the risk and benefits of bringing such technology to light [239]. Therefore, it is essential that, when designing a SERS-based microfluidic immunoassay platform, or other similar technology, each step of the design is considered, to present minimal risk to the environment and human health.

2.7 Malaria current detection methods

Malaria is a vector-borne infectious disease caused by five protozoan parasites of the genus *Plasmodium*, namely, *P. ovale*, *P. knowlesi*, *P. malariae*, *P. vivax*, and *P. falciparum*, the latter being the deadliest and thus the one receiving most attention [241].

The life cycle of *Plasmodium spp.* involves cyclical infection of female *Anopheles* mosquitoes and, thereafter, vertebrate hosts (Figure 2.12). The infection is initiated during the blood feed of a female anopheline mosquito, in which sporozoites are injected into the blood stream of the host and, after traversing several cells, sporozoites effectively invade hepatocytes [241]. Once hepatocytic infection has taken place, the sporozoites mature into schizonts, culminating in the release of merozoites ($\approx 40,000$ per hepatocyte) into the bloodstream [241]. Following merozoite release, the parasites undergo an asexual multiplication in the erythrocytes [242, 243]. The subsequent cell division (schizogony) generates enough merozoites to cause the rupture of the erythrocyte membrane, releasing new merozoites into the bloodstream, so the invasion-lysis process can occur again [244]. The clinical manifestations of the disease are caused by these parasites in this blood stage. During this stage, a fraction of the merozoites differentiate into gametocytes (male - microgametocytes and female - macrogametocytes). The gametocyte maturation occurs

within the bone marrow, until they are released into the peripheral circulation and ingested by an *Anopheles* mosquito. While in the mosquito's stomach, the gametocytes reproduce and form ookinetes followed by oocysts. The oocysts grow, rupture and release sporozoites that migrate to the mosquito's salivary glands. Inoculation of the sporozoites assures the perpetuation of the malaria life cycle [244, 245].

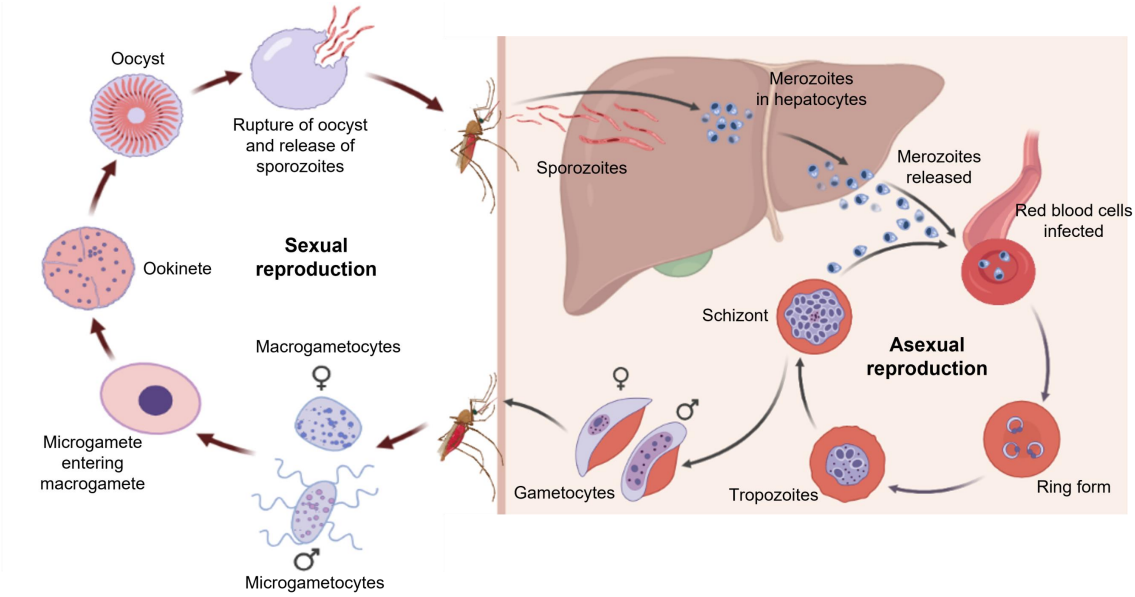

Figure 2.12: The malaria parasite life cycle involves two hosts: the female *Anopheles* mosquito and human.

Microscopic analysis of blood smears for identification of parasites is the gold standard method for diagnosing malaria in patients with fever [246]. Due to the requirement of powered equipment and trained laboratory technicians, rapid diagnostic tests (RDTs) were developed especially for use in rural communities in which these facilities are absent. These rapid and portable immunochromatographic systems capture the parasite antigen from peripheral blood using monoclonal antibodies without any additional instrumentation.

Together with microscopy, WHO has recommended these diagnostic methods prior to medication administration, to avoid mistreating suspected cases and the emergence of drug-resistant parasitic strains [22, 247]. To date, over 120 brands of malaria RDTs have been developed with different levels of performance, fabrication procedure and price (0.55 € to 2.12 € per test) [67].

The selection of highly quality RDTs and national malaria control programmes has allowed malaria RDTs to reach millions of patients every year. Combined with bed nets for preventing transmission, their deployment has resulted in a decrease of malaria infections in many parts of the world [67]. Nevertheless, malaria elimination is still far from being accomplished. Detection of all *Plasmodium* spp. without increasing the cost, detection and quantification at low parasitaemia levels, false-negative results due to deletion cases of one most used biomarker of malaria, and the lack of adequate training and quality

assurance of malaria tests, are a few of the main challenges that remain. Interestingly, as the parasitaemia in infected individuals decreases, ultrasensitive and thus costlier platforms will be needed for antigen detection, no longer providing cost-effectiveness [67, 248].

More sensitive methods rely on nucleic acid detection, including PCR and loop-mediated isothermal amplification (LAMP) [249], which allow detection of drug-resistant strains [250]. Other techniques such as fluorescence *in situ* hybridisation [251], automatic classification of infected blood using phone images [252] with the aid of deep learning algorithms [253], cell dye machine [254], magneto optical technology using polarised light, laser desorption mass spectrometry, magnetic resonance imaging, quantitative buffy coat method, flow cytometry, optical tweezers and attenuated total reflectance (ATR)-IR have been developed [255–257]. However, these methods present some limitations, showing inconsistent performance results and in capturing the heterogeneity of the disease, since most techniques do not provide low limits of detection (required for low abundance biomarkers) or highly sensitive techniques have limited multiplexing ability (required for a complete disease profiling) and low throughput [258, 259]. Moreover, these methods are usually laborious, time-consuming and require high concentrations of analyte which inevitably leads to an increase of coexisting interfering species [67, 246].

2.7.1 Malaria diagnosis using surface-enhanced Raman spectroscopy and microfluidics

Multiple biomarkers have been described for malaria diagnosis, including *Plasmodium falciparum* histidine rich protein 2 (*Pf*HRP2) [260], *Plasmodium falciparum* lactate dehydrogenase (*Pf*LDH) [261–263], *Plasmodium falciparum* aldolase (*Pf*ALD) [261, 264], *Plasmodium falciparum* hypoxanthine guanine phosphoribosyl transferase (*Pf*HGPRT) [265] and *Plasmodium* glutamate dehydrogenase (*P*GluDH) [266], as well as the malaria pigment haemozoin [267–272].

Haemozin is a metabolite found in malaria-infected blood, which is suitable for malaria diagnosis (see section 2.7). Its strong intrinsic Raman signature has shown great promise for malaria diagnosis, since studies have shown it to be possible to localise haemozoin in single *P. falciparum* infected red blood cells (iRBCs) under resonance Raman conditions [273]. By enhancing the Raman signal with nanostructures, haemozoin can be detected even in the early ring stages, normally seen in peripheral blood with very small number of parasites (see section 2.7). Nevertheless, single blood cell analysis depends strongly on the precision of locating the cell, which can be challenging at a low parasitaemia level. To enrich the sample in haemozin, Yuen *et al.* [272] used magnetic NPs composed of an iron oxide core and silver shell to capture the paramagnetic haemozin using an external magnetic field and enhance the amplification due to the NPs silver shell. Improving quantification capability, the same group tested AgNPs synthesised and mixed with or synthesised directly in the blood sample. The synthesis and mixing

approach exhibited lower variation in the SERS spectroscopy measurements, but the second approach yielded higher sensitivity to a low parasitaemia level, reaching 0.00005% parasitaemia level, in the ring stage (2.5 parasites·μL^{-1} of blood) [274]. This group recently improved their system by developing a SERS spectroscopy lab-on-chip, although with a poorer detection limit of 0.0025% parasitaemia level [274]. However, SERS-based detection based only on this biomarker for malaria detection cannot distinguish between haemozoin produced by a viable parasite from the remaining amount followed by a prior infection [274].

Other SERS-based assays have been mainly focused on nucleic acid detection. By promoting a sandwich DNA hybridisation assay with capture magnetic beads coated with DNA probes and ultrabright nanorattles functionalised with SERS reporter DNA probes, Ngo *et al.* [275] were able to concentrate the hybridised complex and achieve a sensitivity of 3 pM, discriminating the single nucleotide polymorphism responsible for artemisinin drug resistance. Nevertheless, these types of assays require target amplification. One striking method from the same group, based malaria detection on ribosomal ribonucleic acid (RNA) in 10 μL of blood lysates. Using the same detection principle, the group developed a lab-in-a-stick integrated device with no need for RNA extraction or PCR amplification, achieving an limit of detection of 200 fM [276].

Most of the detection assays based on protein identification are immunoassays in the format of RDTs, while SERS-based assays remain unexplored. One of the most preeminent studies was based on a SERS-based immunoassay that simultaneously detects antigens from Ebola, Lassa, and malaria within a single blood sample, reaching sensitivities >90% [260]. Table A.4 in Appendix A shows a summary of several examples of SERS spectroscopy detection of malaria markers.

In contrast to immunoassays which are SERS-based, microfluidics platforms have been frequently used for malaria. As mentioned in section 2.6.2, microfluidics can miniaturise and integrate multi-step protocols allowing a reliable and accurate detection. Thus, a wide range of detection methods using microfluidics has been demonstrated for malaria detection, including molecular testing, size-based cell sorting, electrical differentiation of healthy and iRBCs, optical detection of antigen and magnetic detection of haemozoin [255, 277].

Due to the low concentrations of biomarkers that define the profile of a disease, microfluidic devices have been constructed to enrich these biomarkers. Most of the microfluidic devices used to analyse malaria are based on cell analysis [154, 271, 278]. The strategies for biomarker enrichment can be divided on the basis of (i) biological or (ii) physical properties. The first relies on the specific surface markers on the cell membrane, whereas the second is based on parameters as size, deformability, density, electric charge, and others [279]. Cell enrichment through biological properties requires the use of capture ligands (*e.g.* aptamers and antibodies) that recognise cell surface antigens which are pre-immobilised on the microfluidic channel or in magnetic NPs (see section 2.2.2.1). Although very specific, the affinity-based strategy is limited when the molecular profiling

of disease in unknown, and when release of cells is needed for further analysis [279].

Strategies based on physical properties provide a label-free isolation platform, avoiding the pressure applied on the plasma membrane by the antibody-antigen binding [280]. Consequently, the microfluidic architectures for separation offer flexibility and convenience for subsequent downstream analysis. Physical strategies include filtration, hydrodynamics, dielectrophoresis, acousticphoresis and optical [279].

Dielectrophoresis, for instance, is a straightforward way used in many works to detect and separate healthy and iRBCs due to their distinct ionic permeability of their plasma membrane [281]. Because infected cells are more permeable, when both healthy and infected cells are suspended in a low conductivity medium, they exhibit a different dielectrophoretic mobility than healthy ones [281] and can be counted.

Based on all the advantages and work to date in the SERS spectroscopy and microfluidics fields, it is clear that the exploration of SERS-based microfluidics biosensors can lead to an important tool for detection of human diseases altering the paradigm of early diagnostics.

References for chapter 2

[1] R. Aroca. "Theory of Molecular Vibrations. The Origin of Infrared and Raman Spectra". In: *Surface-Enhanced Vibrational Spectroscopy*. Chichester, UK: John Wiley & Sons, Ltd, 2007, pp. 1–33.

[2] R. Aroca. "Surface-Enhanced Raman Scattering". In: *Surface-Enhanced Vibrational Spectroscopy*. Ed. by R. Aroca. 1st ed. West Sussex, UK: John Wiley & Sons, Ltd, 2008. Chap. 3, pp. 73–106.

[3] R. S. Krishnan and R. K. Shankar. "Raman effect: History of the discovery". In: *Journal of Raman Spectroscopy* 10 (1981), pp. 1–8.

[4] P. L. Stiles et al. "Surface-enhanced Raman spectroscopy". In: *Annual Review of Analytical Chemistry* 1.1 (2008), pp. 601–626.

[5] S. Schlücker. "Surface-Enhanced Raman Spectroscopy: Concepts and Chemical Applications". In: *Angewandte Chemie International Edition* 53.19 (2014), pp. 4756–4795.

[6] M. Fleischmann, P. Hendra, and A. McQuillan. "Raman spectra of pyridine adsorbed at a silver electrode". In: *Chemical Physics Letters* 26.2 (1974), pp. 163–166.

[7] A. J. McQuillan. "The discovery of surface-enhanced Raman scattering". In: *Notes and Records of the Royal Society* 63.1 (2009), pp. 105–109.

[8] D. L. Jeanmaire and R. P. Van Duyne. "Surface Raman spectroelectrochemistry". In: *Journal of Electroanalytical Chemistry and Interfacial Electrochemistry* 84.1 (1977), pp. 1–20.

[9] M. G. Albrecht and J. A. Creighton. "Anomalously intense Raman spectra of pyridine at a silver electrode". In: *Journal of the American Chemical Society* 99.15 (1977), pp. 5215–5217.

[10] R. P. Van Duyne. "Laser excitation of Raman scattering from adsorbed molecules on electrode surfaces". In: *Chemical and Biochemical Applications of Lasers*. Ed. by C. Bradley Moore. 4th ed. New York, USA: Elsevier, 1979. Chap. 4, pp. 101–185.

[11] M. R. Philpott. "Effect of surface Plasmons on transitions in molecules". In: *The Journal of Chemical Physics* 62.5 (1975), pp. 1812–1817.

[12] M. Moskovits. "Enhanced Raman scattering by molecules adsorbed on electrodes–a theoretical model". In: *Solid State Communications* 32.1 (1979), pp. 59–62.

[13] H. Baltruschat, E. Rach, and J. Heitbaum. "Correlation of SERS intensity potential profiles with adsorption/desorption peaks of pyridine on Au". In: *Journal of Electroanalytical Chemistry* 194.1 (1985), pp. 109–122.

[14] J. C. Cook et al. "Use of colloidal SERS for the trace detection of organic species: a survey based on pyridine as the probe molecule". In: *Journal of Raman Spectroscopy* 24.9 (1993), pp. 609–619.

[15] J. A. Creighton. "Surface Raman electromagnetic enhancement factors for molecules at the surface of small isolated metal spheres: The determination of adsorbate orientation from sers relative intensities". In: *Surface Science* 124.1 (1983), pp. 209–219.

[16] M. Moskovits. "Surface-enhanced spectroscopy". In: *Reviews of Modern Physics* 57.3 (1985), pp. 783–826.

[17] S. Nie and S. R. Emory. "Probing single molecules and single nanoparticles by surface-enhanced Raman scattering". In: *Science* 275.5303 (1997), pp. 1102–1106.

[18] K. Kneipp et al. "Single molecule detection using Surface-Enhanced Raman Scattering (SERS)". In: *Physical Review Letters* 78.9 (1997), pp. 1667–1670.

[19] B. Pettinger, K. Krischer, and G. Ertl. "Giant Raman scattering cross section for an adsorbed dye at ag colloids associated with low EM field enhancement". In: *Chemical Physics Letters* 151.1-2 (1988), pp. 151–155.

[20] B. Chase. "A New Generation of Raman Instrumentation". In: *Applied Spectroscopy* 48.7 (1994), pp. 14–19.

[21] M. Moskovits. "Persistent misconceptions regarding SERS". In: *Physical Chemistry Chemical Physics* 15.15 (2013), pp. 5301–5311.

[22] R. Salzer and H. W. Siesler. *Surface Enhanced Raman Spectroscopy - Analytical, Biophysical and Life Science Applications*. Ed. by S. Schlücker. Weinheim, Germany: Wiley-VCH Verlag GmbH & Co. KGaA, 2010, pp. 1–354.

[23] J. Langer et al. "Present and Future of Surface-Enhanced Raman Scattering". In: *ACS Nano* 14.1 (2020), pp. 28–117.

[24] E. C. Le Ru et al. "Surface Enhanced Raman Scattering Enhancement Factors:A Comprehensive Study". In: *The Journal of Physical Chemistry C* 111.37 (2007), pp. 13794–13803.

[25] Z. Yi et al. "Arrays of ZnO nanorods decorated with Au nanoparticles as surface-enhanced Raman scattering substrates for rapid detection of trace melamine". In: *Physica B: Physics of Condensed Matter* 451 (2014), pp. 58–62.

[26] F. J. García-Vidal and J. B. Pendry. "Collective Theory for Surface Enhanced Raman Scattering". In: *Physical Review Letters* 77.6 (1996), pp. 1163–1166.

[27] S. Lecomte, P. Matejka, and M. H. Baron. "Correlation between Surface Enhanced Raman Scattering and Absorbance Changes in Silver Colloids. Evidence for the Chemical Enhancement Mechanism". In: *Langmuir* 14.16 (1998), pp. 4373–4377.

[28] A. Otto et al. "Surface-enhanced Raman scattering". In: *Journal of Physics: Condensed Matter* 4.5 (1992), pp. 1143–1212.

[29] W. H. Park and Z. H. Kim. "Charge transfer enhancement in the SERS of a single molecule". In: *Nano Letters* 10.10 (2010), pp. 4040–4048.

[30] R. F. Aroca. "Plasmon enhanced spectroscopy". In: *Physical Chemistry Chemical Physics* 15.15 (2013), pp. 5355–5363.

[31] D. M. Solís et al. "Optimization of Nanoparticle-Based SERS Substrates through Large-Scale Realistic Simulations". In: *ACS Photonics* 4.2 (2017), pp. 329–337.

[32] C. E. Talley et al. "Surface-enhanced Raman scattering from individual Au nanoparticles and nanoparticle dimer substrates". In: *Nano Letters* 5.8 (2005), pp. 1569–1574.

[33] V. Tran et al. "Probing the SERS brightness of individual Au nanoparticles, hollow Au/Ag nanoshells, Au nanostars and Au core/Au satellite particles: Single-particle experiments and computer simulations". In: *Nanoscale* 10.46 (2018), pp. 21721–21731.

[34] D. Lee and S. Yoon. "Effect of Nanogap Curvature on SERS: A Finite-Difference Time-Domain Study". In: *Journal of Physical Chemistry C* 120.37 (2016), pp. 642–650.

[35] J. M. McMahon et al. "Modeling the effect of small gaps in surface-enhanced Raman spectroscopy". In: *Journal of Physical Chemistry C* 116.2 (2012), pp. 1627–1637.

[36] H. Xu et al. "Electromagnetic contributions to single-molecule sensitivity in surface-enhanced Raman scattering". In: *Physical Review E - Statistical Physics, Plasmas, Fluids, and Related Interdisciplinary Topics* 62.3 B (2000), pp. 4318–4324.

[37] S. M. Stranahan and K. A. Willets. "Super-resolution optical imaging of single-molecule SERS hot spots." In: *Nano letters* 10.9 (2010), pp. 3777–3784.

[38] J. Theiss et al. "Plasmonic nanoparticle arrays with nanometer separation for high-performance SERS substrates." In: *Nano letters* 10.8 (2010), pp. 2749–54.

[39] A. X. Wang and X. Kong. "Review of Recent Progress of Plasmonic Materials and Nano-Structures for Surface-Enhanced Raman Scattering." In: *Materials* 8.6 (2015), pp. 3024–3052.

[40] S. L. Kleinman et al. "Structure enhancement factor relationships in single gold nanoantennas by surface-enhanced Raman excitation spectroscopy". In: *Journal of the American Chemical Society* 135.1 (2013), pp. 301–308.

[41] L. Wu, A. Dias, and L. Diéguez. "Surface enhanced Raman spectroscopy for tumor nucleic acid: Towards cancer diagnosis and precision medicine". In: *Biosensors and Bioelectronics* 204.September 2021 (2022), pp. 114075–114095.

[42] R. De La Rica and M. M. Stevens. "Plasmonic ELISA for the detection of analytes at ultralow concentrations with the naked eye". In: *Nature Protocols* 8.9 (2013), pp. 1759–1764.

[43] C. Li et al. "Improvement of enzyme-linked immunosorbent assay for the multicolor detection of biomarkers". In: *Chemical Science* 7.5 (2016), pp. 3011–3016.

[44] Z. Qu et al. "Ultrasensitive ELISA using enzyme-loaded nanospherical brushes as labels". In: *Analytical Chemistry* 86.19 (2014), pp. 9367–9371.

[45] S. A. Kazane et al. "Site-specific DNA-antibody conjugates for specific and sensitive immuno-PCR". In: *Proceedings of the National Academy of Sciences of the United States of America* 109.10 (2012), pp. 3731–3736.

[46] C. Pfitzner et al. "Digital-Direct-RT-PCR: a sensitive and specific method for quantification of CTC in patients with cervical carcinoma". In: *Scientific Reports* 4.1 (2015), p. 3970.

[47] G. Garcia-Schwarz and J. G. Santiago. "Rapid high-specificity microRNA detection using a two-stage isotachophoresis assay". In: *Angewandte Chemie - International Edition* 52.44 (2013), pp. 11534–11537.

[48] H. Lee, J.-E. Park, and J.-M. Nam. "Bio-barcode gel assay for microRNA". In: *Nature Communications* 5.1 (2014), p. 3367.

[49] B. S. S. Guirgis et al. "Gold nanoparticle-based fluorescence immunoassay for malaria antigen detection". In: *Analytical and Bioanalytical Chemistry* 402.3 (2012), pp. 1019–1027.

[50] S. Rana et al. "Ratiometric Array of Conjugated Polymers–Fluorescent Protein Provides a Robust Mammalian Cell Sensor". In: *Journal of the American Chemical Society* 138.13 (2016), pp. 4522–4529.

[51] J. Dong et al. "Nanostructured Substrates for Detection and Characterization of Circulating Rare Cells: From Materials Research to Clinical Applications". In: *Advanced Materials* 32.1 (2020).

[52] L. F. Tadesse et al. "Toward rapid infectious disease diagnosis with advances in surface-enhanced Raman spectroscopy". In: *The Journal of Chemical Physics* 152.24 (2020), pp. 240902–240917.

[53] A. Luchini et al. "Nanoparticle Technology: Addressing the Fundamental Roadblocks to Protein Biomarker Discovery". In: *Current Molecular Medicine* 10.2 (2010), pp. 133–141.

[54] S. Madlener and J. Gojo. "Liquid biomarkers for pediatric brain tumors: Biological features, advantages and perspectives". In: *Journal of Personalized Medicine* 10.4 (2020), pp. 1–15.

[55] S. Roy and A. Jaiswal. "SERS-Based Biosensors as Potential Next-Generation Point-of-Care Cancer Diagnostic Platforms". In: *Next Generation Point-of-care Biomedical Sensors Technologies for Cancer Diagnosis*. Ed. by P. Chandra, Y. N. Tan, and S. P. Singh. 1st ed. Singapore: Springer Nature Singapore Pte Ltd., 2017. Chap. 8, pp. 1–396.

[56] P. D. Howes, S. Rana, and M. M. Stevens. "Plasmonic nanomaterials for biodiagnostics". In: *Chem. Soc. Rev.* 43.11 (2014), pp. 3835–3853.

[57] X. Wu et al. "Improved SERS nanoparticles for direct detection of circulating tumor cells in the blood". In: *ACS Applied Materials and Interfaces* 7.18 (2015), pp. 9965–9971.

[58] X. Cao et al. "Synthesis of Au nanostars and their application as surface enhanced Raman scattering-activity tags inside living cells". In: *Journal of Nanoscience and Nanotechnology* 15.7 (2015), pp. 4829–4836.

[59] M. Fan, G. F. S. Andrade, and A. G. Brolo. "A review on the fabrication of substrates for surface enhanced Raman spectroscopy and their applications in analytical chemistry". In: *Analytica Chimica Acta* 693.1-2 (2011), pp. 7–25.

[60] J. Prakash, R. Harris, and H. Swart. "Embedded plasmonic nanostructures: synthesis, fundamental aspects and their surface enhanced Raman scattering applications". In: *International Reviews in Physical Chemistry* 35.3 (2016), pp. 353–398.

[61] B. Shan et al. "Novel SERS labels: Rational design, functional integration and biomedical applications". In: *Coordination Chemistry Reviews* 371 (2018), pp. 11–37.

[62] Z. Wang et al. "SERS-Activated Platforms for Immunoassay: Probes, Encoding Methods, and Applications". In: *Chemical Reviews* 117.12 (2017), pp. 7910–7963.

[63] H. Mao et al. "Microfluidic surface-enhanced Raman scattering sensors based on nanopillar forests realized by an oxygen-plasma-stripping-of-photoresist technique". In: *Small* 10.1 (2014), pp. 127–134.

[64] K. Ock et al. "Real-time monitoring of glutathione-triggered thiopurine anticancer drug release in live cells investigated by surface-enhanced Raman scattering". In: *Analytical Chemistry* 84.5 (2012), pp. 2172–2178.

[65] J. Chen et al. "Flexible and Adhesive Surface Enhance Raman Scattering Active Tape for Rapid Detection of Pesticide Residues in Fruits and Vegetables". In: *Analytical Chemistry* 88.4 (2016), pp. 2149–2155.

[66] A. Pallaoro, G. B. Braun, and M. Moskovits. "Biotags Based on Surface-Enhanced Raman Can Be as Bright as Fluorescence Tags". In: *Nano Letters* 15.10 (2015), pp. 6745–6750.

[67] K. J. Land et al. "REASSURED diagnostics to inform disease control strategies, strengthen health systems and improve patient outcomes". In: *Nature Microbiology* 4.1 (2019), pp. 46–54.

[68] S. Xu et al. "Surface-enhanced Raman scattering studies on immunoassay". In: *Journal of Biomedical Optics* 10.3 (2005), pp. 031112–1 – 031112–12.

[69] J. R. Crowther. *ELISA: Theory and Practice*. Ed. by J. M. Walker. 1st ed. Vol. 42. New Jersey: Humana Press, 1995, pp. 1–231.

[70] M. Vendrell et al. "Surface-enhanced Raman scattering in cancer detection and imaging". In: *Trends in Biotechnology* 31.4 (2013), pp. 249–257.

[71] L.-K. Lin and L. A. Stanciu. "Bisphenol A detection using gold nanostars in a SERS improved lateral flow immunochromatographic assay". In: *Sensors and Actuators B: Chemical* 276.August (2018), pp. 222–229.

[72] N. Feliu et al. "SERS Quantification and Characterization of Proteins and Other Biomolecules". In: *Langmuir* 33.38 (2017), pp. 9711–9730.

[73] A. Zengin, U. Tamer, and T. Caykara. "A SERS-based sandwich assay for ultrasensitive and selective detection of Alzheimer's tau protein". In: *Biomacromolecules* 14.9 (2013), pp. 3001–3009.

[74] A. Kamińska et al. "SERS-based Immunoassay in a Microfluidic System for the Multiplexed Recognition of Interleukins from Blood Plasma: Towards Picogram Detection". In: *Scientific Reports* 7.1 (2017), pp. 10656–10667.

[75] L. Lin et al. "A bioorthogonal Raman reporter strategy for SERS detection of glycans on live cells". In: *Angewandte Chemie - International Edition* 52.28 (2013), pp. 7266–7271.

[76] M. Schütz and S. Schlücker. "Towards quantitative multi-color nanodiagnostics: spectral multiplexing with six silica-encapsulated SERS labels". In: *Journal of Raman Spectroscopy* 47.9 (2016), pp. 1012–1016.

[77] J. M. Li et al. "Highly sensitive detection of target ssDNA based on SERS liquid chip using suspended magnetic nanospheres as capturing substrates". In: *Langmuir* 29.20 (2013), pp. 6147–6155.

[78] C. M. MacLaughlin et al. "Surface-enhanced Raman scattering dye-labeled Au nanoparticles for triplexed detection of leukemia and lymphoma cells and SERS flow cytometry". In: *Langmuir* 29.6 (2013), pp. 1908–1919.

[79] J. Conde et al. "Revisiting 30 years of biofunctionalization and surface chemistry of inorganic nanoparticles for nanomedicine". In: *Frontiers in Chemistry* 2.7 (2014), pp. 1–27.

[80] V. D. Krishna et al. "Nanotechnology: Review of concepts and potential application of sensing platforms in food safety". In: *Food Microbiology* 75 (2018), pp. 47–54.

[81] C. K. Dixit et al. "Multisubstrate-compatible ELISA procedures for rapid and high-sensitivity immunoassays". In: *Nature Protocols* 6.4 (2011), pp. 439–445.

[82] L. Fabris. "Gold-based SERS tags for biomedical imaging". In: *Journal of Optics (United Kingdom)* 17.11 (2015), p. 114002.

[83] L. Fabris. "SERS Tags: The Next Promising Tool for Personalized Cancer Detection?" In: *ChemNanoMat* 2.4 (2016), pp. 249–258.

[84] Y. Wang, B. Yan, and L. Chen. "SERS Tags: Novel optical nanoprobes for bioanalysis". In: *Chemical Reviews* 113.3 (2013), pp. 1391–1428.

[85] W. R. Algar et al. "Semiconductor quantum dots in bioanalysis: Crossing the valley of death". In: *Analytical Chemistry* 83.23 (2011), pp. 8826–8837.

[86] L. Y. Chou, K. Ming, and W. C. Chan. "Strategies for the intracellular delivery of nanoparticles". In: *Chemical Society Reviews* 40.1 (2011), pp. 233–245.

[87] M. A. Cotta. "Quantum Dots and Their Applications: What Lies Ahead?" In: *ACS Applied Nano Materials* 3.6 (2020), pp. 4920–4924.

[88] S. P. Perfetto, P. K. Chattopadhyay, and M. Roederer. "Seventeen-colour flow cytometry: unravelling the immune system". In: *Nature Reviews Immunology* 4.8 (2004), pp. 648–655.

[89] C. Wang and C. Yu. "Analytical characterization using surface-enhanced Raman scattering (SERS) and microfluidic sampling". In: *Nanotechnology* 26.9 (2015), pp. 092001–092027.

[90] J. P. Nolan, E. Duggan, and D. Condello. "Optimization of SERS tag intensity, binding footprint, and emittance". In: *Bioconjugate Chemistry* 25.7 (2014), pp. 1233–1242.

[91] Pilot et al. "A Review on Surface-Enhanced Raman Scattering". In: *Biosensors* 9.2 (2019), pp. 57–156.

[92] L. Rodriguez-Lorenzo, L. Fabris, and R. A. Alvarez-Puebla. "Multiplex optical sensing with surface-enhanced Raman scattering: A critical review". In: *Analytica Chimica Acta* 745 (2012), pp. 10–23.

[93] M. Salehi et al. "Two-color surface-enhanced Raman spectroscopy microscopy for protein colocalization in prostate tissue with primary antibody-protein A/G-gold nanocluster conjugates". In: *Nanoscale* 6.4 (2014), pp. 2361–2367.

[94] I. L. Medintz et al. "Multiplex charge-transfer interactions between quantum dots and peptide-bridged ruthenium complexes". In: *Analytical Chemistry* 81.12 (2009), pp. 4831–4839.

[95] R. Babaei, S. Goli-Haghighi, and H. Savaloni. "Detection of overtone and combined peaks using Mn/Cu helical star-shaped (pine-tree-like) sculptured thin films in surface-enhanced Raman spectroscopy". In: *Journal of Theoretical and Applied Physics* 13.4 (2019), pp. 305–314.

[96] R. Haldavnekar, K. Venkatakrishnan, and B. Tan. "Non plasmonic semiconductor quantum SERS probe as a pathway for in vitro cancer detection". In: *Nature Communications* 9.1 (2018), pp. 1–18.

[97] Y. Ye et al. "Highly Sensitive W 18 O 49 Mesocrystal Raman Scattering Substrate with Large-Area Signal Uniformity". In: *Analytical Chemistry* 93.6 (2021), pp. 3138–3145.

[98] M. K. Patil, S. H. Gaikwad, and S. P. Mukherjee. "Phase and Morphology Controlled Synthesis of Tunable Plasmonic MoO_{3-x} Nanomaterials for Ultrasensitive Surface-Enhanced Raman Spectroscopy Detection". In: *The Journal of Physical Chemistry C* 124.38 (2020), pp. 21082–21093.

[99] Y. Zhan et al. "Phase-controlled synthesis of molybdenum oxide nanoparticles for surface enhanced Raman scattering and photothermal therapy". In: *Nanoscale* 10.13 (2018), pp. 5997–6004.

[100] J. W. Choi et al. "Graphene/MoS2 nanohybrid for biosensors". In: *Materials* 14.3 (2021), pp. 1–22.

[101] Y. Wang et al. "Microspectroscopic SERS detection of interleukin-6 with rationally designed gold/silver nanoshells". In: *Analyst* 138.6 (2013), pp. 1764–1771.

[102] Y. Zeng et al. "Watching SERS glow for multiplex biomolecular analysis in the clinic: A review". In: *Applied Materials Today* 15 (2019), pp. 431–444.

[103] K. Murphy and C. Weaver. *Janeway's Immunobiology*. Ed. by M. Toledo. 9th ed. Vol. 13. 1. New York, USA: Garland Science, Taylor & Francis Group, LLC, 2017, pp. 1277–1280.

[104] W. Jiang et al. "Nanoparticle-mediated cellular response is size-dependent". In: *Nature Nanotechnology* 3.3 (2008), pp. 145–150.

[105] K. Kneipp. "Surface-enhanced Raman scattering". In: *Physics Today* 60.11 (2007), pp. 40–46.

[106] Y. Wang et al. "Biocompatibility and biodistribution of surface-enhanced Raman scattering nanoprobes in zebrafish embryos: In vivo and multiplex imaging". In: *ACS Nano* 4.7 (2010), pp. 4039–4053.

[107] X. H. Pham et al. "Adenosine triphosphate-encapsulated liposomes with plasmonic nanoparticles for surface enhanced Raman scattering-based immunoassays". In: *Sensors (Switzerland)* 17.7 (2017).

[108] L. Zeng et al. "Raman Reporter-Coupled Agcore@Aushell Nanostars for in Vivo Improved Surface Enhanced Raman Scattering Imaging and Near-infrared Triggered Photothermal Therapy in Breast Cancers". In: *ACS Applied Materials and Interfaces* 7.30 (2015), pp. 16781–16791.

[109] L. Wu et al. "Rapid and reproducible analysis of thiocyanate in real human serum and saliva using a droplet SERS-microfluidic chip". In: *Biosensors and Bioelectronics* 62 (2014), pp. 13–18.

[110] Y. Zhang et al. "Rapid simultaneous detection of multi-pesticide residues on apple using SERS technique". In: *Analyst* 139.20 (2014), pp. 5148–5154.

[111] S. Zong et al. "Surface enhanced Raman scattering traceable and glutathione responsive nanocarrier for the intracellular drug delivery". In: *Analytical Chemistry* 85.4 (2013), pp. 2223–2230.

[112] I. Freestone et al. "The Lycurgus Cup - A Roman nanotechnology". In: *Gold Bulletin* 40.4 (2008), pp. 270–277.

[113] M. Faraday. "The Bakerian Lecture - Experimental relations of gold (and other metals) to light". In: *Spie Milestone Series Ms*. Vol. 147. 1857, pp. 145–181.

[114] M. Wuithschick et al. "Turkevich in New Robes: Key Questions Answered for the Most Common Gold Nanoparticle Synthesis". In: *ACS Nano* 9.7 (2015), pp. 7052–7071.

[115] J. C. Love et al. "Self-Assembled Monolayers of Thiolates on Metals as a Form of Nanotechnology". In: *Chemical Reviews* 105.4 (2005), pp. 1103–1170.

[116] R. A. Sperling and W. J. Parak. "Surface modification, functionalization and bioconjugation of colloidal Inorganic nanoparticles". In: *Philosophical Transactions of the Royal Society A: Mathematical, Physical and Engineering Sciences* 368.1915 (2010), pp. 1333–1383.

[117] M. Moskovits. "Surface-enhanced Raman spectroscopy: A brief retrospective". In: *Journal of Raman Spectroscopy* 36.6-7 (2005), pp. 485–496.

[118] N. G. Bastús, J. Comenge, and V. Puntes. "Kinetically controlled seeded growth synthesis of citrate-stabilized gold nanoparticles of up to 200 nm: Size focusing versus ostwald ripening". In: *Langmuir* 27.17 (2011), pp. 11098–11105.

[119] N. G. Bastús et al. "Synthesis of Highly Monodisperse Citrate-Stabilized Silver Nanoparticles of up to 200 nm: Kinetic Control and Catalytic Properties". In: *Chemistry of Materials* 26.9 (2014), pp. 2836–2846.

[120] A. M. Smith, M. C. Mancini, and S. Nie. "Second window for in vivo imaging Andrew". In: *Nature Nanotechnology* 4.11 (2009), pp. 710–711.

[121] P. A. Mercadal, E. R. Encina, and E. A. Coronado. "Colloidal SERS Substrate for the Ultrasensitive Detection of Biotinylated Antibodies Based on Near-Field Gradient within the Gap of Au Nanoparticle Dimers". In: *The Journal of Physical Chemistry C* 123.38 (2019), pp. 23577–23585.

[122] D. Rodríguez-Fernández et al. "Hybrid Au-SiO2 core-satellite colloids as switchable SERS tags". In: *Chemistry of Materials* 27.7 (2015), pp. 2540–2545.

[123] J. H. Yoon et al. "Surface plasmon coupling of compositionally heterogeneous core-satellite nanoassemblies". In: *Journal of Physical Chemistry Letters* 4.9 (2013), pp. 1371–1378.

[124] N. D. Burrows et al. "Understanding the Seed-Mediated Growth of Gold Nanorods through a Fractional Factorial Design of Experiments". In: *Langmuir* 33.8 (2017), pp. 1891–1907.

[125] H. Park et al. "SERS imaging of HER2-overexpressed MCF7 cells using antibody-conjugated gold nanorods". In: *Physical Chemistry Chemical Physics* 11.34 (2009), p. 7444.

[126] K. Park et al. "Growth mechanism of gold nanorods". In: *Chemistry of Materials* 25.4 (2013), pp. 555–563.

[127] L. Scarabelli et al. "A "Tips and Tricks"Practical Guide to the Synthesis of Gold Nanorods". In: *Journal of Physical Chemistry Letters* 6.21 (2015), pp. 4270–4279.

[128] H. Yuan et al. "Quantitative surface-enhanced resonant Raman scattering multiplexing of biocompatible gold nanostars for in vitro and ex vivo detection". In: *Analytical Chemistry* 85.1 (2013), pp. 208–212.

[129] Q. Zhang et al. "Seed-mediated synthesis of ag nanocubes with controllable edge lengths in the range of 30-200 nm and comparison of their optical properties". In: *Journal of the American Chemical Society* 132.32 (2010), pp. 11372–11378.

[130] S. E. Skrabalak et al. "Facile synthesis of Ag nanocubes and Au nanocages". In: *Nature Protocols* 2.9 (2007), pp. 2182–2190.

[131] L. Scarabelli et al. "Monodisperse gold nanotriangles: Size control, large-scale self-assembly, and performance in surface-enhanced Raman scattering". In: *ACS Nano* 8.6 (2014), pp. 5833–5842.

[132] R. Mei et al. "Lipid Bilayer-Enabled Synthesis of Waxberry-like Core-Fluidic Satellite Nanoparticles: Toward Ultrasensitive Surface-Enhanced Raman Scattering Tags for Bioimaging". In: *ACS Applied Materials and Interfaces* 10.28 (2018), pp. 23605–23616.

[133] Q. Tao et al. "A highly sensitive and recyclable SERS substrate based on Ag-nanoparticle-decorated ZnO nanoflowers in ordered arrays". In: *Dalton Transactions* 44.7 (2015), pp. 3447–3453.

[134] J. Xie et al. "The synthesis of SERS-active gold nanoflower tags for in vivo applications". In: *ACS Nano* 2.12 (2008), pp. 2473–2480.

[135] D. Xu et al. "Development of chitosan-coated gold nanoflowers as SERS-active probes". In: *Nanotechnology* 21.37 (2010).

[136] A. R. Tao, S. Habas, and P. Yang. "Shape Control of Colloidal Metal Nanocrystals". In: *Small* 4.3 (2008), pp. 310–325.

[137] V. Giannini, R. Rodríguez-Oliveros, and J. A. Sánchez-Gil. "Surface Plasmon Resonances of Metallic Nanostars/Nanoflowers for Surface-Enhanced Raman Scattering". In: *Plasmonics* 5.1 (2010), pp. 99–104.

[138] W. Y. Ma et al. "A numerical investigation of the effect of vertex geometry on localized surface plasmon resonance of nanostructures". In: *Optics Express* 18.2 (2010), pp. 843–853.

[139] C. L. Nehl, H. Liao, and J. H. Hafner. "Optical Properties of Star-Shaped Gold Nanoparticles". In: *Nano Letters* 6.4 (2006), pp. 683–688.

[140] Y. I. Park et al. "Nanostar Clustering Improves the Sensitivity of Plasmonic Assays". In: *Bioconjugate Chemistry* 26.8 (2015), pp. 1470–1474.

[141] H. de Puig et al. "Extinction Coefficient of Gold Nanostars". In: *The Journal of Physical Chemistry C* 119.30 (2015), pp. 17408–17415.

[142] H. Yuan et al. "Gold nanostars: surfactant-free synthesis, 3D modelling, and two-photon photoluminescence imaging". In: *Nanotechnology* 23.7 (2012), p. 075102.

[143] J. Depciuch et al. "Control of Arms of Au Stars Size and its Dependent Cytotoxicity and Photosensitizer Effects in Photothermal Anticancer Therapy". In: *International Journal of Molecular Sciences* 20.20 (2019), pp. 1–14.

[144] W. Ahmed et al. "Controlling the morphology of multi-branched gold nanoparticles". In: *Nanotechnology* 21.12 (2010), p. 125605.

[145] M. J. Mulvihill et al. "Anisotropic etching of silver nanoparticles for plasmonic structures capable of single-particle SERS". In: *Journal of the American Chemical Society* 132.1 (2010), pp. 268–274.

[146] M. M. Vega et al. "Long-term stability of surfactant-free gold nanostars". In: *Journal of Nanoparticle Research* 16.11 (2014), pp. 2729–2739.

[147] S. Huang et al. "Molecular selectivity of graphene-enhanced Raman scattering". In: *Nano Letters* 15.5 (2015), pp. 2892–2901.

[148] B. Ananthoju et al. "Controlled Electrodeposition of Gold on Graphene: Maximization of the Defect-Enhanced Raman Scattering Response". In: *Small* 15.48 (2019), pp. 1–10.

[149] C. Muccianti et al. "Coupled 2D Semiconductor–Molecular Excitons with Enhanced Raman Scattering". In: *The Journal of Physical Chemistry C* 124.50 (2020), pp. 27637–27644.

[150] J. L. Lopes et al. "Surface-Enhanced Raman Scattering due to a Synergistic Effect on ZnS and Graphene Oxide". In: *Journal of Physical Chemistry C* 124.23 (2020), pp. 12742–12751.

[151] C. Gu et al. "Synthesis and defect engineering of molybdenum oxides and their SERS applications". In: *Nanoscale* 13.11 (2021), pp. 5620–5651.

[152] A. Pramanik et al. "Giant Chemical and Excellent Synergistic Raman Enhancement from a 3D MoS2- xOx-Gold Nanoparticle Hybrid". In: *ACS Omega* 4.6 (2019), pp. 11112–11118.

[153] Y. Wang and S. Schlücker. "Rational design and synthesis of SERS labels". In: *Analyst* 138.8 (2013), pp. 2224–2238.

[154] Y. Chen et al. "Alkyne-Modulated Surface-Enhanced Raman Scattering-Palette for Optical Interference-Free and Multiplex Cellular Imaging". In: *Analytical Chemistry* 88.12 (2016), pp. 6115–6119.

[155] M. R. Hoonejani et al. "Quantitative multiplexed simulated-cell identification by SERS in microfluidic devices". In: *Nanoscale* 7.40 (2015), pp. 16834–16840.

[156] S. J. Cho et al. "Combinatorial synthesis of a triphenylmethine library and their application in the development of Surface Enhanced Raman Scattering (SERS) probes". In: *Chem. Commun.* 46.5 (2010), pp. 722–724.

[157] K. K. Maiti et al. "Development of biocompatible SERS nanotag with increased stability by chemisorption of reporter molecule for in vivo cancer detection". In: *Biosensors and Bioelectronics* 26.2 (2010), pp. 398–403.

[158] A. Samanta et al. "Ultrasensitive Near-Infrared Raman Reporters for SERS-Based In Vivo Cancer Detection". In: *Angewandte Chemie International Edition* 50.27 (2011), pp. 6089–6092.

[159] K. K. Maiti et al. "Multiplex targeted in vivo cancer detection using sensitive near-infrared SERS nanotags". In: *Nano Today* 7.2 (2012), pp. 85–93.

[160] K. K. Maiti et al. "Multiplex cancer cell detection by SERS nanotags with cyanine and triphenylmethine Raman reporters". In: *Chemical Communications* 47.12 (2011), pp. 3514–3516.

[161] H. Hinterwirth et al. "Quantifying Thiol Ligand Density of Self-Assembled Monolayers on Gold Nanoparticles by Inductively Coupled Plasma–Mass Spectrometry". In: *ACS Nano* 7.2 (2013), pp. 1129–1136.

[162] C. Jehn et al. "Water soluble SERS labels comprising a SAM with dual spacers for controlled bioconjugation". In: *Physical Chemistry Chemical Physics* 11.34 (2009), pp. 7499–7504.

[163] M. Schütz et al. "Synthesis of Glass-Coated SERS Nanoparticle Probes via SAMs with Terminal SiO 2 Precursors". In: *Small* 6.6 (2010), pp. 733–737.

[164] M. Schütz, M. Salehi, and S. Schlücker. "Direct Silica Encapsulation of Self-Assembled-Monolayer-Based Surface-Enhanced Raman Scattering Labels with Complete Surface Coverage of Raman Reporters by Noncovalently Bound Silane Precursors". In: *Chemistry - An Asian Journal* 9.8 (2014), pp. 2219–2224.

[165] B. Küstner et al. "SERS labels for red laser excitation: Silica-encapsulated SAMs on tunable gold/silver nanoshells". In: *Angewandte Chemie - International Edition* 48.11 (2009), pp. 1950–1953.

[166] J. Kneipp, H. Kneipp, and K. Kneipp. "SERS—a single-molecule and nanoscale tool for bioanalytics". In: *Chemical Society Reviews* 37.5 (2008), pp. 1052–1060.

[167] H. Fujioka et al. "Multicolor Activatable Raman Probes for Simultaneous Detection of Plural Enzyme Activities". In: *Journal of the American Chemical Society* 142.49 (2020), pp. 20701–20707.

[168] D. Graham, K. Faulds, and W. E. Smith. "Biosensing using silver nanoparticles and surface enhanced resonance Raman scattering". In: *Chemical Communications* 42 (2006), pp. 4363–4371.

[169] L. Wei et al. "Super-multiplex vibrational imaging". In: *Nature* 544.7651 (2017), pp. 465–470.

[170] K. Koike et al. "Quantitative drug dynamics visualized by alkyne-tagged plasmonic enhanced Raman microscopy". In: *ACS Nano* 14.11 (2020), pp. 15032–15041.

[171] Y. Li et al. "Microarray surface enhanced Raman scattering based immunosensor for multiplexing detection of mycotoxin in foodstuff". In: *Sensors and Actuators, B: Chemical* 266 (2018), pp. 115–123.

[172] Y. Yin et al. "Prussian Blue as a Highly Sensitive and Background-Free Resonant Raman Reporter". In: *Analytical Chemistry* 89.3 (2017), pp. 1551–1557.

[173] D. Zhang et al. "Isotope edited internal standard method for quantitative surface-enhanced Raman spectroscopy". In: *Analytical Chemistry* 77.11 (2005), pp. 3563–3569.

[174] H. Fujioka et al. "Multicolor Activatable Raman Probes for Simultaneous Detection of Plural Enzyme Activities". In: *Journal of the American Chemical Society* 142.49 (2020), pp. 20701–20707.

[175] L. A. Lane, X. Qian, and S. Nie. "SERS Nanoparticles in Medicine: From Label-Free Detection to Spectroscopic Tagging". In: *Chemical Reviews* 115.19 (2015), pp. 10489–10529.

[176] P. A. G. Cormack et al. "Multidentate macromolecules for functionalisation, passivation and labelling of metal nanoparticles". In: *Chemical Communications* 22 (2008), pp. 2517–2519.

[177] F. McKenzie et al. "SERRS coded nanoparticles for biomolecular labelling with wavelength-tunable discrimination". In: *The Analyst* 134.3 (2009), pp. 549–556.

[178] M. Schütz et al. "Hydrophilically stabilized gold nanostars as SERS labels for tissue imaging of the tumor suppressor p63 by immuno-SERS microscopy". In: *Chemical Communications* 47.14 (2011), pp. 4216–4218.

[179] C. Auría-Soro et al. "Interactions of Nanoparticles and Biosystems: Microenvironment of Nanoparticles and Biomolecules in Nanomedicine". In: *Nanomaterials* 9.10 (2019), p. 1365.

[180] L. Blanco-Covián et al. "Au@Ag SERRS tags coupled to a lateral flow immunoassay for the sensitive detection of pneumolysin". In: *Nanoscale* 9.5 (2017), pp. 2051–2058.

[181] S. P. Boulos et al. "Nanoparticle–Protein Interactions: A Thermodynamic and Kinetic Study of the Adsorption of Bovine Serum Albumin to Gold Nanoparticle Surfaces". In: *Langmuir* 29.48 (2013), pp. 14984–14996.

[182] L. N. Furini et al. "pH-responsive Ag@PAH nanoparticles applied in SERS". In: *Materials Letters* 277 (2020), pp. 128346–128350.

[183] L. Sun et al. "Composite organic-inorganic nanoparticles as Raman labels for tissue analysis". In: *Nano Letters* 7.2 (2007), pp. 351–356.

[184] D. H. Tsai et al. "Adsorption and conformation of serum albumin protein on gold nanoparticles investigated using dimensional measurements and in situ spectroscopic methods". In: *Langmuir* 27.6 (2011), pp. 2464–2477.

[185] G. Bodelõn et al. "Au@pNIPAM SERRS Tags for Multiplex Immunophenotyping Cellular Receptors and Imaging Tumor Cells". In: *Small* 11.33 (2015), pp. 4149–4157.

[186] O. E. Eremina et al. "Silver-chitosan nanocomposite as a plasmonic platform for SERS sensing of polyaromatic sulfur heterocycles in oil fuel". In: *Nanotechnology* 31.22 (2020).

[187] F. Fu et al. "Biomimetic synthesis of 3D Au-decorated chitosan nanocomposite for sensitive and reliable SERS detection". In: *Chemical Engineering Journal* 392.December 2019 (2020), p. 123693.

[188] M. Grzelczak et al. "Hydrophobic Interactions Modulate Self-assembly of Gold Nanoparticles". In: *ACS Nano* 6.12 (2012), pp. 11059–11065.

[189] T. Kawano et al. "PNIPAM gel-coated gold nanorods for targeted delivery responding to a near-infrared laser". In: *Bioconjugate Chemistry* 20.2 (2009), pp. 209–212.

[190] T. Liu and B. Thierry. "A solution to the PEG dilemma: Efficient bioconjugation of large gold nanoparticles for biodiagnostic applications using mixed layers". In: *Langmuir* 28.44 (2012), pp. 15634–15642.

[191] B. Mir-Simon et al. "Universal One-Pot and Scalable Synthesis of SERS Encoded Nanoparticles". In: *Chemistry of Materials* 27.3 (2015), pp. 950–958.

[192] D. G. de Oliveira et al. "Chitosan-based improved stability of gold nanoparticles for the study of adsorption of dyes using SERS". In: *Vibrational Spectroscopy* 87 (2016), pp. 8–13.

[193] D. G. de Oliveira, G. A. Pimentel, and G. F. Andrade. "Chitosan stabilization and control over hot spot formation of gold nanospheres and SERS performance evaluation". In: *Vibrational Spectroscopy* 110.June (2020), p. 103119.

[194] P. Pinkhasova et al. "Differential SERS activity of gold and silver nanostructures enabled by adsorbed poly(vinylpyrrolidone)". In: *Langmuir* 28.5 (2012), pp. 2529–2535.

[195] M. Potara, D. Maniu, and S. Astilean. "The synthesis of biocompatible and SERS-active gold nanoparticles using chitosan". In: *Nanotechnology* 20.31 (2009).

[196] B. Ranjani et al. "D-glucosamine chitosan base molecule-assisted synthesis of different shape and sized silver nanoparticles by a single pot method: A greener approach for sensor and microbial applications". In: *International Journal of Biological Macromolecules* 133 (2019), pp. 1280–1287.

[197] X. Tan et al. "Polyvinylpyrrolidone-(PVP-) coated silver aggregates for high performance surface-enhanced Raman scattering in living cells". In: *Nanotechnology* 20.44 (2009), pp. 2–9.

[198] A. Xie et al. "Stimuli-responsive pro-drug-based cancer nanomedicine". In: *eBioMedicine* 56 (2020), p. 102821.

[199] M. Yang et al. "Development of Polymer-Encapsulated Metal Nanoparticles as Surface-Enhanced Raman Scattering Probes". In: *Small* 5.2 (2008), pp. 198–202.

[200] K. Bando et al. "Dynamic pH measurements of intracellular pathways using nanoplasmonic assemblies". In: *The Analyst* 145.17 (2020), pp. 5768–5775.

[201] T. H. Chung et al. "The effect of surface charge on the uptake and biological function of mesoporous silica nanoparticles in 3T3-L1 cells and human mesenchymal stem cells". In: *Biomaterials* 28.19 (2007), pp. 2959–2966.

[202] W. E. Doering and S. Nie. "Spectroscopic Tags Using Dye-Embedded Nanoparticles and Surface-Enhanced Raman Scattering". In: *Analytical Chemistry* 75.22 (2003), pp. 6171–6176.

[203] S. P. Mulvaney et al. "Glass-coated, analyte-tagged nanoparticles: A new tagging system based on detection with surface-enhanced Raman scattering". In: *Langmuir* 19.11 (2003), pp. 4784–4790.

[204] L. Rodríguez-Lorenzo et al. "Intracellular mapping with SERS-encoded gold nanostars". In: *Integrative Biology* 3.9 (2011), pp. 922–926.

[205] C. Wang et al. "Monodispersed Gold Nanorod-Embedded Silica Particles as Novel Raman Labels for Biosensing". In: *Advanced Functional Materials* 18.2 (2008), pp. 355–361.

[206] Y. Wang, L. Chen, and P. Liu. "Biocompatible triplex Ag@SiO 2@mTiO 2 core-shell nanoparticles for simultaneous fluorescence-SERS bimodal imaging and drug delivery". In: *Chemistry - A European Journal* 18.19 (2012), pp. 5935–5943.

[207] X. Su et al. "Phospholipid Encapsulated AuNR@Ag/Au Nanosphere SERS Tags with Environmental Stimulus Responsive Signal Property". In: *ACS Applied Materials and Interfaces* 8.16 (2016), pp. 10201–10211.

[208] S. Avvakumova et al. "Does conjugation strategy matter? Cetuximab-conjugated gold nanocages for targeting triple-negative breast cancer cells". In: *Nanoscale Advances* 1.9 (2019), pp. 3626–3638.

[209] M. Muhammad and Q. Huang. "A review of aptamer-based surface-enhanced Raman scattering biosensors: Design strategies and applications". In: *Talanta* 227.December 2020 (2021), p. 122188.

[210] C. Fasolato et al. "Folate-based single cell screening using surface enhanced Raman microimaging". In: *Nanoscale* 8.39 (2016), pp. 17304–17313.

[211] C. Fasolato et al. "Antifolate SERS-active nanovectors: Quantitative drug nanostructuring and selective cell targeting for effective theranostics". In: *Nanoscale* 11.32 (2019), pp. 15224–15233.

[212] C. H. Zhang et al. "Plasmon Coupling Enhanced Raman Scattering Nanobeacon for Single-Step, Ultrasensitive Detection of Cholera Toxin". In: *Analytical Chemistry* 88.15 (2016), pp. 7447–7452.

[213] J. Ni et al. "Immunoassay Readout Method Using Extrinsic Raman Labels Adsorbed on Immunogold Colloids". In: *Analytical Chemistry* 71.21 (1999), pp. 4903–4908.

[214] M. D. Porter et al. "SERS as a bioassay platform: Fundamentals, design, and applications". In: *Chemical Society Reviews* 37.5 (2008), pp. 1001–1011.

[215] G. T. Hermanson. "Microparticles and Nanoparticles". In: *Bioconjugate Techniques*. Ed. by M. Preap. 3rd ed. London: Elsevier, 2013, pp. 549–587.

[216] K. E. Sapsford et al. "Functionalizing Nanoparticles with Biological Molecules: Developing Chemistries that Facilitate Nanotechnology". In: *Chemical Reviews* 113.3 (2013), pp. 1904–2074.

[217] R. Franco and E. Pereira. "Gold Nanoparticles and Proteins, Interaction". In: *Encyclopedia of Metalloproteins*. Ed. by R. H. Kretsinger, V. N. Uversky, and E. A. Permyakov. 1st ed. Vol. 111. 479. New York, NY: Springer New York, 2013. Chap. G, pp. 908–915.

[218] M. H. Jazayeri et al. "Various methods of gold nanoparticles (GNPs) conjugation to antibodies". In: *Sensing and Bio-Sensing Research* 9 (2016), pp. 17–22.

[219] J. Liu and Q. Peng. "Protein-gold nanoparticle interactions and their possible impact on biomedical applications". In: *Acta Biomaterialia* 55 (2017), pp. 13–27.

[220] S. Balamurugan et al. "Surface immobilization methods for aptamer diagnostic applications". In: *Analytical and Bioanalytical Chemistry* 390.4 (2008), pp. 1009–1021.

[221] S. Puertas et al. "Taking Advantage of Unspecific Interactions to Produce Highly Active Magnetic Nanoparticle-Antibody Conjugates". In: *ACS Nano* 5.6 (2011), pp. 4521–4528.

[222] A. K. Abbas, A. H. Lichtman, and S. Pillai. *Cellular and molecular immunology*. Ed. by E. J. Wood. 9th ed. Vol. 32. 1. Philadelphia, USA: International Union of Biochemistry and Molecular Biology, 2004, pp. 1–565.

[223] D. Wild, J. Rhys, and C. Sheehan, eds. *The Immunoassay Handbook*. 4th ed. Oxford, UK: Elsevier, 2013.

[224] S. Awwad and U. Angkawinitwong. "Overview of antibody drug delivery". In: *Pharmaceutics* 10.3 (2018), pp. 1–24.

[225] T. S. Raju and W. R. Strohl. "Potential therapeutic roles for antibody mixtures". In: *Expert Opinion on Biological Therapy* 13.10 (2013), pp. 1347–1352.

[226] L. Harris et al. *Refined structure of an intact IgG2a monoclonal antibody*. 1997. URL: https://www.rcsb.org/structure/1igt (visited on 11/13/2020).

[227] M. S. Luchansky and R. C. Bailey. "Silicon photonic microring resonators for quantitative cytokine detection and T-cell secretion analysis". In: *Analytical Chemistry* 82.5 (2010), pp. 1975–1981.

[228] K. Ren, J. Zhou, and H. Wu. "Materials for microfluidic chip fabrication". In: *Accounts of Chemical Research* 46.11 (2013), pp. 2396–2406.

[229] B. H. Weigl, R. L. Bardell, and C. Cabrera. "Introduction to Microfluidic Techniques". In: *Handbook of Biosensors and Biochips*. Ed. by R. S. Marks. 1st ed. Chichester, UK: John Wiley & Sons, Ltd, 2008. Chap. 41, pp. 1–19.

[230] Y. Song et al. "Recent Progress in Microfluidics-Based Biosensing". In: *Analytical Chemistry* 91.1 (2019), pp. 388–404.

[231] H. Zhu et al. "Wood-Derived Materials for Green Electronics, Biological Devices, and Energy Applications". In: *Chemical Reviews* 116.16 (2016), pp. 9305–9374.

[232] A. T. Vicente et al. "Multifunctional cellulose-paper for light harvesting and smart sensing applications". In: *Journal of Materials Chemistry C* 6.13 (2018), pp. 3143–3181.

[233] B. Ying et al. "NanoPADs and nanoFACEs: An optically transparent nanopaper-based device for biomedical applications". In: *Lab on a Chip* 20.18 (2020), pp. 322–333.

[234] S. Shin and J. Hyun. "Matrix-Assisted Three-Dimensional Printing of Cellulose Nanofibers for Paper Microfluidics". In: *ACS Applied Materials and Interfaces* 9.31 (2017), pp. 26438–26446.

[235] C. Chang and L. Zhang. "Cellulose-based hydrogels: Present status and application prospects". In: *Carbohydrate Polymers* 84.1 (2011), pp. 40–53.

[236] X. Shen et al. "Hydrogels based on cellulose and chitin: Fabrication, properties, and applications". In: *Green Chemistry* 18.1 (2015), pp. 53–75.

[237] R. Gao et al. "Wash-free magnetic immunoassay of the PSA cancer marker using SERS and droplet microfluidics". In: *Lab on a Chip* 16.6 (2016), pp. 1022–1029.

[238] Y. Li et al. "Surface-enhanced Raman nanoparticles for tumor theranostics applications". In: *Acta Pharmaceutica Sinica B* 8.3 (2018), pp. 349–359.

[239] N. U. M. Nizam, M. M. Hanafiah, and K. S. Woon. "A content review of life cycle assessment of nanomaterials: Current practices, challenges, and future prospects". In: *Nanomaterials* 11.12 (2021), p. 3324.

[240] B. Salieri et al. "Life cycle assessment of manufactured nanomaterials: Where are we?" In: *NanoImpact* 10 (2018), pp. 108–120.

[241] M. Prudêncio, A. Rodriguez, and M. M. Mota. "The silent path to thousands of merozoites: the Plasmodium liver stage". In: *Nature Reviews Microbiology* 4.11 (2006), pp. 849–856.

[242] A. F. Cowman et al. "The Molecular Basis of Erythrocyte Invasion by Malaria Parasites". In: *Cell Host and Microbe* 22.2 (2017), pp. 232–245.

[243] A. Sturm et al. "Manipulation of host hepatocytes by the malaria parasite for delivery into liver sinusoids". In: *Science* 313.5791 (2006), pp. 1287–1290.

[244] A. F. Cowman et al. "Malaria: Biology and Disease". In: *Cell* 167.3 (2016), pp. 610–624.

[245] H. Kumar and N. H. Tolia. "Getting in: The structural biology of malaria invasion". In: *PLoS Pathogens* 15.9 (2019), pp. 1–10.

[246] W. Wang et al. "Antibody-free rapid diagnosis of malaria in whole blood with surface-enhanced Raman Spectroscopy using Nanostructured Gold Substrate". In: *Advances in Medical Sciences* 65.1 (2020), pp. 86–92.

[247] O. G. Ajakaye and M. R. Ibukunoluwa. "Performance evaluation of a popular malaria RDT in Nigeria compared with microscopy". In: *Journal of Parasitic Diseases* 44.1 (2020), pp. 122–125.

[248] A. Björkman and A. Mårtensson. "Risks and benefits of targeted malaria treatment based on rapid diagnostic test results". In: *Clinical Infectious Diseases* 51.5 (2010), pp. 512–514.

[249] J. M. Roth et al. "Molecular malaria diagnostics: A systematic review and meta-analysis". In: *Critical Reviews in Clinical Laboratory Sciences* 53.2 (2016), pp. 87–105.

[250] E. C. Oriero et al. "Novel techniques and future directions in molecular diagnosis of malaria in resource-limited settings". In: *Expert Review of Molecular Diagnostics* 15.11 (2015), pp. 1419–1426.

[251] J. Shah et al. "Fluorescence In Situ hybridization (FISH) assays for diagnosing malaria in endemic areas". In: *PLoS ONE* 10.9 (2015), pp. 1–15.

[252] P. Pattanaik et al. "Malaria detection using deep residual networks with mobile microscopy". In: *Journal of King Saud University - Computer and Information Sciences* 34.5 (2022), pp. 1700–1705.

[253] Vijayalakshmi A and Rajesh Kanna B. "Deep learning approach to detect malaria from microscopic images". In: *Multimedia Tools and Applications* 79.21-22 (2020), pp. 15297–15317.

[254] A. Tiwari, A. Gupta, and M. L. Yadav. "Malaria Associated Pseudoeosinophilia Determined in Automated Hematology Analyzer". In: *Scholars Journal of Applied Medical Sciences* 6691.July (2019), pp. 4073–4076.

[255] L. Hamm, A. Gee, and A. S. D. S. Indrasekara. "Recent Advancement in the Surface-Enhanced Raman Spectroscopy-Based Biosensors for Infectious Disease Diagnosis". In: *Applied Sciences* 9.7 (2019), p. 1448.

[256] B. Heidt et al. *Point of care diagnostics in resource-limited settings: A review of the present and future of PoC in its most needed environment*. 2020.

[257] J. Li et al. "β-Cyclodextrin-Stabilized Au Nanoparticles for the Detection of Butyl Benzyl Phthalate". In: *ACS Applied Nano Materials* 2.5 (2019), pp. 2743–2751.

[258] P. Deng et al. "Atorvastatin Reduces the Expression of COX-2 mRNA in Peripheral Blood Monocytes from Patients with Acute Myocardial Infarction and Modulates the Early Inflammatory Response". In: *Clinical Chemistry* 52.2 (2006), pp. 300–303.

[259] D. Selvarajah et al. "Loop-mediated isothermal amplification (LAMP) test for diagnosis of uncomplicated malaria in endemic areas: A meta-analysis of diagnostic test accuracy". In: *Malaria Journal* 19.1 (2020), pp. 1–10.

[260] D. Sebba et al. "A point-of-care diagnostic for differentiating Ebola from endemic febrile diseases". In: *Science Translational Medicine* 10.471 (2018), eaat0944.

[261] B. E. Barber et al. "Evaluation of the Sensitivity of a pLDH-Based and an Aldolase-Based Rapid Diagnostic Test for Diagnosis of Uncomplicated and Severe Malaria Caused by PCR-Confirmed Plasmodium knowlesi, Plasmodium falciparum, and Plasmodium vivax". In: *Journal of Clinical Microbiology* 51.4 (2013), pp. 1118–1123.

[262] T. Lee et al. "Single Functionalized pRNA/Gold Nanoparticle for Ultrasensitive MicroRNA Detection Using Electrochemical Surface-Enhanced Raman Spectroscopy". In: *Advanced Science* 7.3 (2020), pp. 1902477–1902488.

[263] N. Mhlanga et al. "Sandwich-based surface-enhanced Raman scattering probes for detection and quantification of malaria". In: *Journal of Raman Spectroscopy* 51.12 (2020), pp. 2416–2424.

[264] S. Ghosh et al. "A new microchannel capillary flow assay (MCFA) platform with lyophilized chemiluminescence reagents for a smartphone-based POCT detecting malaria". In: *Microsystems and Nanoengineering* 6.1 (2020), pp. 1–15.

[265] K. V. Ragavan et al. "Advances in biosensors and optical assays for diagnosis and detection of malaria". In: *Biosensors and Bioelectronics* 105.January (2018), pp. 188–210.

[266] N. K. Singh et al. "Capacitive malaria aptasensor using *Plasmodium falciparum* glutamate dehydrogenase as target antigen in undiluted human serum". In: *Biosensors and Bioelectronics* 117.June (2018), pp. 246–252.

[267] J. L. Burnett, J. L. Carns, and R. Richards-Kortum. "In vivo microscopy of hemozoin: towards a needle free diagnostic for malaria". In: *Biomedical Optics Express* 6.9 (2015), p. 3462.

[268] T. Frosch et al. "Morphology-sensitive Raman modes of the malaria pigment hemozoin". In: *The Analyst* 134.6 (2009), p. 1126.

[269] T. Frosch et al. "In Situ Localization and Structural Analysis of the Malaria Pigment Hemozoin". In: *The Journal of Physical Chemistry B* 111.37 (2007), pp. 11047–11056.

[270] B. T. Grimberg and K. O. Grimberg. "Hemozoin detection may provide an inexpensive, sensitive, 1-minute malaria test that could revolutionize malaria screening". In: *Expert Review of Anti-Infective Therapy* 14.10 (2016), pp. 879–883.

[271] F. Milesi et al. "On-chip selective capture and detection of magnetic fingerprints of malaria". In: *Sensors (Switzerland)* 20.17 (2020), pp. 1–12.

[272] C. Yuen. "Magnetic field enriched surface enhanced resonance Raman spectroscopy for early malaria diagnosis". In: *Journal of Biomedical Optics* 17.1 (2012), pp. 017005–1–7.

[273] M. Brückner et al. "Fiber array based hyperspectral Raman imaging for chemical selective analysis of malaria-infected red blood cells". In: *Analytica Chimica Acta* 894 (2015), pp. 76–84.

[274] K. Chen et al. "Towards ultrasensitive malaria diagnosis using surface enhanced Raman spectroscopy". In: *Scientific Reports* 6.1 (2016), pp. 20177–20187.

[275] H. T. Ngo et al. "Sensitive DNA detection and SNP discrimination using ultrabright SERS nanorattles and magnetic beads for malaria diagnostics". In: *Biosensors and Bioelectronics* 81 (2016), pp. 8–14.

[276] H. T. Ngo et al. "Direct Detection of Unamplified Pathogen RNA in Blood Lysate using an Integrated Lab-in-a-Stick Device and Ultrabright SERS Nanorattles". In: *Scientific Reports* 8.1 (2018), pp. 4075–4088.

[277] K. Chen et al. "Review of surface enhanced Raman spectroscopy for malaria diagnosis and a new approach for the detection of single parasites in the ring stage". In: *IEEE Journal of Selected Topics in Quantum Electronics* 22.4 (2016), pp. 179–187.

[278] A. P. Hole and V. Pulijala. "An Inductive-Based Sensitive and Reusable Sensor for the Detection of Malaria". In: *IEEE Sensors Journal* 21.2 (2021), pp. 1609–1615.

[279] H. Pei et al. "Recent advances in microfluidic technologies for circulating tumor cells: enrichment, single-cell analysis, and liquid biopsy for clinical applications". In: *Lab on a Chip* 20.21 (2020), pp. 3854–3875.

[280] R. Nasiri et al. "Design and Simulation of an Integrated Centrifugal Microfluidic Device for CTCs Separation and Cell Lysis". In: *Micromachines* 11.7 (2020), p. 699.

[281] N. M. Pham et al. "Malaria and the 'last' parasite: How can technology help?" In: *Malaria Journal* 17.1 (2018), pp. 1–16.

Chapter

3 Development and characterisation of SERS tags

The results and data presented in this chapter have been published elsewhere: ***Maria João Oliveira****, Miguel P. de Almeida, Daniela Nunes, Elvira Fortunato, Rodrigo Martins, Hugh J. Byrne, Eulália Pereira, Hugo Águas, and Ricardo Franco. Design and Simple Assembly of Gold Nanostar Bioconjugates for Surface-Enhanced Raman Spectroscopy Immunoassays. Nanomaterials 9, 1561 (2019).*
Maria João Oliveira was responsible for the experimental work and the initial drafting of the manuscript with contributions of PhD Daniela Nunes for the scanning electron microscopy (SEM) measurements. ***Maria João Oliveira****, Inês Cunha, Miguel P. de Almeida, Tomás Calmeiro, Elvira Fortunato, Rodrigo Martins, Luís Pereira, Hugh J. Byrne, Eulália Pereira, Hugo Águas, and Ricardo Franco. Reusable and highly sensitive SERS immunoassay utilising gold nanostars and a cellulose hydrogel-based platform. Journal of Materials Chemistry B, 9 (2021).*
Maria João Oliveira was responsible for the system design and the experimental work, except for contributions from PhD Inês Cunha for the production of the regenerated cellulose hydrogel and MSc Tomás Calmeiro for the atomic force microscopy (AFM) measurements. Maria João Oliveira was also responsive for the analysis and initial drafting of the manuscript.

As mentioned in section 1.3, the main objective of this Thesis was to develop an immunoassay SERS-based microfluidic platform. For that, the work was divided in two main assignments: the development and characterisation of SERS tags for the immunoassay, and the fabrication of the microfluidic device. The following chapter describes the work devoted to designing and characterising the SERS tags as labels for detecting biomarkers. Gold nanoparticle (NP) were synthesised, with emphasis on anisotropic geometries since shapes comprising sharp tips result in extremely strong hotspots without requiring aggregation methods, as commonly used for spherical NPs [1]. Nanoparticle synthesis was then followed by their functionalisation with Raman reporters (RRs) (giving NP-Reporter

systems), assuring the proximity between the analyte and the metal surface to yield high enhancements. The specific RRs were selected to have non-overlapping spectra and similar Raman cross sections [2]. NP-Reporter systems were treated with cross-linkers, 1-ethyl-3-(3-(dimethylamino)propyl)carbodiimide (EDC) and N-hydroxysulfosuccinimide (SNHS) (EDC/SNHS), which can be used to generate a peptide bond with antibodies. The incubation of monoclonal antibodies with SERS probe solutions is the final step to fabricate the SERS tags. The SERS tags were characterised by several techniques, including ultraviolet-visible (UV-Vis) spectroscopy, ζ-potential and dynamic light scattering (DLS) to determine their localised surface plasmon resonance (LSPR) band position, polydispersity index, hydrodynamic diameter and nanoparticle functionalisation. Their morphology was determined by SEM. Also, to characterise the density of RR molecules at the NPs surface, electrophoresis in agarose gel and ζ-potential were used [3]. In addition, the batch-to-batch variability of these SERS tags was appraised, and the SERS efficiency was evaluated.

3.1 Introduction

Immunoassays using SERS are especially interesting on account of not only their increased sensitivity, but also due to their ease of translation to point-of-care formats. The basis of these assays is the SERS immunotag, a conjugation of polyclonal antibodies and anisotropic gold NPs functionalised with a RR. These SERS immunotags, once loaded with the antigen analyte, can react in a sandwich format with the same antibodies immobilised on a surface (see Figure 2.4 in section 2.2.2.1). This surface can then be used for detection in a microfluidic or immunochromatographic platform. The excellent enhancement factors presented by RRs provides an easier way to perform quantitative assays and achieve high sensitivity and lower detection limits. The distinctive and narrow Raman lines from such reporters minimise the spectroscopic overlap, allowing multiple label testing [4, 5]. Nevertheless, poor reproducibility and uniformity under complicated experimental conditions still need to be addressed [6]. The lack of standardised methods for characterisation of SERS tag reagents hinders a correct analysis of an assay's analytical performance [7, 8]. For instance, the enhancement factor is frequently used as a performance indicator of SERS tags, but concentration, size heterogeneity and an external intensity standard for comparison may present limitations to the use of this approach.

The NP surface is usually modified to provide a biologically compatible environment (such as alkanethiols for gold surfaces). Nevertheless, the mechanism of interaction between proteins and noble metal NPs needs to be carefully assessed for each specific NP-antibody pair, for the particular intended use in nanomedicine [9]. Conformational changes of the proteins resulting from interactions with metal NPs can affect the physicochemical properties of each component, leading to loss of reactivity and impaired applicability of the bioconjugates in detection methods. A broad variety of techniques, including ultraviolet-visible-infrared (UV-Vis-IR) absorption [10], fluorescence [11], and circular

dichroism spectroscopies [12–14], differential centrifugal sedimentation [3], DLS [15] or even SERS [16] can elucidate the mechanism for these interactions. Several studies have demonstrated that enzymatic activities change upon enzyme conjugated with NPs [9, 14, 17]. For example, laccase electrostatically conjugated with spherical gold NPs proved to be approximately nine times more active than the free enzyme [3]. Other examples include the observation that lysozyme did not experience perturbations to its structure and function, but the silver NPs to which it was conjugated underwent aggregation with increasing protein amounts [12]. Altough, these reports focused on the final fate of bioconjugate structure and function, and its applicability, they highlight the importance of a deep understanding of physicochemical properties of the NP-biomolecule system for successful and reproducible design of bioconjugates.

Here, SERS immunotags were produced with gold nanostars (AuNSs) functionalised with 4-mercaptobenzoic acid (MBA), and with an antibody against horseradish peroxidase (HRP). The assembly was done by either direct physisorption or by covalent conjugation, and agarose gel electrophoresis (AGE) indicated a high AuNS-antibody binding constant. The functionality of the bioconjugates is easy to determine, as the respective antigen presents peroxidase enzymatic activity. Furthermore, the chosen antibody is a generic immunoglobin, IgG antibody, opening the application of these principles to other antibody-antigen systems. All steps of conjugation were fully characterised by UV-Vis spectroscopy, DLS, ζ-Potential, SEM and AGE. Based on the latter technique, a proof-of-concept was established for the proposed immunoassay.

3.2 Materials and Methods

3.2.1 Materials

The following reagents were used: Gold(III) chloride solution 30% wt. Au in dilute hydrochloric acid (99.99%), sodium citrate tribasic dihydrate (99.0%), silver nitrate (99.9999%), Tris(hydroxymethyl)-aminomethane (99.9%), ethylenediamine tetra-acetic acid (EDTA), acetic acid ($\geq$ 99%), ethanol($\geq$99.0%), the RR MBA(99.0%), the cross-linking reagents (EDC and SNHS ($\geq$98%)), buffers (namely, 2-ethanesulfonic acid (MES), and potassium phosphate buffer), as well as the proteins used for the bioconjugate production, bovine serum albumin (BSA) and HRP, were all purchased from Sigma-Aldrich, St. Louis, USA. Hydrochloric acid (37%) was purchased from Fisher Chemical, Loughborough, UK. The polyclonal anti-HRP antibody was from Antibodies-Online, Germany. 2,2'-azino-bis(3-ethylbenzthiazoline-6-sulfonic acid) (ABTS) was from Roche, France, and, hydrogen peroxide (30%) and nitric acid (65%) were purchased from Panreac AppliChem, Germany. L-ascorbic acid (99.9%) was purchased to Fluka, Buchs, Switzerland. Protein determination was by the bicinchoninic acid (BCA) method (based on Smith *et al.* [18]) using a kit from Sigma-Aldrich, St. Louis, USA. Ultrapure™Agarose was from Invitrogen—Thermo Fisher Scientific, Waltham, USA. All chemicals and reagents were

of the highest purity available and ultrapure water (H_2O, 18.2 MΩ·cm at 25ºC, *Milli-Q*®) was used for the preparation of all solutions, unless stated otherwise.

3.2.2 Preparation of gold nanostars and SERS immunotags

3.2.2.1 Gold nanoparticles synthesis and functionalisation

All glassware used for the synthesis of NPs was immersed before use in freshly prepared *aqua regia*, a 1:3 mixture of nitric acid (Panreac AppliChem) and hydrochloric acid (Fisher Chemical). Thereafter, the glassware was vigorously washed with ultrapure water (H_2O, 18.2 MΩ·cm at 25ºC, *Milli-Q*®) . As proposed by Ojea-Jiménez *et al.* [19] as a variation of the conventional Turkevich synthesis protocol of synthesis of spheroidal gold nanoparticles (AuNPs) [20], 2 mL of a 343 mM trisodium citrate (Sigma-Aldrich, St. Louis, MO, USA) solution were added to 98 mL of ultrapure water in a round-bottom flask under heating and vigorous stirring (≈700 rpm) using a magnetic stirrer, whilst kept away from sunlight. After boiling, 69.2 µL of a 1.445 M $HAuCl_4$ solution (30 wt. % Au (III) chloride in dilute HCl, Sigma-Aldrich) were added to initiate the gold reduction reaction. After 5 min, the heating was turned off, and the suspension was cooled down to room temperature. Finally, the suspension was transferred to a glass vial covered with aluminium foil and stored in the dark at 4°C until further use.

After AuNPs synthesis and characterisation, this suspension was used as seed for AuNSs synthesis. AuNSs were synthesised using a seed-mediated growth method adapted from Yuan *et al.* [21]. A solution of 15.5 µL of $HAuCl_4$ at 1.445 M was added to 7 mL of a 2 nM suspension of AuNPs (diameter of 12 nm). Then, 450 µL of a 100 mM ascorbic acid (Fluka) solution and 450 µL of a 4 mM silver nitrate (Sigma-Aldrich) solution were added simultaneously. The resulting suspension was gently stirred for 30 s before centrifugation for 15 min at 3000 *g* (Centurion Scientific K3 Series centrifuge) and resuspension in 10 mL of ultrapure water.

The diameter and concentration of the spherical nanoparticles were determined according to the relationship between LSPR maximum and extinction molar coefficient described by Haiss *et al.* [22]. The same parameters for AuNSs were determined by the method of Puig *et al.* [23].

Gold nanostars were functionalised with a RR, MBA (Sigma-Aldrich). The molecule works simultaneously as a capping agent for the AuNSs, a RR and a bio-compatible intermediate for antibody bioconjugation. According to the desired molar ratio, a suitable volume of a 10 mM ethanolic solution of MBA (ethanol, Sigma-Aldrich) was added to the AuNSs suspension under vigorous stirring. The solution was allowed to react overnight at room temperature to ensure the formation of a complete self-assembled monolayer. Excess MBA was removed through centrifugation at 2500 *g* for 10 min, followed by redispersion. Complete monolayer formation was assessed by AGE. The UV-Vis spectrum of the AuNSs suspension was checked to confirm successful functionalisation and to identify possible aggregation effects.

3.2.2.2 SERS immunotags assembly

The AuNS–MBA–anti-HRP bioconjugates were prepared with an 0.2 nM suspension of the previously functionalised nanoparticles, with appropriate amounts of antibody to obtain bioconjugates with the desired [AuNS]:[anti-HRP] molar ratio. Incubation was in 5 mM phosphate buffer pH 7.4 for 90 min, in an orbital shaker (Biosan TS-100, Latvia) at 250 rpm, at 25°C. Samples were then centrifuged for 10 min at 4°C and 2500 *g*. The supernatant was discarded to remove excess protein and the product was resuspended in 5 mM phosphate buffer pH 7.4, ready for use.

To promote cross-linking of the carboxylic acid groups of MBA to the primary amines from the anti-HRP antibody molecules, several parameters were optimised, namely pH, reaction time, concentration and molar ratios of the reagents. The typical procedure to produce AuNS–MBA–anti-HRP SERS immunotags was executed as follows: AuNS-MBA – 0.2 nM - were washed by centrifugation at 2500 *g* at 4°C for 10 min and resuspended in 5 mM MES buffer pH 6.5. A volume of 10 µL and 20 µL of EDC and SNHS at 10 mM was added to the colloidal suspension which was then allowed to react for 15 min in an orbital shaker at 700 rpm at 25°C. The spent carbodiimide from AuNS–MBA–anti-HRP, was removed through centrifugation (10 min at 4°C and 2500 *g*). Following the carboxylic group activation, anti-HRP was added to obtain SERS immunotags with a [AuNSs]:[anti-HRP] molar ratio of 1:422. The subsequent steps were as previously described for the physisorpbed SERS immunotags.

To block non-specific interactions, BSA was added at the same molar ratio used for the anti-HRP. The AuNS–MBA–anti-HRP–BSA conjugates are hereafter referred as "SERS immunotags". These SERS immunotags were then used to incubate with HRP and/or anti-HRP to simulate the sandwich immunoassay. Incubation and washing steps were performed as done to form the SERS immunotags.

In the case of AGE samples, pellets were resuspended only in 13.5 µL of 5 mM phosphate buffer pH 7.4.

The electrostatic surface potential was calculated to render 3D simulated protein surface projections onto which regions of different surface charges were mapped in different colour gradients. This calculation of electrostatic surface potential provides valuable insight on the structural behaviour of these proteins when interacting with the negatively charged NPs. Using 1IGT (anti-HRP) protein data bank file, the electrostatic surface potential was calculated rendering three-dimensional simulated protein surface projections onto which regions of different surface charges were mapped in different colour gradients. The process started by converting the protein data bank file to PQR format - a modified format in which atomic partial charge and electrostatic radius for each atom is added. This was done through PDB2PQR (version 2.1.1) web server (`http://nbcr-222.ucsd.edu/pdb2pqr_2.1.1/`), using the PARSE (parameters for solvation energy) force field and the PROPKA (version 3.1) web server (hosted at the PDB2PQR web site) to predict residue pKa and whole protein isoelectric point (pI) based

on the three-dimensional structure and assign protonation states at any given medium pH. Then, adaptive Poisson-Boltzmann solver plug-in allows to calculate the electrostatic interactions in the provided molecule and colours regions of its three-dimensional simulated surface projection in accordance with the charge distribution (red is more negative; blue is more positive) by Poisson-Boltzmann equation.

3.2.3 Horseradish peroxidase enzymatic assay

In order to determine the viability of the produced anti-HRP-containing bioconjugates for antigen detection, their capacity to bind HRP antigens was tested via an HRP enzymatic assay [24]. Detection of peroxidase enzymatic activity was based in the Sigma-Aldrich protocol [25], Measurements were carried out at 25°C and pH = 5, Abs_{405} nm and a light pathlength = 1 cm. A 0.001 M potassium phosphate buffer (pH = 5.0) was prepared as a reference sample. The activity of the enzyme HRP (Sigma-Aldrich, St. Louis, MO, USA) was determined by monitoring the formation of the reaction product ABTS which is oxidised in the presence of hydrogen peroxide (Panreac AppliChem). Following this oxidation of ABTS, the absorbance at 405 nm was measured by UV-Vis. Enzyme activity was normalised to the free enzyme.

3.2.4 Optical spectroscopies characterisation

All absorption spectra were recorded by a UV-Vis spectrophotometer Cary 50 Bio (Varian®, Agilent, USA) using quartz cells with 1 cm path length (Hellma®), at room temperature.

Dynamic light scattering and ζ-potential measurements were performed in a SZ-100 Nanopartica series (Horiba, Japan). A 4 mW He–Ne laser (532 nm) was used with a fixed 90° scattering angle. All measurements were carried out at 25°C, and the experiments were started only after the sample reached thermal equilibrium (5 min). A volume of 60 µL was transferred to a cuvette for DLS (quartz cells with 3 mm pathlength from Hellma, Germany) with a scattering angle equal to 90° or to a disposable ζ cell (Horiba, Japan) (ζ-Potential). In DLS, each sample was measured three times and each measurement consisted of 10 acquisitions. Cumulant statistics was used to measure hydrodynamic diameter and polydispersity. In ζ-potential, each sample was measured three times and each measurement consisted of 100 acquisitions.

The crystalline phases of the samples were verified using powder X-ray powder diffraction (XRD). X'Pert PRO PANAlytical X-ray diffractometer was used to obtain X-ray diffraction patterns of the gold nanoparticles previously freeze-dried. The 2θ values were taken from 15° to 80° using a Cu-Kα radiation (k = 1.54060 Å) with a step size of 0.033°. Scherrer's equation was used to measure the average crystallite size.

3.2.5 Morphological characterisation

Scanning electron microscopy observations of the AuNSs were carried out in a Carl Zeiss AURIGA Crossbeam (focused ion beam (FIB)-SEM) workstation equipped for energy-dispersive spectroscopy (EDS) measurements. Samples were prepared by placing one drop of the nanoparticle's solution on a silicon wafer and drying at room temperature.

3.2.6 Agarose gel electrophoresis

Agarose gel electrophoresis was employed to determine the variations in charge and size as previously reported for gold nanoparticles of different functionalities and, consequently, used as a tool to demonstrate the formation of the bioconjugates [3, 9, 26–29]. A horizontal agarose gel system was used in all experiments under a constant voltage of 150 V (E = 10 V/cm) in a mini-sub cell GT (Bio-Rad) with agarose from UltraPure™ Agarose, Invitrogen; 0.3% in Tris-acetate-EDTA buffer 0.125×. Samples were incubated overnight in a 4°C refrigerator, and then centrifuged at ≈9500 g at 10°C for 10 min, and the supernatant was discarded. A volume of 13.5 µL of potassium phosphate buffer (pH = 7.4, 5 mM) was used to resuspend the pellet.

3.2.6.1 Adsorption isotherm fitting to AGE data

Digital pictures of the gels were processed by eReuss software, which provided an accurate measurement of the red bands migration in agarose, and, thus, allowed the calculation of their electrophoretic mobility. Electrophoretic mobility (μ_e) is defined as the observed rate of migration of a component (v_e) divided by the electric field strength (E_e) in a given medium. In the case of AGE, which is a solid support medium, only apparent values can be determined [28, 30]. We represent our AGE mobilities as variations relative to the maximum mobility band ($\Delta\mu_e$).

As more antibodies are adsorbed at the functionalised NP surfaces, the electrophoretic mobility for the newly formed conjugate is reduced as its mass increases. Its surface loses some negative charge. This behaviour is reflected in a reduced migration toward the positive electrode. Eventually, the mobility reaches a plateau corresponding to saturation of the NP-conjugate surface with the antibody. Using eReuss, a gel analysis application currently under development (freely available at `https://github.com/lkrippahl/eReuss`), the migration distances for each concentration ratio were computed from the digital image of the electrophoresis gel by fitting Gaussian curves to the image intensity profiles averaged for each lane. This allowed a more reliable quantification of band migration, since the most relevant bands were very broad. This behaviour was previously observed for BSA binding to AuNP, and data was fitted to a Hill-type adsorption isotherm (equation 3.1).

$$\Delta\mu_e = \frac{\Delta\mu_{e,max} \cdot [anti-HRP]^n}{K_D^n + [anti-HRP]^n} \tag{3.1}$$

in which $\Delta\mu_e$ is the variation of electrophoretic mobility between the data point and the AuNSs conjugate before addition of any antibody, and K_D is the dissociation constant (in M) corresponding to the value of the anti-HRP concentration for one-half of $\Delta\mu_{e,max}$. In the Hill model, a cooperativity parameter, n, accounts for positive (n > 1) or negative (n < 1) cooperativity, when the binding of the next antibody is favoured or unfavoured, respectively, by the binding of the previous one. When n = 1, no cooperativity is present, and a Langmuir-type adsorption isotherm can describe the system.

3.2.7 Raman and SERS measurements

Raman measurements were performed in a Renishaw inVia Qontor micro-Raman spectrometer equipped with an air-cooled charge-coupled-device (CCD) detector and an He–Ne laser operating at 32 mW of 632.81 nm laser excitation. The spectral resolution of the spectroscopic system is 0.3 cm^{-1}. The laser beam was focused with a 5× Leica objective lens (N Plan EPI) of numerical aperture (n.a.) 0.12. An integration time of 10 scans of 20 s each was used for all measurements to reduce the random background noise induced by the detector, without significantly increasing the acquisition time. The intensity of the incident laser was 3.2 mW at the sample. Triplicates were taken of all spectra. Between different Raman sessions, the spectrograph was calibrated using the Raman line of an internal Si wafer at 520.7 cm^{-1} for minimise possible variations of the Raman system. A volume of 300 µL of each sample was deposited on a multi-well (n = 96) plate and the laser was focused inside the well. All SERS spectra were recorded at room temperature. All the raw data were collected digitally with Wire 5.0 software for processing. Vibrational line areas were determined with the aid of the Wire 5.0 software for all spectra.

3.2.8 Statistical analysis

For AGE, enzymatic assays, results were presented as mean ± standard-deviation from at least three independent experiments run in triplicates. Normality of the data distribution was assessed firstly by the Kolmogorov-Smirnov [31] and then by Shapiro-Wilk [32] test for increased statistical power. The conjugation efficiency and antigen detection in AGE assays, and antigen detection in covalent and electrostatic methods in enzymatic assays, were statistically compared using two-sample Student t-test, acquiring the $p - value$ accordingly with Welch correction [33]. To perform a statistical group comparison tests, one-way analysis of variance (ANOVA) [34] followed by the Tukey's multiple comparison test were applied [35]. Outliers were identified by Grubbs test [36]. Significance was considered when $p - values \leq 0.05$.

3.3 Results and Discussion

3.3.1 Preparation of gold nanoparticles and bioconjugates

The assembly scheme of the bioconjugates for the SERS immunotag is represented in Figure 3.1. The process consists of three consecutive steps: (1) synthesis of citrate capped gold nanospheres and gold nanostars, for which AuNPs were used as seeds for AuNSs synthesis; (2) functionalisation with a RR (MBA) allowing SERS detection of the bioconjugates [37–39], and (3) bioconjugation with polyclonal anti-rabbit HRP antibodies for detection and BSA for blocking, increasing the specificity of antibody detection [24]. The AuNPs were used as a reference due to their well-known stability and available reproducible modification protocols and to compare their SERS signal intensities with AuNSs.

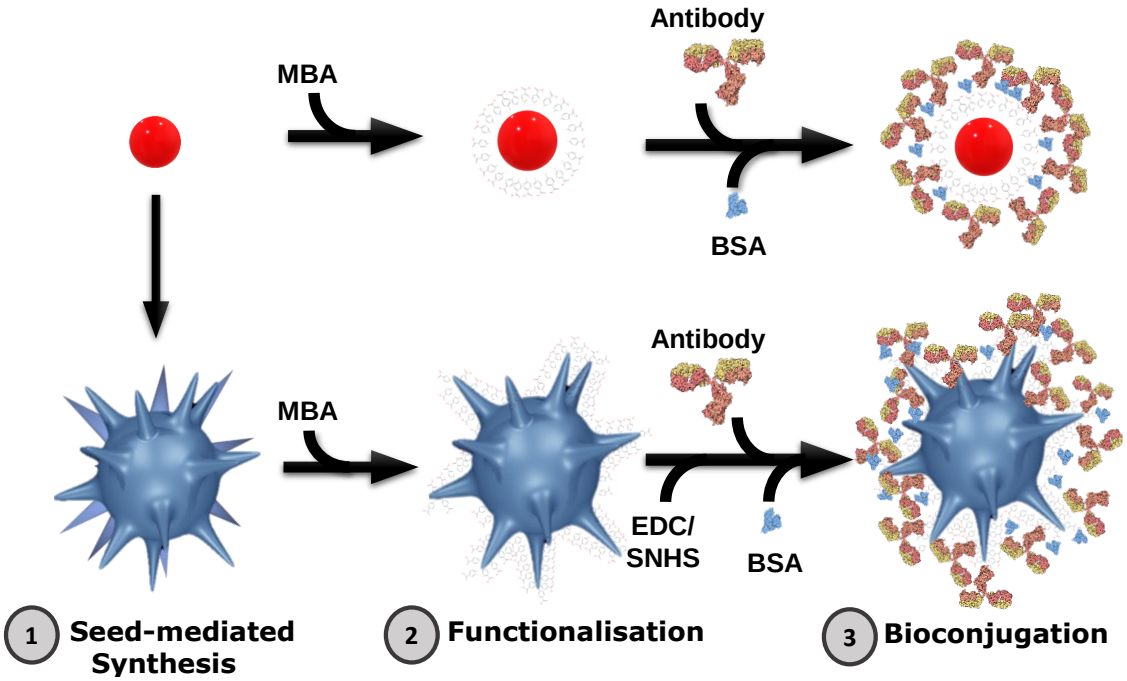

Figure 3.1: Schematic representation of the process to produce SERS-active bioconjugates. Firstly, citrate-capped gold nanospheres are synthesised and used as seeds for the gold nanostars synthesis. Secondly, the nanoparticles are functionalised with a RR. Thirdly, bioconjugation with antibodies and blocking with BSA is by physiosorption or covalent conjugation mediated by EDC/SNHS.

3.3.1.1 Characterisation of the synthesised gold nanoparticles

Gold nanoparticle samples were characterised by UV-Vis spectroscopy and SEM (Figure 3.2). Further UV-Vis, DLS and XRD measurements allowed the determination of diameters and colloidal concentrations (Table 3.1). The UV-Vis spectrum after the synthesis of AuNPs shows a LSPR band centred at ≈519 nm. The low absorbance values at 600–700 nm indicate negligible colloid aggregation [40] (Figure 3.2a). The LSPR band

was used to determine the average size and molar concentration of spheres (12.0 ± 0.2 nm and ≈ 14 nM) [22].

XRD analysis allowed confirmation of the crystalline nature of AuNPs and AuNSs (Figure 3.2b). The diffraction pattern revealed peaks at 38.17°, 44.51°, 64.65° and 77.69° and finally, 81.87°. The first four correspond to (111), (200), (220) and (311) Bragg reflection planes of crystalline metallic gold, respectively. This profile is in good agreement with reference to the unit cell of face centre cubic lattice of metallic gold (International Centre for Diffraction Data, File No. 00-004-0784[41]) with a lattice parameter of a = 4.0640 Å and with a space group of Fm-3m. The broadening of the Bragg peaks indicates the formation of nanoparticles [42, 43]. The crystalline structure of both gold nanoparticles, spheres and stars, is cubic since the (111) is the dominant plane orientation as previously reported [42, 43]. The mean size of AuNPs was calculated using the Debye–Scherrer's equation, yielding a value of 13 nm (Table 3.1), which is in agreement with DLS measurements and with the UV-Vis spectral analysis. However, an appropriate modelling is still needed for anisotropic nanoparticles.

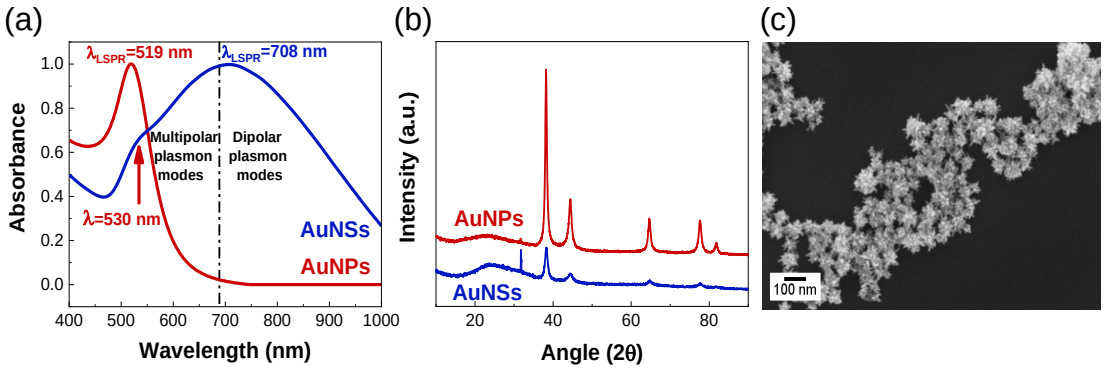

Figure 3.2: Characterisation of AuNPs and AuNSs: (a) UV-Vis spectra of AuNPs (red line) and AuNSs (blue line). The Ojea-Jiminéz [19] synthesis method allowed a diameter of 12 nm (λ_{LSPR} = 519 nm) for AuNPs. The AuNSs present a LSPR band centred approximately at 708 nm and a large broadening. (b) XRD pattern of as-prepared sphere and star gold nanoparticles. (c) SEM micrograph of AuNSs after synthesis.

Table 3.1: Summary of the obtained diameters and concentration for AuNPs and AuNSs synthesised.

NP type	λ_{LSPR} (nm)	Diameter (nm)			[NP] (nM)[1]
		UV-Vis	DLS	XRD	
AuNP	519	12.0 ± 0.2	13.0 ± 0.3	13	13.8 ± 0.2
AuNS	708	-	67.9 ± 0.4	-	0.60 ± 0.01

[1] by UV-Vis spectroscopy.

The morphology of the synthesised nanostars is characterised by a central core with multiple spikes as confirmed by SEM (Figure 3.2c) [44]. The average tip-to-tip length

observed was ≈ 70 nm. AuNS suspensions are typically polydisperse, with small differences in shape, length, orientation of spikes and sharpness of their tips, as the SEM micrograph shows (Figure 3.2c). Consequently, the optical response from AuNSs is complex, originating as it does from both the cores and the spikes. The high anisotropy gives rise to plasmonic modes of different orders, producing hybridisation of resonances at distinct wavelengths in the visible and near-IR [45, 46]. The resonances observed around 720 and 800 nm can be assigned to dipolar plasmon modes and ≈ 675 nm to multipolar plasmon modes (Figure 3.2a) [44]. The small broad resonance at ≈ 530 nm is associated with transverse resonances within the branches or to plasmonic resonances of spherical protuberances [23, 47]. These spherical protuberances might be non-fully grown or reconstructed spikes, and it is also possible that the spherical core contributes to the overall spectrum [23, 47]. Thus, even within the same batch, the AuNSs have quite heterogeneous morphologies, especially compared with AuNPs, which is consistent with the broad peaks of the UV-Vis spectrum shown in Figure 3.2a (blue line). However, the reproducibility among batches of AuNSs measured on the same day of the synthesis was good (relative standard-deviation (RSD) of 0.87%) (Figure 3.3).

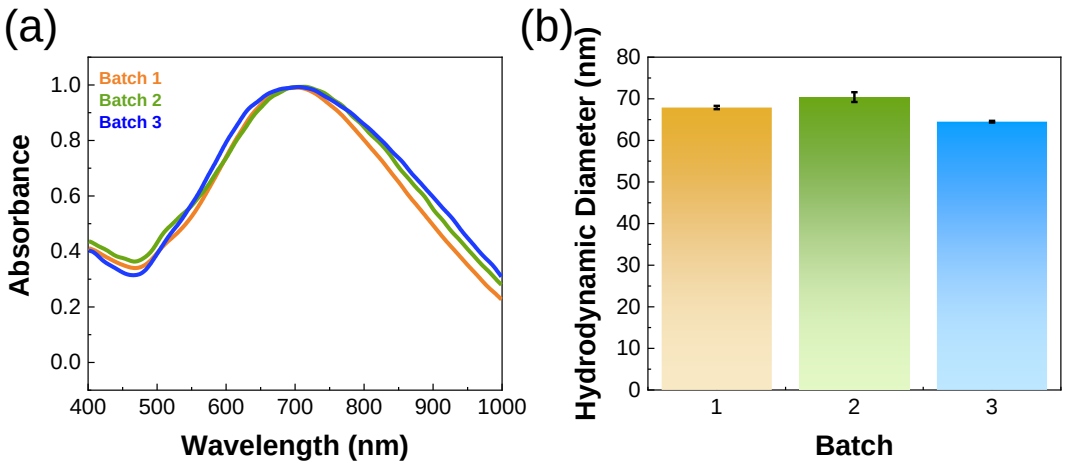

Figure 3.3: Reproducibility between AuNSs batches. (a) UV-Vis-near-IR spectra and (b) hydrodynamic diameter of three independent AuNSs syntheses.

3.3.1.2 Functionalisation with the Raman reporter

The gold nanostars synthesised in this work are electrostatically stabilised in a colloid by adsorbed citrate anions [47]. Thiolated bifunctional linkers such as MBA, bind to the AuNSs surface by chemisorption through a terminal thiol group, presenting at the other end a carboxylic group that is deprotonated, thus negatively charged, at the pH of the conjugation reaction. Moreover, MBA is commonly used as RR in SERS-based immunoassays [39, 48]. The Raman spectrum of MBA and the respective line assignments are presented in Figure 3.4 and Table 3.2.

To determine the amount of MBA needed to form a monolayer around the NPs, AuNPs

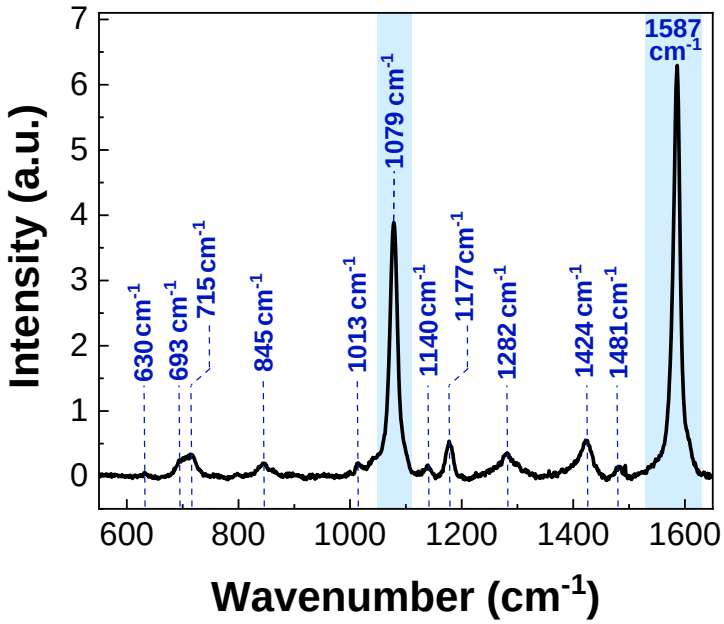

Figure 3.4: Raman spectrum of MBA (2 M) in ethanolic solution.

Table 3.2: Vibrational lines assignments for MBA [49].

Observed bands (cm^{-1})	Strength[1]	Assignment
630	vw	CCC bending
693	w	CC Stretching
715	w	Ring breathing
845	vw	COO- bending
1013	vw	Ring breathing
1079	s	CC and CS stretching, aromatic ring breathing
1140	vw	CH bending
1177	m	CS binding, CC stretching
1481	w	Aromatic ring bending
1587	s	CC stretching, CH in plane bending
1623	vw	C=O stretching

[1] Abbreviations: vw: very weak; w: weak; m: medium; s: strong.

and AuNSs were functionalised with different MBA molar ratios (Figure 3.5). The functionalisation process was characterised by UV-Vis spectroscopy as a 48 nm red-shift of the LSPR (Figure 3.5d), a consequence of an increase in the local refractive index at the nanoparticle surface [50]. The red-shift upon MBA functionalisation for spherical AuNP is only 3 nm (Figure 3.5a). In fact, anisotropic NPs show a large change in the refractive index due to the presence of hotspots (especially at tips or edges) responsible for enhanced electromagnetic fields [50–52].

Confirmation of AuNPs and AuNSs functionalisation with the RR was achieved by running SERS spectra of functionalised AuNPs and AuNSs for the different MBA to NPs molar ratios (Figure 3.5b and e). After extensive washing to remove non-bound MBA, SERS spectra of MBA-functionalised both types of NPs had two very intense vibrational lines at 1079 cm^{-1} and 1587 cm^{-1}, the most intense lines also appearing in the Raman spectrum of MBA solution (Figure 3.5) [53]. The SERS spectrum of the control citrate-capped AuNPs and AuNSs, showed broad bands in the region of 1350-1450 cm^{-1}, related to carboxylic group bending and stretching vibrations derived from the citrate molecules (Figure 3.5b and e) [54].

The electrophoretic mobility of NPs is affected by their mass, shape and superficial charge [55]. Hence, this parameter can be used to verify the correct amount of the negatively charged MBA functionalisation agent necessary to fully cover the NPs. AGE is a particularly useful technique to study NPs and their bioconjugates as it uses simple equipment, and bands can be easily located without any dyeing step, due to the intense colours for both types of NPs (red in the case of AuNPs, blue in the case of AuNSs). In Figure 3.5c and f, an AGE image for AuNPs and AuNS functionalised with increasing molar ratios of MBA is shown. Two types of bands are observed in the AGE: (i) corresponding to aggregated NPs present in the gel wells, that did not migrate in the gel; and (ii) NPs presenting an electrophoretic mobility corresponding to a full MBA layer covering the AuNPs or AuNSs (Figure 3.5c and f). The lack of migration observed for non-functionalised NPs is probably caused by the loss of the weakly bound citrate ions or the presence of specific interactions between the gel and the NPs [27].

To ensure that all the AuNPs and AuNSs were functionalised with a full MBA layer, a NP:MBA molar ratio of 1:500 and 1:50 000 was chosen for AuNPs and AuNSs, respectively, since only in this case did all functionalised NPs migrate in the AGE, without any aggregation in the wells.

Interestingly, AGE was also able to distinguish the concentrations needed for functionalisation according to the capping agent used (see Figure 3.6). For instance, when 11-mercaptoundecanoic acid (MUA) was used as capping agent, the molar ratio for covering NP surface is lower (1:10 000) than the required with MBA (1:50 000) (Figure 3.6). This difference might be related to the capping agent molecular structure. MUA has an aliphatic chain and thus is a larger molecule than MBA with one aromatic ring [56, 57]. As observed by Hinterwirth *et al.* the ligand density decreases with increasing ligand chain length due to sterical hindrance explaining the lower molar ratio needed for MUA [58].

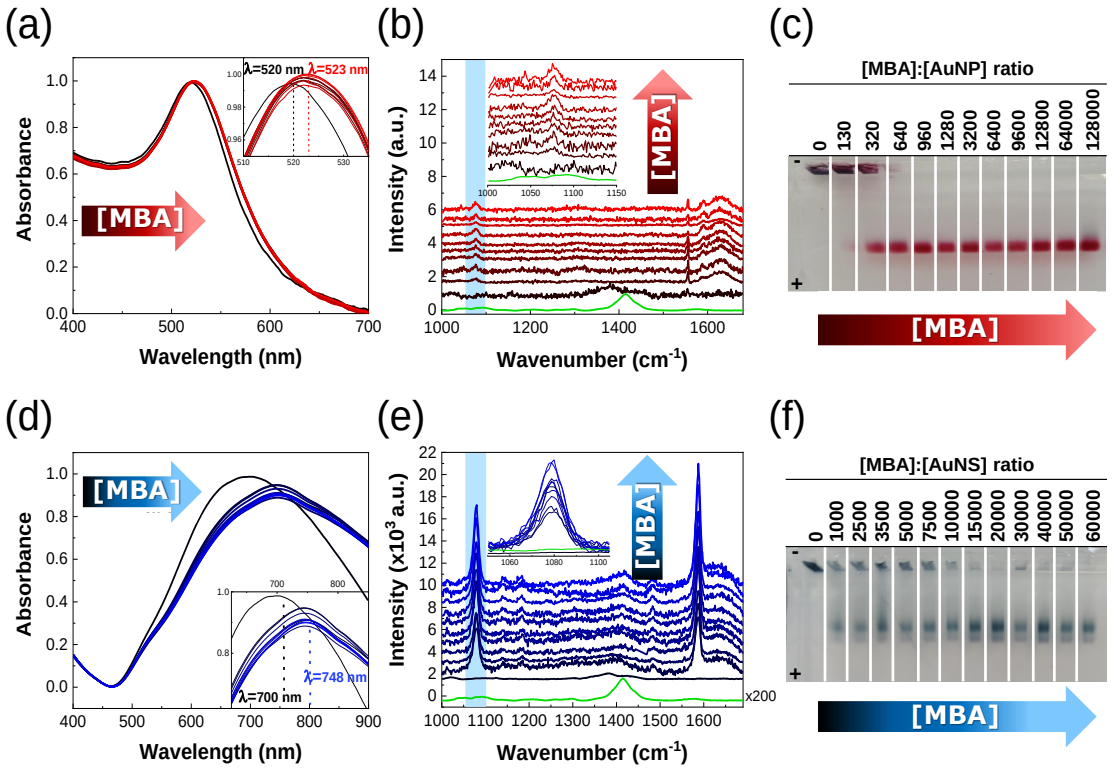

Figure 3.5: Analysis of MBA-functionalised (a, b, c) AuNPs and (d, e, f) AuNSs by UV-Vis spectroscopy, SERS and AGE. (a, d) Normalised UV-Vis spectra of AuNPs and AuNSs functionalised with increasing MBA molar ratios. Comparing the LSPR bands of AuNSs capped with citrate from the synthesis (black line), with AuNSs functionalised with increasing molar ratios of MBA (blue lines) a bathochromic shift of 48 nm is observed while for the functionalised AuNPs the bathochromic shift observed is only of 3 nm. (b, e) SERS spectra of functionalised AuNPs and AuNSs, presented increasingly more intense lines at 1079 cm^{-1} (inset) and 1587 cm^{-1}, thus confirmed the changing of capping agent by disappearing citrate lines and appearing MBA lines, as the molar ratio of MBA increases. Citrate SERS spectrum is presented in green, for comparison. (c, f) Photograph of an agarose gel with AuNPs and AuNSs samples functionalised with increasing molar ratios of MBA.

Thus, AGE reflects the importance of testing the amount to form a monolayer around the NP's surface for the different capping agents.

These results highlight the importance of confirming the formation of a RR monolayer at the NPs surface using complementary techniques and how important it is to consider the physicochemical properties of the NP and the RR for successful and reproducible design of bioconjugates.

3.3.1.3 Time stability of non-functionalised and functionalised AuNSs

Immediately after synthesis, the colloidal solution of AuNSs exhibited an UV-Vis spectrum with LSPR band maximum centred at 677 nm. After seven days, the LSPR band of the same solution was observed to have blue-shifted to 672 nm (Figure 3.7). Therefore, the changes in absorption wavelength maximum (λ_{LSPR}) of two AuNSs batches,

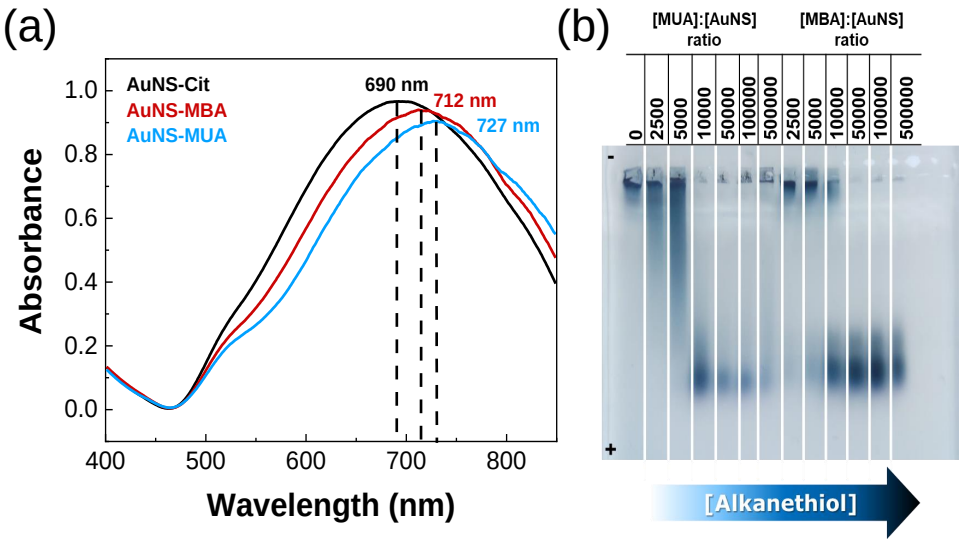

Figure 3.6: AuNSs surface analysis by UV-Vis spectroscopy and AGE. (a) Normalised UV-Vis spectra of AuNSs functionalised with MUA and MBA (molar ratio corresponds to the full coverage of AuNSs, namely, 10 000 and 50 000 to MUA and MBA respectively). Comparing the LSPR bands of AuNSs capped with citrate from the synthesis (black lines), with AuNSs functionalised with increasing MUA (blue line) and MBA (red line) a bathochromic shift of 22 nm and 37 nm is observed, respectively. (c) AGE of AuNSs functionalised with increasing molar ratios of MUA and MBA.

non-functionalised and MBA functionalised, were analysed to evaluate the stability for subsequent conjugation studies. As seen in Figure 3.7, for the non-functionalised AuNSs, λ_{LSPR} decreases with time and the blue-shift rate varies between batches (also observed by Vega, *et al.* [59]), 20 nm over seven days in one batch (marked as B1 in Figure 3.7) and 80 nm in the other (B2). This change can also be observed by the change of colour in solution from dark blue to purple indicating morphological alterations in the nanostars. This behaviour can be attributed to the loss of AuNSs tips, as reported by Jiang and co-workers [60] and Vega *et al.* [59]. In the work by Vega *et al.*, the measurement of the radius at the curvature of the nanostar tips revealed an increase for the non-functionalised nanostars and no significant change for the 3-mercaptopropionic acid-capped nanostars [59]. Is possible that the Au-S bond from the capping agent and the nanostar limits the diffusion of Au atoms from tips toward the core, whereas in the non-functionalised AuNSs, the gold atoms move, driven by the chemical potential difference associated to the respective curvatures [59, 61].

The changes in SEM of an AuNSs batch, non-functionalised and MBA functionalised, were analysed to evaluate the stability for subsequent conjugation studies (see Figure 3.8). However, the images do not confirm the change observed in LSPR band due to the lack of SEM image resolution for such nanometric size particles. Thus, it is plausible that the AuNSs lost part of the tips but nevertheless remain highly anisotropic, which is also in agreement with the UV-Vis spectral analysis. For a more detailed analysis, high resolution transmitance electron microscopy (TEM) would be more suitable. Nevertheless,

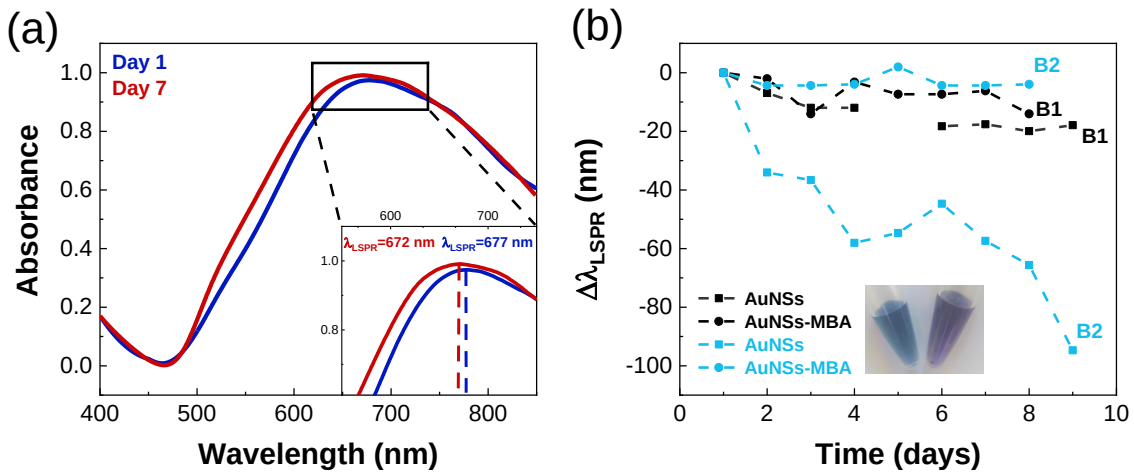

Figure 3.7: Time stability of AuNSs. (a) UV-Vis spectrum after a synthesis of AuNSs (day 1) and after seven days where a blue-shift is perceived indicating the loss of some sharp edges. (b) Shift of the wavelength at maximum absorption for two batches (B1 and B2), both were non-functionalised and MBA functionalised. The samples were stored at 4°C and sonicated before each measurement.

the functionalised AuNSs proved to be appropriate for the next step of SERS immunotag production.

3.3.1.4 Bioconjugation via physisorption

RR functionalised AuNP and AuNS, were conjugated with anti-HRP. This polyclonal antibody was used to evaluate the parameters needed to performed conjugation and as a model system for the proposed SERS-based immunoassays. Each tested molar ratio was performed in similar conditions maintaining the buffer and AuNP/AuNS–MBA volume.

The electrostatic surface potentials were mapped onto computer generated representations of each protein at pH 6 – 8 to understand how pH alters the electronegativity at the surface of this protein and how the adsorption to the negatively charged AuNS is affected. In order to promote conjugation based mainly on the establishment of physisorption and considering that IgG pI ranges from 6 to 9, using phosphate buffer at pH 7.2 is appropriate to guarantee that the antibody surface has groups positively charged in the Fc fragment (see Figure 3.9). These positive charges at the antibody surface promote adsorption to the negatively charged nanoparticle surface provided by the carboxylic groups of MBA [62].

AGE was used to assess AuNP–MBA–anti-HRP and AuNS–MBA–anti-HRP bioconjugates for various molar ratios of antibody (Figure 3.10). The first well corresponds to NPs functionalised with MBA which, having negative charge, migrate towards the positive pole. Upon anti-HRP binding, the hydrodynamic size increases, and the global net charge can be partially cancelled. Consequently, the bioconjugates migrate less towards the positive pole. As the molar ratio at which anti-HRP is incubated with functionalised NPs increases, a higher number of antibodies is expected to adsorb to the surface, leading

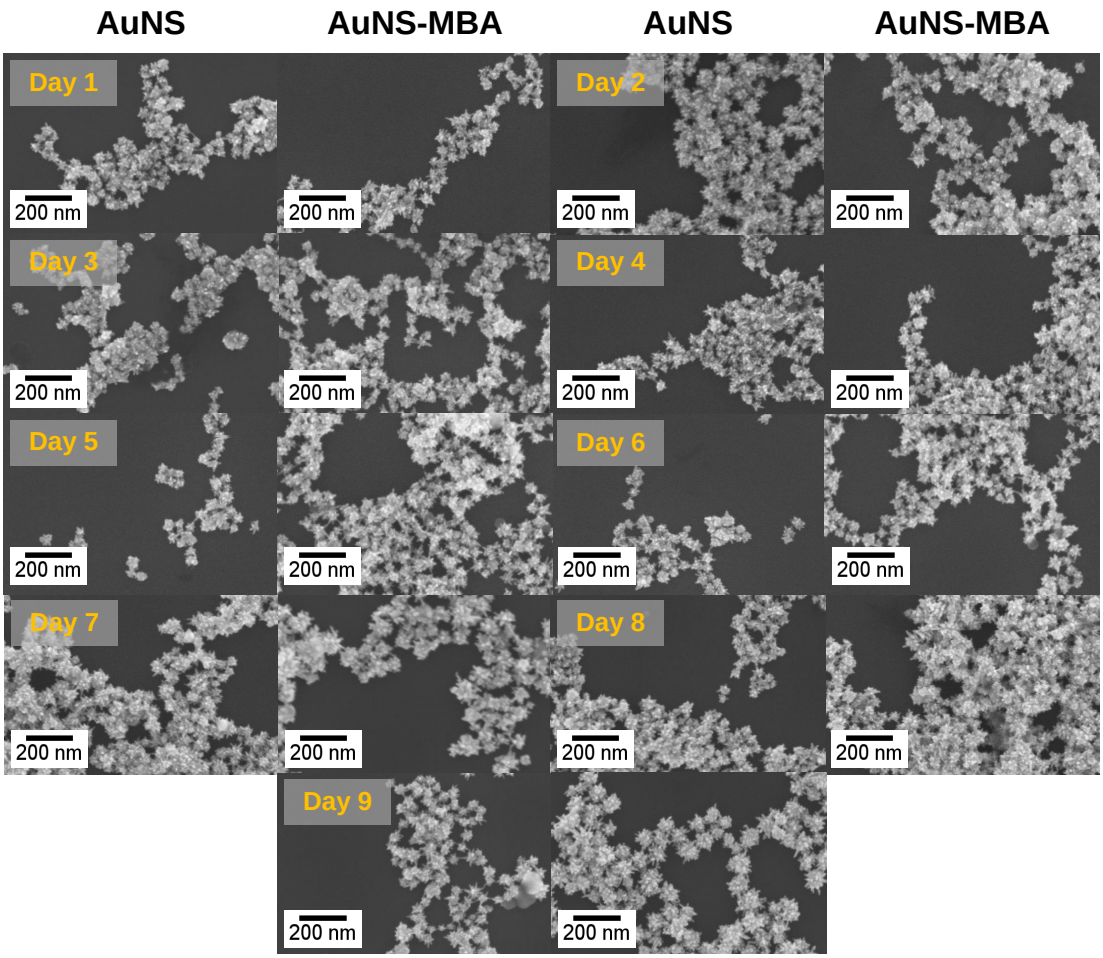

Figure 3.8: SEM micrographs of AuNSs surfactant free and functionalised with MBA throughout nine days.

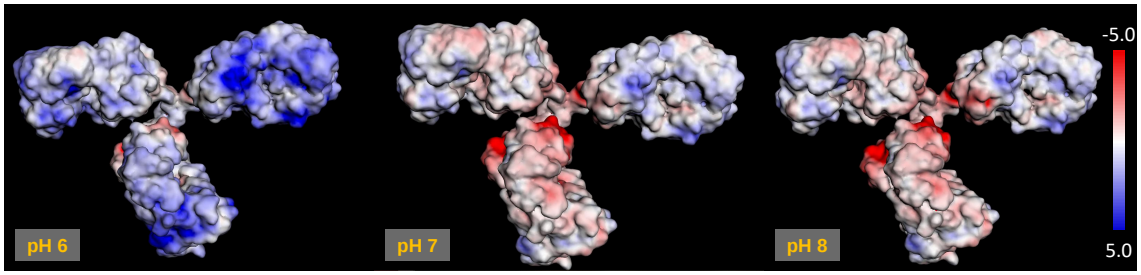

Figure 3.9: Electrostatic potential mapped onto a surface projection of anti-HRP (protein data bank file: 1IGT) at pH 6, 7 and 8 in a colour gradient (red is negative, white neutral and blue positive) ranging from -5.0 to 5.0 $k_BT \cdot ec^{-1}$.

to a decrease of the electrophoretic mobility. The anti-HRP solution concentration corresponding to the stabilisation of the electrophoretic mobility (*plateau*) is assumed to be the concentration necessary to form a full corona at the NPs surface. The intermediate ratios possibly present smeared bands due to the variability in conjugations stages. Since the anti-HRP to NP conjugation process is a dynamic adsorption equilibrium, the concentration of antibody at intermediate ratios is not sufficient to fully cover the NPs, giving rise to multiple equilibria. Moreover, the antibody molecule orientation upon adsorption might vary more at these intermediate ratios, this effect being more evident when the protein has more positive charged groups [63]. These wider bands can be more or less evident, due to some variation during experiment such as small variations in AuNPs and AuNSs concentration (loss during resuspension), different concentration of agarose gels affected by different humidity and air exposures, higher concentrations of agarose, decreasing the pore size and leading to a stronger resistance to the NPs movement [64]. When the antibody concentration increases, bands become narrower, as a result of antibody saturation of the NP surface. It is important to stress that the conjugation ratio does not correspond to the total antibody at the NPs surface, but rather to the amount of antibody present in the incubation sample.

Electrophoretic mobilities for several different AGE were calculated with the eReuss software and fitted to an adsorption isotherm of the Hill type (see section 3.2.6.1) (Figure 3.10c). The fitting for AuNP-MBA showed a dissociation constant, $K_D = (8 \pm 4) \times 10^{11}$ M^{-1} of anti-HRP, and $n = 0.6 \pm 0.1$, the latter indicating that anti-HRP antibodies bind to AuNP–MBA in a negative cooperative manner, possibly due to steric hindrance. The dissociation constant obtained for AuNSs conjugated anti-HRP is similar to the one that was reported for 15 nm citrate-capped AuNP with BSA [11]. According to the conjugation fitting curve, the concentration of anti-HRP at 120 nM, for a constant AuNP-MBA concentration of 2 nM, guarantees a full antibody corona at the AuNP surface.

Regarding the AuNS-MBA, the fitting resulted in a dissociation constant, $K_D = (3.8 \pm 7) \times 10^{-8}$ M^{-1} of anti-HRP, and $n = 1.0 \pm 0.1$, the latter indicating that anti-HRP antibodies bind to AuNS–MBA in a non-cooperative manner, basically following a Langmuir adsorption model (see section 3.2.6.1). Interestingly, the value obtained for the dissociation constant is of the same order of magnitude as the one found for the binding of another IgG antibody to 30 nm citrate-capped spherical AuNPs [9]; and about two orders of magnitude lower than the dissociation constant for the binding of BSA to 15 nm citrate-capped AuNP, a reference system for strong protein-AuNP binding [11]. Although these values cannot be directly compared, as they refer to protein binding to gold NPs with different morphologies and concentrations, the low value obtained for the anti-HRP to AuNS–MBA dissociation constant implies the formation of rather stable bioconjugates. Analysing the conjugation fitting curve, and in order to guarantee a full antibody corona at the AuNS surface, further assembly of anti-HRP containing conjugates was performed with the concentration of anti-HRP at 211 nM, for a constant AuNS–MBA concentration of 0.2 nM.

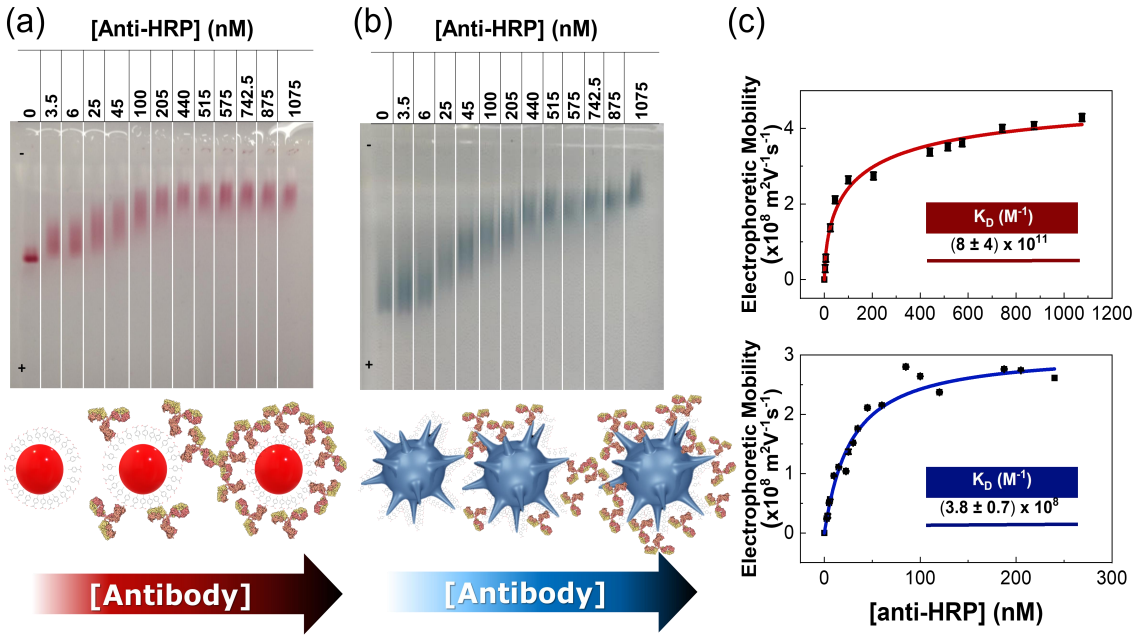

Figure 3.10: AGE of AuNP-MBA and AuNS-MBA with increasing molar ratios of anti-HRP. (a) Exemplary 0.3% (w/v) agarose gel for concentrations of anti-HRP from 3.5 to 1075 nM corresponding to [anti-HRP] to [AuNP-MBA] ratios from 7 to 2150. (b) Exemplary 0.3% (w/v) agarose gel for concentrations of anti-HRP from 3.5 to 1075 nM corresponding to [anti-HRP] to [AuNS-MBA] ratios from 7 to 2150. (c) Top: Variation of electrophoretic mobility ($\Delta\mu_e$) versus anti-HRP concentration of the various AuNP–MBA-anti-HRP conjugates. Bottom: Variation of electrophoretic mobility ($\Delta\mu_e$) versus anti-HRP concentration of the various AuNS-MBA-anti-HRP conjugates. Data was fitted to an adsorption isotherm of the Hill type with parameters AuNPs: $\Delta\mu_{e,max} = (5.7 \pm 0.7) \times 10^{-8}$ m^2· V^{-1}·s^{-1}); $K_D = (8 \pm 4) \times 10^{11}$ M^{-1}; $n = 0.6 \pm 0.1$; and adjusted r^2 = 99% AuNSs: $\Delta\mu_{e,max} = (3.1 \pm 0.2) \times 10^{-8}$ m^2· V^{-1}·s^{-1}); $K_D = (3.8 \pm 0.7) \times 10^8$ M^{-1}; $n = 1.0 \pm 0.1$; and adjusted r^2 = 98%. Electrophoretic mobility is normalised for the maximum mobility, corresponding to the sample without antibody. Data presented in the graph derive from three different AGE, each using a different set of anti-HRP concentration values.

Knowing the concentrations of anti-HRP to add to the AuNP-MBA and AuNS-MBA for a full antibody corona, SERS spectra were taken of both bioconjugates at the same concentration (Figure 3.11). Comparing the SERS activity of the AuNS-based SERS bioconjugates with the more traditional spherical-based SERS bioconjugates, it is possible to observe a smaller SERS intensity from the SERS bioconjugates with AuNPs. The presence of several hotspots from the star-shape NPs give rise to a higher SERS signal than the more isotropic NPs, and thus they were chosen for the subsequent steps of the SERS-based immunoassay [65].

3.3.1.5 Bioconjugation *via* EDC/SNHS cross-linking

Bioconjugation with the antibody, in this case anti-HRP, is a critical step to obtain highly efficient SERS immunotags. Depending on the method used, the antibody molecules can bind to the surface of the NPs in a random or oriented conformation, and this interferes with the ability to recognise and specifically bind the antigen. In order

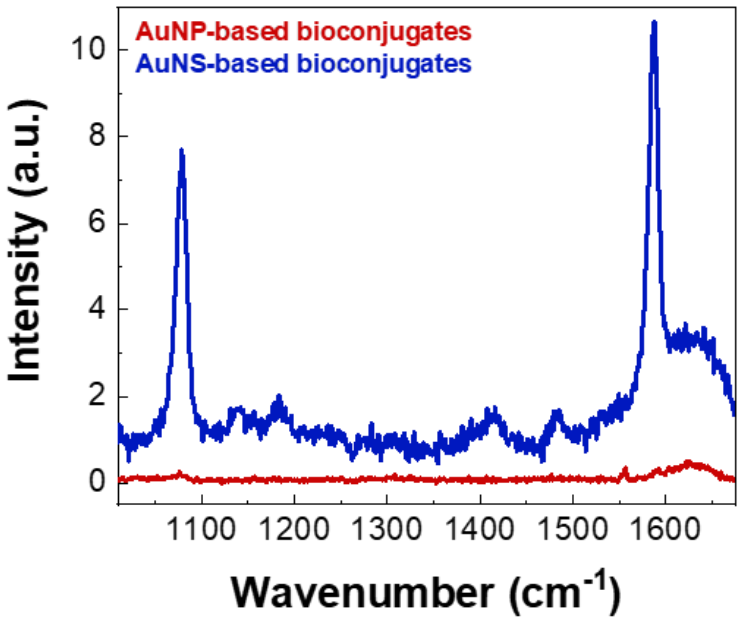

Figure 3.11: SERS spectra comparison between bioconjugates fabricated with spheres (red) and star-shaped (blue) NPs.

to obtain a highly efficient binding to HRP, the covalent bioconjugation between SERS-probe-AuNSs and anti-HRP was performed using the EDC/SNHS method [66].

EDC, a widely known zero-length cross-linker, together with SNHS, can promote the binding between MBA-coated NPs and antibodies [66–68]. Altough EDC is ubiquitously used in water-soluble colloids, there is a dearth of studies on the optimisation of methods for binding biomolecules to particles. Depending on the author, different concentrations, molar ratios, pH of EDC/SNHS coupling reaction are applied even for similar protein-NP systems [66, 68, 69]. Moreover, the binding efficiency and consequent stability of these biomolecules-NPs is low, as they are sensitive to pH variations [68].

As for anti-HRP binding to AuNS-MBA by physisorption interactions, covalent conjugation also leads to a lower migration of SERS immunotags toward the positive pole. As shown in Figure 3.12, the electrophoretic mobility of SERS immunotags was lower for covalent conjugation (red triangles) than for the physisorption-based conjugation (blue circles), in all conditions tested. In physisorption conjugation, the decrease in electrophoretic mobility is related to a higher number of antibodies adsorbed to the AuNSs surface, thus increasing the hydrodynamic size and partially cancelling the global net charge [70]. Herein, the amount of anti-HRP used corresponded to the full antibody corona around the AuNSs by physisorption adsorption. Thus, differences in electrophoretic mobility between the physisorption and the covalent SERS immunotags are determined by the coupling efficiency; as more antibody bound to the AuNSs translates into a decrease of electrophoretic mobility [66]. Hence, it is plausible to assume that the cross-linking reaction allowed a higher amount of the anti-HRP molecules to be attached to the AuNS-MBA. This is possible even in full antibody corona conditions,

due to rearrangements during the incubation with AuNS-MBA activated by EDC/SNHS that maximise the bioconjugation [24]. All electrophoretic mobilities were subjected to one-way ANOVA with Tukey's multiple comparison test for the means. Only when the means between physisorption and covalent bioconjugations were significantly different, the covalent bioconjugation was considered successful.

Several different experimental parameters were optimised, namely:

pH - MES buffer is a non-coordinating buffer and was chosen as it is known as one of the most effective for coupling reaction [15, 24, 67]. In Figure 3.12a, from all the tested pH, the antibody was mostly coupled to AuNSs at pH 6.5. At pH 7, the coupling reaction is less effective since the pH of the reaction is more alkaline than that recommended for EDC activation reaction [71]. As a result, the amount of antibody conjugated with AuNSs is lower (as seen by the higher value of electrophoretic mobility in Figure 3.12a). However, at pH 6, the diminished colour of the migration band observed reflects the aggregation of AuNSs during the coupling reaction. As Figure 3.9 shows, using a pH more acidic, is possible to promote the correct orientation of the antibody (from the Fc fragment) due to the different rates of ionic adsorption and covalent reaction [24]. Using a pH 6.5, lower than the pI value, induces fast ionic adsorption of the antibody molecules to the negative charges of the carboxylic groups of the NPs. Then, the incubation for a longer period of time (90 min) allows to covalently attach the antibodies preserving its biological activity. This approach allows to increase antigen binding capacity than antibodies immobilised in a random manner.

Time - The effect of incubation time on the coupling efficiency was evaluated for 1, 7.5, 15 and 30 min. The amount of antibody bound to the AuNSs increased for longer incubation time, as demonstrated by the lower electrophoretic mobility (Figure 3.12b). Since the reactions for 30 and 15 min showed similar efficiencies, the 15 min was chosen for further assays as it ensures a quicker, yet efficient, process.

[EDC]/[SNHS] - The molar ratio of SNHS to EDC is a parameter mentioned in several works, although very few report a systematic investigation to maximise the coupling efficiency [66, 68, 69]. The molar ratios of EDC and SNHS used were varied from 1:0 to 1:10. As verified in Figure 3.12c, for the molar ratios 1:0 and 1:0.5, the coupling reaction resulted in lower coupling efficiency, thus highlighting the importance of using SNHS to stabilise the active intermediate with carboxylates. Increasing the molar ratio led to the same range of electrophoretic mobilities. There was a small decrease in conjugation yield with an excess amount of SNHS, since the migration bands showed a higher aggregation level (1:6 and 1:10 molar ratios). Excess of SNHS might lead to the competition with the protein by the carboxyl groups activated with EDC [68]. The ratio of EDC:SNHS chosen was 1:2, since it showed a higher significantly difference with no signs of aggregation.

The final crucial parameter evaluated was the concentration of EDC/SNHS necessary for the coupling reaction (Figure 3.12d). A series of EDC/SNHS concentrations ranging from 0.005 to 100 mM were tested, while the ratio was fixed at 1:2. It is evident from the lower electrophoretic mobility that the most effective coupling conditions are observed

for the EDC final concentrations of 10 and 50 mM. Lower amounts of EDC and SNHS resulted in a higher variance ($p - value > 0.05$), which might be due to several populations of bioconjugates with distinct loads of antibody that result in different hydrodynamic sizes and electric charges. Also, lower coupling efficiency was observed at higher concentrations of EDC and SNHS, possibly due to a competitive process between the highly concentrated antibody, thus reducing the available quantity to react to the nanoparticle surface [66].

Optimised bioconjugation parameters for covalent conjugation, as evaluated by AGE, were MES buffer at pH 6.5, for a duration of 15 min and with a molar ratio of EDC:SNHS of 1:2 at an EDC concentration of 10 mM.

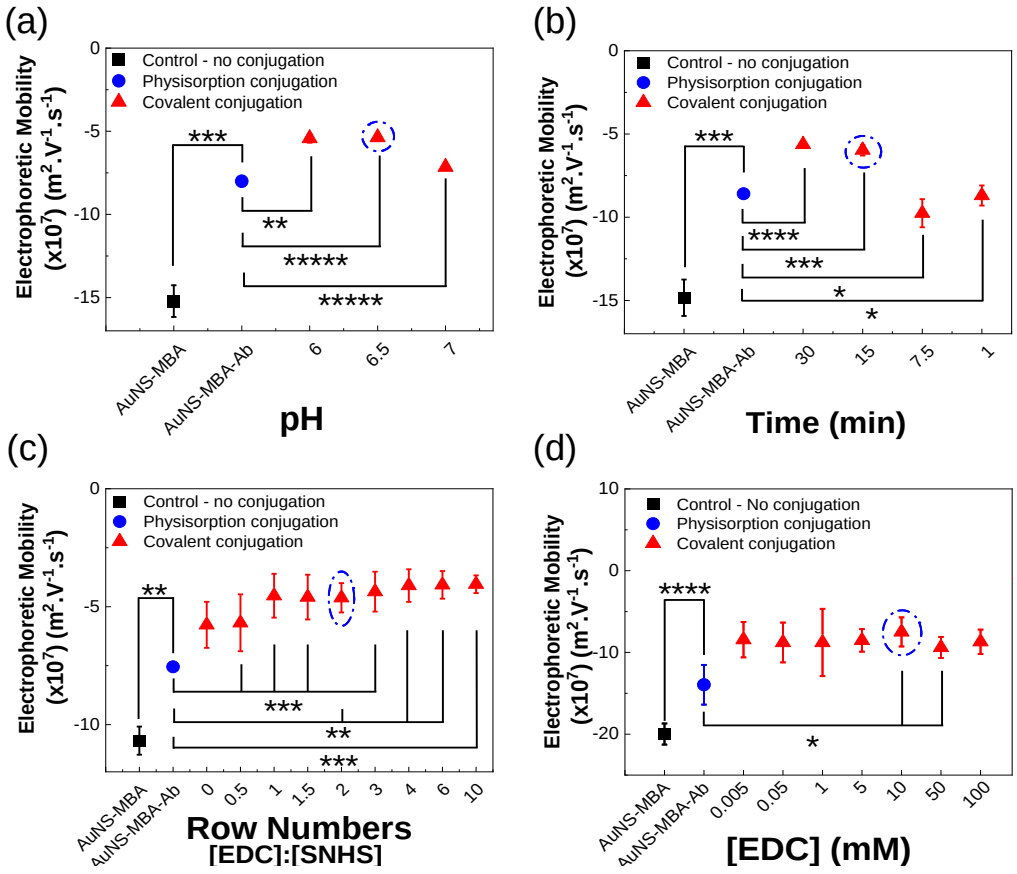

Figure 3.12: Covalent bioconjugation efficiency evaluation. Optimisation of covalent bioconjugation was achieved by varying several parameters including (a) pH, (b) duration of the coupling reaction, (c) molar ratio between EDC:SNHS, and (d) concentration of both cross-linking reagents. "Ab"refers to antibody. Error bars correspond to standard deviation from three independent experiments (different sets of bioconjugates). One-way ANOVA followed by the Tukey's multiple comparison test were applied for statistical comparisons. * $p \leq 0.05$, ** $p \leq 0.01$, *** $p \leq 0.005$, **** $p \leq 0.001$, ***** $p \leq 0.0001$ covalent versus physisorption conjugation, and between AuNS-MBA and physisorption conjugation.

3.3.2 Characterisation of the SERS immunotag

The SERS immunotag formation process was completed with a BSA blocking step to promote a specific HRP antigen binding to the anti-HRP antibodies [63]. A concentration of BSA of 211 nM (same as anti-HRP antibody) was added, affording blocked bioconjugates with lowered electrophoretic mobility after washing excess BSA by centrifugation. Increase of the amount of BSA added to the anti-HRP loaded AuNS–MBA conjugates did not change their electrophoretic mobility further, so the concentration of BSA added in further experiments was always equal to the anti-HRP concentration.

To test the functionality of the SERS immunotags, colloidal suspensions were incubated with the respective antigen for the chosen antibody (HRP), followed by free anti-HRP antibody, simulating a positive assay result. Each stage of the bioconjugation formation and immunoassay simulation was monitored by UV-Vis spectroscopy, DLS and ζ-Potential. The adsorption of macromolecules on the AuNS-MBA surface caused a red-shift of the plasmon resonance band (Figure 3.13). As mentioned before, the LSPR wavelengths shifts are a consequence of the changes in the refractive index of medium surrounding the nanostructures [72]. The slight broadening of the LSPR band can be a result of AuNSs aggregation or the higher degree of heterogeneity of AuNSs with different loads of proteins.

DLS and ζ-potential measurements of the SERS immunotags were also obtained to further characterise SERS immunotags formation (Table 3.3 and Figure 3.14). A consistent increase of the average hydrodynamic diameter and in the values of ζ-potential can be correlated to the amount of protein bound at the nanoparticle surface on each step of the conjugation [73, 74].

The average hydrodynamic diameter observed for AuNS-MBA alone was 67.9 ± 0.4 nm (Figure 3.14 and Table 3.3). Then, for both conjugation processes, the subsequent additions of antibody, antigen and antibody again, resulted in shifts of the average hydrodynamic diameter to higher values. In the covalent conjugation, the size increases from 67.9 ± 0.4 nm to 149.1 ± 1.7 nm when the SERS immunotag is formed. Compared to the physisorption bioconjugation approach, the hydrodynamic diameter of SERS immunotag is ≈ 67 nm higher when the EDC/SNHS is used to promote the covalent bond. It is possible that the cross-linking event allows attachment of more antibodies to the AuNSs surface or even promotes alternative binding, such as nanoparticle-antibody-antibody. This might also explain the small shift observed when HRP is added to the physisorption bioconjugates and the lack of shift in the covalent bioconjugates. The dimensions of HRP are small, compared to SERS immunotags ($3.0 \times 6.5 \times 7.5$ nm) [75], so there is no appreciable hydrodynamic size increase when the SERS immunotags are incubated with HRP to form SERS immunotags-HRP. This limitation of the method highlights the need of care when using DLS data [73]. The polydispersion index values after each step of conjugation confirmed the results observed in UV-Vis spectroscopy.

Furthermore, similar to the use of AGE, ζ-potential can also be used for evaluating the

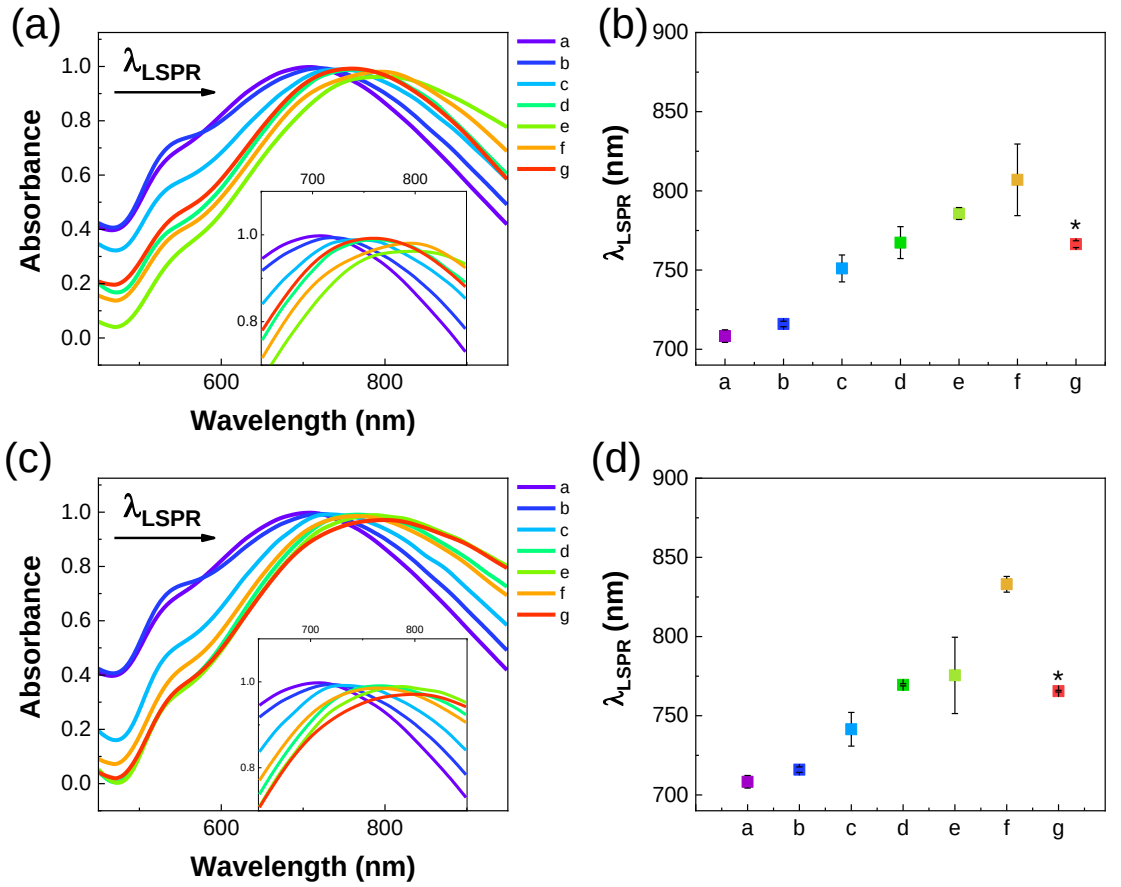

Figure 3.13: UV-Vis spectra and LSPR maximum of SERS immunotag formation process. (a, b) represent the physisorption bioconjugation process and (c, d) show the covalent bioconjugation process. Normalised optical spectra of bare nanostars (AuNS; a), with functionalisation (AuNS-MBA; b), after antibody conjugation (AuNS-MBA-anti-HRP; c) and blocking with BSA (SERS immunotag; d). Followed the SERS immunotag production, HRP was added to form (SERS immunotag-HRP; e) and the sandwich SERS immunotag was completed with the antibody (SERS immunotag-HRP-anti-HRP; f). The negative control of the sandwich SERS immunotag was made whereby the anti-HRP was added to the SERS immunotag solution with no HRP; g*). Error bars correspond to the standard deviation from three independent experiments.

nanoenvironment. At pH 7, the AuNSs are negatively charged due to physisorbed citrate ions (Table 3.3 and Figure 3.14). The coverage of the NP surface leads to an electric double layer formation, responsible for preventing aggregation and adsorptive interactions with the walls of the recipients [73, 76]. The global negative charge interacts with the positive charged residues of anti-HRP, resulting in an increase of the ζ-potential from -32 mV to -25 mV, consistent with adsorption of antibody on AuNSs surfaces. The following steps of HRP and further anti-HRP addition revealed small decreases in ζ-potential to -22 mV and -19 mV, respectively, confirming successful adsorptions. The ζ-potential observed is indicative of the colloidal suspension stability. These values show that the colloidal particles are electrically stabilised and hence can be used in the following assays for determining the positive detection of peroxidase by enzymatic assay and SERS activity.

SEM has been extremely useful in monitoring morphology and size distribution of

Table 3.3: DLS and ζ-potentials of immunotags and following steps toward immunoassay.

	Hydrodynamic Diameter (nm)	**ζ-Potential (mV)**	**Polydispersion index**
AuNS - MBA	67.9 ± 0.4	-31.6 ± 0.8	0.223
Physisorbed			
AuNS - MBA - anti-HRP	75.4 ± 1.3	-25.4 ± 0.8	0.226
SERS immunotags	82.2 ± 1.3	-24.7 ± 0.9	0.234
SERS immunotags – HRP	91.9 ± 1.6	-23.8 ± 1.8	0.334
SERS immunotags – HRP – anti-HRP	135.9 ± 9.3	-22.2 ± 0.8	0.432
Covalent			
AuNS - MBA - anti-HRP	130.2 ± 1.6	-25.1 ± 0.8	0.321
SERS immunotags	149.1 ± 1.7	-25.6 ± 1.1	0.355
SERS immunotags – HRP	149.0 ± 3.2	-22.1 ± 0.8	0.367
SERS immunotags – HRP – anti-HRP	161.0 ± 1.3	-19.3 ± 0.9	0.368

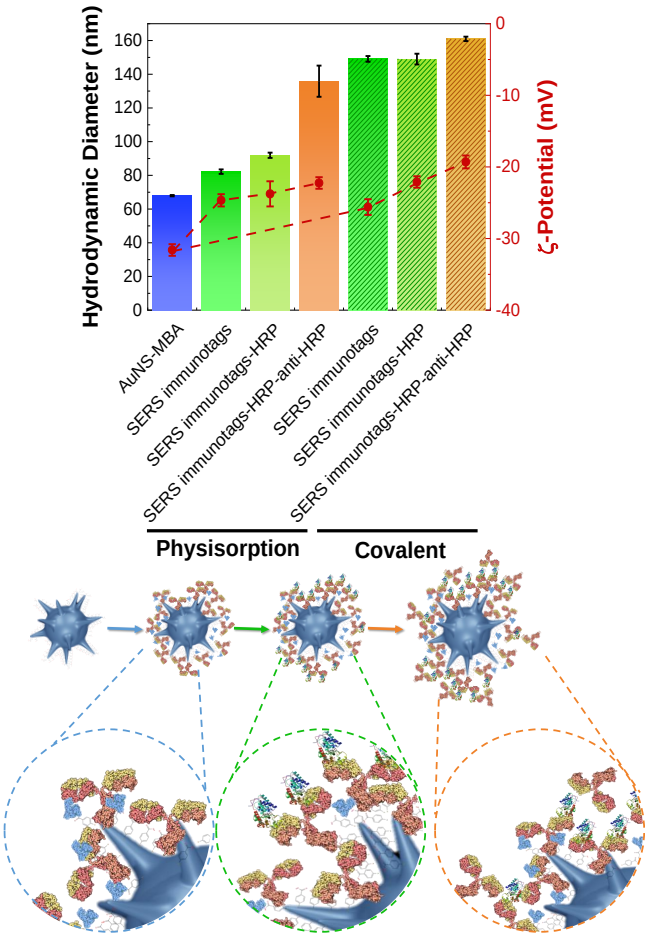

Figure 3.14: Characterisation of physisorbed and covalent bioconjugates by DLS and ζ-potential. Top: hydrodynamic diameter and ζ-potential of the several steps of bioconjugate formation (error bars are measurements of $n = 3 \pm$ standard deviation). Bottom: bioconjugation formation scheme.

nanostructures. Figure 3.15 depicts SEM images of AuNSs upon interaction with capping agent, and various additions of protein. SEM confirmed the prevalence of AuNSs morphology during several steps of conjugation and washes.

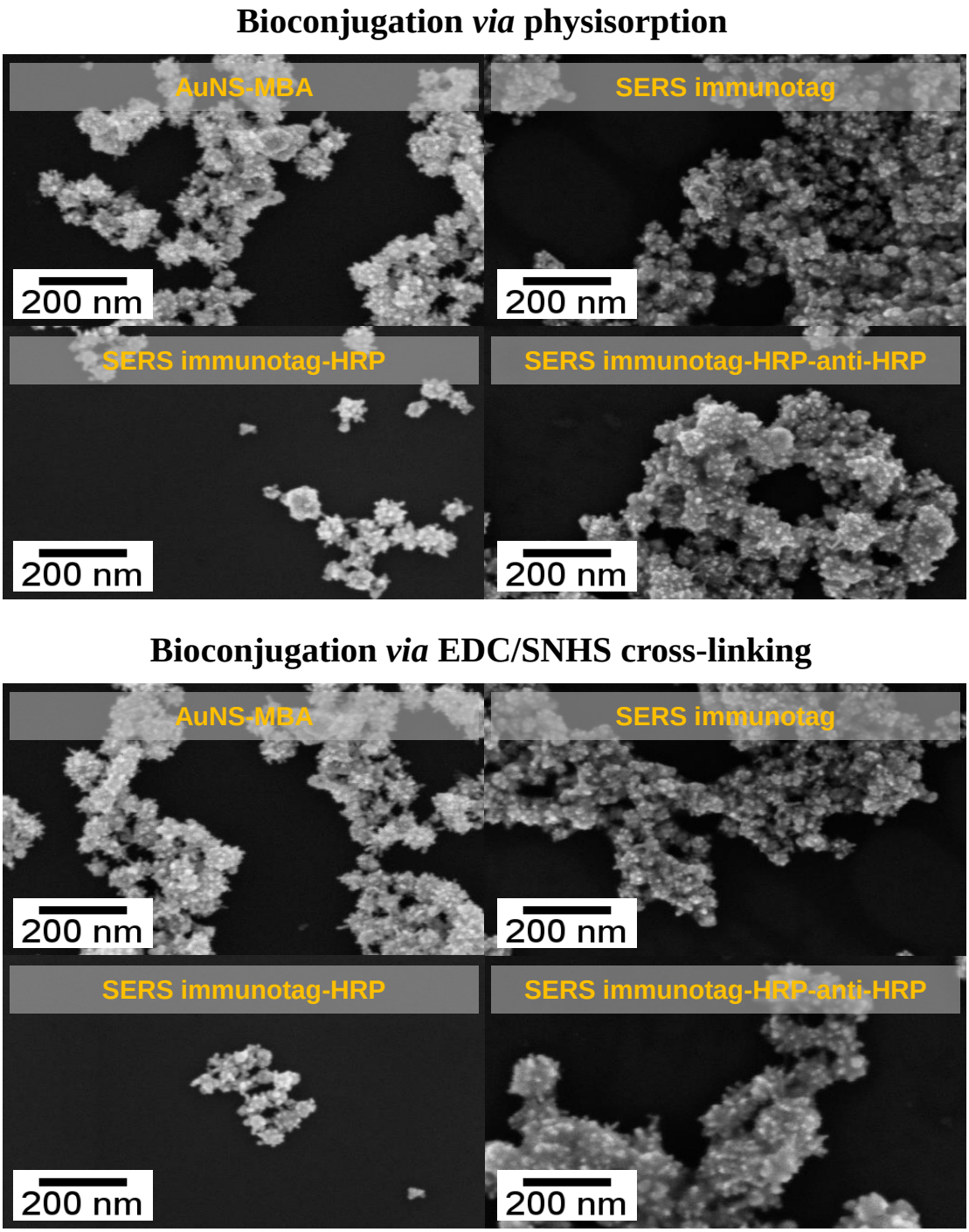

Figure 3.15: Morphological characterisation of gold nanostars. SEM images of AuNSs after functionalisation, and conjugation steps. The samples were dispersed in ultrapure water. The AuNSs morphology was not lost with increasing amount of protein coupled to the nanoparticles.

3.3.2.1 SERS activity of the SERS immunotag

SERS spectra were obtained of several dilutions from the stock suspension of SERS immunotags produced via physisorption and via EDC/SNHS cross-linking methods. The detection was considered successful when both dominant vibrational lines for MBA were identified, at 1079 cm^{-1} and 1587 cm^{-1}. The vibrational mode at 1079 cm^{-1}, assigned to the C–S stretching, is strong since the gold surface has high affinity to thiol groups provided by the MBA [53]. Reducing the concentration of the SERS immunotags lowers the observed intensity in the SERS spectra (Figure 3.16). The analytical area threshold for the Raman treatment software (see section 3.2.7) to detect the 1079 cm^{-1} line of MBA was 0.5 a.u.. Having this threshold, both types of SERS immunotags were detected at 0.01 nM, indicating a highly sensitive assay.

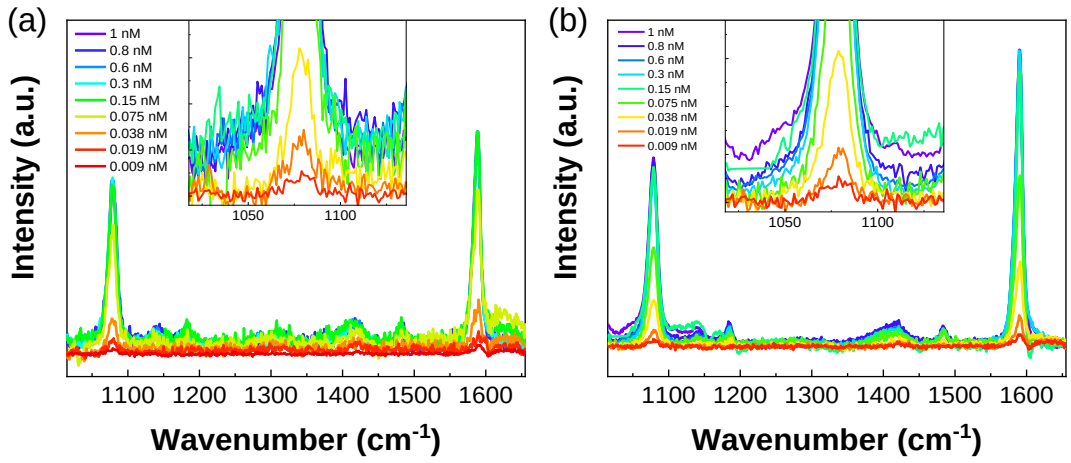

Figure 3.16: SERS spectra from all the performed dilutions for (a) physisorpted and (b) covalent SERS immunotags with bound HRP antigen. These concentrations are related to the concentration determined for AuNSs after synthesis.

3.3.2.2 Functionality of the SERS immunotag

The functionality of SERS immunotags in the biosensor was assessed by measuring the enzymatic peroxidase activity of HRP bound to SERS immunotags. Four different concentrations of anti-HRP antibody were used to form the SERS immunotags, namely 53, 105, 211 and 422 nM for 0.2 nM AuNSs, corresponding to two concentrations below and one above the one previously determined to guarantee a complete antibody corona in the SERS immunotags (211 nM, see section 3.3.1.4). Incubation of these SERS immunotags with an equimolar amount of HRP (based in the amount of anti-HRP), was followed by a washing step by centrifugation and resuspension, and HRP enzymatic activity was measured.

The observed enzymatic activity for all the samples was compared with the free enzyme (Figure 3.17a). Samples with no addition of HRP showed no enzymatic activity.

Results indicated that the prepared SERS immunotags do in fact contain functional anti-HRP antibodies, as increasing the amount of antibody within the conjugate leads to a higher amount of HRP capture, translating into a higher enzymatic activity for the bioconjugate (Figure 3.17). Samples with 422 nM of anti-HRP demonstrated similar activity to the 211 nM, thus evidencing the fully cover of AuNSs with an anti-HRP concentration of 211 nM.

For both types of SERS immunotags, maximal relative enzymatic activity was obtained for 211 nM anti-HRP, but SERS immunotags prepared by covalent conjugation were approximately five times more active than their physisorption counterparts (compare green and orange bars, Figure 3.17a). The lower activity observed in the physisorpted SERS immunotag might be related to disulphide bridges in the antibody that bind to the nanoparticle, thus leading to a lower load of functional antibody and a lower amount of captured HRP [77].

Interestingly, the increase in enzymatic activity obtained for the covalent SERS immunotags relative to their physisorbed counterparts is similar to that obtained for conjugates of protein-A mediated anti-HRP antibody immobilisation on 60 nm spherical gold NPs [78]. The use of protein-A allows orientation of antibodies at the surface of the NPs in a favourable position for antigen binding. Possibly, the reason for a favourable orientation of anti-HRP antibodies, in present study, is the low pH used for the EDC/SNHS coupling reaction. In fact, using a pH lower than the pI value induces rapid electrostatic adsorption in the correct orientation of the antibody molecules to the negatively charged surface of the AuNSs [24].

To further assess the activity of the SERS immunotags, the sandwich SERS-based immunoassay was simulated in AGE, by which the electrophoretic mobilities of the different stages in both bioconjugation processes were measured. In Figure 3.17b, the positive sandwich complex, SERS immunotag with bound HRP and further bound to anti-HRP (a solution simulation of a positive sandwich assay), is represented by a green bar, whereas the red bar corresponds to the negative result. The electrophoretic mobility from the negative result is analogous to the SERS immunotag alone, since the anti-HRP antibodies added to the SERS immunotags did not have the antigen to form the sandwich complex. The results on Figure 3.17 are a proof-of-principle for application of the SERS immunotags to the SERS-based immunoassay.

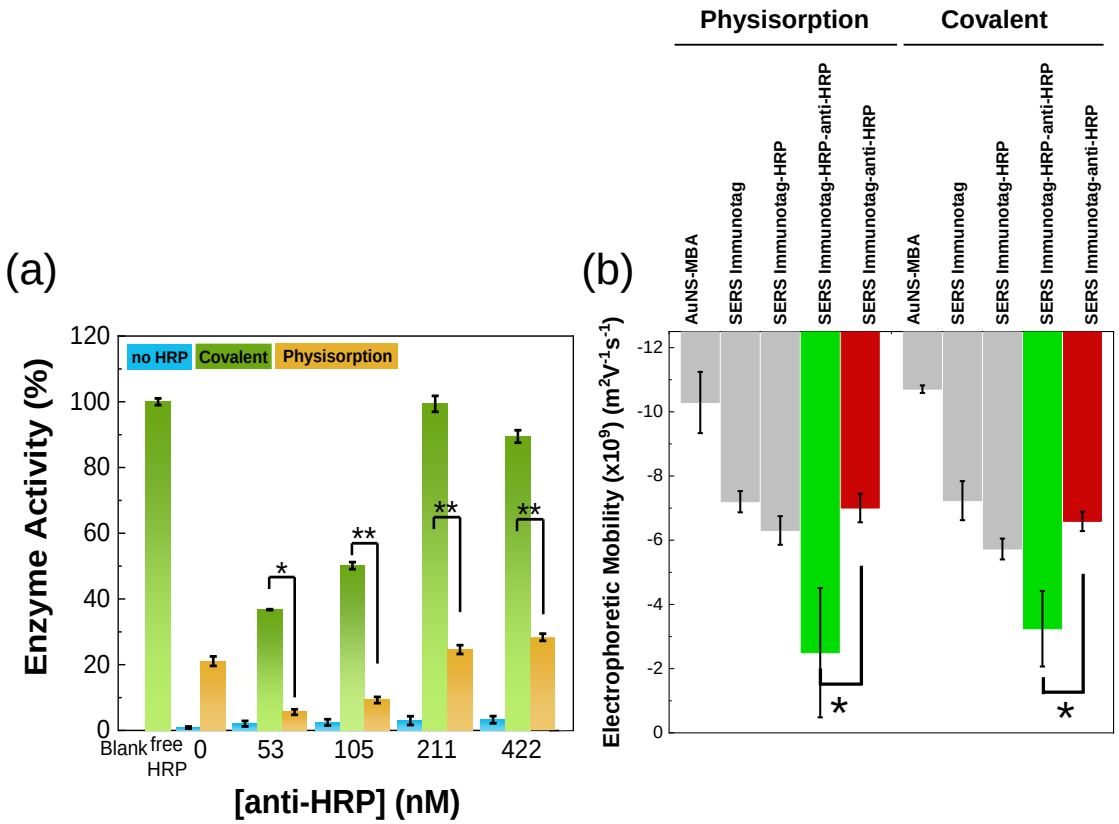

Figure 3.17: Functionality of the SERS immunotags and proof-of-principle of the SERS-based immunoassay.(a) Functionality of the SERS immunotags obtained by physisorption (orange bars) or covalent (green bars) methods, as evaluated by percent enzyme activity of bound HRP relative to free HRP. "Blank": assay without HRP. "Free-HRP": assay with 422 nM of free HRP as added to the bioconjugates. Four concentrations of anti-HRP, 53, 105, 211 and 422 nM, bound to 0.2 nM AuNSs, were incubated with HRP at 422 nM, followed by washing. For the maximal relative enzymatic activity (SERS immunotags with 211 nM anti-HRP), covalent conjugates are ca. five times more active than their physisorbed counterparts. (b) Proof-of-principle of the SERS-based immunoassay. Electrophoretic mobility as determined by AGE for the different stages of bioconjugation. The green bar corresponds to the sandwich complex formed during HRP antigen detection (positive result). The red bar corresponds to the negative result when no HRP antigen is present. Error bars correspond to the standard deviation from five independent experiments (different sets of SERS immunotags). One-way ANOVA was applied for statistical comparison followed by the Tukey's multiple comparison test, $*p \leq 0.05, *p \leq 0.01$.

3.4 Conclusions

In this work, the seed-mediated growth of AuNSs allowed highly branched nanostructures, as confirmed by UV-Vis spectroscopy and SEM. A general approach was designed for a simple and effective functionalisation of the AuNSs by a RR, and further conjugation with antibodies for final use as a SERS immunoassay. AGE was instrumental in determining the appropriate amounts of the RR MBA and antibody to AuNSs, in order to fully cover the AuNS surface. An MBA to AuNSs molar ratio of 50,000, showed excellent electrophoretic mobility without any signs of aggregation. The electrophoretic migration pattern of the conjugation samples (AuNS–MBA-anti-HRP) obtained by simple incubation, was fitted to the Langmuir model achieving a dissociation constant, $K_D = (38 \pm 7)$ nM^{-1} of anti-HRP, indicating the formation of rather stable bioconjugates, although they were obtained by simple incubation. Furthermore, analysis of the Langmuir curve indicated that the conjugation condition that provides a complete coverage of the AuNSs corresponds to an anti-HRP concentration of 211 nM added during incubation.

The functionality of the bioconjugates with anti-HRP is easy to determine as the respective antigen (HRP) presents peroxidase enzymatic activity. After incubation of the bioconjugates with the respective antigen, peroxidase activity determined after washing revealed that the bioconjugated anti-HRP antibodies, were competent for antigen binding. The optimised SERS-active bioconjugates, due to their anisotropic nanostructures, present several hotspots at tips and edges leading to an effective SERS detection down to 0.01 nM of bioconjugates. The approach for covalent attachment of antibodies guaranteed a 5-fold increase in their biological activity in the final SERS immunotags (as compared to attachment of antibodies by physisorption), without the need for more expensive and laborious procedures, such as protein-A based immobilisation. All steps of conjugation were fully characterised by UV–Visible spectroscopy, DLS, ζ-Potential, SEM and AGE. The latter technique was used to establish a proof-of-concept for the proposed immunoassay, including the sandwich binding of a second antibody to the HRP-loaded bioconjugates, which denotes a positive result for the immunoassay.

The fact that the antibody used, anti-HRP, represents a generic IgG antibody, opens various applications using the same detection principles but employing different antibody–antigen systems. Results presented here are a proof-of-concept for a SERS-based immunoassay with easy adaptation to a microfluidics platform.

References for chapter 3

[1] F. Tian et al. "Surface enhanced Raman scattering with gold nanoparticles: effect of particle shape". In: *Anal. Methods* 6.22 (2014), pp. 9116–9123.

[2] M. R. Hoonejani et al. "Quantitative multiplexed simulated-cell identification by SERS in microfluidic devices". In: *Nanoscale* 7.40 (2015), pp. 16834–16840.

[3] M. A. S. Cavadas et al. "Unravelling Malaria Antigen Binding to Antibody-Gold Nanoparticle Conjugates". In: *Particle & Particle Systems Characterization* 33.12 (2016), pp. 906–915.

[4] A. B. Chinen et al. "Nanoparticle Probes for the Detection of Cancer Biomarkers, Cells, and Tissues by Fluorescence". In: *Chemical Reviews* 115.19 (2015), pp. 10530–10574.

[5] J. P. Nolan, E. Duggan, and D. Condello. "Optimization of SERS tag intensity, binding footprint, and emittance". In: *Bioconjugate Chemistry* 25.7 (2014), pp. 1233–1242.

[6] S. Schlücker. "Surface-Enhanced Raman Spectroscopy: Concepts and Chemical Applications". In: *Angewandte Chemie International Edition* 53.19 (2014), pp. 4756–4795.

[7] J. H. Jett. "Raman spectroscopy comes to flow cytometry". In: *Cytometry Part A* 73.2 (2008), pp. 109–110.

[8] J. P. Nolan et al. "Single cell analysis using surface enhanced Raman scattering (SERS) tags". In: *Methods* 57.3 (2013), pp. 272–279.

[9] R. Franco and E. Pereira. "Gold Nanoparticles and Proteins, Interaction". In: *Encyclopedia of Metalloproteins*. Ed. by R. H. Kretsinger, V. N. Uversky, and E. A. Permyakov. 1st ed. Vol. 111. 479. New York, NY: Springer New York, 2013. Chap. G, pp. 908–915.

[10] L. Shang et al. "pH-Dependent Protein Conformational Changes in Albumin:Gold Nanoparticle Bioconjugates: A Spectroscopic Study". In: *Langmuir* 23.5 (2007), pp. 2714–2721.

[11] S. P. Boulos et al. "Nanoparticle–Protein Interactions: A Thermodynamic and Kinetic Study of the Adsorption of Bovine Serum Albumin to Gold Nanoparticle Surfaces". In: *Langmuir* 29.48 (2013), pp. 14984–14996.

[12] S. Ashrafpour and T. Tohidi Moghadam. "Interaction of silver nanoparticles with Lysozyme: Functional and structural investigations". In: *Surfaces and Interfaces* 10 (2018), pp. 216–221.

[13] I. Gomes et al. "Probing Surface Properties of Cytochrome c at Au Bionanoconjugates". In: *The Journal of Physical Chemistry C* 112.42 (2008), pp. 16340–16347.

[14] A. Käkinen et al. "Interaction of firefly luciferase and silver nanoparticles and its impact on enzyme activity". In: *Nanotechnology* 24.34 (2013), p. 345101.

[15] M. Peixoto de Almeida et al. "Measurement of adsorption constants of laccase on gold nanoparticles to evaluate the enhancement in enzyme activity of adsorbed laccase". In: *Physical Chemistry Chemical Physics* 20.24 (2018), pp. 16761–16769.

[16] S. Reymond-Laruinaz et al. "Protein–nanoparticle interaction in bioconjugated silver nanoparticles: A transmission electron microscopy and surface enhanced Raman spectroscopy study". In: *Applied Surface Science* 389 (2016), pp. 17–24.

[17] J. Cortez et al. "Bionanoconjugates of tyrosinase and peptide-derivatised gold nanoparticles for biosensing of phenolic compounds". In: *Journal of Nanoparticle Research* 13.3 (2011), pp. 1101–1113.

[18] P. Smith et al. "Measurement of protein using bicinchoninic acid". In: *Analytical Biochemistry* 150.1 (1985), pp. 76–85.

[19] I. Ojea-Jiménez, N. G. Bastús, and V. Puntes. "Influence of the sequence of the reagents addition in the citrate-mediated synthesis of gold nanoparticles". In: *Journal of Physical Chemistry C* 115.32 (2011), pp. 15752–15757.

[20] J. Turkevich, C. Stevenson, and J. Hillier. "A Study of the Nucleation and Growth Processes in the synthesis of colloidal gold". In: *Discussions of the Faraday Society* 11.c (1951), pp. 55–75.

[21] H. Yuan et al. "Gold nanostars: surfactant-free synthesis, 3D modelling, and two-photon photoluminescence imaging". In: *Nanotechnology* 23.7 (2012), p. 075102.

[22] W. Haiss et al. "Determination of size and concentration of gold nanoparticles from extinction spectra". In: *Analytical Chemistry* 79.17 (2007), pp. 4215–4221.

[23] H. de Puig et al. "Extinction Coefficient of Gold Nanostars". In: *The Journal of Physical Chemistry C* 119.30 (2015), pp. 17408–17415.

[24] S. Puertas et al. "Taking Advantage of Unspecific Interactions to Produce Highly Active Magnetic Nanoparticle-Antibody Conjugates". In: *ACS Nano* 5.6 (2011), pp. 4521–4528.

[25] Sigma-Aldrich. *Enzymatic Assay of Peroxidase (EC 1.11.1.7) with 2,2'-Azino-bis (3-Ethylbenzthiazoline-6-Sulfonic Acid) as a Substrate*. 2019. URL: https://www.sigmaaldrich.com/technical-documents/protocols/biology/enzymatic-assay-of-peroxidase-abts-as-substrate.html (visited on 07/29/2019).

[26] M. Hanauer et al. "Separation of Nanoparticles by Gel Electrophoresis According to Size and Shape". In: *Nano Letters* 7.9 (2007), pp. 2881–2885.

[27] M. S. Jimenez et al. "Evaluation of agarose gel electrophoresis for characterization of silver nanoparticles in industrial products". In: *Electrophoresis* 37.10 (2016), pp. 1376–1383.

[28] J.-Y. Kim, H.-B. Kim, and D.-J. Jang. "Electrophoretic separation of gold nanoparticles according to bifunctional molecules-induced charge and size". In: *Electrophoresis* 34.6 (2013), pp. 911–916.

[29] L. Piantanida, D. Naumenko, and M. Lazzarino. "Highly efficient gold nanoparticle dimer formation via DNA hybridization". In: *RSC Advances* 4.29 (2014), pp. 15281–15287.

[30] G. M. Rothe. "Porosity Gradient Gels". In: *Encyclopedia of Separation Science*. Ed. by I. D. Wilson. 1st ed. Cheshire, UK: Elsevier Science Ltd., 2000. Chap. Level II: pp. 1315–1342.

[31] D. Sheskin. *Handbook of Parametric and Nonparametric Statistical Procedures*. Ed. by Chapman & Hall/CRC. 5th ed. Boca Raton, Florida: Taylor & Francis, 2011.

[32] S. S. Shapiro and M. B. Wilk. "An Analysis of Variance Test for Normality (Complete Samples)". In: *Biometrika* 52.3/4 (1965), pp. 591–610.

[33] B. L. Welch. "The Generalization of 'Student's' Problem when Several Different Population Variances are Involved". In: *Biometrika* 34.1/2 (1947), pp. 28–35.

[34] P. T. Munroe. "ANOVA (Analysis of Variance)". In: *The Blackwell Encyclopedia of Sociology*. Ed. by P. T. Munroe. 1th ed. Oxford, UK: John Wiley & Sons, Ltd, 2015. Chap. 15.

[35] J. W. Tukey. "The Philosophy of Multiple Comparisons". In: *Statistical Science* 6.1 (1991), pp. 100–116.

[36] F. E. Grubbs. "Sample Criteria for Testing Outlying Observations". In: *The Annals of Mathematical Statistics* 21.1 (1950), pp. 27–58.

[37] B. Mir-Simon et al. "Universal One-Pot and Scalable Synthesis of SERS Encoded Nanoparticles". In: *Chemistry of Materials* 27.3 (2015), pp. 950–958.

[38] M. Schütz and S. Schlücker. "Towards quantitative multi-color nanodiagnostics: spectral multiplexing with six silica-encapsulated SERS labels". In: *Journal of Raman Spectroscopy* 47.9 (2016), pp. 1012–1016.

[39] S. Xu et al. "Surface-enhanced Raman scattering studies on immunoassay". In: *Journal of Biomedical Optics* 10.3 (2005), pp. 031112–1 – 031112–12.

[40] M. Peixoto de Almeida et al. "Gold Nanoparticles as (Bio)Chemical Sensors". In: *Comprehensive Analytical Chemistry*. Ed. by M. Valcárcel and Á. I. López-Lorente. 1st ed. Vol. 66. Oxford, UK: Elsevier B.V, 2014. Chap. 13, pp. 529–567.

[41] H. Swanson and E. Tatge. "X-Ray Diffraction Powder Patterns (00-004-0784)". In: *Natl. Bur. Standard. (U.S.)* 20.1 (1953), pp. 1–539.

[42] G. H. Jeong et al. "High-yield synthesis of multi-branched gold nanoparticles and their surface-enhanced Raman scattering properties". In: *Journal of Colloid and Interface Science* 329.1 (2009), pp. 97–102.

[43] S. Krishnamurthy et al. "Yucca-derived synthesis of gold nanomaterial and their catalytic potential". In: *Nanoscale Research Letters* 9.1 (2014), pp. 1–9.

[44] W. Ahmed et al. "Controlling the morphology of multi-branched gold nanoparticles". In: *Nanotechnology* 21.12 (2010), p. 125605.

[45] A. Garcia-Leis, J. V. Garcia-Ramos, and S. Sanchez-Cortes. "Silver Nanostars with High SERS Performance". In: *The Journal of Physical Chemistry C* 117.15 (2013), pp. 7791–7795.

[46] A. Garcia-Leis et al. "Hollow Au/Ag nanostars displaying broad plasmonic resonance and high surface-enhanced Raman sensitivity". In: *Nanoscale* 7.32 (2015), pp. 13629–13637.

[47] T. V. Tsoulos et al. "A closer look at the physical and optical properties of gold nanostars: An experimental and computational study". In: *Nanoscale* 9.11 (2017), pp. 3766–3773.

[48] M. Lee et al. "Highly reproducible immunoassay of cancer markers on a gold-patterned microarray chip using surface-enhanced Raman scattering imaging". In: *Biosensors and Bioelectronics* 26.5 (2011), pp. 2135–2141.

[49] M. Gellner, K. Kömpe, and S. Schlücker. "Multiplexing with SERS labels using mixed SAMs of Raman reporter molecules". In: *Analytical and Bioanalytical Chemistry* 394.7 (2009), pp. 1839–1844.

[50] S. Barbosa et al. "Tuning size and sensing properties in colloidal gold nanostars". In: *Langmuir* 26.18 (2010), pp. 14943–14950.

[51] V. Giannini, R. Rodríguez-Oliveros, and J. A. Sánchez-Gil. "Surface Plasmon Resonances of Metallic Nanostars/Nanoflowers for Surface-Enhanced Raman Scattering". In: *Plasmonics* 5.1 (2010), pp. 99–104.

[52] C. L. Nehl, H. Liao, and J. H. Hafner. "Optical Properties of Star-Shaped Gold Nanoparticles". In: *Nano Letters* 6.4 (2006), pp. 683–688.

[53] D. Li et al. "Selective Capture and Quick Detection of Targeting Cells with SERS-Coding Microsphere Suspension Chip". In: *Small* 11.18 (2015), pp. 2200–2208.

[54] S. Sánchez-Cortés and J. V. García-Ramos. "Anomalous Raman bands appearing in surface-enhanced Raman spectra". In: *Journal of Raman Spectroscopy* 29.5 (1998), pp. 365–371.

[55] C. Pfeiffer et al. "Interaction of colloidal nanoparticles with their local environment: the (ionic) nanoenvironment around nanoparticles is different from bulk and determines the physico-chemical properties of the nanoparticles". In: *Journal of The Royal Society Interface* 11.96 (2014), p. 20130931.

[56] *PubChem Compound Summary for CID 543502, 11-Mercaptoundecanoic acid.* 2021. URL: https://pubchem.ncbi.nlm.nih.gov/compound/11-Mercaptoundecanoic-acid (visited on 08/17/2021).

[57] *PubChem Compound Summary for CID 95738, 4-Mercaptobenzoic acid*. 2021. URL: https://pubchem.ncbi.nlm.nih.gov/compound/95738 (visited on 08/17/2021).

[58] H. Hinterwirth et al. "Quantifying Thiol Ligand Density of Self-Assembled Monolayers on Gold Nanoparticles by Inductively Coupled Plasma–Mass Spectrometry". In: *ACS Nano* 7.2 (2013), pp. 1129–1136.

[59] M. M. Vega et al. "Long-term stability of surfactant-free gold nanostars". In: *Journal of Nanoparticle Research* 16.11 (2014), pp. 2729–2739.

[60] X. Meng, A. Baride, and C. Jiang. "Ligand Controlled Morphology Evolution of Active Intermediates for the Syntheses of Gold Nanostars". In: *Langmuir* 32.26 (2016), pp. 6674–6681.

[61] W. D. Kingery et al. *Introduction to Ceramics*. Ed. by B. Kingery, H. K. Bowen, and W. D. Kingery. 2nd ed. Vol. 124. 3. New York, USA: John Wiley & Sons, Inc., 1977, pp. 152C–152C.

[62] I. A. Sidorov, P. Prabakaran, and D. S. Dimitrov. "Non-Covalent Conjugation of NPs to Antibodies via Electrostatic Interactions — A Computational Model". In: *Journal of Computational and Theoretical Nanoscience* 4.6 (2007), pp. 1103–1107.

[63] G. Judy, M. Vessels, and M. Rothenberg. *Effective Blocking Procedures in ELISA Assays*. Kennebunk, ME USA, 2001.

[64] A. Drabik, A. Bodzoń-Kułakowska, and J. Silberring. "Gel Electrophoresis". In: *Proteomic Profiling and Analytical Chemistry*. Ed. by P. Ciboeowski and J. Silberring. 2nd ed. Oxford, UK: Elsevier B.V., 2016. Chap. 7, pp. 115–143.

[65] M. J. Oliveira et al. "Office paper decorated with silver nanostars - an alternative cost effective platform for trace analyte detection by SERS". In: *Scientific Reports* 7.1 (2017), pp. 2480–2494.

[66] D. Bartczak and A. G. Kanaras. "Preparation of peptide-functionalized gold nanoparticles using one pot EDC/Sulfo-NHS coupling". In: *Langmuir* 27.16 (2011), pp. 10119–10123.

[67] M. J. E. Fischer. "Amine Coupling Through EDC/NHS: A Practical Approach". In: *Surface Plasmon Resonance. Methods in Molecular Biology*. Ed. by N. de Mol and M. Fischer. 1st ed. Switzerland: Humana Press, 2010. Chap. 3, pp. 55–73.

[68] G. T. Hermanson. "Microparticles and Nanoparticles". In: *Bioconjugate Techniques*. Ed. by M. Preap. 3rd ed. London: Elsevier, 2013, pp. 549–587.

[69] M. H. Jazayeri et al. "Various methods of gold nanoparticles (GNPs) conjugation to antibodies". In: *Sensing and Bio-Sensing Research* 9 (2016), pp. 17–22.

[70] M. Rabe, D. Verdes, and S. Seeger. "Understanding protein adsorption phenomena at solid surfaces". In: *Advances in Colloid and Interface Science* 162.1-2 (2011), pp. 87–106.

[71] Thermo Fisher. *Chemical Reactivity of Crosslinkers and Modification Reagents*. Thermo Fisher, 2012, pp. 3–4.

[72] J. Liu and Q. Peng. "Protein-gold nanoparticle interactions and their possible impact on biomedical applications". In: *Acta Biomaterialia* 55 (2017), pp. 13–27.

[73] S. Bhattacharjee. "DLS and zeta potential – What they are and what they are not?" In: *Journal of Controlled Release* 235 (2016), pp. 337–351.

[74] J. Stetefeld, S. A. McKenna, and T. R. Patel. "Dynamic light scattering: a practical guide and applications in biomedical sciences". In: *Biophysical Reviews* 8.4 (2016), pp. 409–427.

[75] A. Henriksen et al. "Structural interactions between horseradish peroxidase C and the substrate benzhydroxamic acid determined by X-ray crystallography". In: *Biochemistry* 37.22 (1998), pp. 8054–8060.

[76] H. L. Wu, C. H. Chen, and M. H. Huang. "Seed-mediated synthesis of branched gold nanocrystals derived from the side growth of pentagonal bipyramids and the formation of gold nanostars". In: *Chemistry of Materials* 21.1 (2009), pp. 110–114.

[77] N. Stephanopoulos and M. B. Francis. "Choosing an effective protein bioconjugation strategy". In: *Nature Chemical Biology* 7.12 (2011), pp. 876–884.

[78] K. Tripathi and J. D. Driskell. "Quantifying Bound and Active Antibodies Conjugated to Gold Nanoparticles: A Comprehensive and Robust Approach to Evaluate Immobilization Chemistry". In: *ACS Omega* 3.7 (2018), pp. 8253–8259.

Chapter

4 Proof-of-concept SERS assay

The results and data presented in this chapter have been published elsewhere:
***Maria João Oliveira**, Inês Cunha, Miguel P. de Almeida, Tomás Calmeiro, Elvira Fortunato, Rodrigo Martins, Luís Pereira, Hugh J. Byrne, Eulália Pereira, Hugo Águas, and Ricardo Franco. Reusable and highly sensitive SERS immunoassay utilising gold nanostars and a cellulose hydrogel-based platform. Journal of Materials Chemistry B, 9 (2021).*
Maria João Oliveira was responsible for the experimental work, except for contributions from PhD Inês Cunha for the production of the regenerated cellulose hydrogel and MSc Tomás Calmeiro for the atomic force microscopy measurements. In addition, Maria João was responsible for the analysis and writing the article.

The present chapter describes the steps required to test the capability of the SERS immunotags to perform an immunoassay using a substrate functionalised with antibodies to provide the support for a SERS-based immunoassay. The choice of the substrate used as capture platform is important, since it can influence the sensing capability [1]. In addition, it can provide the ability to reuse the assay in a continuous process, and also considerably increase its stability [2]. With a view towards adopting sustainable biosensor designs, cellulose is a key player in the role of (bio)economy. This naturally abundant, renewable and environmentally friendly raw material was used to prepare a hydrogel [3, 4]. The cellulose-based hydrogels represent an attractive substrate for immunoassays due to combining cellulose biocompatibility with other fascinating properties such as high-water absorption capacity, stretchability, moldability and stimuli-responsiveness from the hydrogels [5, 6]. This easy to prepare and transparent regenerated cellulose hydrogel (RCH) platform, was used to capture antibodies by the same covalent approach as used on SERS immunotags (described in chapter 3), generating a highly active capture platform.

Following the functionalisation of the capture platform with antibodies, the immunoassay was performed. For that, the respective antigen, and the SERS immunotags were incubated and using confocal Raman imaging, maps were constructed to confirm the presence and specificity of SERS probes bonded to target antigens. Special attention was made for the discrimination of SERS signals from the background and development of a robust method for quantitative mapping of the SERS signals along the capture platform. Imaging SERS tags provided a means to labelling multiple biomarkers, and this mixture was then resolved into individual components using direct classical least squares (DCLS). DCLS uses the shape of the full mixed spectrum to isolate each SERS tag over the capture surface and individual SERS tag spectra and the background Raman spectrum as inputs [7].

4.1 Introduction

The relevance of biosensors that are both highly sensitive and specific, with easy translation into portable health applications, has been particularly highlighted by the need for rapid screening of large populations during the SARS-CoV-2 pandemic [8]. SERS-based immunosensors are especially suited to fulfil the criteria of highly sensitive and specific analyte detection, with easy adaptation to a variety of point-of-care testing (POCT) formats. Examples include lateral flow [9, 10], magnetic beads [11, 12], and microfluidic devices [13, 14].

In a traditional SERS-immunometric assay, the analyte is sandwiched between the capture antibody and the labelled antibody. The capture antibody is immobilised on a substrate, whereas the "top bread slice" of the sandwich consists of the same antibody attached to a plasmonic metal nanoparticle (NP) labelled with a Raman probe (the SERS immunotag) [10, 15–17]. This design offers a more sensitive and versatile option for biosensing than label-free strategies [18], with easy adaptation to a microfluidics setup.

Challenges to overcome for POCT application of SERS-immunosensors are; low reproducibility, inherent to SERS-based detection methods; reduction of costs of the device, including use of low reagent and sample volumes; and easy operation and readout. Additional desirable features for the POCT assay are high sensitivity and specificity, rapidity and robustness, and an environmentally friendly design, with a view towards disposability [19]. For POCT applications, a microfluidic platform exhibits numerous advantages, including rapid response, low sample consumption, high-throughput screening ability, and portability. The high surface-to-volume ratio of micrometre-sized channels of microfluidic devices increases reaction rates of immunoassays compared to those on solid substrates or in the aqueous phase [17, 20]. In addition, the continuous flow environment helps to reduce nonspecific adsorption of SERS nanoprobes, which in turn increases the sensitivity and accuracy for a quantitative detection [14].

In a SERS-immunosensor based on the sandwich design, sensitivity and selectivity improvements can be brought by the SERS immunotag. This should present an optimal

loading of antibodies that are active for antigen capture, making antibody functionalisation of the NPs a key step in the preparation of SERS immunotags [21]. Antibody-orientation strategies at the surface of the NPs have been developed [22, 23], but are expensive and laborious. Another necessary improvement of the SERS immunotag lies in maximising the detected signal and thus the biosensor sensitivity. Multibranched metal NPs, such as gold nanostars (AuNSs), show remarkable SERS performance due to their large number of intrinsic hotspots and high surface-to-volume ratio, as compared to the more commonly used spherical NPs [20, 24]. The sharp bands of SERS spectra obtained from selected Raman probes are ideal candidates for optical encoding, which can further facilitate multiplex and high-throughput immuno-detection [20, 25]. Substrates commonly used in microfluidic devices and enzyme-linked immunosorbent assay (ELISA) plates, such as polydimethylsiloxane, polystyrene, or even glass, can lead to fluorescence or scattering background and partial overlap of vibrational bands from samples when using SERS tags for biological applications [26, 27]. These traditional rigid substrates lack reusability and sensitivity, due to possible leaching of the randomly non-covalently attached antibodies. Flexible substrates such as paper for SERS can present several advantages over conventional rigid substrates, in terms of cost and processability, achieving Raman enhancements factors (EF $\approx 10^5 - 10^7$) comparable with conventional supports [24, 28]. Cellulose nanofibers are one of the most attractive green bioresources, due to their high abundancy, renewability, biodegradability, biocompatibility, and hydrophilicity. In particular, RCHs are an attractive choice, not only due to low energy requirements for fabrication, but also by providing a smooth surface, highly appropriate for immunoassays due to the high water-absorption capacity [29]. Their moldability allows construction of microfluidic devices using simple fabrication methods, such as matrix-assisted 3D printing [30]. Importantly, cellulose-based hydrogels are transparent and have low background fluorescence, two essential characteristics for their application on highly-sensitive SERS-based microfluidics devices [31].

Finally, a POCT platform requires a simple readout of SERS spectra. A method that integrates data processing, analysis and readout should be applied to improve the limit of detection (LOD) and efficiency of SERS detection, even in the presence of high background signals. Although the conventional peak integral method still prevails in Raman data processing, multivariate curve resolution (MCR) methods are becoming increasingly popular [27, 32, 33]. These methods allow identification of the chemically meaningful components by demultiplexing the complete profile of Raman spectrum, improving the limit of detection and assay robustness [7, 33]. The success of these methods has been demonstrated in digital SERS imaging for multiplex detection at ultralow concentrations [32].

In this chapter, a highly sensitive and selective SERS immunoassay is presented using horseradish peroxidase (HRP) detection as a proof-of-concept analyte in a sandwich format. The strength of the reported SERS-based biosensor lies in merging:

1. SERS immunotags based on gold nanostars, that proved to be strong SERS enhancers of the attached 4-mercaptobenzoic acid (MBA) or 5,5-dithio-bis-(2-nitrobenzoic acid) (DTNB) Raman reporter (RR). A highly active antibody corona was created by improving the method of covalent binding of antibodies to the Raman probe, giving rise to robust and stable SERS immunotags (developed in chapter 3).

2. An easy to prepare, transparent, RCH platform, to which capture antibodies were also bound by the same simple covalent approach as used on SERS immunotags, generating a highly active capture platform.

The robustness of the DCLS is demonstrated for the SERS data analysis of the key Raman bands derived from SERS immunotags, partially overlapping those of the RCH platform. This approach allows quantitative mapping of the SERS signals along the capture platform and exclusion of interfering background signals. Simultaneous detection of two unrelated antigens (duplexing) is also demonstrated, and shelf-life and reusability studies are conducted, in view of POCT microfluidics applications.

4.2 Materials and Methods

4.2.1 Materials

The materials used in this chapter to produce the SERS immunotags have been already described in chapter 3 section 3.2.1 with the exception of DTNB as alternative RR of MBA that was purchased from Sigma-Aldrich, St. Louis, USA. The following reagents were used in RCH preparation and in antibody immobilisation protocol: ethanol (≥99.0%), the cross-linking reagents (1-ethyl-3-(3-(dimethylamino)propyl)carbodiimide (EDC) and N-hydroxysulfosuccinimide (SNHS), ≥98%), buffers (namely, 2-ethanesulfonic acid (MES), phosphate-buffered saline (PBS), and potassium phosphate buffer), as well as, lithium hydroxide (≥98%), microcrystalline cellulose (powder: 20 μm), glacial acetic acid, 2,2,6,6,-tetramethylpipelidine-1-oxyl radical (TEMPO), sodium bromide (≥99.0%), sodium hypochlorite, bovine serum albumin (BSA), skimmed milk powder, Tween 20, poly-l-lysine solution, and the antigen HRP, were all purchased from Sigma-Aldrich, St. Louis, USA. Urea (≥ 99.5%) was purchased from Carl Roth GmbH, Germany, and hydrochloric acid (37%) was purchased from Fisher Chemical, Loughborough, UK. The antigen *Plasmodium falciparum* histidine rich protein 2 (*Pf*HRP2) used for the selectivity and duplex assays was produced at Bionanolab (see chapter 6, section 6.2.3 for detail). The polyclonal anti-HRP antibody and monoclonal anti-*Pf*HRP2 antibody were from Antibodies-Online, Germany. The substrate 2,2'-azino-bis(3-ethylbenzthiazoline-6-sulfonic acid) (ABTS) was from Roche, France, and, hydrogen peroxide (30% v/v) and nitric acid (65%) were purchased from Panreac AppliChem, Germany. Protein determination was by the bicinchoninic acid (BCA) method (based on Smith *et al.* [34]) using a kit from Sigma-Aldrich, St. Louis, USA. All chemicals and reagents were of the highest

purity available and ultrapure water (H_2O, 18.2 MΩ·cm at 25ºC, *Milli-Q*®) was used for the preparation of all solutions, unless stated otherwise.

4.2.2 Regenerated cellulose hydrogel for antibody immobilisation

Based on procedures reported in the literature for the dissolution of cellulose [35–37], the cellulose dissolution medium was prepared by mixing 4.6 wt.% LiOH, 15 wt%. urea in 80.4 wt.% deionised water. The solvent mixture was pre-cooled in a freezer at -25°C, until it becomes a frozen solid. The frozen solution was then allowed to thaw at room temperature, and 6 wt.% of microcrystalline cellulose (powder: 20 μm) was immediately added into the solvent system under vigorous stirring at -8°C until its complete dissolution (≈30 min). A freezing-thawing cycle was performed to improve cellulose dissolution. Then, 5 mL of the resulting viscous solution were evenly spread on a glass plate (10×10 cm^2), and cellulose was regenerated for 60 min with glacial acetic acid. The sheet-like hydrogel membrane was thoroughly washed with deionised water to remove the remaining salts, dried at room temperature for 3 days and stored in air.

In order to immobilise antibodies, the RCHs were oxidised by using TEMPO/ NaBr/ NaClO system as described by Isogai *et al.* [38]. Firstly, 52 mL of ultrapure water were added to approximately 1 g of RCH. TEMPO and NaBr were dissolved and added to a final concentration of 2.5 mM and 15.28 mM, respectively. Then, 879.68 mM of NaClO were added in the solution and the pH was adjusted to 10 by adding 0.5 M NaOH. The TEMPO-oxidised RCHs (referred as "TEMPO-oxidised (TO)-RCH") were kept in the solution for 1 h under vigorous stirring (≈700 rpm). Finally, the TO-RCHs were thoroughly washed in ultrapure water and kept at 4°C in a solution of 10% (v/v) of H_2O_2.

The TO-RCH was made amine-reactive via EDC/SNHS activation to couple antibodies as follows: the hydrogel (0.5 cm × 0.5 cm) was washed with ultrapure water and immersed in 100 μL of 10 mM MES buffer pH 6.5. EDC/SNHS activation was achieved through the protocol described by Dixit *et al.* [39]. Volumes of 100 μL of EDC and SNHS at 20.86 mM and 50.66 mM, respectively, were allowed to react with the hydrogel for 15 min in an orbital shaker at 250 rpm, at 25°C, and the volume was discarded. Afterwards, 100 μL of antibody at 50 $\mu g \cdot mL^{-1}$ in MES buffer 10 mM pH 6.5 were added. The solution was mixed with the pipette and incubated for 15 min in the orbital shaker. The sample was left incubating overnight at 4°C. The cross-linking reaction was stopped by washing the TO-RCH three times with 20 mM PBS buffer at pH 7.4 to remove electrostatically bound antibodies. A volume of 100 μL of skimmed milk as blocking agent at 0.5% (w/v) with Tween 20 at 0.05% (w/v) was added to the membrane and incubated in the orbital shaker for 30 min at 25°C. Since the antibody used herein is polyclonal *i.e.*, is able to recognise multiple epitopes, the ratio between antibody and antigen can be considered as 1:1 [22]. Therefore, 100 μL of 50 $\mu g \cdot mL^{-1}$ of HRP were incubated for 30 min at 25°C and then the hydrogel was washed as previously described for the cross-linking reaction. Special care was taken during the washing steps, as it is essential in ELISA assays to

remove unbound material [40]. Washing was done with buffer three times, after which the washing solution was removed completely. Antibody concentration was optimised to maximise the response of the substrate. The SERS-based sandwich immunoassay was finalised by incubation of 100 µL at 1 nM of SERS immunotags for 15 min at 25°C and washing with buffer three times.

4.2.3 Preparation of gold nanostars and SERS immunotags

The SERS immunotags, namely, the AuNSs synthesis and functionalisation, as well as the bioconjugation, were prepared as described in previous sections 3.2.2.1 and 3.2.2.2, respectively in chapter 3.

4.2.4 Biosensor characterisation

To characterise the biosensor, several features were examined, namely, reproducibility, selectivity towards the antigen, reuse through regeneration, time-stability, and multiplexing. In terms of SERS-based immunoassay, the whole procedure was the same as previously described in section 4.2.2 entitled "Regenerated Cellulose Hydrogel for antibody immobilisation", with the following exceptions: for the selectivity assay, and, as a negative control, an irrelevant antigen (*Pf*HRP2 - an antigen used for malaria detection assays) was used. For time stability studies, SERS immunotags and the RCH functionalised with the anti-HRP were kept in phosphate buffer pH 7.4 and PBS 10 mM at 4°C during assays; the regeneration study was accomplished by immersing the SERS immuno-platform in 100 µL of 0.2 M glycine-HCl pH 2.8 for 15 min, and subsequently 1 µL of 1 M Tris-HCl pH 9 was added to restore the original pH of the solution and avoid denaturation of anti-HRP, followed by washing with PBS three times before repeating the incubation step with HRP and the SERS-active SERS immunotags. A multiplex assay was performed by adding SERS immunotags with two different RRs (MBA and DTNB) that recognise different antigens, namely, SERS immunotags with MBA, were formed with monoclonal anti-*Pf*HRP2 that recognises *Pf*HRP2, and SERS immunotags with DTNB were formed with anti-HRP that recognises HRP. The SERS immunotags at 1 nM were allowed to incubate with the RCH immuno-platform loaded with equivalent amounts of anti-HRP and anti-*Pf*HRP2 and incubated with the respective antigens), as described before in section 4.2.2, to allow the formation of the sandwich immunoassay.

4.2.5 SERS immunotags and regenerated cellulose hydrogel characterisation

4.2.5.1 Horseradish peroxidase enzymatic assay

To determine the viability of anti-HRP antibodies, either in the SERS immunotags or immobilised in the TO-RCH capture platform, its capacity to bind HRP antigens was tested via an HRP peroxidase enzymatic activity assay. Incubation times were 90 min for

SERS immunotags and 30 min for the TO-RCH capture platform. Both the SERS immunotags and the capture platform, before addition of HRP, had non-detectable enzymatic activity. Detection of peroxidase enzymatic activity was based on the Sigma-Aldrich protocol [41]. Measurements were carried out at 25°C and pH = 5, Abs_{405} nm and a light pathlength = 1 cm. A 0.001 M potassium phosphate buffer (pH = 5.0) was prepared as a reference sample. The oxidation of a coloured substrate, ABTS (Roche, France) by the enzyme HRP in the presence of hydrogen peroxide, was followed by measuring the absorbance at 405 nm.

4.2.5.2 Optical spectroscopies characterisation

All absorption spectra were recorded by a UV-Vis spectrophotometer Cary 50 Bio (Varian, Agilent, USA) using quartz cells with 1 cm pathlength (Hellma), at room temperature. The absorbance at 405 nm for the enzymatic assays performed on the RCH was measured in a multifunctional microplate reader TECAN SPARK 10M (Tecan Trading AG, Switzerland).

Fourier-transform infrared spectroscopy (FTIR) spectroscopy characterisation of RCH samples was performed using a Thermo Nicolet 6700 Spectrometer (Waltham, MA, USA) equipped with a single bounce diamond crystal attenuated total reflectance (ATR) sampling accessory (Smart iTR). The spectra were acquired with a 4 cm^{-1} resolution in the range of 4000–525 cm^{-1} with a 45° incident angle.

4.2.5.3 Morphological characterisation

Scanning electron microscopy (SEM) observations of the RCH were carried out in a Carl Zeiss AURIGA Crossbeam (focused ion beam (FIB)-SEM) workstation equipped for energy-dispersive spectroscopy (EDS) measurements (AZtec, Oxford Instruments, Oxford, UK). Cellulose membrane samples were placed directly on the SEM support. Atomic force microscopy (AFM) analyses used an Asylum Research MFP-3D Standalone AFM system (Oxford Instruments). Samples were immobilised on glass slides, previously treated with a 0.01% (w/v) poly-l-lysine solution. AFM measurements were performed in AC mode with samples immersed in a PBS buffer solution. Silicon AFM probes (Olympus AC240TS, Olympus Corporation, Japan; k = 2 N/m, f_0 = 70 kHz) were used for AFM topographs which were then low-level plane fitted and exported to images with the Gwyddion open-source software.

4.2.6 Raman and SERS Measurements

Raman measurements were performed using a Renishaw inVia Qontor micro-Raman spectrometer equipped with an air-cooled charge-coupled-device (CCD) as detector and a He–Ne laser operating at 32 mW of 632.81 nm laser excitation. For the SERS immunotags in solution (300 µL), and the final immunoassay performed on the membrane placed onto

a microscope slide, the laser beam was focused with 5× (n.a. 0.12) and long-distance 50× (n.a. 0.5) Leica objectives lens (N Plan EPI), respectively. An integration time of 10 scans of 20 s each was used for all SERS immunotags measurements. The laser was filtered by ≈10%, such that the power at the sample was ≈3.2 mW. Raman images of sandwich immunocomplexes on the RCH were obtained using a Raman point mapping method (scan of 21×21 μm, step of 1 μm). Triplicates were taken of all spectra making a total of 1233 points (pixels) per sample. Between different Raman sessions, the spectrograph was calibrated using the 520.7 cm^{-1} Raman line of an internal Si wafer. All SERS spectra were recorded at room temperature.

All raw data were collected digitally with Wire 5.0 software. Noise reduction, available on the software, was used to estimate and remove the noise through principal components analysis (PCA). Baseline correction using a polynomial fitting (11^{th} order) was then performed, taking care to ensure minimal alteration of raw data.

4.2.7 Direct classical least squares model

MCR methods are used for demultiplex the mixed spectrum into the different chemically meaningful components and provide a way to quantify the contribution of each component on the original mixed spectrum. The mixed Raman spectrum is assumed as a linear combination of the spectra of several pure components and the MCR methods aim to minimise the Euclidean distance between the pure components and an estimate of the transpose of coefficients from the corresponding components quantifying the contribution [42]. In a direct classical least squares model, we assume that the raw data is a product of a weighted sum of reference component spectra (4.1),

$$D = KC + E \tag{4.1}$$

Where D is the measure spectrum, K is a vector of the Raman spectrum of pure components and C is the vector of coefficients which quantify the contribution of each corresponding component in K. In other words, C is the coefficient values vector which dictates "how much" each basis vector contributes to each pixel from the measured signal, D. Because the measured spectrum and the pure substances spectra contain noise, the residuals are expressed by E, and represent the experimental error or remaining background. Usually, E is considered as noise and normally distributed [42]. Being a least square model means that we want to minimise the error in the reproduction of values of D over all wavenumbers, so from equation 4.1, we obtain equation 4.2:

$$E = D - KC \tag{4.2}$$

Applying the Euclidean norm of ε, *i.e.* $\|\varepsilon\|_2^2 = xTx$, we get equation 4.3:

$$\|D - KC\|_2^2 = (D - KC)^T(D - KC) = C^T K^T KC - 2D^T KC + D^T D \tag{4.3}$$

To find the minimum of the function, we derive, $\nabla_x \left(x^T M x\right) = 2Mx$, and set equal to zero to find the contribution coefficients[42] (equation 4.4):

$$\begin{aligned} \nabla_c \left(C^T K^T K C - 2D^T K C + D^T D\right) = 2K^T K C - 2K^T D = 0 \iff \\ \iff K^T K C = K^T D \iff \\ \iff C = \left(K^T K\right)^{-1} K^T D \end{aligned} \tag{4.4}$$

The DCLS analysis was then carried out with in-house scripts written in Python 3.8 (see section B.1 in appendix B). The method assumes each point in the raw spectral map to be a mixture of reference component spectra. In other words, the raw spectrum is considered as a weighted sum of the linear contributions of the reference components, and the (supervised) DCLS fitting process generates scores to represent the weightings of each constituent contribution[7]. The reference components were the pure Raman spectra of MBA and DTNB bioconjugates and the functionalised TO-RCH.

4.2.8 Statistical analysis

For enzymatic assays and SERS-activity assays, results were presented as mean ± standard-deviation from at least three independent experiments run in triplicates. Normality of the data distribution was assessed firstly by the Kolmogorov-Smirnov [43] and then by Shapiro-Wilk [44] test for increased statistical power. The conjugation efficiency and antigen detection in enzymatic assays, were statistically compared using two-sample Student t-test, acquiring the $p-value$ accordingly with Welch correction [45]. To perform a statistical group comparison tests, one-way analysis of variance (ANOVA) [46] followed by the Tukey's multiple comparison test were applied [47]. Outliers were identified by Grubbs test [48]. Significance was considered when $p-values \leq 0.05$. Non-parametric analysis of variance (Kruskal-Wallis test [43]) was performed on the CLS score of individual immunoassay samples across all populations to test the statistical difference between groups.

4.3 Results and Discussion

As illustrated in Figure 4.1a, the sandwich SERS immunoassay has two main components: (I) SERS immunotags and (II) a capture platform. The preparation of the SERS immunotags (Figure 4.1a, I) was performed in three steps, as previously described (chapter 3). The capture platform, based on RCH, was fabricated as previously described [35], with minor modifications. After activation of the RCH membrane by partial oxidation/-carboxylation of hydroxyl surface groups, immobilisation of anti-HRP antibodies was also performed by covalent cross-linking using EDC and SNHS [29](Figure 4.1a, II). In order to increase the specificity of HRP binding to this capture platform, a blocking step with skimmed milk was performed [49].

Figure 4.1b is a schematic representation of the sandwich assay reported here. The sample containing HRP (antigen) is incubated with the capture platform, to allow for binding of HRP to immobilised anti-HRP antibodies. After washing, a solution containing SERS immunotags is added, promoting the formation of the detection sandwich. After washing excess SERS immunotags, quantification of HRP in the sample is performed by detecting the SERS signal of SERS immunotags that remained immobilised in the platform.

4.3.1 Development and characterisation of capture platform

Hydrogels for the platform for immunological detection were strategically designed using an economically efficient dissolution method of cellulose that fits the compromise of environmental awareness: it is fast, non-polluting, easy to handle and uses common chemicals [50]. This method consists of the dissolution of microcrystalline cellulose in pre-cooled aqueous LiOH/urea solvent system [35, 37, 51–53], assisted by a freezing-thawing cycle to optimise the efficiency of the dissolution process. The mechanism involved in the dissolution of cellulose under such low-temperature conditions relies on the formation of a channel inclusion complex, whereby a stable hydrogen network structure formed between LiOH, water clusters and urea leads to the cellulose macromolecules confinement by the urea hydrates, thus preventing cellulose to self-aggregate [25, 53–55]. The "sheet-like" hydrogels are obtained by shear-casting dissolved cellulose on a cleaned glass plate, followed by treatment with glacial acetic acid. The acid breaks the cellulose inclusion complex, exposing the hydroxyl groups of cellulose that promote its self-aggregation, allowing the formation of cross-linked hydrogels [36, 53].

The robust membrane thus obtained is transparent, a desirable feature for integration into microfluidics devices [56] (see inset in Figure 4.2a). As opposed to other cellulose-based substrates, no interfering fluorescence from additives of paper manufacturing production is present, a major advantage for sensitive Raman measurements [24]. The RCH membrane thickness was ≈43.5 µm, as evaluated by SEM (Figure 4.2b). Before immobilisation of anti-HRP, the membrane was activated by oxidation of the hydroxyl surface groups to carboxylic moieties, using the TEMPO/NaBr/NaClO in water at pH 10–11 [57] (see appendix B.2). This is an efficient and selective conversion reaction, that can be used in large scale processes providing the required surface carboxylic groups for EDC/SNHS cross-linking [29].

SEM micrographs presented in Figure 4.2a and b, reveal the topography of the hydrogel that shows a reasonably smooth surface formed by several stacked layers of regenerated cellulose. Comparing the unmodified RCH with the activated, TO-RCH, the cellulose structure seems to be covered by a "gel-like" layer after activation, leading to an increase in the surface roughness from 67.31 nm for the unmodified-RCH to 84.26 nm for TO-RCH as evaluated by AFM (Figure 4.2c and d). In the work of Orelma *et al.*, an increase in phase difference was also observed, which was attributed to a higher

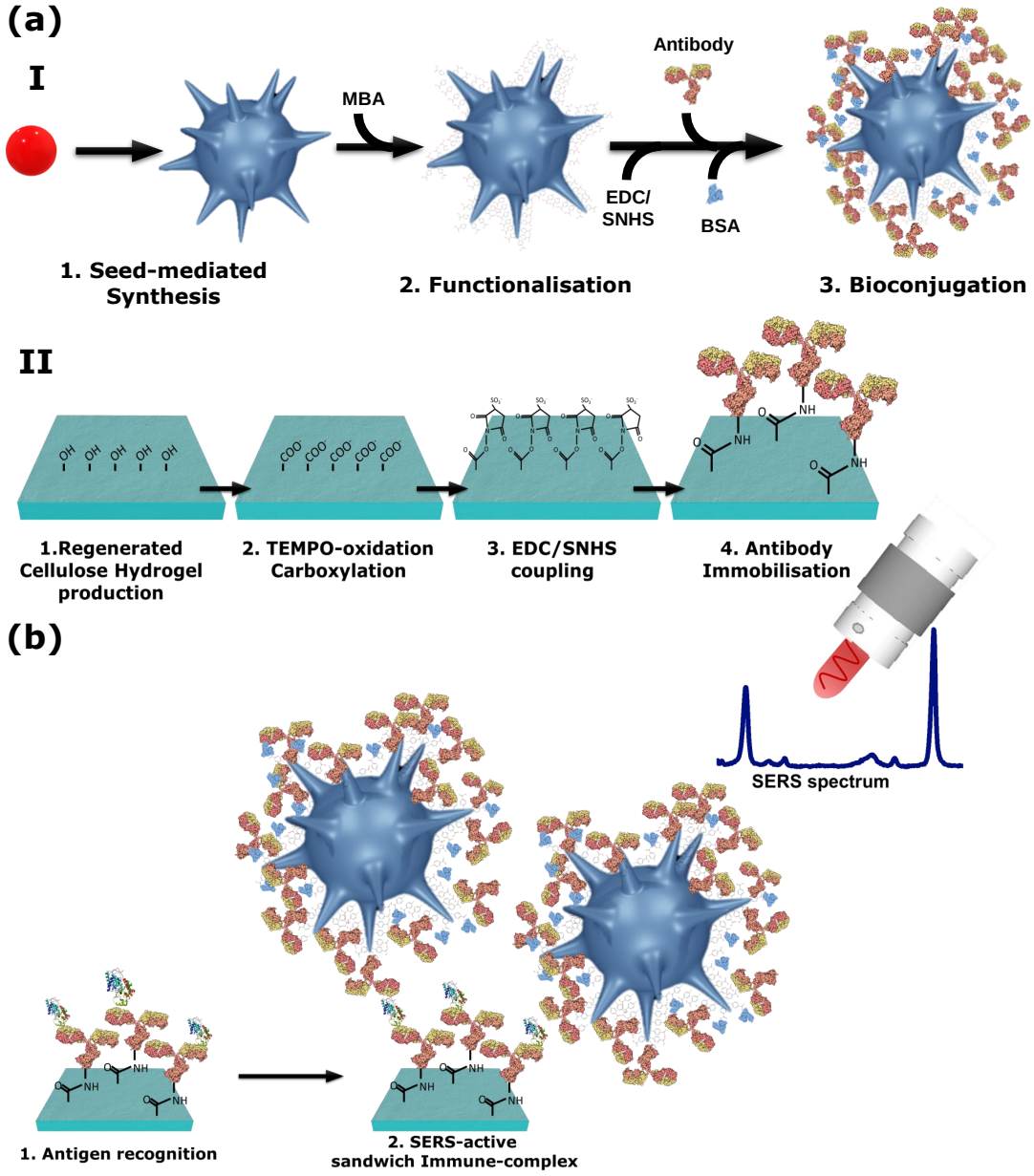

Figure 4.1: Design of the sandwich SERS-based immunoassay. (a) Components of the immunoassay (I) Preparation of the AuNS-based SERS immunotags; and (II) Fabrication of the capture platform, an oxidised regenerated cellulose-based hydrogel with immobilised antibodies. In both cases, functionalisation with anti-HRP antibodies was by covalent cross-linking, mediated by EDC/SNHS. (b) Antigen recognition by the immobilised capture antibody and by the SERS immunotags gives rise to a sandwich immunoassay complex. Quantification of antigen in the sample is made by detecting the SERS signal of immobilised SERS immunotags.

hydrophilic nature [58]. However, in this case, the RCH and TO-RCH samples were immersed in PBS buffer during AFM analysis which might eliminate the hysteretic nature of the capillary force that happens in AFM analysis in air conditions (Figure 4.2e and f) [59]. The hydrophilic properties of the RCH can extend its application to other studies of biological systems, as their processes take place in aqueous environments [60].

The RCH membrane was also characterised by FTIR (Figure 4.2g) before and after oxidation. Results show the typical vibrational bands from cellulose, with the appearance of carboxyl bands in the 1600-1700 cm^{-1} region after oxidation [61, 62].

Functionalisation of the TO-RCH platform with antibodies was performed by both physisorption and covalent methods, with further blocking with skimmed milk in order to decrease non-specific binding in the membrane maximising antigen recognition by the immobilised antibodies. The efficiency of covalent anti-HRP immobilisation on the platform was evaluated upon capture of HRP, by measuring the enzymatic activity, and compared with immobilisation of anti-HRP by physisorption on an equivalent platform. The noncovalently bound sample acts as a negative control because it expresses the possibility of protein (antibody and antigen) being physically entrapped in the TO-RCH matrix or even coupled to the TO-RCH through electrostatic interactions. As shown in Figure 4.3a, the enzymatic activity of the HRP on the capture platform obtained by covalent anti-HRP immobilisation (green bar) is approximately twice that observed for the corresponding platform obtained by physisorption (orange bar). This difference can be explained by a combination of two effects, namely, (i) the covalent-binding approach allows for a correct orientation of the anti-HRP antibodies, maximising HRP binding (see section 3.3.1.5 Bioconjugation *via* EDC/SNHS cross-linking); and (ii) the cross-linking reaction avoids the elution of the antibody during the washing steps, leading to a higher load of HRP captured and consequently a higher enzymatic activity. As a blocking control, the enzymatic activity of the HRP on the platform without anti-HRP (TO-RCH alone, grey bar), was found to be residual, confirming efficient blocking of the platform by the skimmed milk. Moreover, this residual activity from HRP adventitiously bound to the TO-RCH platform, confirms that HRP is in fact bound to anti-HRP antibodies in the two other cases in which antibodies are present.

The amount of antibody on the TO-RCH can also affect the immunoreaction efficiency and sensitivity. To optimise the capture of HRP to the platforms, the concentration of anti-HRP used in the chemical cross-linking procedure was varied from 67 to 600 nM (Figure 4.3b). Upon HRP binding, maximum enzymatic activity was found for an antibody concentration of 333 nM. The decrease in enzymatic activity for higher concentrations indicates that steric hindrance of the antibodies compromises the binding of the antigen. This is a factor which must be taken into consideration in defining the limit of detection of the present biosensor. The most suited antibody concentration for immobilisation on the TO-RCH was thus determined to be 333 nM.

Furthermore, the stability of TO-RCH was inspected by comparing the enzymatic activity produced by freshly prepared samples with those measured after 8 months of its

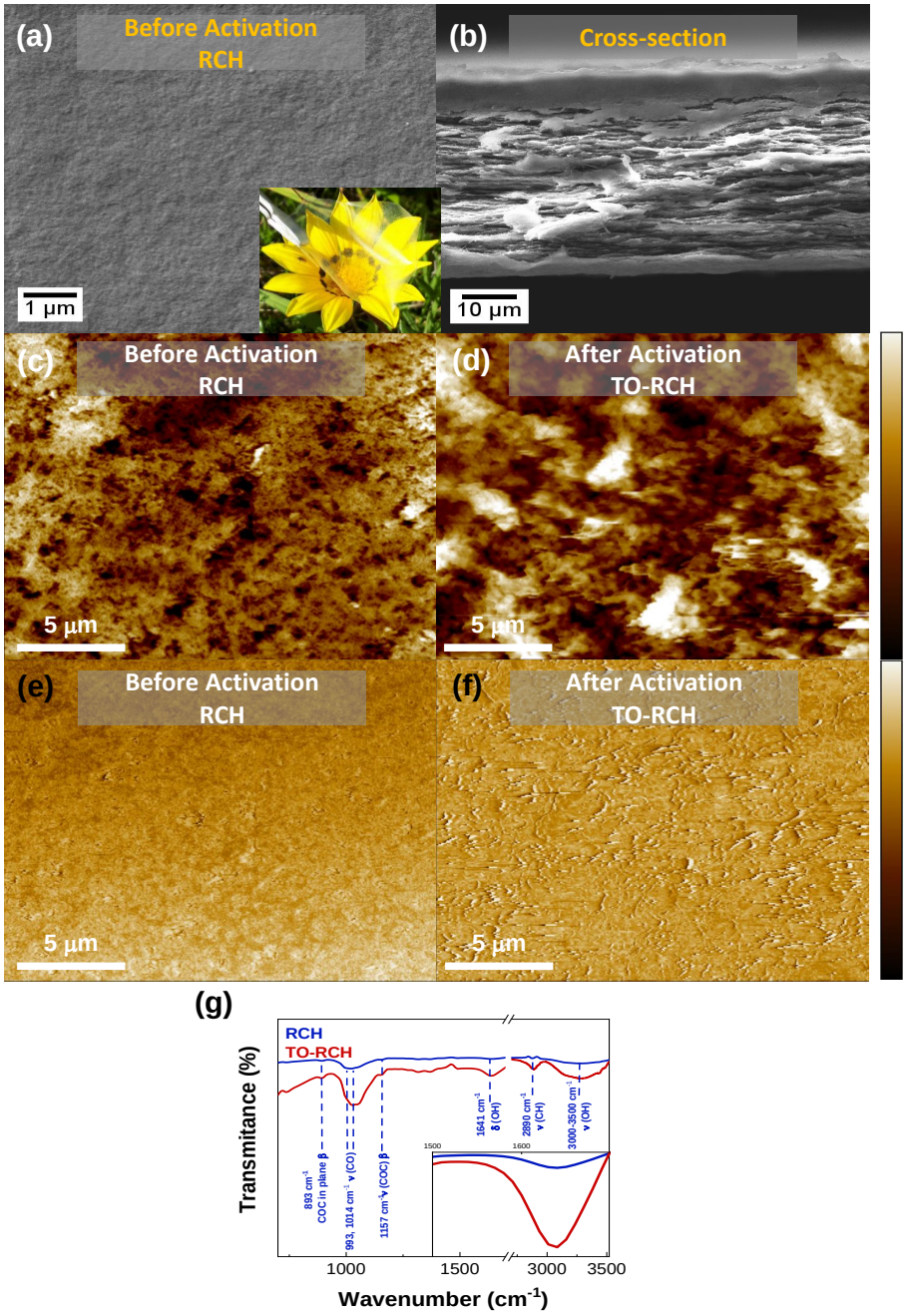

Figure 4.2: SEM micrographs from the (a) surface and (b) cross-section of the as-prepared RCH. The inset in (a) shows a photograph of the as-prepared RCH in front of a flower, evidencing its transparency. AFM topography images of surfaces from RCH before and after oxidation for antibody immobilisation: (c) As-prepared RCH (maximum height of 400 nm); (d) Activated, RCH after treatment with TEMPO for protein immobilisation (TO-RCH) (maximum height of 1200 nm). AFM images of the (e) as-prepared RCH (44.2–78.8°) and (f) Activated TO-RCH (14–91°). (g) FTIR spectrum of the as-prepared (RCH, blue) and after activation by TEMPO (TO-RCH, red), with band assignments for the typical bands of cellulose [62]. The inset is a magnification of the 1500–1700 cm^{-1} region, evidencing the appearance of carboxyl-group broad bands, after TEMPO oxidation.

production (Figure 4.3c). The enzymatic activity of both TO-RCH samples is very similar, indicating good stability.

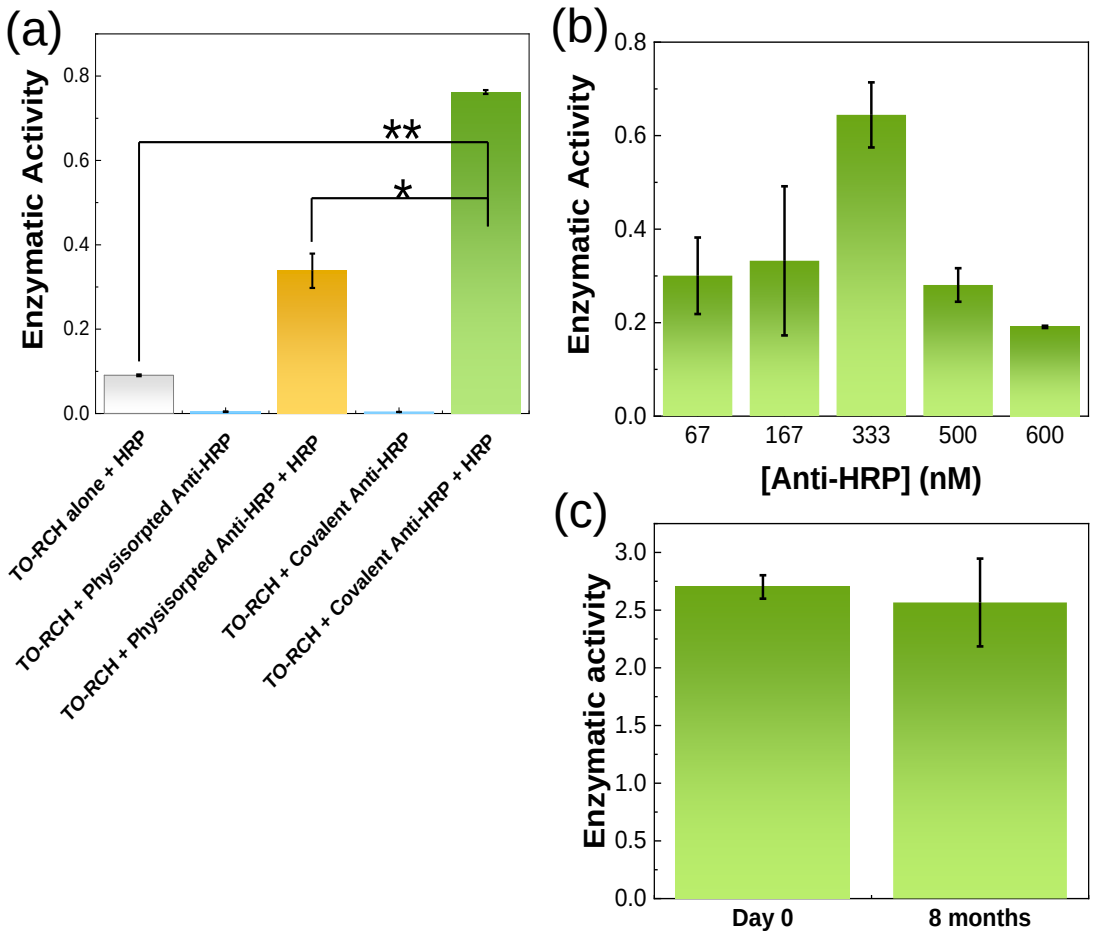

Figure 4.3: HRP enzymatic activity (ΔA_{405}·min^{-1}) evaluates anti-HRP antibodies immobilisation on TO-RCH. (a) Covalently bound antibodies (green bar) have double the HRP activity that their physiosorbed counterparts (yellow bar). The residual activity from HRP bound to TO-RCH alone (grey bar), and the lack of activity in samples without HRP confirms efficient blocking of the platform, and that HRP is in fact bound to anti-HRP antibodies in the two other cases. (b) Different anti-HRP concentrations allow optimisation of HRP capture efficiency. (c) HRP activity acquired from the same batch of TO-RCH over eight months at 4°C. Error bars correspond to the standard deviation from three independent experiments (different sets of SERS immunotags). One-way ANOVA followed by the Tukey's multiple comparison test were applied for statistical comparisons. $*p \leq 0.05$, $**p \leq 0.001$.

4.3.2 SERS-based immunoassay

4.3.2.1 Characterisation of the sandwich immunocomplex

To characterise the formation of the sandwich immunocomplex at the capture surface, AFM images were obtained to compare the capture platform containing anti-HRP, and the platform containing the sandwich immunocomplexes formed in the presence HRP and SERS immunotags (Figure 4.4a and b). The capture platform shows globular features

homogeneously distributed over the surface, with diameters around 40 nm, which are absent in the AFM images of TO-RCH before antibody immobilisation (Figure 4.2d). These features are bigger than expected, based on the diameter of the free antibody in solution (≈16 nm), which might be explained by the compound effect of side reactions occurring during the formation of a chemically cross-linked antibody together with the convolution effect produced by measuring structures with dimensions similar to the AFM probe's terminal diameter (tip ≈14 nm), and also by the roughness of the bare TO-RCH surface, that precludes a rigorous measurement of the size of small features [29, 63]. When HRP and SERS immunotags are added to form the sandwich immunocomplex, the diameter of these globular features increases to ≈150 nm (Figure 4.4b), a size within the expected range for the sandwich immunocomplex. Further corroboration of the presence of sandwich immunocomplexes was obtained by SEM coupled with EDS, by the detection of gold at the globular aggregates, confirming the presence of AuNSs from the SERS immunotags and thus the identity of these aggregates as sandwich immunocomplexes (Figure 4.4c and d).

The sandwich immunocomplexes were also characterised by Raman spectroscopy, to evaluate the feasibility of the present sensor. Figure 4.5 shows Raman spectra of the as-prepared TO-RCH platform, and of the platform after covalent immobilisation of anti-HRP. For comparison, SERS spectra of the SERS immunotags (with MBA as RR) deposited onto a glass surface and of the total sandwich immunoassay, are also presented. SERS spectra of MBA in the SERS immunotags and in the sandwich immunoassay show two highly enhanced sharp bands at 1079 and 1590 cm^{-1}. In this spectral region, the capture platform shows a strong Raman band at 1097 cm^{-1}, with weaker shoulders up to 1160 cm^{-1} and weaker broad bands in the 1200-1500 cm^{-1} region, typical of cellulose bands [64]. Raman spectra of the TO-RCH platform have a much lower intensity than the SERS signal from the MBA reporter in the SERS immunotags, as is noticeable in Figure 4.5, in which these spectra are represented with a 10-fold signal amplification. Nevertheless, platform contribution to the background signal, the strongest band at 1097 cm^{-1}, can partially overlap with the 1079 cm^{-1} band of MBA, and can be falsely attributed to the MBA signal, leading to a decrease in biosensor performance.

Interference from the background and low reproducibility are two of the major obstacles to the successful implementation of SERS as a highly sensitive detection technique [27]. To overcome these issues, we used a combination of two approaches was used. Firstly, SERS data were collected using a point mapping method, in a scan of 21 × 21 μm, in triplicate, with a total of 1233 pixels per sample. This approach allows the detection of a larger number of reporter signals, reducing the problem associated with inhomogeneity of the sample, and avoiding prolonged laser illumination that may lead to photodecomposition. The second strategy was to use the DCLS (see section 4.2.7 for details), for efficient removal of the background signal arising from the platform. DCLS has been reported as a suitable method to resolve complex spectra even in high background situations [27], allowing for accurate quantification of the SERS signals from the SERS immunotag, even

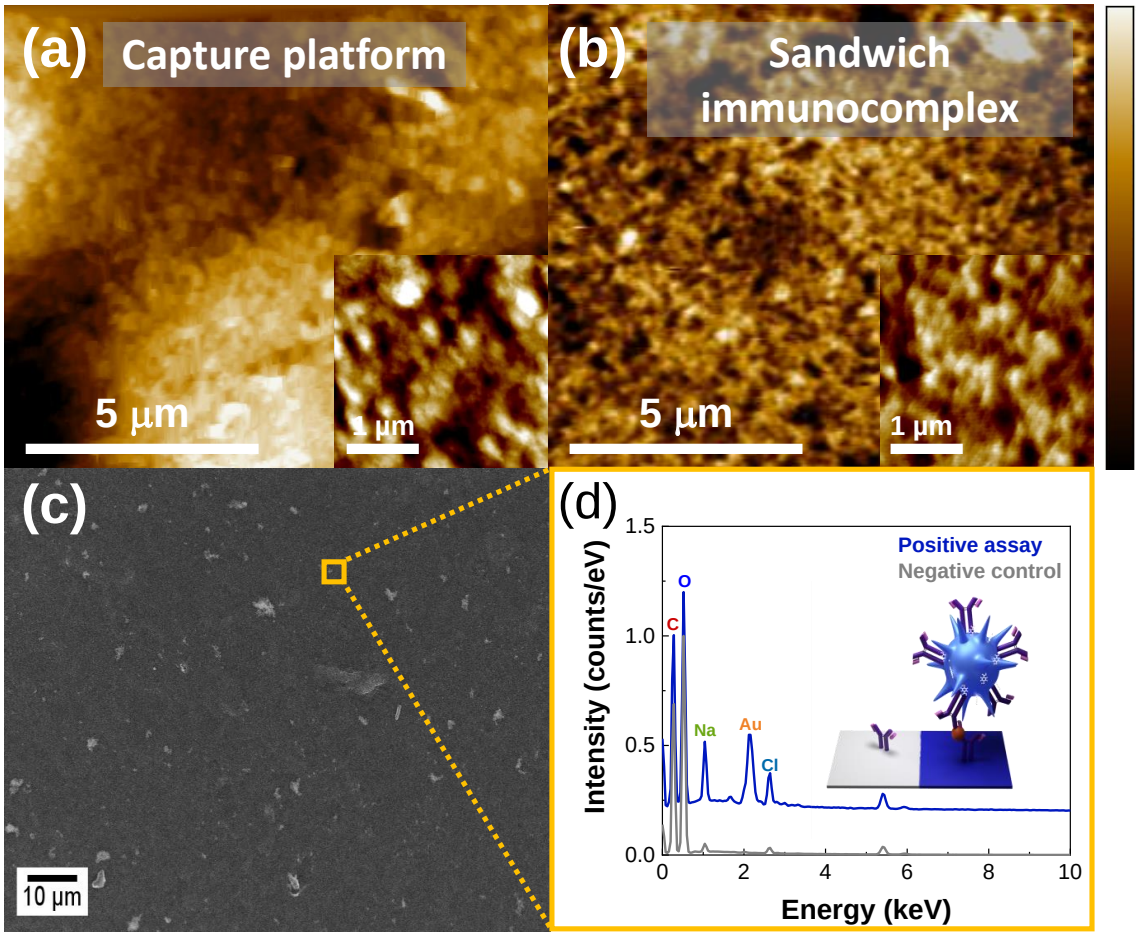

Figure 4.4: AFM topography images of surfaces from (a) Capture platform *i.e.*, TO-RCH platform functionalised with anti-HRP (maximum height of 500 nm, inset maximum height of 60 nm); (b) Sandwich immunocomplex, *i.e.*, capture platform as incubated with the antigen, HRP, and then incubated with the SERS immunotags to form the sandwich immunocomplex (maximum height of 300 nm, inset maximum height of 60 nm). (c) SEM image of the surface with a positive sandwich immunocomplex assay; (d) Comparison between EDS spectra of sandwich immunocomplex assay (blue trace) and the negative control (grey trace). The blue spectrum was taken from the area highlighted by a yellow square in (c).

at very low concentrations. The method relies on spectral deconvolution, using as references, both the Raman spectrum of the capture platform and the SERS spectrum of the SERS immunotag.

Figure 4.6a shows SERS spectra of the capture platform after incubation with HRP and SERS immunotags, *i.e.*, the total sandwich immunoassay. HRP concentration was varied between 0.01-0.10 ng·mL^{-1}, and SERS maps were performed in three different areas for each sample. Figure 4.6b shows a comparison between the DCLS method versus peak integral method using either the 1079 or the 1590 cm^{-1} bands, for SERS data analysis. Both methods provide a linear correlation between the intensity of the probe and the concentration of HRP, but for the DCLS method the coefficient of determination (r^2) is 99.6% versus 87.4% or 88.3% for the band integral method using the 1079 or the 1590

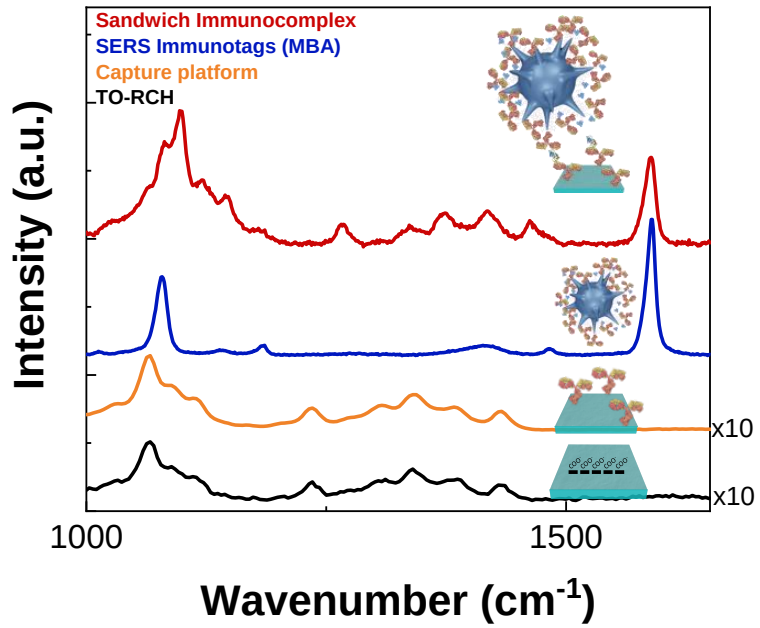

Figure 4.5: Relevant Raman and SERS spectra. From bottom to top: 10× amplified Raman spectra of the as-prepared TO-RCH platform (black) and of the capture platform, *i.e.*, after covalent immobilisation of anti-HRP (orange); SERS spectra of SERS immunotags with MBA as RR (blue), and of the total sandwich immunoassay (red).

cm^{-1} bands, respectively. Therefore, the frequently used band integral method was ill-favoured toward DCLS, implemented to resolve the mixed spectra from each pixel of the Raman map.

When applying the DCLS method, the corresponding coefficients of the MBA RR from the SERS immunotags from all the pixels were plotted, thus constructing the sandwich complex image (Figure 4.6c inset). Since the SERS signal of MBA is obtained from a positive detection of HRP bound to anti-HRP immobilised on the capture platform, the number of events *i.e.*, pixels, can be correlated with the concentration of HRP. The higher the DCLS score, the more intense is the blue colour, indicating that HRP has been specifically detected. The low counts in the control sample show that non-specific binding of the SERS immunotags to the platform is negligible, confirming that the assay is highly specific to detect and quantify HRP. A threshold value of 0.352 component coefficient was established for positive detection (Figure 4.6c) since, from all coefficient values obtained in the control sample, 95% were at or below 0.352. This was important to minimise the error for the components tested, as well as loss of information from the dataset [65].

The advantage of using the DCLS method for low concentrations of HRP is evident in Figure 4.6d, in which the deconvolution of the experimental spectrum using DCLS is compared with experimental data. As can be clearly seen, DCLS can demultiplex and allow quantification of the signal from SERS immunotags at low concentrations, decreasing the influence of overlapped bands from the background. The fitting result

indicates that the DCLS best-fit spectrum can reproduce all bands both from the SERS immunotags and the platform, that are present in the experimental spectrum.

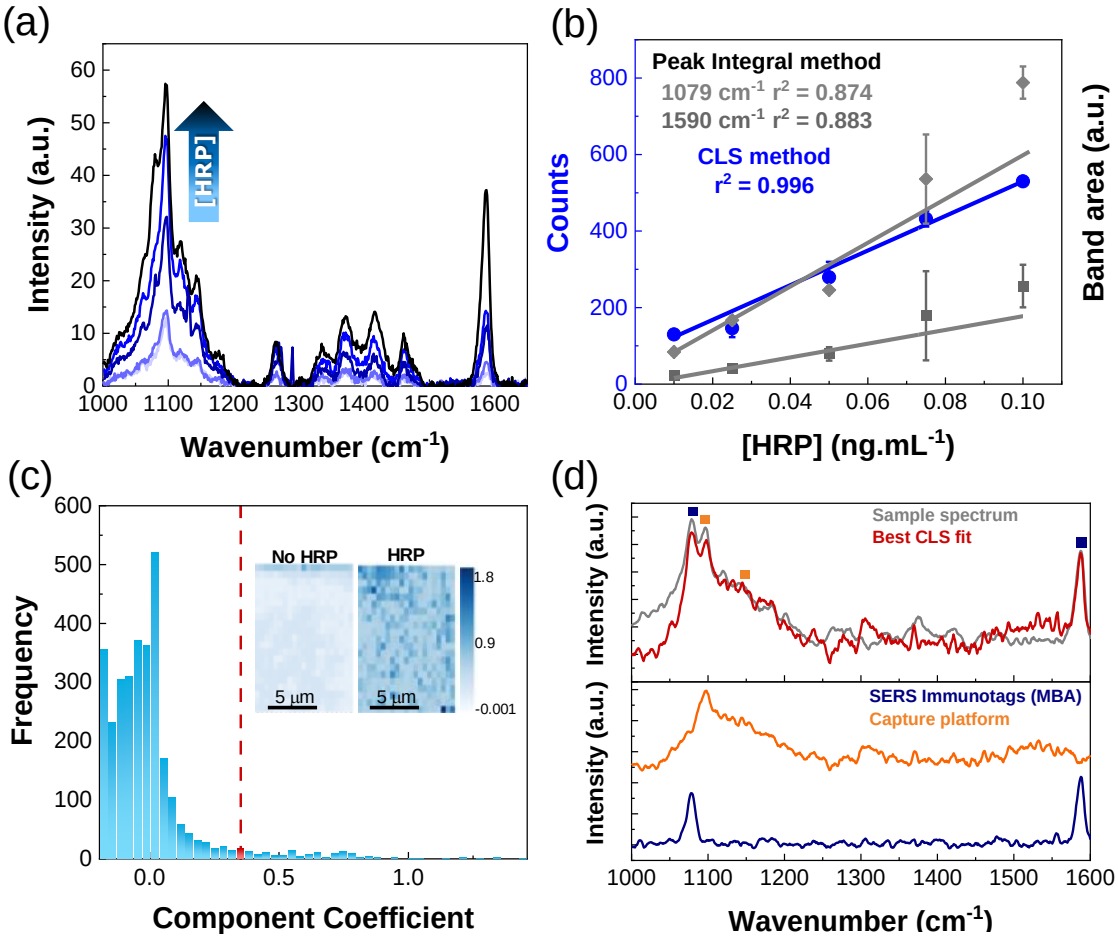

Figure 4.6: Data treatment of SERS results for the sandwich immunoassay applied for HRP concentrations in the range 0.01-0.10 ng·mL^{-1}. (a) Average SERS spectra for each HRP concentration; (b) Linear fit and corresponding SERS counts from the immunoassay, obtained by the DCLS method (blue points and line with a coefficient of determination r^2 = 99.6%), or by the band integral method (grey points and lines with a coefficient of determination r^2 = 87.4% for the 1079 cm^{-1} band; and r^2 = 88.3% for the 1590 cm^{-1} band). Error bars indicate the standard deviation of three independent experiments. (c) Histogram of component coefficient frequencies for blanks in the SERS immunoassay. The red dashed line represents the 0.352 component coefficient that was considered as the threshold for the positive detection of a SERS immunoassay. Inset: Pixelated SERS maps obtained in the presence or absence of HRP. The higher the DCLS score, the more intense is the blue colour. (d) Top: Measured multiplexed SERS spectrum (grey) and the best-fit spectrum by the DCLS algorithm (red). Blue squares indicate SERS bands from MBA signal of the SERS immunotags and orange squares bands indicate Raman from the capture platform. Bottom: Demultiplexed pure Raman spectra of MBA and the capture platform, from the best-fit spectrum.

The LOD and the limit of quantification (LOQ) of the immunoassay, were calculated by the standard IUPAC method as 7.5 ± 0.5 pg ·mL^{-1} and 33.2 ± 0.2 pg ·mL^{-1}, respectively [66]. The major sensing properties of this work were compared with other detection systems and have been summarised in Table 4.1. These results further confirm the robustness of the immunoassay, making our biosensor superior to the ELISA [67], and other

SERS immunoassays [68] and comparable to others [69]. The RCH-based platform presented here is also more sensitive, stable and easier of fabricate than alternative designs [9, 10, 14, 70, 71].

Table 4.1: Comparison of the sensitivity of analytical methods for SERS-based immunoassay detection.

Analytical method	LOD ($pg \cdot mL^{-1}$)	References
ELISA	2.0×10^{9}	[67]
Magnetic SERS immunoassay	1.0×10^{4}	[11]
Vertical flow paper-based SERS immunoassay	3.0×10^{3}	[68]
Hydrophobic paper-based SERS immunoassay	9.0×10^{0}	[69]
MIP[1] based sensors	1.0×10^{2}	[70]
Electrochemical biosensors	2.7×10^{6}	[71]
Paper-based microfluidics systems	4.7×10^{4}	[14]
SERS-improved Lateral Flow Assay	7.3×10^{1}	[10]
Paper-based SERS assay	1.0×10^{-1}	[9]
TO-RCH capture platform	7.5×10^{0}	This work

[1] MIP: molecularly imprinted polymer.

4.3.3 Reproducibility and selectivity of the immunoassay

The inter and intra-reproducibility of the SERS-based immunoassay were evaluated by performing the immunoassay using three independent batches of TO-RCH platforms. Similar responses were obtained between different batches and within each batch with a relative standard-deviation (RSD) for the SERS signal of 13%, indicating a high reproducibility between the four performed immunoassays for each sample (Figure 4.7a and b).

The selectivity of the SERS-based immunoassay was assessed by testing the responses to a purified sample of a non-target antigen, namely *Pf*HRP2, used for malaria infection detection [72] versus positive detection using the target antigen, HRP (Figure 4.7c). The low coefficients (mean of 0.05) obtained show a negative response for the non-target antigen, whereas the high coefficients (mean of 1.05) represent the positive detection of the target antigen. As can be seen in Figure 4.7c, high DCLS scores SERS signals are only obtained in the presence of the immunocomplex, confirming an excellent and consistent selectivity response in detecting the presence of the intended antigen, HRP.

4.3.4 Duplexing detection

A duplexed SERS immunoassay was performed to further demonstrate the versatility and usefulness of the proposed system. Two SERS immunotags containing, two different RR molecules (DTNB and MBA) and two different antibodies (anti-HRP and anti-*Pf*HRP2), respectively, were incubated with a TO-RCH platform containing similar amounts of both antibodies covalently bound. Functionalisation with each of the RRs

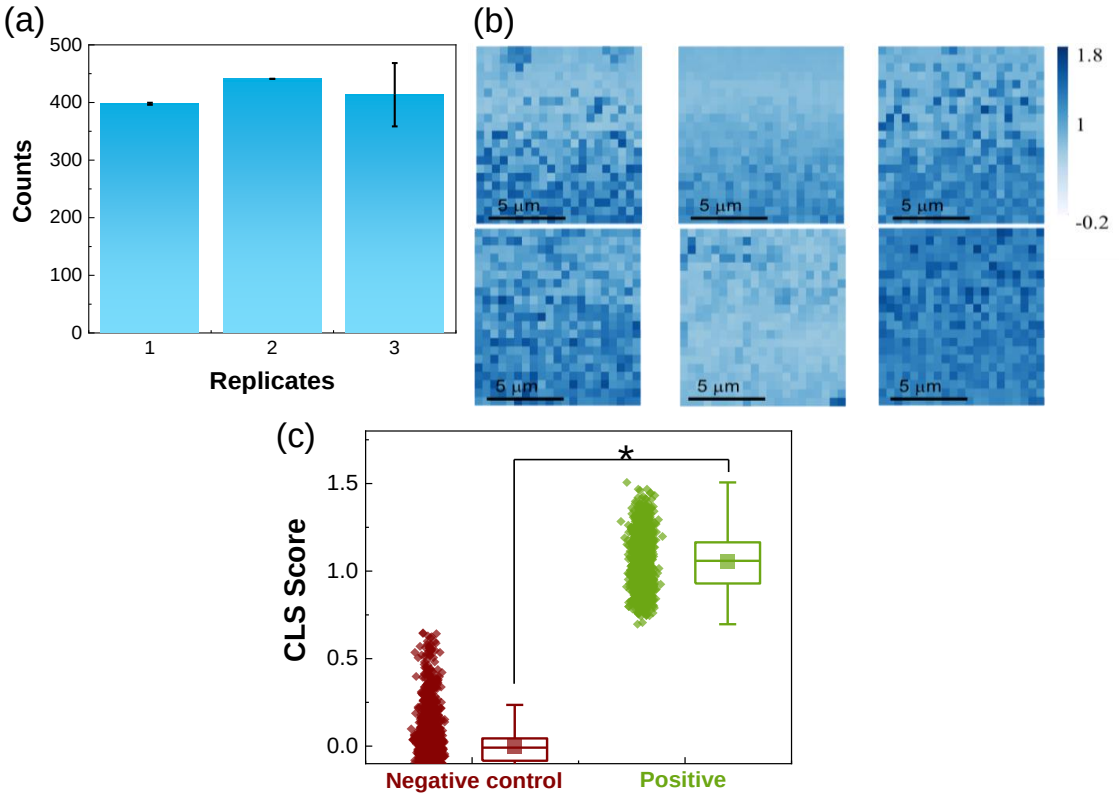

Figure 4.7: (a) Immunoassay activity over three independent batches of capture platform with HRP and SERS immunotags. Error bars correspond to the standard deviation from three independent experiments. (b) Randomly false-colour SERS maps for the HRP reproducibility study. (c) Selectivity response of the immunoassay based on DCLS results. The DCLS technique was used to quantify the contributions of a "Negative control" (red data), obtained when using an irrelevant antigen (*Pf*HRP2) and a "Positive" (green data) for the target antigen, HRP. In the box plots, squares are the mean value for each distribution, the middle line represents the median and the top and bottom lines of each box represent the 75 and 25 percentile values, respectively. Whiskers show upper and lower adjacent values which is 3× interquartile range. Non-parametric analysis of variance by Kruskal-Wallis test (ANOVA) was performed for statistical comparisons. $*p \leq 0.05$.

(MBA or DTNB) was performed as previously reported, and assessed by UV-Vis spectroscopy and AGE (see section 3.3.1 for SERS immunotags with MBA and appendix B.3 for SERS immunotags with DTNB). Usually, the SERS signals from several reporters are identified and quantified by the peak integral method, which relies on separated specific bands [9, 10, 73]. In fact, the two RR present fairly separated specific Raman bands (*e.g.*, MBA: 1588 cm^{-1} and DTNB: 1335 cm^{-1}). However, they also have other bands with a partial overlap (between 1063 and 1079 cm^{-1}), which is around the broad band at 1098 cm^{-1} related to the weak cellulose spectra. By applying the DCLS method, it was possible to resolve the mixed spectra from each pixel. DCLS coefficients for MBA, DTNB from all the pixels were plotted in a coloured scheme Figure 4.8. Also in this duplexing application, the DCLS method was able to identify and clearly distinguish the two specific SERS reporters from the background, in contrast with the peak integral method, as illustrated

for example by the work of Tan *et al.* [27].

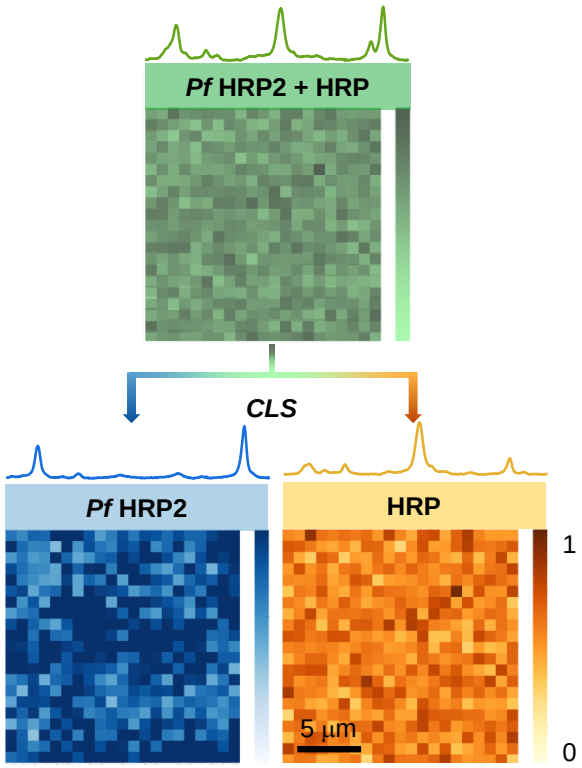

Figure 4.8: Pixelated SERS maps for duplexing detection. Top: Green map of an immunoassay containing equimolar amounts of anti-*Pf*HRP2 and anti-HRP antibodies in the capture platform, equimolar amounts of the respective antigens in the assay solution, and equimolar amounts of MBA-SERS immunotags containing anti-*Pf*HRP2 antibodies and DTNB-SERS immunotags containing anti-HRP antibodies. Bottom: The DCLS method allowed excellent data deconvolution of the green map into its blue (*Pf*HRP2 detection) and yellow (HRP detection) components. Reference SERS spectra of the contents are represented above each pixelated SERS-map.

4.3.5 Long-term stability and activity of SERS immunoassay

The stability of the SERS immunotags and of the capture platform are critical factors for the application of the biosensor. Therefore, the antigen-binding ability was monitored independently by measuring the enzymatic activity after HRP-binding for SERS immunotags or the capture platform after 16 h, 24 h and 168 h (one week), after the respective preparation. The SERS activity of the sandwich immunoassay was also monitored at the same time points (Figure 4.9). The anti-HRP antibodies bound to the capture platform showed great stability, retaining 83% of their initial binding activity, even after one week of storage. This high stability might be attributed to intermolecular cross-linking as already reported by others [29]. The SERS immunotags, after one week, showed 52% of their original binding activity (Figure 4.9a), a drop probably due to some agglomeration occurring in their stock solution. In terms of the SERS activity of the sandwich immunoassay, it did not vary appreciably after 24 h, and it was reduced by only 13% after one week

(Figure 4.9). These results underscore the excellent properties of the RCH platform, providing a high-water content environment that contributes to biomolecules stabilisation. This is an advantage over many polymer matrices and other functional surfaces (*e.g.* ELISA plates, paper-based substrates and glass) used for immobilisation [29].

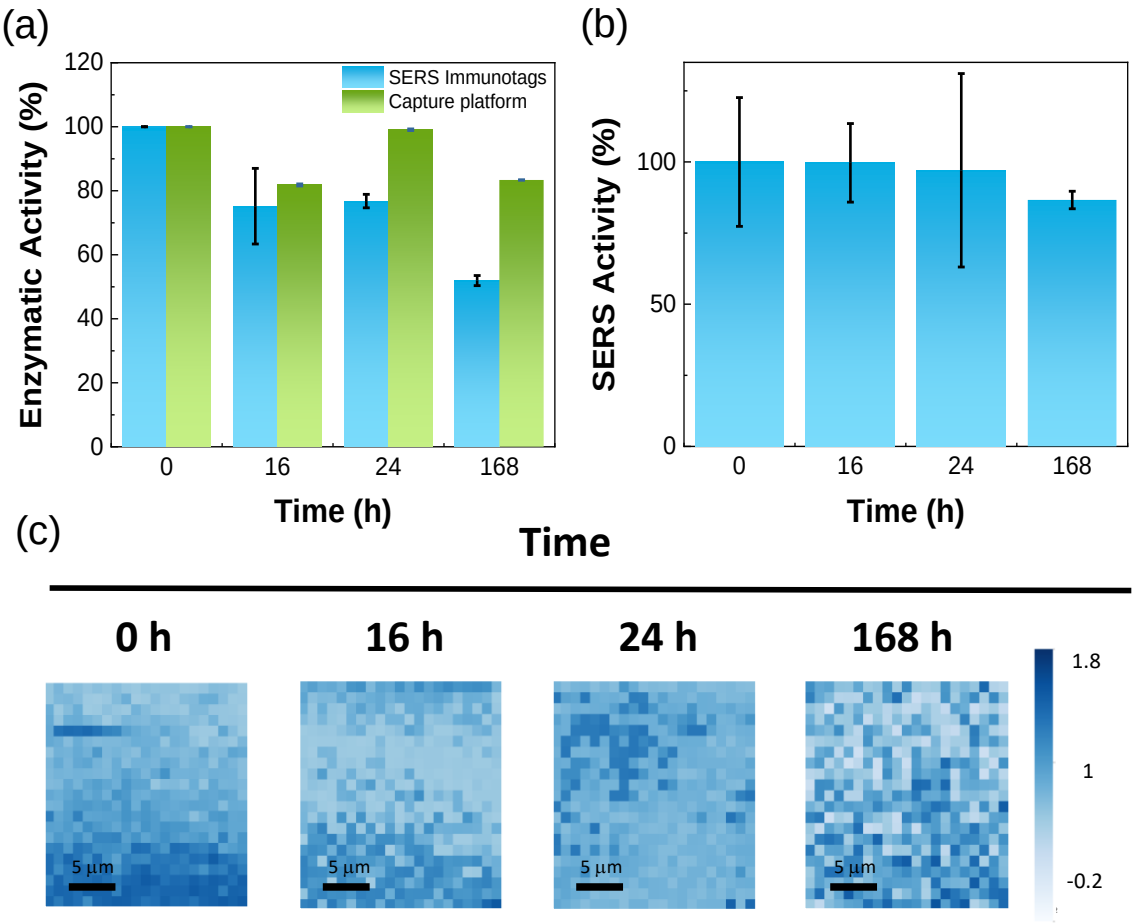

Figure 4.9: Time stability study. (a) Sandwich immunoassay SERS results for three independent batches of the capture platforms and MBA-SERS immunotags. (b) Enzymatic activity for 0 h, 16 h, 24 h and after 168 h, for SERS immunotags (blue bars) and the capture platform (green bars). Error bars correspond to the standard deviation from three independent experiments. (c) Four, randomly selected, pixelated SERS maps from the HRP stability study presented in (b).

The ability to consecutively reuse the assay was also studied. Biosensor regeneration was done by removing the SERS immunotags and the target analyte, HRP, from the capture platform with 0.2 M glycine-HCl, and then washing with PBS to restore the capture platform for another analytical cycle with HRP. Figure 4.10a and b show SERS activity along seven analytical cycles with a regeneration step between each cycle. Figure 4.10c and d show the SERS activity as well as the enzymatic activity for the entire process of regeneration including the decrease in SERS and enzymatic activity when the capture platform is cleaned from the HRP and SERS immunotags. Even after seven cycles, the SERS activity achieved was 87%. Although no consensus exists on defining a successful regeneration process [74], this cellulose-based SERS immunoassay was able to retain its

activity over several cycles while reducing the overall cost of the SERS immunoassay, an feature absent in other cellulose-based assays [9, 75], thus proving to be suitable for repeated sensing applications in POCT, with minimal activity loss.

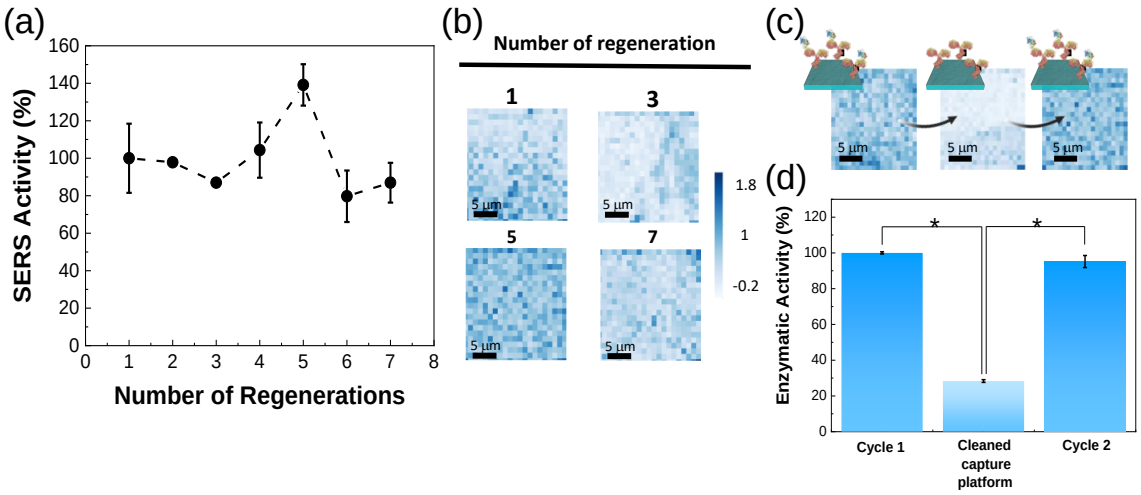

Figure 4.10: Capture platform reusability. (a) SERS activity of the biosensor along seven regeneration cycles of the capture platform (b) Examples of pixelated SERS maps obtained for the indicated number of regeneration cycles. (c) False-coloured SERS maps showing the SERS activity of the biosensor along two regeneration cycles of the capture platform as well as between the cycles. (d) Enzymatic activity of the biosensor along two regeneration cycles of the capture platform as well as between cycles. Error bars correspond to the standard deviation from three independent experiments. One-way ANOVA followed by the Tukey's multiple comparison test were applied for statistical comparisons. $*p \leq 0.05$.

4.4 Conclusions

In this chapter, a highly sensitive and selective SERS immunoassay using HRP detection as a proof-of-concept analyte in a sandwich format has been presented. SERS immunotags were based on AuNSs, a type of plasmonic NPs that combine the stability of gold with the exceptional Raman-enhancing properties of its hotspots. These AuNSs were functionalised with the Raman probes MBA or DTNB, well known for their high Raman cross-sections. Moreover, the approach to perform these functionalisation reactions in solution leads to high reproducibility of the SERS signal and hints at easier scalability, compared to conventional methods of surface chemistry. The capture platform was easily prepared from regenerated cellulose-based hydrogel platform, a renewable and transparent material with low background fluorescence. Capture antibodies were also bound by the same simple covalent approach as used on SERS immunotags, and here presented double biological activity as compared to physiosorbed antibodies. The presence of the sandwich complexes on the platform during a detection event was confirmed by the detection of globular features by AFM. SEM/EDS confirmed the association of these globular features with the presence of gold, further confirming their identity. For SERS data analysis, the robustness of the DCLS method was demonstrated, in situations of partially

overlapping key Raman bands derived from SERS immunotags and the RCH capture platform. In fact, application of the DCLS method to SERS data treatment revealed superior discrimination of Raman probes signals from the background, a serious disadvantage of the more commonly used peak integral method. Also, DCLS allowed a much better data fit in antigen concentrations in the 0.01 to 0.1 ng·mL^{-1} range. The DCLS method was also advantageously applied to a duplexing application of the SERS-immunosensor, as compared to peak integral method, and opens the way for multiplexing applications. The developed SERS-based immunoassay greatly improves the detection limits of traditional ELISA approaches, from mg to pg levels of detection, and its performance is better or comparable to other SERS-based immunosensors reported in the literature. Transparency of the capture platform opens the way to its integration in microfluidic devices, allowing measurements directly inside the microchannels. The reusability of the capture platform reduces implementation cost of the biosensor, thus increasing its commercial attractiveness, while it also represents an environmentally sustainable option. The capture platform can withstand at least seven cycles of regeneration, making it highly attractive for future POCT microfluidics applications. In conclusion, the approach to SERS immunoassay construction could successfully overcome the main challenges for application at POCT, including increasing reproducibility, sensitivity, and specificity, associated with an environmentally friendly and robust design. Also, the proposed design opens the way for multiplexing applications on a microfluidics POCT platform.

References for chapter 4

[1] Z. Liu et al. "Paper-Based Immunoassays". In: *Handbook of Immunoassay Technologies*. Ed. by S. K. Vashist and J. H. Luong. 1st ed. London: Elsevier, 2018. Chap. 8, pp. 183–201.

[2] L. Cao. "Immobilised enzymes: Science or art?" In: *Current Opinion in Chemical Biology* 9.2 (2005), pp. 217–226.

[3] C. Chang and L. Zhang. "Cellulose-based hydrogels: Present status and application prospects". In: *Carbohydrate Polymers* 84.1 (2011), pp. 40–53.

[4] X. Shen et al. "Hydrogels based on cellulose and chitin: Fabrication, properties, and applications". In: *Green Chemistry* 18.1 (2015), pp. 53–75.

[5] S. Chen et al. "Rapid and sensitive biomarker detection using molecular imprinting polymer hydrogel and surface-enhanced Raman scattering". In: *Royal Society Open Science* 5.1 (2018), pp. 171488–171497.

[6] J. Neng et al. "Sensitive and Selective Detection of New Red Colorant Based on Surface-Enhanced Raman Spectroscopy Using Molecularly Imprinted Hydrogels". In: *Applied Sciences* 9.13 (2019), pp. 2672–2684.

[7] H. J. Byrne et al. "Spectral pre and post processing for infrared and Raman spectroscopy of biological tissues and cells". In: *Chemical Society Reviews* 45.7 (2016), pp. 1865–1878.

[8] P. Ranjan, V. Thomas, and P. Kumar. "2D materials as a diagnostic platform for the detection and sensing of the SARS-CoV-2 virus: a bird's-eye view". In: *Journal of Materials Chemistry B* 9.23 (2021), pp. 4608–4619.

[9] C. Li et al. "A paper-based SERS assay for sensitive duplex cytokine detection towards the atherosclerosis-associated disease diagnosis". In: *Journal of Materials Chemistry B* 8.16 (2020), pp. 3582–3589.

[10] L.-K. Lin and L. A. Stanciu. "Bisphenol A detection using gold nanostars in a SERS improved lateral flow immunochromatographic assay". In: *Sensors and Actuators B: Chemical* 276.August (2018), pp. 222–229.

[11] Z. Cheng et al. "Simultaneous Detection of Dual Prostate Specific Antigens Using Surface-Enhanced Raman Scattering-Based Immunoassay for Accurate Diagnosis of Prostate Cancer". In: *ACS Nano* 11.5 (2017), pp. 4926–4933.

[12] G. Li et al. "A magnetic surface-enhanced Raman scattering platform for performing successive breast cancer exosome isolation and analysis". In: *Journal of Materials Chemistry B* 9.11 (2021), pp. 2709–2716.

[13] A. Kamińska et al. "Detection of Circulating Tumor Cells Using Membrane-Based SERS Platform: A New Diagnostic Approach for 'Liquid Biopsy'". In: *Nanomaterials* 9.3 (2019), pp. 366–381.

[14] S. Mabbott et al. "Detection of cardiovascular disease associated miR-29a using paper-based microfluidics and surface enhanced Raman scattering". In: *Analyst* 145.3 (2020), pp. 983–991.

[15] A. Kamińska et al. "SERS-based Immunoassay in a Microfluidic System for the Multiplexed Recognition of Interleukins from Blood Plasma: Towards Picogram Detection". In: *Scientific Reports* 7.1 (2017), pp. 10656–10667.

[16] L. Lin et al. "A bioorthogonal Raman reporter strategy for SERS detection of glycans on live cells". In: *Angewandte Chemie - International Edition* 52.28 (2013), pp. 7266–7271.

[17] Z. Wang et al. "SERS-Activated Platforms for Immunoassay: Probes, Encoding Methods, and Applications". In: *Chemical Reviews* 117.12 (2017), pp. 7910–7963.

[18] M. Arabi et al. "Label-free SERS detection of Raman-Inactive protein biomarkers by Raman reporter indicator: Toward ultrasensitivity and universality". In: *Biosensors and Bioelectronics* 174.September 2020 (2021), pp. 112825–112834.

[19] K. J. Land et al. "REASSURED diagnostics to inform disease control strategies, strengthen health systems and improve patient outcomes". In: *Nature Microbiology* 4.1 (2019), pp. 46–54.

[20] J. Langer et al. "Present and Future of Surface-Enhanced Raman Scattering". In: *ACS Nano* 14.1 (2020), pp. 28–117.

[21] M. A. S. Cavadas et al. "Unravelling Malaria Antigen Binding to Antibody-Gold Nanoparticle Conjugates". In: *Particle & Particle Systems Characterization* 33.12 (2016), pp. 906–915.

[22] S. Puertas et al. "Taking Advantage of Unspecific Interactions to Produce Highly Active Magnetic Nanoparticle-Antibody Conjugates". In: *ACS Nano* 5.6 (2011), pp. 4521–4528.

[23] K. Tripathi and J. D. Driskell. "Quantifying Bound and Active Antibodies Conjugated to Gold Nanoparticles: A Comprehensive and Robust Approach to Evaluate Immobilization Chemistry". In: *ACS Omega* 3.7 (2018), pp. 8253–8259.

[24] M. J. Oliveira et al. "Office paper decorated with silver nanostars - an alternative cost effective platform for trace analyte detection by SERS". In: *Scientific Reports* 7.1 (2017), pp. 2480–2494.

[25] H. Huang et al. "NMR Study on the Roles of Li + in the Cellulose Dissolution Process". In: *ACS Sustainable Chemistry & Engineering* 7.1 (2019), pp. 618–624.

[26] L. M. Fullwood et al. "Effect of substrate choice and tissue type on tissue preparation for spectral histopathology by Raman microspectroscopy". In: *The Analyst* 139.2 (2014), pp. 446–454.

[27] Z. Tan et al. "Improvement of surface-enhanced Raman scattering detection and imaging by multivariate curve resolution methods". In: *Journal of Applied Physics* 125.17 (2019), pp. 173101–173113.

[28] A. T. Vicente et al. "Multifunctional cellulose-paper for light harvesting and smart sensing applications". In: *Journal of Materials Chemistry C* 6.13 (2018), pp. 3143–3181.

[29] S. Arola et al. "Immobilization–Stabilization of Proteins on Nanofibrillated Cellulose Derivatives and Their Bioactive Film Formation". In: *Biomacromolecules* 13.3 (2012), pp. 594–603.

[30] S. Shin and J. Hyun. "Matrix-Assisted Three-Dimensional Printing of Cellulose Nanofibers for Paper Microfluidics". In: *ACS Applied Materials and Interfaces* 9.31 (2017), pp. 26438–26446.

[31] B. Ying et al. "NanoPADs and nanoFACEs: An optically transparent nanopaper-based device for biomedical applications". In: *Lab on a Chip* 20.18 (2020), pp. 322–333.

[32] C. D. L. de Albuquerque et al. "Digital Protocol for Chemical Analysis at Ultralow Concentrations by Surface-Enhanced Raman Scattering". In: *Analytical Chemistry* 90.2 (2018), pp. 1248–1254.

[33] M. E. Keating et al. "Multivariate statistical methodologies applied in biomedical Raman spectroscopy: assessing the validity of partial least squares regression using simulated model datasets". In: *The Analyst* 140.7 (2015), pp. 2482–2492.

[34] P. Smith et al. "Measurement of protein using bicinchoninic acid". In: *Analytical Biochemistry* 150.1 (1985), pp. 76–85.

[35] I. Cunha et al. "Reusable Cellulose-Based Hydrogel Sticker Film Applied as Gate Dielectric in Paper Electrolyte-Gated Transistors". In: *Advanced Functional Materials* 27.16 (2017), pp. 1606755–1606766.

[36] M. He et al. "Fast Contact of Solid–Liquid Interface Created High Strength Multi-Layered Cellulose Hydrogels with Controllable Size". In: *ACS Applied Materials & Interfaces* 6.3 (2014), pp. 1872–1878.

[37] Q. Yang et al. "Role of sodium zincate on cellulose dissolution in NaOH/urea aqueous solution at low temperature". In: *Carbohydrate Polymers* 83.3 (2011), pp. 1185–1191.

[38] A. Isogai and Y. Kato. "Preparation of polyuronic acid from cellulose by TEMPO-mediated oxidation". In: *Cellulose* 5.1 (1998), pp. 153–164.

[39] C. K. Dixit et al. "Multisubstrate-compatible ELISA procedures for rapid and high-sensitivity immunoassays". In: *Nature Protocols* 6.4 (2011), pp. 439–445.

[40] D. Wild, J. Rhys, and C. Sheehan, eds. *The Immunoassay Handbook*. 4th ed. Oxford, UK: Elsevier, 2013.

[41] Sigma-Aldrich. *Enzymatic Assay of Peroxidase (EC 1.11.1.7) with 2,2'-Azino-bis (3-Ethylbenzthiazoline-6-Sulfonic Acid) as a Substrate*. 2019. URL: https://www.sigmaaldrich.com/technical-documents/protocols/biology/enzymatic-assay-of-peroxidase-abts-as-substrate.html (visited on 07/29/2019).

[42] C. K. Bayne and R. Kramer. "Chemometric Techniques for Quantitative Analysis". In: *Technometrics* 41.2 (1999). Ed. by R. Kramer, p. 173.

[43] D. Sheskin. *Handbook of Parametric and Nonparametric Statistical Procedures*. Ed. by Chapman & Hall/CRC. 5th ed. Boca Raton, Florida: Taylor & Francis, 2011.

[44] S. S. Shapiro and M. B. Wilk. "An Analysis of Variance Test for Normality (Complete Samples)". In: *Biometrika* 52.3/4 (1965), pp. 591–610.

[45] B. L. Welch. "The Generalization of 'Student's' Problem when Several Different Population Variances are Involved". In: *Biometrika* 34.1/2 (1947), pp. 28–35.

[46] P. T. Munroe. "ANOVA (Analysis of Variance)". In: *The Blackwell Encyclopedia of Sociology*. Ed. by P. T. Munroe. 1th ed. Oxford, UK: John Wiley & Sons, Ltd, 2015. Chap. 15.

[47] J. W. Tukey. "The Philosophy of Multiple Comparisons". In: *Statistical Science* 6.1 (1991), pp. 100–116.

[48] F. E. Grubbs. "Sample Criteria for Testing Outlying Observations". In: *The Annals of Mathematical Statistics* 21.1 (1950), pp. 27–58.

[49] G. T. Hermanson. "Microparticles and Nanoparticles". In: *Bioconjugate Techniques*. Ed. by M. Preap. 3rd ed. London: Elsevier, 2013, pp. 549–587.

[50] C. Olsson and G. Westm. "Direct Dissolution of Cellulose: Background, Means and Applications". In: *Cellulose - Fundamental Aspects*. Ed. by T. G. V. D. Ven. 1st ed. London, UK: InTech, 2013. Chap. 6, pp. 1–378.

[51] J. Cai et al. "Dynamic Self-Assembly Induced Rapid Dissolution of Cellulose at Low Temperatures". In: *Macromolecules* 41.23 (2008), pp. 9345–9351.

[52] J. Cai and L. Zhang. "Rapid Dissolution of Cellulose in LiOH/Urea and NaOH/Urea Aqueous Solutions". In: *Macromolecular Bioscience* 5.6 (2005), pp. 539–548.

[53] J. Cai et al. "Hydrogen-Bond-Induced Inclusion Complex in Aqueous Cellulose/LiOH/Urea Solution at Low Temperature". In: *ChemPhysChem* 8.10 (2007), pp. 1572–1579.

[54] M. Egal, T. Budtova, and P. Navard. "The dissolution of microcrystalline cellulose in sodium hydroxide-urea aqueous solutions". In: *Cellulose* 15.3 (2008), pp. 361–370.

[55] A. Lue, L. Zhang, and D. Ruan. "Inclusion Complex Formation of Cellulose in NaOH–Thiourea Aqueous System at Low Temperature". In: *Macromolecular Chemistry and Physics* 208.21 (2007), pp. 2359–2366.

[56] J. Guo et al. "Preparation and application of microfluidic SERS substrate: Challenges and future perspectives". In: *Journal of Materials Science & Technology* 37 (2020), pp. 96–103.

[57] A. Isogai, T. Saito, and H. Fukuzumi. "TEMPO-oxidized cellulose nanofibers". In: *Nanoscale* 3.1 (2011), pp. 71–85.

[58] H. Orelma et al. "Surface Functionalized Nanofibrillar Cellulose (NFC) Film as a Platform for Immunoassays and Diagnostics". In: *Biointerphases* 7.1 (2012), p. 61.

[59] B. Voigtländer. *Atomic Force Microscopy Designs*. Ed. by P. Avouris et al. 2nd. Aachen, Germany: Springer Nature Switzerland AG, 2019, pp. 69–86.

[60] P. Ball. "Water is an active matrix of life for cell and molecular biology". In: *Proceedings of the National Academy of Sciences of the United States of America* 114.51 (2017), pp. 13327–13335.

[61] Y. Dong, L. Hou, and P. Wu. "Exploring the diffusion behavior of urea aqueous solution in the viscose film by ATR-FTIR spectroscopy". In: *Cellulose* 27.5 (2020), pp. 2403–2415.

[62] J. Łojewska et al. "Cellulose oxidative and hydrolytic degradation: In situ FTIR approach". In: *Polymer Degradation and Stability* 88.3 (2005), pp. 512–520.

[63] C. Bustamante and D. Keller. "Scanning Force Microscopy in Biology". In: *Physics Today* 48.12 (1995), pp. 32–38.

[64] K. Castro et al. "Assessment of the weathering effects on cellulose based materials through a multianalytical approach". In: *Nuclear Instruments and Methods in Physics Research, Section B: Beam Interactions with Materials and Atoms* 269.12 (2011), pp. 1401–1410.

[65] M. E. Keating, F. Bonnier, and H. J. Byrne. "Spectral cross-correlation as a supervised approach for the analysis of complex Raman datasets: the case of nanoparticles in biological cells". In: *The Analyst* 137.24 (2012), pp. 5792–5802.

[66] M. Nič et al., eds. *IUPAC Compendium of Chemical Terminology*. Research Triagle Park, NC: IUPAC, 2009.

[67] A. Kim et al. "A sensitive and reliable quantification method for Bisphenol A based on modified competitive ELISA method". In: *Chemosphere* 68.7 (2007), pp. 1204–1209.

[68] R. Frimpong et al. "Rapid vertical flow immunoassay on AuNP plasmonic paper for SERS-based point of need diagnostics". In: *Talanta* 223.P2 (2021), p. 121739.

[69] W. Lu et al. "Combination of an Artificial Intelligence Approach and Laser Tweezers Raman Spectroscopy for Microbial Identification". In: *Analytical Chemistry* 92.9 (2020), pp. 6288–6296.

[70] J. Huang et al. "Electrochemical sensor for bisphenol A detection based on molecularly imprinted polymers and gold nanoparticles". In: *Journal of Applied Electrochemistry* 41.11 (2011), pp. 1323–1328.

[71] L. Wu et al. "Tyrosinase nanocapsule based nano-biosensor for ultrasensitive and rapid detection of bisphenol A with excellent stability in different application scenarios". In: *Biosensors and Bioelectronics* 165.June (2020), pp. 112407–112414.

[72] I. Gomes et al. "Nanoimunoensaios para diagnóstico de malária". In: *Anais Instituto de Higiene e Medicina Tropical* 14 (2015), pp. 21–30.

[73] J. Li et al. "A universal strategy for the one-pot synthesis of SERS tags". In: *Nanoscale* 10.17 (2018), pp. 8292–8297.

[74] J. A. Goode, J. V. Rushworth, and P. A. Millner. "Biosensor Regeneration: A Review of Common Techniques and Outcomes". In: *Langmuir* 31.23 (2015), pp. 6267–6276.

[75] W. W. Yu and I. M. White. "Inkjet-printed paper-based SERS dipsticks and swabs for trace chemical detection". In: *Analyst* 138.4 (2013), pp. 1020–1025.

Chapter

5 Design, simulation, and fabrication of the microfluidics system for SERS analysis

Results and data presented in this chapter are under review to be published elsewhere: ***Maria João Oliveira****, Soraia Caetano, Ana Dalot, Filipe Sabino, Elvira Fortunato, Rodrigo Martins, Miguel Prudêncio, Hugh J. Byrne, Ricardo Franco, and Hugo Águas. Polystyrene-based microfluidic device for malaria detection by SERS analysis. Maria João Oliveira was responsible for the experimental work, except for contributions from PhD Soraia Caetano for the biological sample preparation, BSc Ana Dalot for the expression and purification of the malaria antigen, and MSc Tomás Calmeiro for atomic force microscopy measurements. Maria João was also responsible for data analysis and writing the first version of article.*

The two previous chapters were focused on the development of SERS immunotags and their application in a proof-of-concept assay. To make this SERS-based immunoassay suitable for point-of-care testing (POCT) application, a device is needed that offers automatisation and portability. Thus, this chapter is focused on a microfluidic system integrating in a single unit, both the capture platform and the SERS immunotags developed in the previous chapters.

As a low-cost and promising alternative to photolithography, directly pre-patterned polystyrene (PS) sheets were stacked to construct a complex 3D microfluidic chip. This approach is based on "Shrinky-Dinks" PS sheets, a children's toy, usually used to draw pictures that can then be shrunk to a small fraction of its original size[1, 2]. Chen *et al.* used these "Shrinky-Dinks" PS sheets that shrink upon heating to generate thinner and deeper micro-channels compared to its original size[1]. This fabrication process allowed the current disadvantages of polydimethylsiloxane (PDMS)-based prototyping, in terms of cost, adaptability, and complexity, to be overcome [3]. This multilayer 3D chip was characterised and adapted to the SERS-based immunoassay. The design of the microchip was based on the simulations performed *a priori*. These simulations allowed assessment of the process of targeted molecules transport to the capture surface of the biosensor

and evaluation of its performance. The functionality of the PS-based microfluidic chip was verified by applying enzymatic and SERS analysis using a proof-of-concept antigen-antibody pair, namely, the horseradish peroxidase (HRP)/anti-HRP antibody system.

5.1 Introduction

One of the main challenges in the healthcare industry is to provide access to health monitoring and assessment in regions with limited or no healthcare facilities either due to geographic or economic constrains [4–6]. Implementation of POCT systems can not only reduce the healthcare costs and improve efficiency by decentralisation of healthcare centres but is critical in the provision of diagnostic and monitoring in countries with large populations or rural areas [4–6]. This need becomes even more pivotal in epidemic situations.

Microfluidics has become essential in the development of POCT systems [4–6]. For a drop of blood, microfluidics can combine sample collection, pre-treatment such as on-chip filtration, reagent mixing, signal detection and readout into a single device, in other words, integrate all molecular diagnostic laboratory methods in one chip, hence the term "lab-on-a-chip" [7, 8].

This is all possible due to their downscaling properties whereby handling small volumes of liquids to perform biochemical reactions at micrometre length scale can be precisely controlled and predictable [9]. This increases the reaction rates, making them shorter while minimising the consumption of expensive reagents when compared to macroscopic systems, thus decreasing diagnostic test cost [10].

Since their invention, microfluidics systems have attracted attention in a variety of biodiagnostic methods including polymerase chain reaction (PCR) [11], loop-mediated isothermal amplification (LAMP) [12], chemiluminescence-based assays [13], and immunosensors [7, 14–17] platforms. Microfluidic immunosensors can be much more efficient and rapid than conventional immunoassay methods, due to the increase of surface-to-volume ratio that maximises mass transport in immunoreactions which, in turn leads to a more rapid analysis [7, 18]. Moreover, the potential for a parallel operation, replicate experimental conditions, and/or integration with other miniaturised components, provide a more reliable diagnostic [19]. Together with the aforementioned advantages, microfluidic immunosensors can achieve the POCT goal identified in the WHO guidelines for biosensors in low-resource settings (see section 1.1 in chapter 1).

The first-generation chips were made from silicon and glass in a clean room enviroment, based on well-established microfabrication techniques that included photolithography and wet-etching methods [20, 21]. The second generation focused on alternative, polymer based materials. Polymers such as poly(methyl methacrylate) (PMMA) [22], cyclic olefin copolymer [23], PS [24–26] and PDMS [16, 27] provide a simpler fabrication process (moulding, embossing, and printing) at a lower cost. PDMS, a silicone-based elastomer, is by far the most commonly used in microfluidic immunoassays because it

is flexible, optically transparent, biocompatible, and has low-autofluorescence properties [21]. Also, the fabrication process usually employed for PDMS-based microfluidics chips is by replica moulding [27–29]. Using a photoresist (usually SU-8) film spin-coated on a silicon wafer, the photoresist is subsequently patterned by photolithography and then used as a mould for PDMS [27–29]. Although a straightforward process, it is time-consuming, generates a significant amount of chemical waste, and is still not able to respond to the great demand for the output of chips in large-scale production. Thermoplastic elastomers on the contrary, can be manipulated by the already full developed industrial polymer manufacturing technologies which simplifies and reduces the cost of mass production[30–32]. Additionally, PDMS adsorbs and absorbs biomolecules, later leaching them into solution in contact and allow liquid evaporation [33]. These disadvantages hinder the use of PDMS for biodetection applications.

Recently, thermoplastics have become an attractive choice to surpass the current limitation of PDMS. Their inherent robustness to mechanical deformation and chemical resistance makes these materials suitable for biochemical microfluidic applications [11, 24, 26, 34, 35]. Microfluidic devices made of these materials can be produced by high-volume fabrication methods such as microinjection moulding [36], micro-milling [37], hot embossing [38], 3D printing [39–41], and laser ablation [25, 42, 43].

Laser machining has emerged an alternative method to fabricate microchannels without requiring master moulds [25, 42, 43]. UV lasers were the firsts used, and their laser ablation mechanism resulted in a combination of photochemical and photothermal process, in which, some chemical bonds of the material are broken directly from photon absorption while others are thermally broken by the released heat from the excited molecules that did not break photochemically [42, 44]. Using carbon dioxide laser sources, emitting IR radiation at a wavelength of 10.6 µm, the ablation occurs solely through photothermal process [22, 42].

Carbon dioxide laser systems have been widely used for rapid and low-cost per unit production of microfluidic systems in a variety of materials including paper [45], polycarbonate [34], PMMA [46], cyclic olefin copolymer [13, 47], PS [2, 22, 25, 48, 49], among others. PS, in particular, poses several advantages as it is already a standard material used in cell-culture plates and enzyme-linked immunosorbent assay (ELISA) applications due to its biocompatibility [50]. PS is optically transparent, inert, rigid, and has a surface that can be easily functionalised [25]. In 2008, Chen *et al.* [48] used pre-stressed transparent PS sheets that retract upon heating. As a result, the pre-etched microfluidic channels shrink isotropically, becoming thinner and deeper (*i.e.* the PS sheet becomes thicker). This process eliminates the need of masks, templates, and the typical microfabrication facilities and consumables that usually result in large amounts of waste. Thus, PS-based microfluidic devices significantly reduce prototyping time and cost. Although promising, there is a shortage of biosensors using this approach [26].

Microfluidic detection systems allow to automatise several protocols and accelerate

the reactions needed for a rapid and reliable analysis[19]. Nevertheless, a sensitive transducer system is required. SERS can provide strong Raman signatures if combined with metallic nanostructures. The advantage of combining the high sensitivity and specificity of SERS with microfluidics has been demonstrated by various examples in the literature[51–55]. Among the different approaches, SERS-based immunoassays can indirectly identify multiple target molecules through a labelled optical detection[56]. The labels consist in combining metallic nanostructures with Raman reporters and a biorecognition element, to fabricate a "SERS tag"[57, 58].

Hence, as presented in previous chapters, a highly sensitive and robust SERS-based sandwich immunoassay was developed using SERS immunotags and a TEMPO-oxidised (TO)-regenerated cellulose hydrogel (RCH) platform with immobilised antibodies. Moreover, direct classical least squares (DCLS) method provide a reliable analysis for the immunoassay that could be applicable in a biosensor for POCT settings. Presently, the challenge to demonstrate this SERS-based sandwich immunoassay appropriate for POCT sites is to combine it with microfluidics. Thus, the present chapter is dedicated to integrating the SERS-based sandwich immunoassay inside a microfluidic device.

This work demonstrates for the first time a novel microfluidic device for SERS-based immunoassay entirely based on PS sheets. The design and fabrication steps required for the microfluidic device fabrication are fully described as well as its characterisation while avoiding the expensive and non-scalable lithography resources. Finally, a proof-of-concept is performed to prove its functionality and future applicability towards an analyte of interest. Based on shrinkable PS sheets, and combined with the previous work, it allows a fully transparent, inexpensive, and fast production device with a remarkable design flexibility to meet the required needs in POCT sites.

5.2 Materials and methods

5.2.1 Materials

The materials used in this chapter have already been described in the chapter 4 (Proof-of-concept SERS assay) with the exception of: transparent PS sheets purchased from Vaessen Creative shrink sheets, China; Tygon Tubing Coil - 1/16 OD X 0.02"(500 µm) and Blunt-end Luer Lock Syringe Needles from Darwin Microfluidics, France; and Hamilton® GASTIGHT® syringe, 1700 series, PTFE luer lock 1750TLL from Sigma-Aldrich, St. Louis, USA. All chemicals and reagents were of the highest purity available and ultrapure water (H_2O, 18.2 MΩ·cm at 25ºC, *Milli-Q*®) was used for the preparation of all solutions, unless stated otherwise.

5.2.2 PS chip design

COMSOL Multiphysics v5.6 (Comsol Inc., Burlington, MA), incorporating the modules fluid flow and chemical species transport was used to simulate the transport of the

diluted species within the flowing solution across the microfluidic channel and the binding kinetics occurring over the surface of the capture platform.

5.2.2.1 Balance equations

Figure 5.1 schematically illustrates a typical configuration of a microchannel used in immunoassays. The first step consisted in using a 2D model since the concentration variation across the width of the microchannel can be neglected (due to negligible side wall effects on reaction surface), which was compared to a 3D model (as shown in Figure 5.1). The proposed model is based upon the last chapter 4, *i.e.*, binding of the antigen in the bulk liquid phase to the capture platform (a surface-immobilised antibody). In this first approach, the SERS immunotags will be added in excess concentration related to the detection analyte to ensure a fast binding. Therefore, the detection step is not a limiting factor and can be excluded from the model.

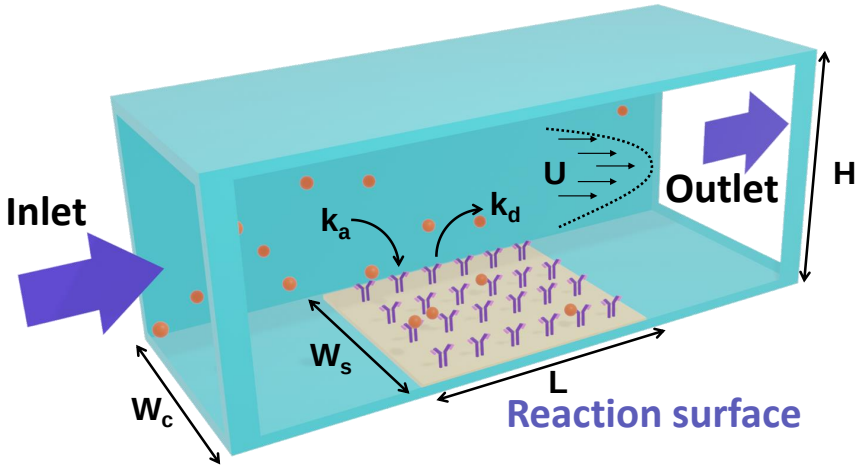

Figure 5.1: Schematic of a heterogeneous immunoassay in a microfluidic channel (not in scale). The analyte sample containing antigen (orange spheres) enters the microfluidic channel of W_c width and H height through the inlet and flows through the channel at a plug-like velocity (U). The antibodies are immobilised in a specified area of the bottom surface (reaction surface of W_s width and L length). When the analyte reaches the reaction surface, the antibodies retain the analyte through antigen-antibody binding with adsorption (k_a) and desorption (k_d) rates.

To perform the simulation of the specific recognition of antigens by the immobilised antibodies that leads to the generation of the SERS signal, three physical processes can be considered:

- The mass transport of the fluid flow inside the microfluidic channel.
- The diffusion of chemical species (in this case the antigen) to the active site (5.1):

$$A_{bulk} \rightleftharpoons A_{surface} \tag{5.1}$$

- The surface reaction at a solid-liquid interface, *i.e.*, the recognition of the analyte onto the functionalised surface (5.2):

$$\mathrm{A_{surface}} + \mathrm{B} \underset{\mathrm{k_b}}{\overset{\mathrm{k_a}}{\rightleftharpoons}} \mathrm{AB} \tag{5.2}$$

where A_{bulk} is the concentration of the antigen in the bulk, $A_{surface}$ is the antigen concentration at the reaction surface, B is the antibodies concentration, AB is the antigen-antibody complex concentration, k_a is the adsorption rate and k_d is the desorption rate.

Fluid flow

The simulation was made for a microfluidic channel, meaning a low Reynolds number and thus the turbulence is absent in this microfluidic system and the flow is laminar. The flow velocity can be described by the Navier-Stokes equations - the fluid is assumed to be Newtonian isothermal and incompressible. A steady flow can be assumed because the adsorption time scale is larger than the flow field time scale (*i.e.* the flow field reaches a steady state within a few seconds while the surface where the reaction occurs reaches saturation in few hundreds of seconds). In addition, in real-life experiments the initiation of SERS measurements will occur at least a few seconds after the antigen and the SERS tags are allowed to bind [59] (equation 5.3):

$$\frac{\partial \rho}{\partial t} + \rho \nabla . \overrightarrow{U} = 0 \tag{5.3}$$

$$\rho \left[\frac{\partial \overrightarrow{U}}{\partial t} + \overrightarrow{U} . \nabla \overrightarrow{U} \right] = -\nabla P + \overrightarrow{F} + \eta \nabla \overrightarrow{U}$$

where t (s) is time, U ($\mathrm{m \cdot s^{-1}}$) the velocity; P (Pa) is the pressure; F ($(\mathrm{Kg \cdot m}) \cdot \mathrm{s^{-2}}$) designs the body force; ρ ($\mathrm{Kg \cdot m^{-3}}$) represents the density and η ($\mathrm{Kg \cdot m^{-1} \cdot s^{-1}}$) indicates the dynamic viscosity. The fluid properties (density and dynamic viscosity) are assumed to be constant. The concentration of biological species in this case is significantly low, so any effect on density or viscosity of the carrier fluid is neglected.

Transport of diluted species

The antigen solution is driven into the microchannel containing a sensitive surface from the left inlet with a concentration of A_0, due to diffusion and convection as shown in Figure 5.1. The spatial and temporal variations from the transport of the antigen inside the microfluidic channel can be described by Fick's second law (equation 5.4):

$$\frac{\partial A}{\partial t} + u \frac{\partial A}{\partial x} + v \frac{\partial A}{\partial y} + w \frac{\partial A}{\partial z} = D \left(\frac{\partial^2 A}{\partial x^2} + \frac{\partial^2 A}{\partial y^2} + \frac{\partial^2 A}{\partial z^2} \right) + G \tag{5.4}$$

$$\overrightarrow{u} . \nabla A = D \nabla^2 A$$

where D is the diffusion coefficient, u, v, w ($m \cdot s^{-1}$) represent the velocity components in x, y, z directions, A is the concentration of antigen in bulk and G denotes the reaction rate. Here G equals to zero because no reactions take place in the fluid bulk but only at the sensor surface.

Surface reaction

The recognition event of an antigen in buffer solution by the antibody bound to the sensing area can be described by the first order time-dependent Langmuir equation. This model is frequently used to study the dynamics of molecular reactions in biodevices known as heterogeneous biosensors [60–62]. Including the surface diffusion, the mass balance for antigen-antibody formation as function of time is expressed as follow (equation 5.5):

$$\frac{\partial AB}{\partial t} = D_{AB}\nabla^2 AB + k_a A\,(B_0 - AB) - k_d AB \tag{5.5}$$

where B_0 is the unit thickness concentration (surface concentration) of the ligand; AB is the unit thickness concentration (surface concentration) of the analyte-ligand complex. The targeted antigens are constantly trapped by the antibodies ($k_a A\,(B_0 - AB)$) and dissociate from the same antibodies at a smaller rate ($k_d AB$). Ignoring the spatial diffusion term $D_{AB}\nabla^2 AB$ in equation 5.5 (because the convective and diffusive processes transport antigen molecules more quickly than reactions can bind them), the equilibrium AB complex concentration can be expressed (equation 5.6):

$$AB_{eq} = \frac{k_a AB_0}{k_d + k_a A} \tag{5.6}$$

where $\frac{k_a}{k_d} = K$ represents the affinity constant. The response of a biosensor is proportional to the amount of the complex AB formed on the sensing region. Thus, following the behaviour of the complex formation rate $AB(t)$ allows us to maximise the sensor response as function of the fabrication parameters.

5.2.2.2 Boundary and initial conditions

The boundary conditions for the Navier-Stokes equations can be defined as follows:

1. At the inlet of the microchannel, the fluid flows in the lengthwise direction (x), with a uniform velocity.

2. The boundary condition specifies the velocity components at the upper and lower solid boundaries as zero (no slip and no penetration):

   2.1 Upper wall: $u\,(x,h,z) = v\,(x,h,z) = 0$

   2.2 Lower wall: $u\,(x,0,z) = v\,(x,0,z) = 0$

3. At the outflow boundary, pressure is set to zero and allows the mass flow to exit through the outlet.

The boundary conditions used for the convection-diffusion equation were:

1. Initially, the antigen concentration is equal to zero $A = 0$.
2. At the inlet $A = A_0$, which consists of a uniform concentration.
3. At the outlet, the profile of the analyte concentration is assumed to be fully established, thus $\overrightarrow{n}(D\nabla A) = 0$.
4. The upper wall and the lower wall remain impermeable and do not interact with the analyte.
5. At the reaction surface, the mass flow of the analyte is affected by the kinetics of the reaction. As a result, a boundary condition must define the coupling between the concentration distribution in the bulk liquid and the concentration distribution at the surface (equation 5.7):

$$\overrightarrow{n}\left(-D\nabla A + A\overrightarrow{u}\right) = k_a A(B - AB) - k_d AB \tag{5.7}$$

   where $\overrightarrow{n}$ is the unit normal vector to the surface.
6. The initial concentration of the complex is zero $AB = 0$.

5.2.3 PS chip fabrication

The fabrication of the PS chip begins with the patterning of the transparent PS sheets (Vaessen Creative shrink sheets, China) by CO_2 laser ablation (VLS 3.50, 50 W, Universal Laser Systems, Scottsdale, AZ, USA) with a wavelength of 10.6 µm, a focal length of 50.8 mm, a beam diameter of 0.127 mm, and maximum power output of 50 W. To provide the smoothest channels, the frequency was set to the maximum, 1000 pulses per inch [25, 44]. Note that this pulses per inch parameter is the number of pulses that fall per inch on the surface during laser beam movement. This repetition rate was used through all the optimisation experiments regarding power and speed. Adobe Illustrator (Adobe systems software, Ireland) was used to design the patterns on the PS sheets. This procedure is represented in Figure 5.4. The patterned PS sheets were cleaned by ultrasonic cleaning machine with ethanol for 10 min, followed by 10 min in deionised water. This allows to decrease the influence of other impurities on the hot bonding of plates. The sheets were then stacked together with the immobilisation surface, the TO-RCH, and proceeded to thermal bonding.

Thermal bonding was achieved by thermal pressing at 110°C for 20 min. The bottom and upper sides of the device in contact with the hot side of the press were changed every 5 min to maintain both sides in contact with the hot side. The microfluidic chip fabrication process was completed by shrinking the PS bound sheets in a furnace (Nabertherm

l3/11/B170, Nabertherm GmbH, Lilienthal, Germany) at 155°C for 5 min. The final chip was washed with ultrapure water and stored in phosphate-buffered saline with Tween 20 (PBS-T) at 4°C until further use.

5.2.4 SERS-based immunoassay inside the microfluidic device

The SERS-based immunoassay using the TO-RCH was performed as previously described in the previous chapters. This includes the procedures executed in the preparation of gold nanostars, SERS immunotags, and regenerated cellulose hydrogel production. Detailed information can be found in sections 3.2.2.2 and 4.2.2 of chapters 3 and 4, respectively.

Polyethylene tubes and syringes were washed with ethanol, and, simultaneously with the chip, were pre-blocked with PBS-T to avoid non-specific adsorption of protein in subsequent experiments. To start the antibody immobilisation, MES buffer at 10 mM pH 6.5 was inserted in the device at 0.5 $\mu L \cdot min^{-1}$ for 1 h at room temperature through pumps (Legato 210P and Legato 210, KD Scientific). Meanwhile, to withdraw the reacted liquid, a syringe was connected to the outlet. The antibody immobilisation reaction started with the insertion of 25 µL 1-ethyl-3-(3-(dimethylamino)propyl)carbodiimide (EDC) and N-hydroxysulfosuccinimide (SNHS) at 20.86 mM and 50.66 mM, respectively, inside the device at 0.5 $\mu L \cdot min^{-1}$ for 15 min, followed by the 25 µL of antibody at 3.5 $\mu g \cdot mL^{-1}$ in 2-ethanesulfonic acid (MES) buffer at 10 mM pH 6.5. The chip was left incubating overnight at 4°C. The crosslinking reaction was stopped by washing three times the TO-RCH with 20 mM PBS buffer at pH 7.4 to remove electrostatically bound antibodies. A volume of 25 µL of skim milk as blocking agent at 0.5% (w/v) with Tween 20 at 0.05% (w/v) was added and incubated for 30 min at 25°C. The sequential insertion of the reagents is represented in Figure 5.2.

Afterwards, 25 µL of the sample with the antigen were incubated for 10 min at 25°C. Between each step, the TO-RCH was washed with 20 mM PBS buffer at pH 7.4 three times, after which the washing solution was removed completely. The SERS-based sandwich immunoassay was finalised by incubation of 25 µL at 1 nM of SERS immunotags for 10 min at 25°C and washing with buffer three times. The antibody immobilisation and blocking were performed in the perpendicular direction to the detection zone while the insertion of the antigen and SERS immunotags were done in the parallel direction of the detection zone.

5.2.5 Horseradish peroxidase enzymatic assay

To determine the viability of the immobilised antibodies on the capture platform, inside and outside the microfluidic chip, the capacity of anti-HRP antibodies to bind HRP antigens was tested via a horseradish HRP enzymatic activity assay. Detection of HRP enzymatic activity was based on the Sigma-Aldrich protocol [63]. Measurements were carried out at 25°C and pH = 5, Abs_{405} nm and a light pathlength = 1 cm. A 0.001 M

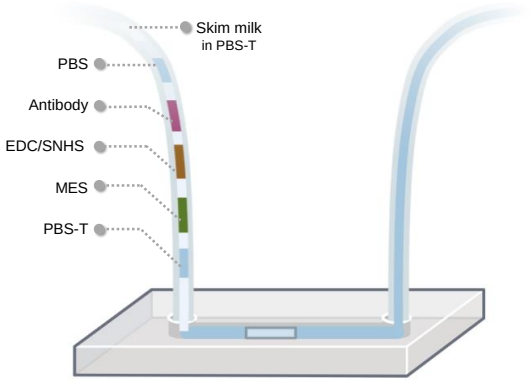

Figure 5.2: Sequential insertion of the reagents into the microfluidic device. The polyethylene tube is loaded with reagents, with each kind of fluid separated by air. They sequentially pass the detection chamber which is functionalised with the antibody.

potassium phosphate buffer (pH = 5.0) was prepared as a reference sample. The oxidation of a coloured substrate, ABTS (Roche, France) by the enzyme HRP in the presence of hydrogen peroxide, was followed by measuring the absorbance at 405 nm.

5.2.6 Optical spectroscopies characterisation

The absorbance at 405 nm for the enzymatic assays performed on the TO-RCH off- and on-chip was measured in a multifunctional microplate reader TECAN SPARK 10M (Tecan Trading AG, Switzerland). The optical response of the PS was measured with a double beam UV-VIS-NIR spectrometer (Lambda 950, PerkinElmer) equipped with an integrating sphere, in the wavelength range of 250–1100 nm.

5.2.7 Thermal material characterisation

Thermal material characterisation of PS was realised using thermogravimetric analysis (TGA) and differential scanning calorimetry (DSC) at nitrogen and air environments. TGA-DSC analysis were carried out in a simultaneous thermal analyser (TGA-DSC—STA 449 F3 Jupiter) from Netzsch. The samples (10 mg of PS) were load into a closed aluminium crucible and heated from room temperature to 700°C at 10°C·min^{-1} rate.

5.2.8 Morphological characterisation

Scanning electron microscopy (SEM) observations of the microfluidic chip were carried out in a HitachiTM 3030Plus tabletop workstation (Hitachi High-Tech Europe GmbH, Krefeld, Germany). Atomic force microscopy (AFM) analysis used an Asylum Research MFP-3D Standalone AFM system (Oxford Instruments). AFM measurements were performed in the AC mode in air. Silicon AFM probes (Olympus AC240TS, Olympus Corporation, Japan; k =2 N·m^{-1}, f_0 = 70 kHz) were used for AFM topographs. Static water contact angle measurements were performed with DataPhysics OCA 15 Plus, using 2 µL droplets of deionised water. The side view of the droplet was acquired by the system

and the contact angle analysis was subsequently performed using the Laplace–Young approximation model.

5.2.9 Raman and SERS measurements

Raman measurements were performed in a Renishaw inVia Qontor micro-Raman spectrometer equipped with an air-cooled charge-coupled-device (CCD) as detector and a He–Ne laser delivering at 32 mW of 632.81 nm laser radiation. The final immunoassay inside the microfluidic chip was performed on a microscope slide as a support and the laser beam was focused with a 5× (n.a. 0.12) Leica objective lens (N Plan EPI). An integration time of 10 scans of 20 s each was used for all SERS immunotags measurements. The intensity of the incident laser was reduced 3.2 mW at the sample. Triplicates were taken of all spectra per sample. Between different Raman sessions, the spectrometer was calibrated using the Raman line at 520.7 cm^{-1} of an internal Si wafer. All SERS spectra were recorded at room temperature. All raw data were collected digitally with Wire 5.0 software. Noise reduction, available on the software, was used to estimate and remove the noise through principal components analysis (PCA). Baseline correction using a polynomial fitting (11^{th} order) was then performed, taking care to ensure minimal alteration of raw data.

5.2.10 Statistical analysis

For enzymatic assays and SERS-activity assays, results were presented as mean ± standard-deviation from at least three independent experiments run in triplicates. Normality of the data distribution was assessed firstly by the Kolmogorov-Smirnov [64] and then by Shapiro-Wilk [65] test for increased statistical power. The antibody immobilisation efficiency and antigen detection in microfluidic assays were statistically compared using two-sample Student t-test, acquiring the p-value accordingly with Welch correction [66]. To perform a statistical group comparison tests, one-way analysis of variance (ANOVA) [67] followed by the Tukey's multiple comparison test were applied [68]. Outliers were identified by Grubbs test [69]. Significance was considered when $p - values \leq 0.05$.

5.3 Results and Discussion

5.3.1 SERS-based immunoassay microfluidic chip design

Figure 5.3 illustrates the design of the proposed microfluidic device integrated with TO-RCH for highly sensitive immunoassays. Two different set of channels are depicted: (i) channels that only serve for antibody immobilisation, and (ii) channels that lead the sample and SERS immunotags towards the detection chamber. Each detection chamber has an TO-RCH entrapped, suitable for the antibody immobilisation and subsequent

SERS-based sandwich immunoassay. The operating mode of the microfluidic device is similar to the lateral flow immunoassays with two detection chambers as opposed having two lines[70, 71]. Each detection chamber has a TO-RCH entrapped whereby the first detection chamber is functionalised with the antibody specific for the analyte of interest and the second chamber is functionalised with an antibody against immunoglobin (IgG), allowing to bind antibodies form the SERS immunotags and acts as a control for the SERS immunoassay.

The assays parallelisation into one single working unit means that the detection chambers should be spatially well defined to clearly distinguishing them. Thus, the functionalisation of the detection chamber *i.e.*, the region with the antibodies immobilised, should ensure that no possible cross-contamination between different antibodies occurs. Having different channels for the antibody immobilisation assures that distinct antibodies can be used in each detection chamber and that no reaction occurs outside these areas. Upon antibody immobilisation on the detection chambers, the channels and chambers are filled with buffer and the sample is introduced from the inlet and pumped through the channel to the detection chamber, where the antibody is covalently conjugated onto the TO-RCH. The target antigen in the sample binds to the capture antibody on the surface. The injection of the SERS tags concludes the sandwich type immunoassay. The microfluidic chip is placed in the Raman microscope for SERS analysis of the detection chambers.

The device was designed in a 3D multilayered system (Figure 5.4) that can be easily adjusted for other applications. In this design, the PS device is composed by three staked layers. The top layer was patterned with only the inlets and outlets. The middle layer is where the immunoassay will be situated so is patterned with the channels, detection chambers and inlets and outlets. Finally, to seal the middle layer, a flat non-patterned PS sheet is placed as bottom layer. Between the middle and bottom layer, a TO-RCH membrane is placed to provide the surface for the SERS-based immunoassay. The fabrication procedure used throughout this work and its comparison with the conventional PDMS microfluidic chip fabrication are represented in Figure 5.4.

As indicated in Figure 5.1 and Figure 5.3, the performance of the biosensor depends on the transport of target molecules to the capture surface, as well as the chemical reaction itself. The free target molecules diffuse randomly within the solution and are convected along the following solution inside the microfluidic channel. Upon reaching the detection chamber, they may bind to the adjacent capture surface (where the antibodies are immobilised). Then, some of the bound target molecules may unbind and re-enter the flowing solution.

It is possible to identify multiple effects that compete for dominance even in this simplified view of biosensor functioning. A simulation was performed to indicate the time-scale in which the SERS-based immunoassay microfluidic chip operates and elucidate the parameters that most influence the biosensor's performance. Three physical processes were considered to perform the simulation of the specific recognition of antigens by the immobilised antibodies that lead to the generation of the SERS signal [60–

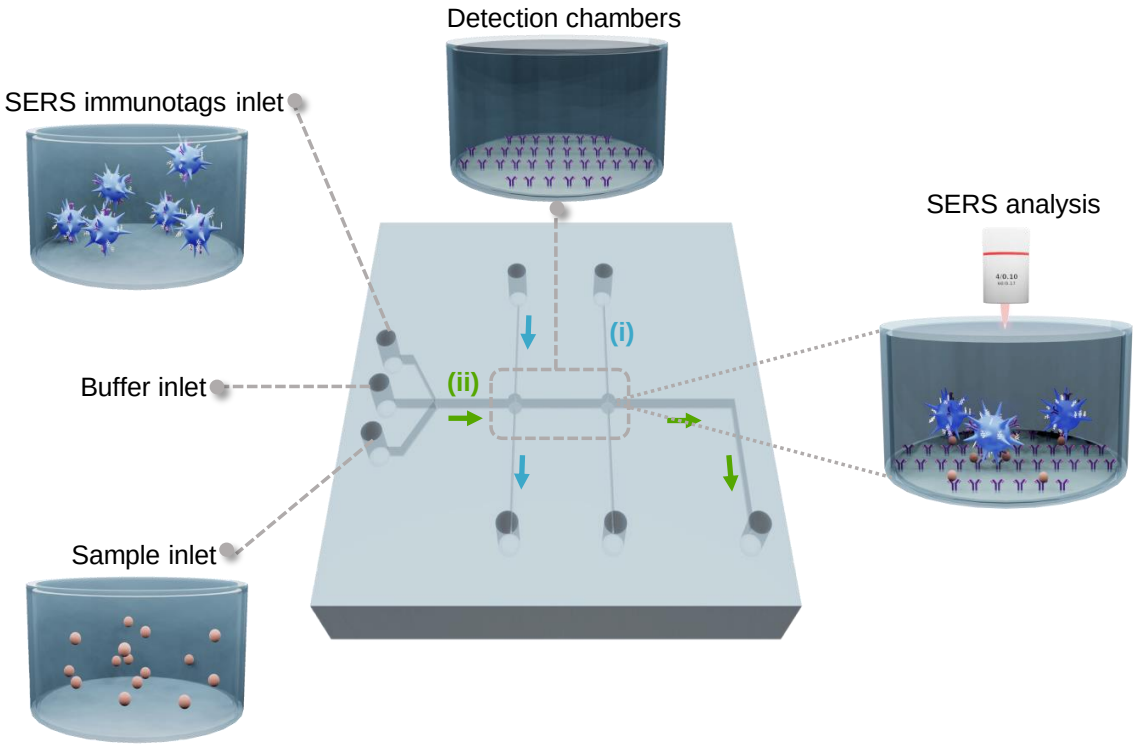

Figure 5.3: Conceptual illustration of the flow-through microfluidic device integrated with TO-RCH for the SERS-based immunoassay. The detection chambers with TO-RCH membranes are functionalised with antibodies to function as capture platforms - (i) and blue arrows indicate the flow direction. The sample containing target biomarkers is introduced through the sample inlet and captured by the antibodies in the detection chambers. The SERS immunotags flow through the detection chamber to form the sandwich complex - (ii) and green arrows indicate the flow direction. The SERS signal from the complex is measured and analysed through a confocal Raman microscope. The presence of two detection chambers allows to functionalise the capture platform with different antibodies, for instance, the first one with the test antibody and the second with an antibody to serve as a control for the assay. The flow rate and total reaction time are defined by the capillary pumps. The area of the microfluidic chip is 3×3 cm^2, a channel of 200 µm and both detection chambers have 500 µm of radius.

62, 72]: (i) the convection transport of the fluid flow inside the microfluidic channel; (ii) the diffusion of the analyte to the active site; (iii) the surface reaction at a solid-liquid interface, *i.e.* the recognition of the analyte onto the functionalised surface.

The finite elements method was used to solve the equations that translate the described physical processes. This method allows solution of partial differential equations by discretising the space into smaller and simpler parts – finite elements [60, 73–75]. As a result, a mesh of the object is constructed and is resolved using the damped Newton method. Two- and three-dimensional (2D and 3D) configurations were studied (Figure 5.5). The 2D geometry consists of the middle plane of the 3D geometry, *i.e.*, the channel has 8 mm of length, 1 mm of width and, at the middle position of the channel, a surface reaction chamber was inserted with 500 µm of diameter. The mesh herein was composed of triangular and tetrahedral elements for 2D and 3D configurations respectively, with a mesh refinement in the vicinities of the reaction surface (Figure 5.5a and d).

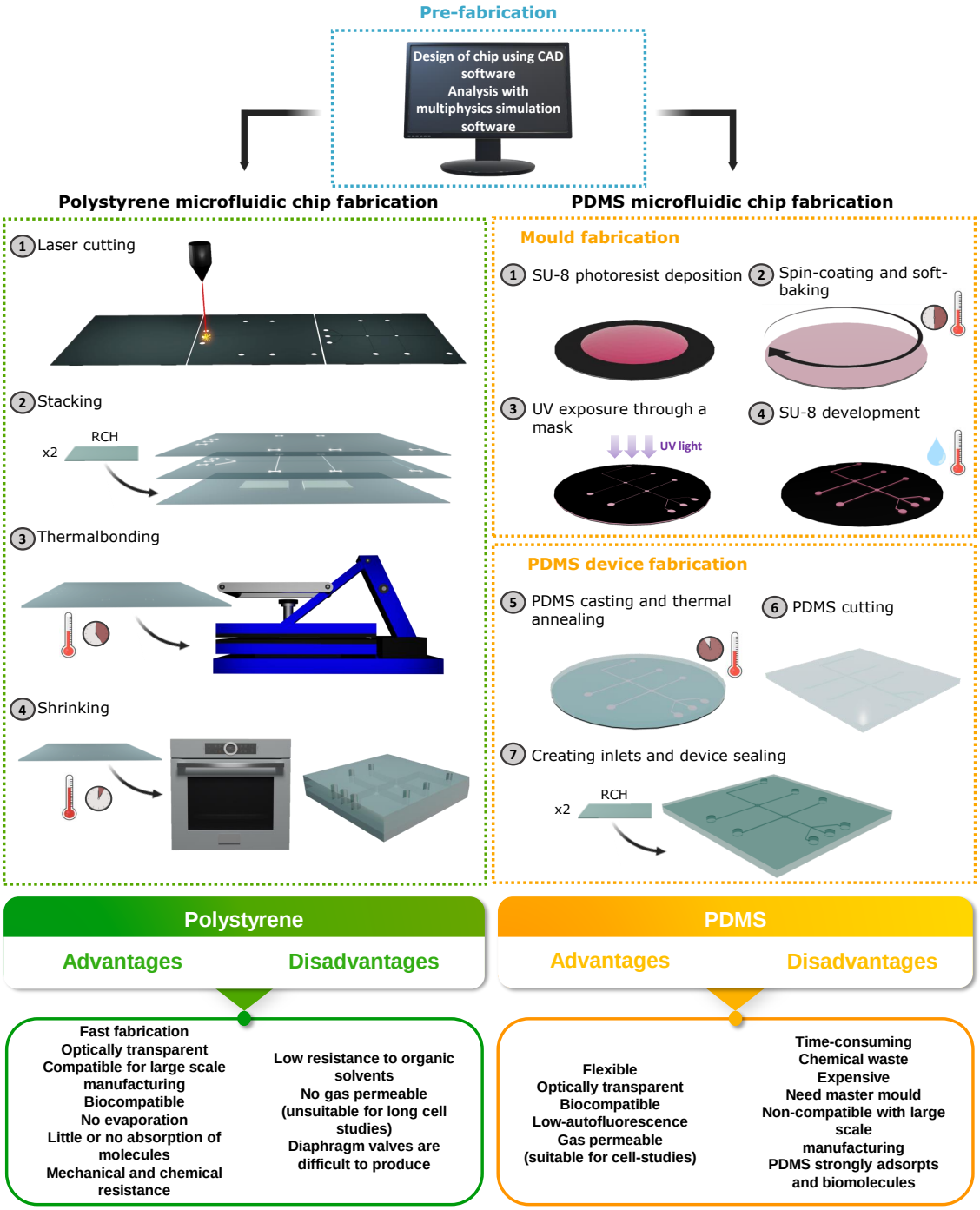

Figure 5.4: Schematic illustrations of the fabrication process using PS or PDMS as the material of the chip. The pre-fabrication step is common to both fabrication processes. A chip design is drawn in computer-aided design (CAD in the image) software and performance analyses can be performed in multiphysics simulation software. Left: PS microfluidic chip fabrication process. (1) Laser cutting and engraving of PS substrates; (2) Stacking of the layers to form the 3D multilayer device; (3) Thermal treatment with pressure to bond the three layers of the chip; (4) Shrinking the device in an oven. Right: (1) SU-8 photoresist application to Si wafer; (2) Spin-coating and soft baking to evaporate the solvent of the SU-8 photoresist; (3) Mask alignment and exposure to UV light; (4) SU-8 development, baking, and rinsing; (5) PDMS casting and thermal annealing; (6) PDMS chip cut and peeling-off; (7) Create inlets and sealing of the chip.

The velocity field was calculated over a specific position of the microchannel for several mesh grids and the parabolic velocity profile from the unidirectional pressure-driven flow through can be seen in all the tested meshes (Figure 5.5b and c) [72]. For the 2D configuration, using a total number of 90808 elements gives a more defined profile than using 14328 and 48288 elements, and a similar profile as using 120389 and 179462 elements without requiring too much computational power (Figure 5.5c). Similarly, the mesh chosen for the 3D configuration was with a total number of 716568 elements.

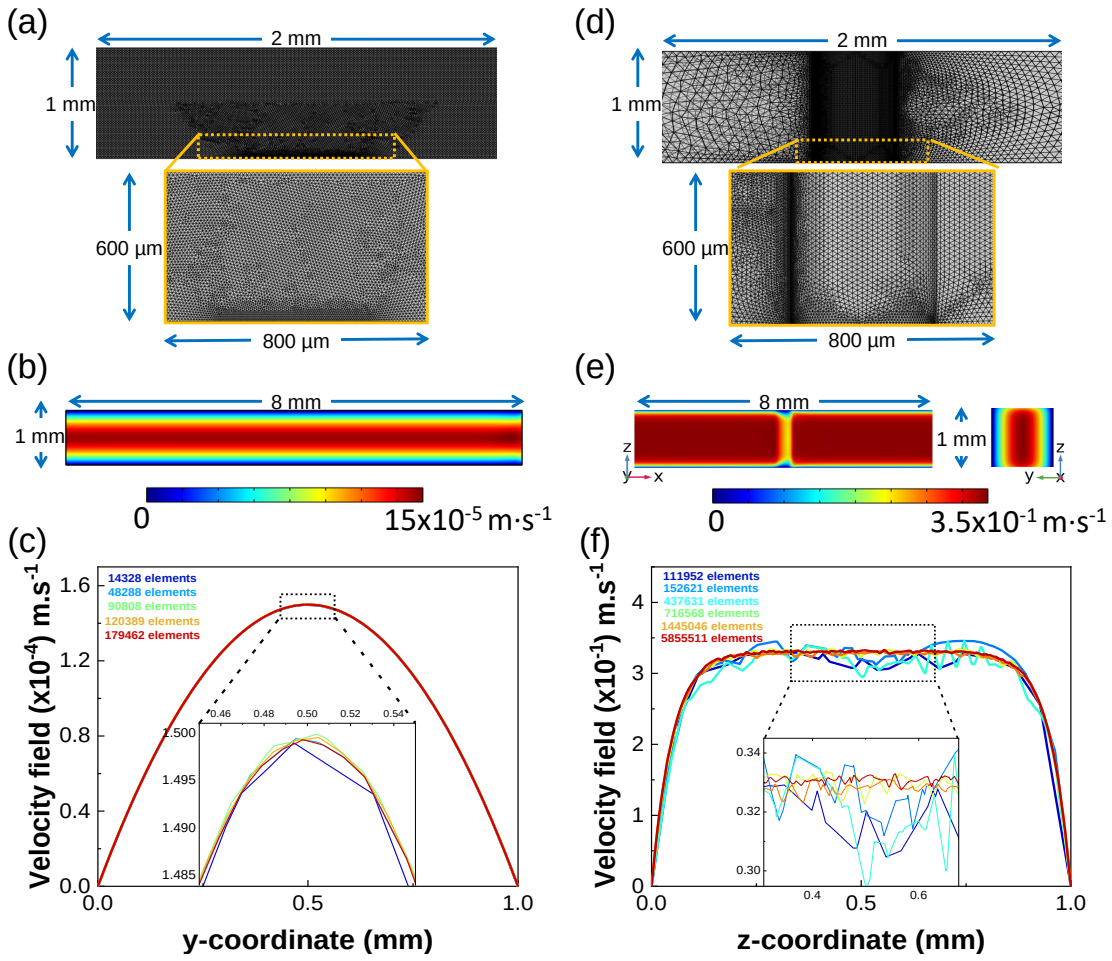

Figure 5.5: Fluid dynamics simulation. (a) 2D mesh grid with 90808 triangular elements (a higher definition can be seen in the proximity of the sensor area); (b) velocity field surface plot; (c) velocity field at x = 3 mm of the microchannel for several meshes; (d) 3D mesh grid with 716568 tetrahedral elements (a higher definition can be seen in the proximity of the sensor area); (e) velocity field surface plot; and (f) velocity field at x = 3 mm of the microchannel for several meshes.

The model was based on previous works [60–62, 72] and consists of three coupled simulations namely, fluid dynamics convection, diffusion and surface reaction simulations. For the calculations, the Navier-Stokes equations were solved first to obtain the velocity field. To solve the analyte concentration field, equations of antigen transport and complex concentration must be solved simultaneously. These last two equations are time dependent. Table 5.1 shows the parameters used for the proposed computer model.

Table 5.1: Parameters used for the simulation. The diffusion coefficients of the antigen and antibody were based on [60, 61] while the flow speed, and concentrations of antigen and antibody were based on the current work.

Parameters of simulation			
U	Flow speed	5×10^{-4}	$m \cdot s^{-1}$
D_A	Diffusion coefficient of antigen	1×10^{-11}	$m^2 \cdot s^{-1}$
D_B	Diffusion coefficient of antibody	1×10^{-9}	$m^2 \cdot s^{-1}$
A	Concentration of antigen	2×10^{-6}	$mol \cdot m^{-3}$
B	Concentration of antibody on surface	1×10^{-4}	$mol \cdot m^{-2}$
ρ	Fluid density	1×10^{3}	$Kg \cdot m^{-3}$
μ	Dynamic viscosity	1×10^{-3}	$Pa \cdot s$
k_a	Adsorption rate constant	1×10^{5}	$M^{-1} \cdot s^{-1}$
k_d	Dissociation rate constant	1×10^{-3}	s^{-1}

In biosensors based on heterogeneous immunoassays, the detection time depends on the transport of the antigen to the sensing zone to bind with the surface-immobilised antibodies [72]. This mass transport is governed by convection and diffusion and presents a critical parameter with strong impacts on the device performance. Figure 5.7a shows the 2D profile of the antigen concentration along the microchannel for the first ten seconds of the reaction. The profile shows that as the antigen molecules are carried downstream before they can diffuse very far and the only antigen molecules that can be collected by the sensor, are the ones that lie in the thin layer above the sensor. Consequently, the diffusion of boundary layer is affected by the formation of the antigen-antibody complex causing a small depletion of antigen concentration after contact with the reaction surface. It is possible to infer the mass transport regime around the sensor in which a given device operates by determining two Peclet numbers related to the channel and sensor surface, Pe_H and Pe_s, respectively [18, 72] (see section 2.6 in chapter 2 for the description of Peclet number). In this case, the $Pe_H = 1.67 \times 10^4$ for protein targets is higher than 1, yielding a depletion zone that is thinner than the channel which is congruent with what can be seen in Figure 5.7a at $t = 1000s$. The $Pe_s = 2.5 \times 10^4$, also superior to 1, indicates that the depletion zone is thinner than the detection chamber.

If a horizontal cross-section across the reaction surface (the length of 500 µm) is drawn, is possible to see that the concentration distribution of the antigen is affected on the extremities of the surface (Figure 5.6b). A higher concentration is observed closer to the inlet and to the outlet (position near $x = 3.75$ mm and $x = 4.25$ mm respectively), although to a lesser extent at the outlet. In both cases, the higher concentration is due to a diffusion phenomenon. Since the antigen concentration distribution is affected by the edges of the channel, so is the reaction rate. The reaction rate is always faster closer to the inlet position than closer to the outlet. As shown in the inset of Figure 5.6b, the average of reaction rate over the sensor surface decreases with time, until it reaches $\approx$ 300 s yielding a steady state. This occurs when the bound antibody concentration starts to approach its equilibrium concentration, slowing the surface reaction, increasing the

antigen concentration on the surface, and consequently the system will leave the diffusion limited regime and depend on the reaction itself [62, 72, 76].

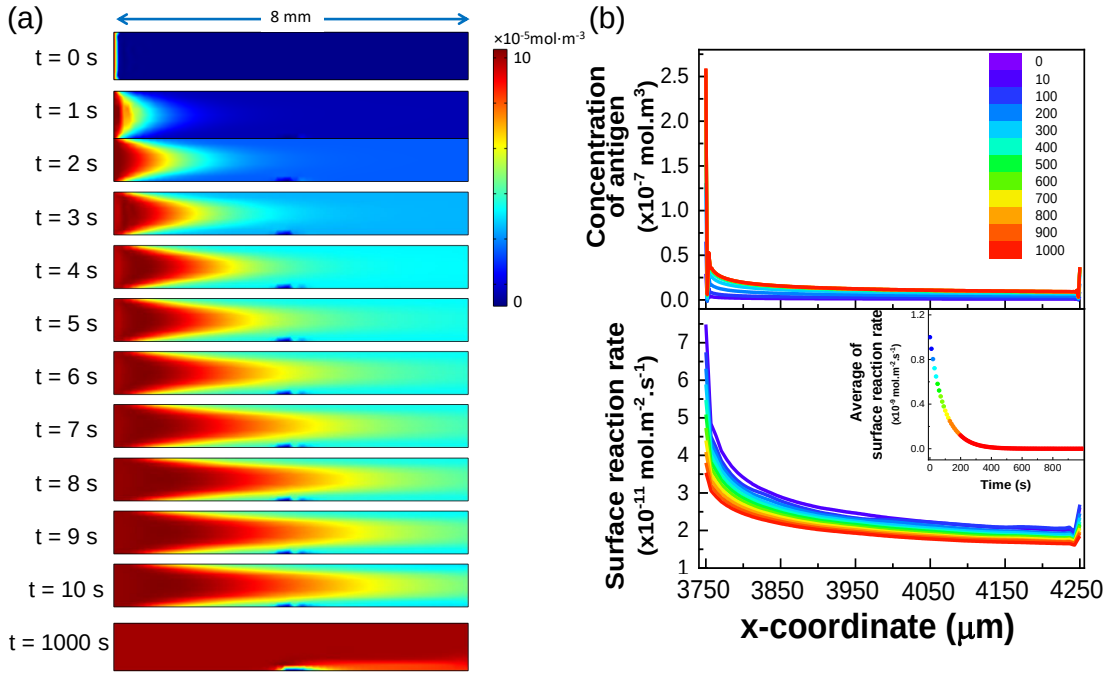

Figure 5.6: Mass transport and surface reaction across with the x-coordinate. (a) Concentration profile of antigen along the reaction surface from the first 10 s, followed by 1000 s. (b) Top: concentration profile of antigen (A) along the reaction surface from 10:100:1000 s; Bottom: surface reaction rate of antigen-antibody (AB) complex formation along the reaction surface and the average reaction rate in function of time (inset).

As illustrated in Figure 5.7, the results of the current numerical study are in agreement with other works [62, 72]. The concentration of the antigen-antibody complex is proportional to the surface coverage and increases rapidly over a short period of time, after which it reaches a saturation value. Also, as the surface coverage increases, the fraction of free sites decreases.

The time that it takes for the sensor to equilibrate depends upon the Damköhler number (Da), the ratio of reactive to diffusive flux. If $Da \gg 1$, mass transport is rate limiting, whereas $Da \ll 1$ indicates that the system is reaction limited. In this case, $Da \approx 38$ which means that this sensor does not operate strongly in either limit. One extremely relevant parameter that defines the biosensor's performance is the time that it takes for the reaction to reach equilibrium. The equilibrium binding time is defined as the response time T_R of the biosensor for which the average concentration of antigen-antibody equals 95% of its saturation value. In the case of the 2D simulation, T_R is ≈ 340 s. This value is important since it influences the detection time of biomolecules and ultimately, the efficiency of the microfluidic-based biosensor [62].

The next step was to compare the 2D simulation with 3D using the same parameters. Comparing both simulations, the T_R obtained through 3D simulation is ≈ 230 s which is

110 s lower than the T_R obtained for the 2D simulation. Nevertheless, both simulations indicate that the equilibrium will be reached in less than 10 min which is ideal for this type of cost-efficient rapid diagnostic tests.

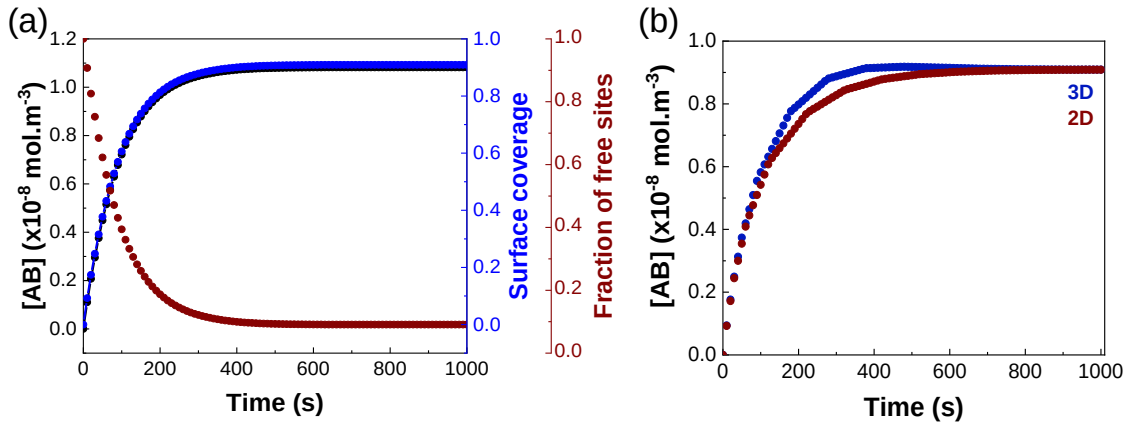

Figure 5.7: Surface reaction in function of time. (a) Black: Average concentration of antigen-antibody (*AB*) complex formation; Blue: Surface coverage; Red: Fraction of free sites. (b) Concentration of antigen-antibody (*AB*) complex formation - as function of time for 2D and 3D simulations.

Although these simulations can give an insight to the physical phenomena that operate inside a microchannel with a sensor platform, it remains approximations. The binding kinetics can be influenced by several factors. Electrostatic interactions, for instance, can play a tremendous role in accelerating the binding, between charged molecules of opposite charges particularly at low ionic strengths where the screening length is large. This has been demonstrated by 100-fold enhancement in cognate immunity of colicin nucleases [77], or by 80-fold increase in DNA hybridisation rates [78]. Other mechanisms not related to electrostatic interactions can also defy the diffusion limit. LacI repressor for example, finds the target sequence at rates 100-fold faster in a near-optimal fashion [79]. For a more precise prediction, numerical computation using more detailed parameters would be required. Nevertheless, the simulation performed herein, can confidently predict the expected time scale required for sensor equilibration (for instance, 20 s versus 20 min or 20 h). Thus, simply computing these parameters provides a good sense for the behaviour of the system and that it is compatible with PS-based microfluidic device fabrication method.

5.3.2 Microfluidic device fabrication and characterisation

One of the striking features of PS for SERS applications is it is transparency. The UV-Vis-near-IR spectra show the typical behaviour of PS, with a high transparency for the wavelengths in the visible and near-IR range (Figure 5.8) [80]. The transmittance at 633 nm from a single sheet of unshrunk PS is ≈90% and this value is reduced by only ≈3% after the shrinkage process. This proves that PS is suitable for creating fully transparent chambers allowing further on-chip and real-time SERS analysis under the 633 nm laser.

Thus, the detection chamber is enclosed by a single sheet of PS, to assure the transparency and to minimise possible optical defects while performing the SERS assay.

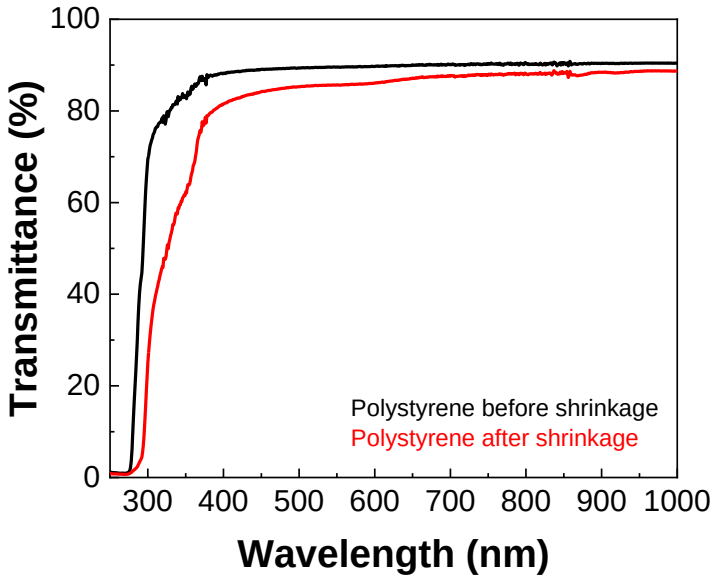

Figure 5.8: UV-Vis-NIR specular transmittance spectra of PS sheets, before and after shrinkage process. The presented spectra are the median of three independent measures.

The patterning of channels on PS was done by photoablation with a CO_2 laser. The photoablation process occurs by pulsing a CO_2 laser focused onto the material increasing the temperature in the irradiated spot which causes its thermal diffusion and evaporation [25, 44]. The temperature at the material's surface is determined by a balance of heat input and the amount of material which can be removed by evaporation at that temperature [81]. When the evaporation temperature is achieved, the material absorbs energy, and its removal is attained. The heat conduction during the photoablation can be described by equation 5.8 [22]:

$$\frac{\partial^2 T}{\partial x^2} + \frac{\partial^2 T}{\partial y^2} + \frac{\partial^2 T}{\partial z^2} - \frac{\rho c_p}{k}\frac{\partial T}{\partial t} = -\frac{I}{k} \tag{5.8}$$

where T is the temperature at a specific point at x, y, z coordinates, I is the laser power, k describes the thermal conductivity of the material, ρ its density and c_p its specific heat. Thermal analysis of PS allows the determination of the evaporation temperature which depends on whether the degradation process is performed in a dry air or nitrogen environment. Since the photoablation takes place in nitrogen environment, and the following procedures of the microfluidic chip production are performed under air atmosphere, TGA/DSC analysis in both atmospheres were performed. TGA/DSC analysis in nitrogen represent better the laser machining process, and thermal bonding and shrinking processes are better represented in air.

Figure 5.9 depicts the temperature dependent mass change, and temperature dependent heat flux. In nitrogen, PS degrades in a single step, beginning approximately at 250°C and ending at 500°C, whereas in air, the degradation process occurs from 200°C to 450°C. The degradation temperature for the PS sheet was 415°C under nitrogen and 410°C under air atmosphere. These are congruent with the steep decrease of mass observed in Figure 5.9b and with the endothermic peak from Figure 5.9c, which is characteristic of typical depolymerisation mechanisms [82]. Additionally, a small endothermic peak is shown at around 116°C under air atmosphere that does not correlate with mass change. This might be related to the glass transition temperature which contributes to the increase of surface smoothness of the patterned PS sheet [83]. Furthermore, this temperature is highly relevant to determine a suitable temperature for the thermal bonding process between the different PS sheets. The exothermic peak at 465°C in air atmosphere, and the endothermic at 674°C in nitrogen atmosphere are not relevant for the present work, since the photoablation process has already occurred as can be seen in Figure 5.9b. It should be mentioned that this study operates in a different time scale. In pulse laser ablation, heating and evaporation occurs in the interval between the beginning and end of the laser pulse which is on the order of milliseconds for the laser, while it is around 60 min in DSC.

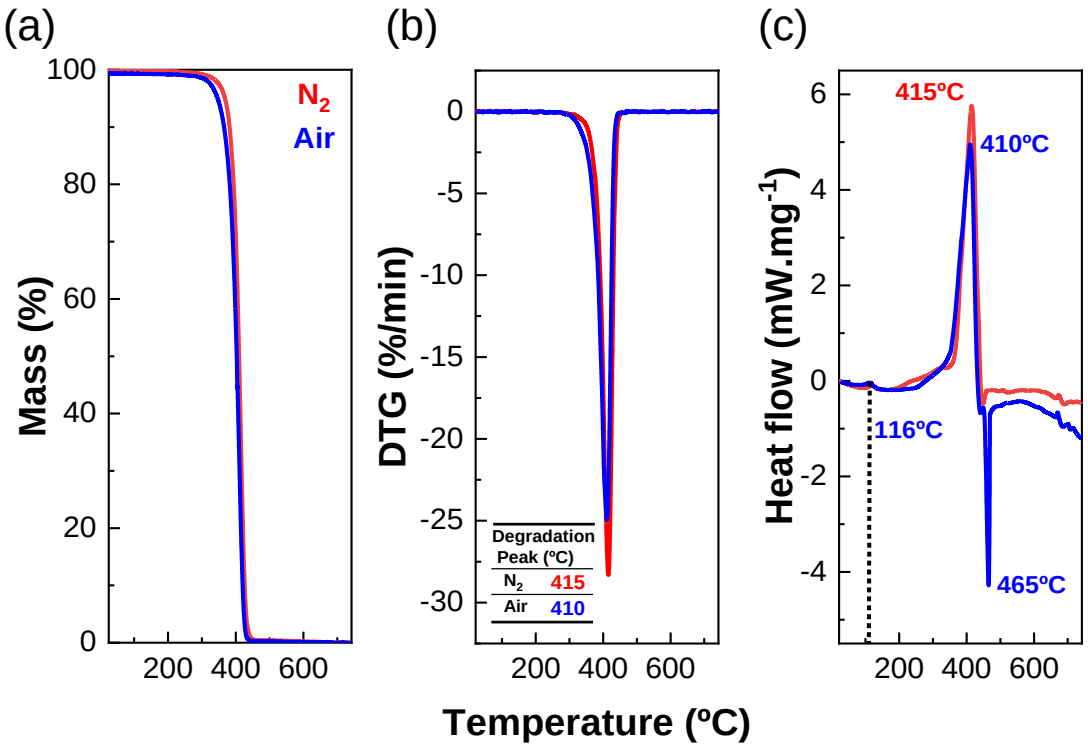

Figure 5.9: TGA/DSC analysis of a PS sheet. (a) TGA curves for the thermal decomposition of PS in nitrogen (red line) and air (blue line). (b) Derivative graph of mass loss for degradation in nitrogen (red line) and air (blue line). (c) DSC scans of measured heat flow for degradation of PS in nitrogen (red line) and air (blue line). The heating rate was 10°C·min^{-1} from 20°C - 75°C.

Besides the thermal diffusivity and composition of the material, the microchannels patterning depends on the intensity distribution of the laser beam (being focused or unfocused) [84], the laser power, and cutting speed [25]. Thus, to pattern a microfluidic channel with the desired width, two patterning parameters were studied – velocity and power. For each case, the laser beam was focused on a PS sheet to achieve a narrower area of highly concentrated energy for a precise ablation [84]. The best resolution was assessed by patterning lines with widths of 0.1 to 1 mm. As shown in Figure 5.10, the photoablation process produced broader channels than the ones imposed with a higher deviation proportional to the applied laser power.

At low laser power (1.25 W) and high velocities (0.0508 $m{\cdot}s^{-1}$), the laser was not effective to cut the channel. In fact, the pulsed character of the laser beam can be seen on the surface (Figure 5.10c). Notably, when the sheet is not successfully cut, the resultant channels are smooth and curvilinear in a Gaussian shape (due to the laser beam [42]) as can be seen in SEM micrograph (Figure 5.10d). This is due to PS thermal conductivity 0.033 $W{\cdot}m^{-1}K^{-1}$ [85] that leads to more diffusion of heat and homogenous ablation in all directions. Conversely, high laser power ($\geq$ 10 W) and lower speeds ($\geq$ 0.00635 $m{\cdot}s^{-1}$) leads to higher diffusion times which degraded the pattern due to accumulation of material on the pattern edges. The smallest deviation observed was obtained for the laser power 2.5 W and velocities 0.0381 and 0.0254 $m{\cdot}s^{-1}$ (Figure 5.10a, b and e) representing a good balance between patterning quality and degradation.

Following the patterning resolution test, a channel of 0.2 mm of width was repeated 10 times. Using a double line design assures that the channels have a uniform flat surface. The dimensions of the microchannel obtained for the conditions of 2.5 W laser power and 0.0254 $m{\cdot}s^{-1}$ velocity were 239 $\pm$ 2 µm of height (corresponding to the thickness of a single PS sheet) and 230 $\pm$ 23 µm of width with a relative standard-deviation (RSD) of 10.2% indicating a good reproducibility.

After patterning, it is possible to observe a Gaussian-like cross-section profile of the microchannel followed by small bumps in the edges of the microchannel (Figure 5.11a). The small bumps result from the surface tension gradient of the melted PS. Upon irradiation, the temperature decreases from the centre of the laser beam to the edges. This creates a temperature gradient inversely proportional to the surface tension which drives the melted material towards the cooler region and with higher surface tension. However, the melted PS is confined by the solid edges of the material leading to its accumulation and re-solidification forming the small bumps [86].

Notably, when the cover plate was bonded by heating in the thermal press with the middle layer, the bumps disappeared, and no deformation of the channel is observed (Figure 5.11b).

After the photoablation process, all the layers were stacked with a TO-RCH platform between the middle and bottom layer and their bond was promoted by a thermal press at 110°C for 20 min. This temperature was chosen to ensure the glass transition which not only allows to firmly bond the layers but also to obtain a smooth surface inside the

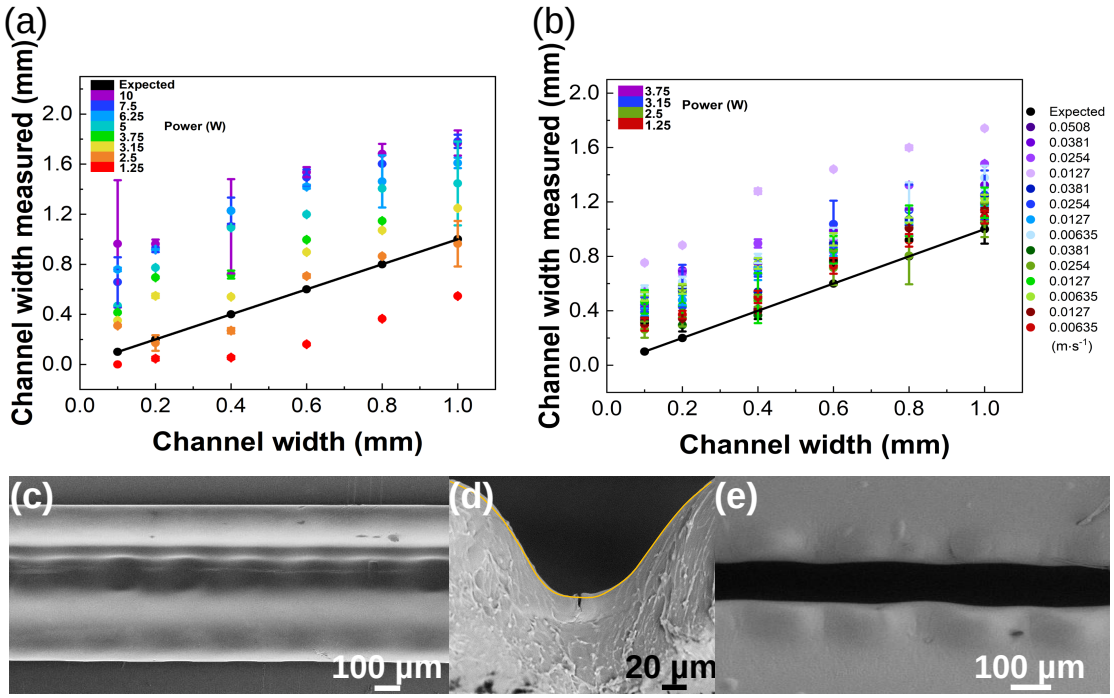

Figure 5.10: CO_2 laser resolution tests comparing the pattern from the digital drawing to the produced by the laser. Comparison between imposed channel width, and the channel width produced by ablation; The black line represents the ideal values *i.e.* imposed and produced channels widths have the same values. (a) Channel width produced by laser ablation with different powers (1.25 to 10 W) at constant velocity (0.0381 $m{\cdot}s^{-1}$). (b) Channel width produced by laser ablation with different powers (1.25 to 10 W) and different velocities (0.00635 – 0.0508 $m{\cdot}s^{-1}$). Error bars correspond to the standard deviation from ten independent measures. SEM images of the patterned microchannel when the laser ablation process is not effective to cut the channel: (c) top view and (d) cross-section view. (e) SEM image of the top view of the patterned microchannel after the laser ablation process.

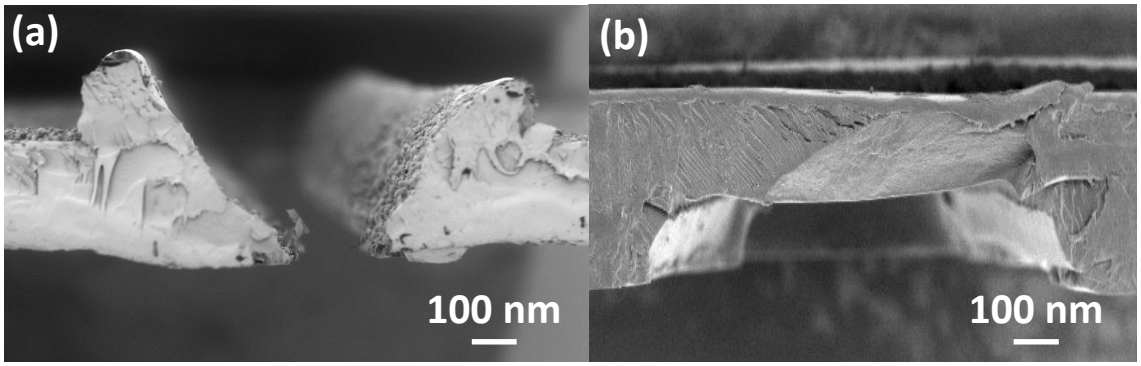

Figure 5.11: SEM images of the cross-section views of a microchannel (a) after the photoablation process and (b) after the thermal bonding.

microchannels due to thermal reflow [39]. The pressure during thermal bonding ensures that no delamination of the layers occurs and that the chip structure is not compromised which avoids channel leakage.

The final PS chip was obtained by shrinkage in an oven at 155°C for 5 min. Since the shrinking process is dependent on the aspect ratio of the chip, the design of the chip was always done in the ratio of 1. The shrinkage ultimately results in thickness increase (63%), as also reported by other authors using this type of thermoplastics [1, 2]. This process decreases the transparency of the device as can be seen in Figure 5.12. Nevertheless, as the detection chamber corresponds only to one sheet, the transmittance is still ≈87% (see Figure 5.8). The final dimensions of the chip were ≈ 3×3 cm^2 with microchannels of 129 ± 8 µm of width and 998 ± 53 µm of height and a detection chamber with 559 ± 10 µm giving a miniaturisation of ≈58% (Figure 5.12).

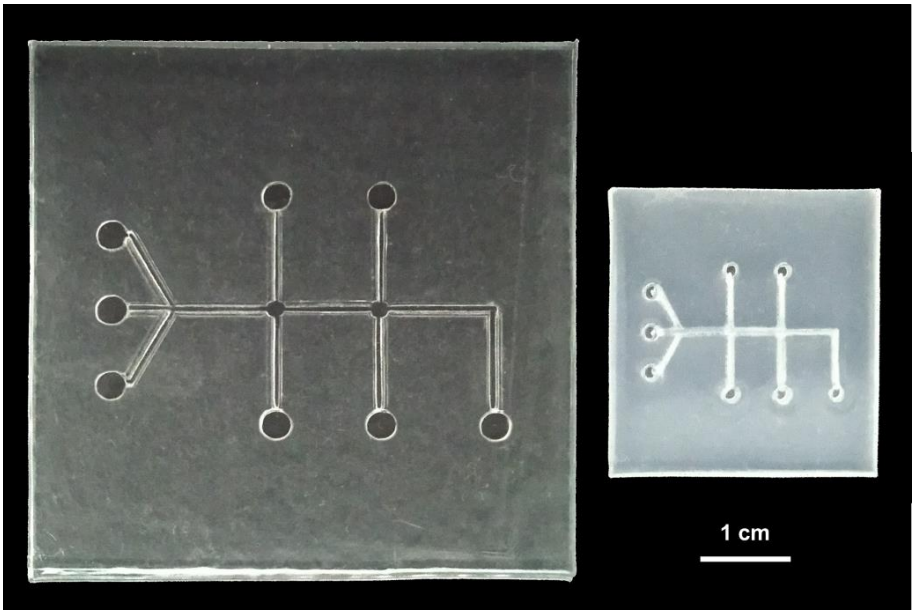

Figure 5.12: Top perspective of the PS microfluidic chip. 3D multilayer chip with microchannels patterning after photoablation and thermal bonding with an area of ≈ 6×6 cm^2. The same multilayer chip after shrinking with an area of ≈ 3×3 cm^2.

Hydrophobicity of a material is an important parameter when developing a device for biodiagnostic applications. The more hydrophobic a material is, the higher absorption of small hydrophobic molecules onto the channel wells [9, 21]. This is one of the main problems of PDMS-based microfluidic devices. PS on the other hand, has little or no absorption of molecules [33]. The contact angles of PS before and after laser ablation, and after shrinking were measured to verify the surface wettability of the device. Before the laser treatment, PS had a contact angle of 70° ± 1 which is in agreement with the literature [9, 22]. After the laser ablation, PS maintains the hydrophilicity giving a water contact angle of 68° ± 4. Additionally, after the thermal bonding and shrinking processes, the hydrophilicity of PS increases to 64.3° ± 0.4, and 55° ± 3, respectively, which might be the result of a change in surface topography that decreases the surface roughness as

can be seen by AFM measurements (Figure 5.13). This is due to the re-solidification of PS after laser ablation and shrinking processes [22]. Thus, it is possible to assume that the fabricated microchannels engraved in PS are hydrophilic (contact angle <90°).

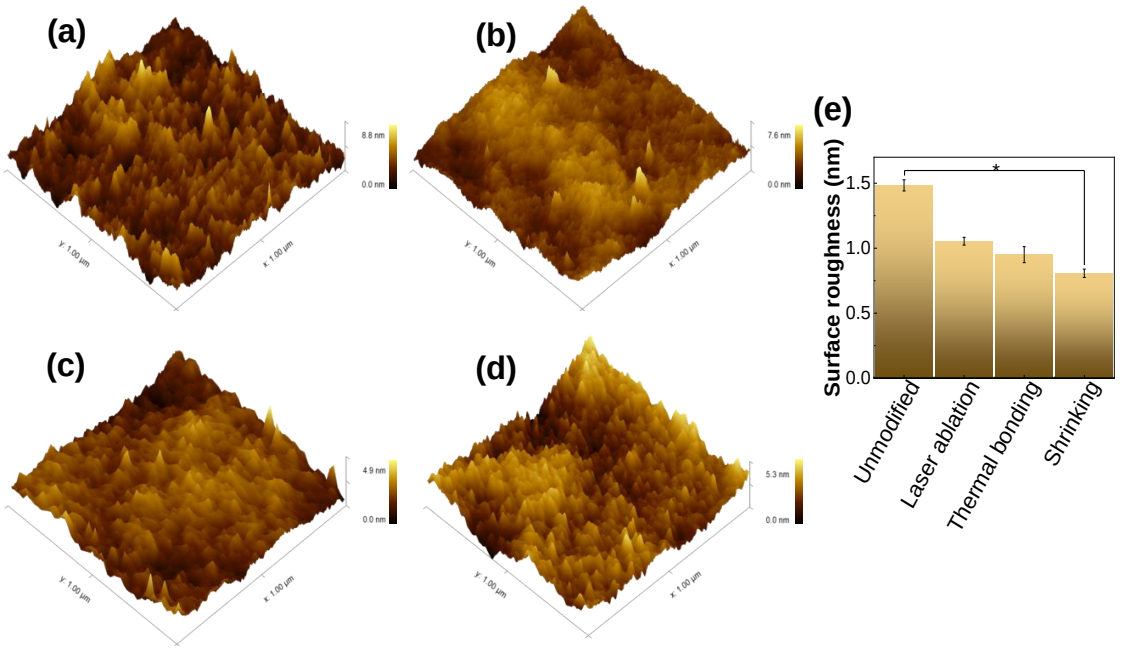

Figure 5.13: (a) unmodified (before laser ablation) (b) after laser ablation; (c) after thermal bonding and (d) after shrinking. (e) surface roughness of PS samples from all the steps performed during the fabrication of the device. The surface roughness was measured on three different samples each with an area of 1 μm^2. Two-sample Student *t*-tests with Welch correction was applied for statistical comparisons. $*$ $p \leq 0.00005$.

5.3.3 Proof-of-concept of the microfluidic chip

To demonstrate the viability of the PS microfluidic chip, enzymatic and SERS assays were performed with anti-HRP antibodies immobilised on the TO-RCH platform that capture HRP upon its addition, a method which has already been proven to be successful in assessing the functionality of the biosensor (see section 4). To simulate the temperature experienced by the TO-RCH during the shrinking process, the samples were heated at 110°C for twenty minutes and 155°C for a further five, before the antibody immobilisation step was performed. As shown in Figure 5.14, the enzymatic activity observed by the TO-RCH inside the chip (termed as "on-chip") is approximately twice that observed for the corresponding samples measured outside the chip (termed as "off-chip"). This difference can be accounted by the fact that inside the microfluidic device the biochemical reaction occurs on the micrometre length scale, maximising the mass transport in immunoreactions [7, 72]. Additionally, the samples with the physiosorbed HRP either on, or off-chip, showed a smaller enzymatic activity than the samples for which the HRP immobilisation is mediated by covalently immobilised antibodies. This might occur due to some bleaching of HRP during the washing procedure following their incubation with

TO-RCH alone. These results indicate a successful detection of antigen-antibody complex presence, thus confirming the viability of the PS microfluidic device for immunoassays application, and that TO-RCH can withstand the fabrication process of the microfluidic device.

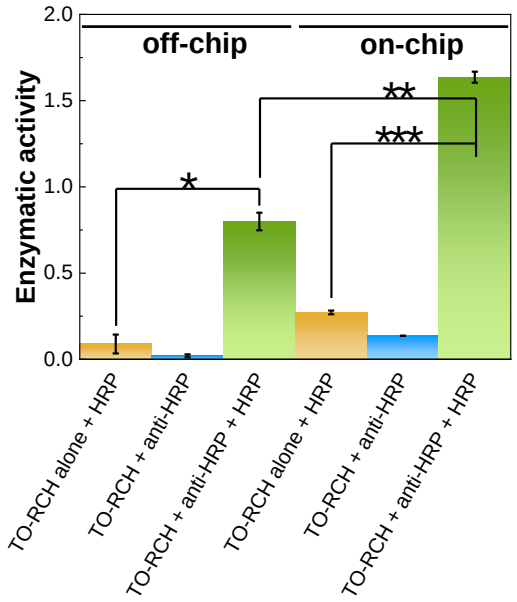

Figure 5.14: Performance of the PS-based microfluidic device evaluation by HRP enzymatic activity. The samples above the term "off-chip" were performed on the TO-RCH without being inserted in the microfluidic device whereas the samples above the term "on-chip" referred to the enzymatic reaction on the TO-RCH integrated in the microfluidic device. The samples on-chip have the double HRP activity than their off-chip counterparts. The residual activity from HRP physiosorbed to TO-RCH alone (yellow bars) and the lack of activity in samples without HRP confirm efficient blocking of the TO-RCH and the microfluidic device, and that the HRP is in fact bound to anti-HRP antibodies in the two other cases. One-way ANOVA was applied for statistical comparison followed by the Tukey's multiple comparison test, * $p \leq 0.005$, ** $p \leq 0.0001$, *** $p \leq 0.00001$.

Raman spectroscopy was also used to characterise and evaluate the feasibility of the SERS-based microfluidic immunoassay. Figure 5.15a shows the Raman and SERS spectra of the different elements that composed the microfluidic assay, namely, the PS as the material of the microfluidic chip, the capture platform (TO-RCH) where the immobilised antibodies recognise the antigen, and the SERS immunotags (with 4-mercaptobenzoic acid - MBA - as the Raman reporter). When the SERS immunotags bind to the antigen-antibody complex in the capture platform, the SERS active sandwich immunocomplex is formed inside the detection chamber of the microfluidic device. The SERS spectra of MBA in the SERS immunotags and in the sandwich immunoassay show two intense bands at 1080 and 1587 cm^{-1}, confirming the recognition of the SERS immunotag with the antigen-antibody complex. Additionally, it is possible to observe other Raman bands when the sandwich immunocomplex is formed inside the detection chamber. These bands are characteristic of the Raman spectrum of PS and their respective bands assignments are shown in Figure 5.15b [87].

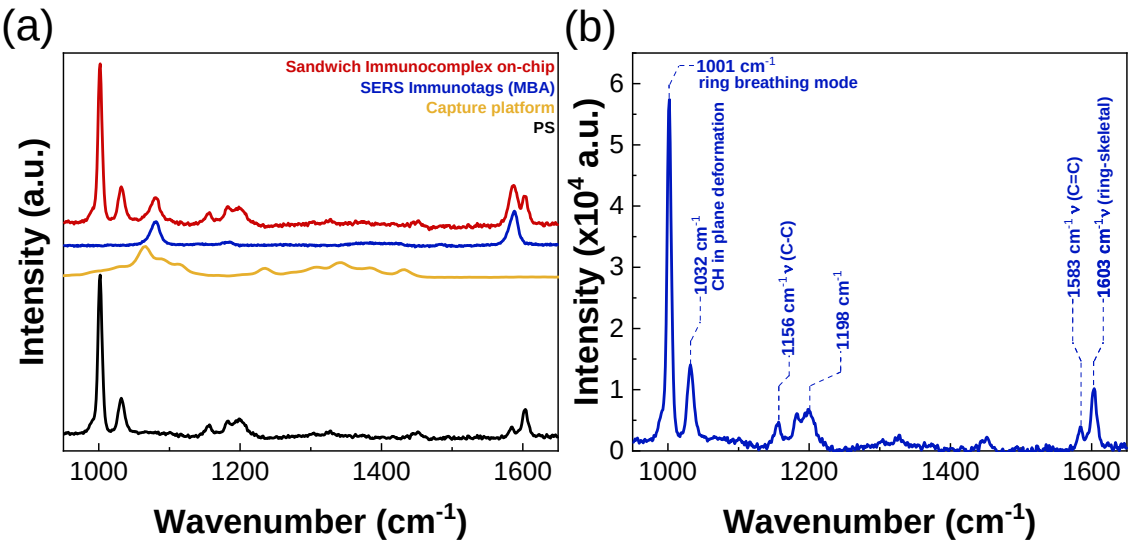

Figure 5.15: Relevant Raman and SERS spectra of the microfluidic SERS immunoassay. (a) From bottom to top: Raman spectra of the PS, the material of the microfluidic chip (black); the capture platform, *i.e.*, after covalent immobilisation of antibodies (orange) amplified ×200; the SERS spectra of SERS immunotags with MBA as Raman reporter (blue); and of the SERS active sandwich immunoassay formed inside the microfluidic chip (red). (b) PS Raman spectra with the main vibrational modes assigned [87].

5.4 Conclusions

This work presents a novel microfluidic device for SERS-based immunoassay based on laser engraving of shrinkable PS sheets known as "Shrinky-dink". This microfluidic device integrates the TO-RCH as capture platform developed in the previous chapter 4 as well as the SERS immunotags created in chapter 3.

A numerical simulation was performed to understand how the transport of the target molecules as well as the chemical reaction can influence the performance of the biosensor. The simulation showed that the diffusion of the boundary layer is formed due the formation of the antigen-antibody complex and consequently, a thin depletion of antigen concentration appears after the antigen contact with the reaction surface. Additionally, the simulation revealed that the reaction does not occurs at the same rate at the surface, being much faster at edges of the sensor surface. Furthermore, this analysis allowed determination of the T_R as less than 10 min, which is compatible with the type of biosensors suitable for POCT sites.

Following the simulation, shrinkable PS sheets were used for their optimal transparency (87% of transmittance at 633 nm) and feasibility in development of a PS-based microfluidic chip. This fabrication process allowed to develop a 3D multilayer chip in less than 30 min. In addition, this was the first time that a PS-based microfluidic chip was applied for SERS analysis.

The thermal analysis demonstrated that PS sheets can withstand the temperatures needed for the fabrication process without suffering any degradation. Moreover, the

TGA/DSC analysis helped to optimise the temperature for bonding the patterned PS sheets by thermal bonding. The laser ablation power and speed were optimised for cutting the PS sheet. A good quality pattern with no degradation was obtained with the laser power 2.5 W and velocity 0.0381 $m \cdot s^{-1}$, yielding a channel with height 239 ± 2 µm and width 230 ± 23 µm, with a RSD of 10.2% indicating good reproducibility. The thermal bonding of the multilayer chip with an integrated TO-RCH platform ensured that all layers were bound, and no leaks happened while performing the assay. The final microfluidic chip was obtained by shrinking the bound PS sheets in an oven yielding a chip with channels of width 129 ± 8 µm, height 998 ± 53 µm and a detection chamber with a diameter of 559 ± 10 µm. This process allowed reduction of the dimensions by 58%.

Due to the thermal steps involved in the fabrication of the chip, the re-solidification of PS led to a decrease in surface roughness as shown by AFM measurements and by the 55° ± 3 water contact angle. This proved that the microfluidic chip is hydrophilic overcoming one of the main problems of using PDMS in microfluidic devices, that of its hydrophobic nature making it prone to the adsorption of small molecules.

Finally, the enzymatic and SERS assays demonstrated the viability of the PS-based microfluidic chip. The enzymatic activity observed by the TO-RCH platform inside the chip was *ca.* twice that observed for the corresponding samples outside the chip. This response might be because microfluidic systems can maximise the mass transport in immunoreactions. Having demonstrated that TO-RCH can withstand the fabrication process of the microfluidic device, the immunoassay was performed and analysed by SERS. The SERS measurements confirmed the recognition of the SERS immunotags upon the formation of the sandwich immunocomplex.

In conclusion, the approach to fabricate a PS-based microfluidic device for SERS immunoassay could successfully overcome the main challenges of PDMS-based microfluidic devices for POCT application. This microfluidic device produced herein allows a fully transparent, inexpensive, and fast production device with a remarkable design flexibility for multiple applications.

References for chapter 5

[1] C.-S. Chen et al. "Shrinky-Dink microfluidics: 3D polystyrene chips". In: *Lab on a Chip* 8.4 (2008), pp. 622–624.

[2] A. Grimes et al. "Shrinky-Dink microfluidics: rapid generation of deep and rounded patterns". In: *Lab Chip* 8.1 (2008), pp. 170–172.

[3] K. Ren, J. Zhou, and H. Wu. "Materials for Microfluidic Chip Fabrication". In: (2001).

[4] A. P. Dhawan et al. "Current and Future Challenges in Point-of-Care Technologies: A Paradigm-Shift in Affordable Global Healthcare With Personalized and Preventive Medicine". In: *IEEE Journal of Translational Engineering in Health and Medicine* 3 (2015), pp. 1–10.

[5] F. Inci et al. "A disposable microfluidic-integrated hand-held plasmonic platform for protein detection". In: *Applied Materials Today* 18 (2020), pp. 14–16.

[6] H.-T. Nguyen et al. "Low-Cost, Accessible Fabrication Methods for Microfluidics Research in Low-Resource Settings". In: *Micromachines* 9.9 (2018), pp. 461–471.

[7] K. N. Han, C. A. Li, and G. H. Seong. "Microfluidic chips for immunoassays". In: *Annual Review of Analytical Chemistry* 6.1 (2013), pp. 119–141.

[8] J. Li et al. "β-Cyclodextrin-Stabilized Au Nanoparticles for the Detection of Butyl Benzyl Phthalate". In: *ACS Applied Nano Materials* 2.5 (2019), pp. 2743–2751.

[9] B. H. Weigl, R. L. Bardell, and C. Cabrera. "Introduction to Microfluidic Techniques". In: *Handbook of Biosensors and Biochips*. Ed. by R. S. Marks. 1st ed. Chichester, UK: John Wiley & Sons, Ltd, 2008. Chap. 41, pp. 1–19.

[10] M. Hitzbleck and E. Delamarche. "Reagents in microfluidics: An 'in' and 'out' challenge". In: *Chemical Society Reviews* 42.21 (2013), pp. 8494–8516.

[11] S. M. Restaino and I. M. White. "Real-time multiplexed PCR using surface enhanced Raman spectroscopy in a thermoplastic chip". In: *Lab on a Chip* 18.5 (2018), pp. 832–839.

[12] B. J. Coelho et al. "Digital Microfluidics-Powered Real-Time Monitoring of Isothermal DNA Amplification of Cancer Biomarker". In: *Biosensors* 12.4 (2022), pp. 201–213.

[13] S. Ghosh et al. "A new microchannel capillary flow assay (MCFA) platform with lyophilized chemiluminescence reagents for a smartphone-based POCT detecting malaria". In: *Microsystems and Nanoengineering* 6.1 (2020), pp. 1–15.

[14] R. Gao et al. "Wash-free magnetic immunoassay of the PSA cancer marker using SERS and droplet microfluidics". In: *Lab on a Chip* 16.6 (2016), pp. 1022–1029.

[15] A. Kamińska et al. "Detection of Hepatitis B virus antigen from human blood: SERS immunoassay in a microfluidic system". In: *Biosensors and Bioelectronics* 66 (2015), pp. 461–467.

[16] J. Sun et al. "Power-free polydimethylsiloxane femtoliter-sized arrays for bead-based digital immunoassays". In: *Biosensors and Bioelectronics* 139.January (2019), pp. 111339–111346.

[17] Y. Wang et al. "Cyclodextrin capped gold nanoparticles (AuNP@CDs): from synthesis to applications". In: *Journal of Materials Chemistry B* (2021), pp. 2584–2593.

[18] T. M. Squires and S. R. Quake. "Microfluidics: Fluid physics at the nanoliter scale". In: *Reviews of Modern Physics* 77.3 (2005), pp. 977–1026.

[19] Y. Song et al. "Recent Progress in Microfluidics-Based Biosensing". In: *Analytical Chemistry* 91.1 (2019), pp. 388–404.

[20] J. Melin and S. R. Quake. "Microfluidic large-scale integration: The evolution of design rules for biological automation". In: *Annual Review of Biophysics and Biomolecular Structure* 36 (2007), pp. 213–231.

[21] K. Ren, J. Zhou, and H. Wu. "Materials for microfluidic chip fabrication". In: *Accounts of Chemical Research* 46.11 (2013), pp. 2396–2406.

[22] I. Bilican and M. Tahsin Guler. "Assessment of PMMA and polystyrene based microfluidic chips fabricated using CO2 laser machining". In: *Applied Surface Science* 534.July (2020), pp. 147642–147651.

[23] S. Hin et al. "VectorDisk: A Microfluidic Platform Integrating Diagnostic Markers for Evidence-Based Mosquito Control". In: *Processes* 8.12 (2020), pp. 1677–1693.

[24] X. Hu et al. "Fabrication of a polystyrene microfluidic chip coupled to electrospray ionization mass spectrometry for protein analysis". In: *Journal of Chromatography B: Analytical Technologies in the Biomedical and Life Sciences* 990 (2015), pp. 96–103.

[25] H. Li et al. "Fabrication of polystyrene microfluidic devices using a pulsed CO2 laser system". In: *Microsystem Technologies* 18.3 (2012), pp. 373–379.

[26] B. Oliveira et al. "Fast prototyping microfluidics: Integrating droplet digital lamp for absolute quantification of cancer biomarkers". In: *Sensors (Switzerland)* 20.6 (2020).

[27] Iwona Bernacka-Wojcik. "Design and development of a microfluidic platform for use with colorimetric gold nanoprobe assays". PhD thesis. 2014, pp. 1–225.

[28] I. Bernacka-Wojcik et al. "Single nucleotide polymorphism detection using gold nanoprobes and bio-microfluidic platform with embedded microlenses". In: *Biotechnology and Bioengineering* 112.6 (2015), pp. 1210–1219.

[29] I. Bernacka-Wojcik et al. "Bio-microfluidic platform for gold nanoprobe based DNA detection—application to Mycobacterium tuberculosis". In: *Biosensors and Bioelectronics* 48 (2013), pp. 87–93.

[30] H. Cong and N. Zhang. "Perspectives in translating microfluidic devices from laboratory prototyping into scale-up production". In: *Biomicrofluidics* 16.2 (2022), p. 021301.

[31] E. K. Sackmann, A. L. Fulton, and D. J. Beebe. "The present and future role of microfluidics in biomedical research". In: *Nature* 507.7491 (2014), pp. 181–189.

[32] S. M. Yang et al. "Microfluidic Point-of-Care (POC) Devices in Early Diagnosis: A Review of Opportunities and Challenges". In: 22.4 (2022), p. 1620.

[33] S. Halldorsson et al. "Advantages and challenges of microfluidic cell culture in polydimethylsiloxane devices". In: *Biosensors and Bioelectronics* 63 (2015), pp. 218–231.

[34] M. Hashimoto, F. Barany, and S. A. Soper. "Polymerase chain reaction/ligase detection reaction/hybridization assays using flow-through microfluidic devices for the detection of low-abundant DNA point mutations". In: *Biosensors and Bioelectronics* 21.10 (2006), pp. 1915–1923.

[35] K. Tsougeni et al. "Lab-on-Chip platform and protocol for rapid foodborne pathogen detection comprising on-chip cell capture, lysis, DNA amplification and surface-acoustic-wave detection". In: *Sensors and Actuators, B: Chemical* 320.5 (2020), pp. 128345–128354.

[36] N. Xiang et al. "Circular-channel particle focuser utilizing viscoelastic focusing". In: *Microfluidics and Nanofluidics* 23.2 (2019), pp. 16–26.

[37] K. K. Zeming et al. "Microfluidic label-free bioprocessing of human reticulocytes from erythroid culture". In: *Lab on a Chip* 20.18 (2020), pp. 3445–3460.

[38] M. Focke et al. "Lab-on-a-Foil: Microfluidics on thin and flexible films". In: *Lab on a Chip* 10.11 (2010), pp. 1365–1386.

[39] O. Bar-On et al. "High Quality 3D Photonics using Nano Imprint Lithography of Fast Sol-gel Materials". In: *Scientific Reports* 8 (2018), pp. 7833–7840.

[40] K. Kadimisetty et al. "Automated 4-sample protein immunoassays using 3D-printed microfluidics". In: *Analytical Methods* 10.32 (2018), pp. 4000–4006.

[41] S. Shin and J. Hyun. "Matrix-Assisted Three-Dimensional Printing of Cellulose Nanofibers for Paper Microfluidics". In: *ACS Applied Materials and Interfaces* 9.31 (2017), pp. 26438–26446.

[42] H. Klank, J. P. Kutter, and O. Geschke. "CO2-laser micromachining and back-end processing for rapid production of PMMA-based microfluidic systems". In: *Lab on a Chip* 2.4 (2002), pp. 242–247.

[43] M. Riahi. "CO2 Laser and Micro-Fluidics". In: *CO2 Laser - Optimisation and Application*. Ed. by D. C. Dumitras. 1st ed. London, UK: InTech, 2012. Chap. 12, pp. 308–328.

[44] S. Prakash and S. Kumar. "Fabrication of microchannels on transparent PMMA using CO2 Laser (10.6 μm) for microfluidic applications: An experimental investigation". In: *International Journal of Precision Engineering and Manufacturing* 16.2 (2015), pp. 361–366.

[45] C. B. Zhou et al. "Fabrication of Paper-Based Microfluidics by Single-Step Wax Printing for Portable Multianalyte Bioassays". In: *Advanced Materials Research* 881-883 (2014), pp. 503–508.

[46] S. A. M. Shaegh et al. "Rapid prototyping of whole-thermoplastic microfluidics with built-in microvalves using laser ablation and thermal fusion bonding". In: *Sensors and Actuators, B: Chemical* 255 (2018), pp. 100–109.

[47] O. Rahmanian, C.-F. Chen, and D. L. DeVoe. "Microscale Patterning of Thermoplastic Polymer Surfaces by Selective Solvent Swelling". In: *Langmuir* 28.35 (2012), pp. 12923–12929.

[48] C.-S. Chen et al. "Shrinky-Dink microfluidics: 3D polystyrene chips". In: (2008).

[49] H. Li et al. "Fabrication of polystyrene microfluidic devices using a pulsed CO2 laser system". In: *Microsystem Technologies* 18.3 (2012), pp. 373–379.

[50] J. Kai et al. "A novel microfluidic microplate as the next generation assay platform for enzyme linked immunoassays (ELISA)". In: *Lab on a Chip* 12.21 (2012), pp. 4257–4262.

[51] M. R. Hoonejani et al. "Quantitative multiplexed simulated-cell identification by SERS in microfluidic devices". In: *Nanoscale* 7.40 (2015), pp. 16834–16840.

[52] A. Kamińska et al. "Detection of Circulating Tumor Cells Using Membrane-Based SERS Platform: A New Diagnostic Approach for 'Liquid Biopsy'". In: *Nanomaterials* 9.3 (2019), pp. 366–381.

[53] S. Mabbott et al. "Detection of cardiovascular disease associated miR-29a using paper-based microfluidics and surface enhanced Raman scattering". In: *Analyst* 145.3 (2020), pp. 983–991.

[54] L. F. Tadesse et al. "Toward rapid infectious disease diagnosis with advances in surface-enhanced Raman spectroscopy". In: *The Journal of Chemical Physics* 152.24 (2020), pp. 240902–240917.

[55] R. E. Wilson et al. "Immunomagnetic Capture and Multiplexed Surface Marker Detection of Circulating Tumor Cells with Magnetic Multicolor Surface-Enhanced Raman Scattering Nanotags". In: *ACS Applied Materials & Interfaces* 12.42 (2020), pp. 47220–47232.

[56] J. Langer et al. "Present and Future of Surface-Enhanced Raman Scattering". In: *ACS Nano* 14.1 (2020), pp. 28–117.

[57] B. Shan et al. "Novel SERS labels: Rational design, functional integration and biomedical applications". In: *Coordination Chemistry Reviews* 371 (2018), pp. 11–37.

[58] Z. Wang et al. "SERS-Activated Platforms for Immunoassay: Probes, Encoding Methods, and Applications". In: *Chemical Reviews* 117.12 (2017), pp. 7910–7963.

[59] D. Barak-Shinar et al. "A Computational Fluid Dynamic Model of Antigen - Antibody Surface Adsorption on a Piezoelectric Immunosensor". In: *Annals of Biomedical Engineering* 28.5 (2000), pp. 565–571.

[60] H. Hajji et al. "Finite element simulation of antigen-antibody transport and adsorption in a microfluidic chip". In: *Physica E: Low-Dimensional Systems and Nanostructures* 104.June (2018), pp. 177–186.

[61] G. Hu, Y. Gao, and D. Li. "Modeling micropatterned antigen-antibody binding kinetics in a microfluidic chip". In: *Biosensors and Bioelectronics* 22.7 (2007), pp. 1403–1409.

[62] M. Selmi, M. H. Gazzah, and H. Belmabrouk. "Optimization of microfluidic biosensor efficiency by means of fluid flow engineering". In: *Scientific Reports* 7.1 (2017), pp. 1–11.

[63] Sigma-Aldrich. *Enzymatic Assay of Peroxidase (EC 1.11.1.7) with 2,2'-Azino-bis (3-Ethylbenzthiazoline-6-Sulfonic Acid) as a Substrate*. 2019. URL: https://www.sigmaaldrich.com/technical-documents/protocols/biology/enzymatic-assay-of-peroxidase-abts-as-substrate.html (visited on 07/29/2019).

[64] D. Sheskin. *Handbook of Parametric and Nonparametric Statistical Procedures*. Ed. by Chapman & Hall/CRC. 5th ed. Boca Raton, Florida: Taylor & Francis, 2011.

[65] S. S. Shapiro and M. B. Wilk. "An Analysis of Variance Test for Normality (Complete Samples)". In: *Biometrika* 52.3/4 (1965), pp. 591–610.

[66] B. L. Welch. "The Generalization of 'Student's' Problem when Several Different Population Variances are Involved". In: *Biometrika* 34.1/2 (1947), pp. 28–35.

[67] P. T. Munroe. "ANOVA (Analysis of Variance)". In: *The Blackwell Encyclopedia of Sociology*. Ed. by P. T. Munroe. 1th ed. Oxford, UK: John Wiley & Sons, Ltd, 2015. Chap. 15.

[68] J. W. Tukey. "The Philosophy of Multiple Comparisons". In: *Statistical Science* 6.1 (1991), pp. 100–116.

[69] F. E. Grubbs. "Sample Criteria for Testing Outlying Observations". In: *The Annals of Mathematical Statistics* 21.1 (1950), pp. 27–58.

[70] F. D. Krampa et al. "Recent Advances in the Development of Biosensors for Malaria Diagnosis". In: *Sensors* 20.3 (2020), pp. 799–820.

[71] N. M. Pham et al. "Malaria and the 'last' parasite: How can technology help?" In: *Malaria Journal* 17.1 (2018), pp. 1–16.

[72] T. M. Squires, R. J. Messinger, and S. R. Manalis. "Making it stick: convection, reaction and diffusion in surface-based biosensors". In: *Nature Biotechnology* 26.4 (2008), pp. 417–426.

[73] M. Bahri et al. "2D simulation of a microfluidic biosensor for CRP detection into a rotating micro-channel". In: *SN Applied Sciences* 1.10 (2019), pp. 1199–1209.

[74] H. Nguyen and T. Hoang. "Numerical Simulation of Laminar Flow Through a Pipe using COMSOL Multiphysics". In: *International Journal of Scientific & Engineering Research* 8.6 (2017), pp. 290–295.

[75] E. Orabona et al. "Numerical optimization of a microfluidic assisted microarray for the detection of biochemical interactions". In: *Sensors* 11.10 (2011), pp. 9658–9666.

[76] F. Shahbazi et al. "A computational simulation platform for designing real-time monitoring systems with application to COVID-19". In: *Biosensors and Bioelectronics* 171.June 2020 (2021), p. 112716.

[77] R. Wallis et al. "Protein-Protein Interactions in Colicin E9 DNase-Immunity Protein Complexes. 1. Diffusion-Controlled Association and Femtomolar Binding for the Cognate Complex". In: *Biochemistry* 34.42 (1995), pp. 13743–13750.

[78] Y. Belosludtsev et al. "Nearly instantaneous, cation-independent, high selectivity nucleic acid hybridization to DNA microarrays". In: *Biochemical and Biophysical Research Communications* 282.5 (2001), pp. 1263–1267.

[79] Y. M. Wang, R. H. Austin, and E. C. Cox. "Single molecule measurements of repressor protein 1D diffusion on DNA". In: *Physical Review Letters* 97.4 (2006), pp. 1–4.

[80] E. Lee and D. H. Kim. "Fabrication of transparent superhydrophobic polydimethylsiloxane elastomer by controlling the degree of combustion using thermal convection". In: *Korean Journal of Chemical Engineering* 38.2 (2021), pp. 2–7.

[81] D. Yuan and S. Das. "Experimental and theoretical analysis of direct-write laser micromachining of polymethyl methacrylate by CO2 laser ablation". In: *Journal of Applied Physics* 101.2 (2007), pp. 024901–024908.

[82] J. D. Peterson, S. Vyazovkin, and C. Wight. "Kinetics of the Thermal and Thermo-Oxidative Degradation of Polystyrene, Polyethylene and Poly(propylene)". In: *Macromolecular Chemistry and Physics* 202.6 (2001), pp. 775–784.

[83] J. Rieger. "The glass transition temperature of polystyrene". In: *Journal of Thermal Analysis* 46.3-4 (1996), pp. 965–972.

[84] T.-F. Hong et al. "Rapid prototyping of PMMA microfluidic chips utilizing a CO2 laser". In: *Microfluidics and Nanofluidics* 9.6 (2010), pp. 1125–1133.

[85] D. R. Lide. *CRC Handbook of Chemistry and Physics*. Ed. by D. R. Lide. 85th ed. New York, USA: Taylor and Francis, 2005.

[86] S. C. Chen, D. G. Cahill, and C. P. Grigoropoulos. "Melting and surface deformation in pulsed laser surface micromodification of Ni-P disks". In: *Journal of Heat Transfer* 122.1 (2000), pp. 107–112.

[87] T. E. Bridges, M. P. Houlne, and J. M. Harris. "Spatially Resolved Analysis of Small Particles by Confocal Raman Microscopy: Depth Profiling and Optical Trapping". In: *Analytical Chemistry* 76.3 (2004), pp. 576–584.

Chapter

6 PS-based microfluidic device for malaria detection by SERS analysis

Results and data presented in this chapter are under review to be published elsewhere: ***Maria João Oliveira****, Soraia Caetano, Ana Dalot, Filipe Sabino, Elvira Fortunato, Rodrigo Martins, Miguel Prudêncio, Hugh J. Byrne, Ricardo Franco, and Hugo Águas. Polystyrene-based microfluidic device for malaria detection by SERS analysis. Maria João Oliveira was responsible for the experimental work, except for contributions from PhD Soraia Caetano for the biological sample preparation, BSc Ana Dalot for the expression and purification of the malaria antigen, and MSc Tomás Calmeiro for atomic force microscopy measurements. Maria João was also responsible for data analysis and writing the first version of article.*

To validate the final microfluidic SERS immunoassay system, relevant samples were tested for biomarker detection. This chapter describes the steps and results taken to demonstrate that the developed microfluidic system is suitable for applicability in point-of-care testing (POCT).

Malaria was chosen as a disease to be detected since poses a severe worldwide health threat and there is a need for fast and accurate detection techniques, which surpass the performance of currently used rapid diagnostic tests (RDTs) and are more cost-effective than acid nucleic-based detection methods. Accordingly, the performance of capture platform developed in chapter 4 was firstly evaluated towards *Plasmodium falciparum* histidine rich protein 2 (*Pf*HRP2) using supernatant samples of red blood cells (RBCs) cultures, non-infected or infected with *P. falciparum* with spiked concentrations of *Pf*HRP2.

This protein was chosen because it has been used as a biomarker for detecting *P. falciparum*. *Pf*HRP2 is more sensitive than other malaria biomarkers and several studies have shown a strong correlation between plasma concentration levels of this biomarker and disease severity, and prognosis [1]. Furthermore, recombinant *Pf*HRP2 could be produced in Bionano laboratory, using an overexpression plasmid with *Escherichia coli* BL21 (DE3) as host. The same *Pf*HRP2 detection assay, was performed inside the microfluidic device

to determine its applicability. Furthermore, the sensitivity of the microfluidic SERS immunoassay was evaluated with supernatant and lysed samples of *in vitro P. falciparum* infected red blood cell (iRBC) culture. Parameters such as reproducibility, selectivity, duplex capability, and time and temperature stability were determined to characterise the biosensor as a possible POCT technique.

6.1 Introduction

Malaria is an infectious disease which still prevails despite the significant efforts towards the development of efficient prevention measures, diagnosis and treatment strategies. In fact, the pandemic caused by SARS-CoV-2 in 2020, only exacerbated the number of new clinical episodes, resulting in 69 000 more deaths than in 2019 [2–4]. Nevertheless, the prevalence of the disease is likely related to a combination of inaccurate diagnosis, increased drug resistance, climate changes and political and social factors [5]. Consequently, malaria is still considered a major public health problem worldwide. The disease is the result of infection with the *Plasmodium* parasite, with *P. falciparum* accounting for 90% of worldwide malaria mortality especially in sub-Saharan Africa (≈100% of the cases in 2020)[6]. Nevertheless, *P. vivax* has been associated with severe and fatal outcomes and predominates in the region of Americas (75% of the cases in 2020) and in similar prevalence with *P. falciparum* in Southeast Asia region[2]. It is thus highly relevant to develop new and improved diagnosis approaches, namely for *P. falciparum* infection.

The success of a detection system culminates in the biomolecular event of recognition between the biomarker and the target-specific ligand. *P. falciparum* has various biomarkers including *Plasmodium falciparum* lactate dehydrogenase (*Pf*LDH), *Pf*HRP2, aldolase and hypoxanthine phosphoribosyl transferase, and haemozoin [7]. *Pf*HRP2 belongs to a family of proteins synthetised in *P. falciparum*. This protein has an amino acid sequence composed by 37% of histidine, and 85% being repeats of histidine and alanine but this composition and its molecular weight present a high variability [1]. *Pf*HRP2 is exclusively produced by *P. falciparum* during the asexual stages and young gametocytes of *P. falciparum* being exported by the parasite into the RBCs cytosol and released into the bloodstream when the parasites rupture from the host cell. It has been described as having multiple functions, including hemozoin crystallisation, actin formation, T-cell suppression, glycosamino-glycan binding, and pro-coagulation [8–10]. It is used as a biomarker since several studies showed a correlation between plasma *Pf*HRP2 levels with the disease severity [11, 12]. However, using *Pf*HRP2 as a biomarker means negative results for cases of non-*falciparum* malaria due to inadequacy of detecting other *Plasmodium* spp. and in cases of *pfhrp2/pfhrp3* deletions[13]. *Pf*LDH, conversely, shares epitopes with other *Plasmodium* species, allowing it to be use as a biomarker irrespective of the parasite species, and may therefore aid in cases of malaria misdiagnosis[14]. *Pf*LDH, is a most expressed enzyme required for anaerobic adenosine triphosphate (ATP) generation in *P. falciparum* and is produced by sexual and asexual stages of the parasite[14]. Due to

its function, *Pf*LDH is indicative of a recent infection as opposed to *Pf*HRP2 that due to its stability, remains detectable for 1–5 weeks after treatment. As a result, *Pf*LDH is more reliable to identify unresolved infections[7].

Optical microscopic analysis is still considered the gold standard technique for malaria diagnosis, immediately followed by antibody based RDTs [15–18]. Contrary to optical analysis, RDTs do not require highly trained personnel. These RDTs come mostly in lateral flow immunoassays format, which are rapid (<30 min), user-friendly, and cost-effective, making them applicable for widespread implementation at POCT sites [19]. However, sensitivity limitations, *i.e.* limit of detections (LODs) higher than the threshold recommended by the WHO (200 parasites·μL^{-1}), allied with the inability to detect parasitaemia levels, and susceptibility of the kits to climate conditions (extreme temperatures and distinct humidity levels), may yield false positive and false negative results [15, 19]. Other highly accurate diagnosis methods such as fluorescence immunoassays, polymerase chain reaction (PCR) and its on-field version known as loop-mediated isothermal amplification (LAMP) [20], suffer from complicated operating procedures, long incubation times and need specialised equipment [21].

Several microfluidics systems have been developed to address the limitations of the existing POCT detection methods, as they increase the sensitivity in an automated and portable analysis system. Lee *et al.* [22], used the high surface to volume ratio provided by the reduction of size of the Optimiser™microfluidic chip [23] to improve conventional enzyme-linked immunosorbent assay (ELISA) resulting in a LOD of 1 pg·mL^{-1} for *Pf*LDH in human serum. In a similar approach, Ghosh *et al.* [24] developed a microchannel capillary flow assay platform capable of performing chemiluminescence-based ELISA reporting a LOD of 8 ng·mL^{-1} for *Pf*HRP2 by a smartphone analyser. LabDisks platforms [25] have been employed to improve multiplex detection by PCR, whereas others combined droplet-based microfluidics with magnetic nanoparticles in a fluorescence assay [26]. Interestingly, the paramagnetic property of infected erythrocytes and haemozoin crystal can be explored in a microchip, enabling their concentration to be detected by impedance [27].

While *Pf*HRP2 is the prevalent biomarker in RDTs (due to be only produced by *P. falciparum* and not by any other *Plasmodium* species), haemozoin is the established analyte in Raman spectroscopy [28]. Due to its strong Raman signature, haemozoin has been detected in early ring stages and, if combined with metallic nanostructures, the Raman signal can be enhanced due to the phenomenon of SERS [28, 29]. The advantage of combining the high sensitivity and specificity of SERS with microfluidics was demonstrated by Chen *et al.* [30] with a SERS lab-on-chip system capable of reaching sensitivities of 0.0025% parasitaemia levels. However, SERS-based detection on biomarkers such as haemozoin cannot distinguish between haemozoin from a viable parasite, from the remaining followed by a prior infection [7, 30]. To overcome this limit, other strategies must be designed. One of these strategies is to indirectly detect a biomarker mediated by a SERS tag. Using the Raman signatures combined with plasmonic active metallic

nanostructures and a bio-recognition elements, the fabricated SERS tag can detect target analytes in a complex medium with high sensitivity and specificity [29].

The work developed in this chapter is the culmination of the entire work performed in the previous chapters to fabricate a microfluidic SERS immunoassay. Herein, the rapid and low-cost fabrication of a microfluidic device based on shrinkable PS sheets was used as a system to integrate the sandwich SERS immunoassay. The sandwich SERS immunoassay is composed by SERS immunotags and a capture platform, both with an antibody against *Pf*HRP2. Upon the binding event between *Pf*HRP2 and the anti-*Pf*HRP2, the SERS signal of 4-mercaptobenzoic acid (MBA) from the SERS immunotags is generated and identified by direct classical least squares (DCLS) method for a reliable sensitivity. In a tentative to circumvent the occurrence of deletions of *Pf*HRP2, *Pf*LDH was also detected. Through this duplex recognition, a simple, rapid, and accurate detection of Malaria antigen is achieved.

6.2 Materials and Methods

6.2.1 Materials

The reagents and materials used in the work described in this chapter have already been described in previous chapters. More precisely, the reagents used to produce the SERS immunotags are indicated in chapter 3, section 3.2.2 as well as the capture platform in chapter 4, section 4.2.2, with the exception of the following antibodies used to specifically recognise *Pf*HRP2, *Pf*LDH, and SERS immunotags, namely, anti-*Pf*HRP2, anti-*Pf*LDH and anti-immunoglobinG (IgG), respectively. The mouse monoclonal anti-*Pf*HRP2 and anti-*Pf*LDH antibodies were from Meridian Life Science, Luckenwalde, Germany and Gentaur, Kampenhout, Belgium, respectively. The immunopure mouse anti-IgG was purchased from ThermoFisher Scientific, Waltham, USA. Additionally, in western-blot to detect *Pf*HRP2 mediated by anti-*Pf*HRP2, an anti-Mouse - IgG - peroxidase antibody produced in rabbit was used and purchased from Sigma-Aldrich, St. Louis, MO, USA. Also, the materials used for the fabrication of the microfluidic device have been already defined in chapter 5, section 5.2.1.

Reagents used for obtaining *P. falciparum* culture supernatant, RBCs and iRBCs, and parasite lysate: Roswell Park Memorial Institute (RPMI) - 1640, albumax II, glucose, 4-(2-hydroxyethyl)-1-piperazineethanesulfonic acid (HEPES), sodium bicarbonate, gentamycin, hypoxanthine and L-glutamine, all purchased to GIBCO, Thermo Fisher Scientific, Waltham, USA.

For expression, purification, and biochemical characterisation of *Pf*HRP2 the following reagents were used: Glycerol, ampicillin, potassium phosphate salts, magnesium sulphate, glycine, tris(hydroxymethyl)-aminomethane, citric acid, 3,3,5,5 tetramethylbenzidine, β-mercaptoethanol, polyvinylidene fluoride membrane, and sodium chloride, all purchased by Sigma-Aldrich, St. Louis, MO, USA. Yeast extract, tryptone, and

sodium dodecyl sulphate (SDS), were purchased by Panreac AppliChem, Gatersleben, Germany. Isopropyl β-d-1-thiogalactopyranoside (IPTG), Ponceau S, and molecular weight NZYTech marker I was from NZYTech, Lisbon, Portugal. Imidazole, Coomassie Blue R-250, methanol, and ammonium per-sulphate were from Alfa Aesar – Thermo Fisher Scientific, Waltham, USA. Protease inhibitors (Mini ethylenediamine tetra-acetic acid (EDTA)-free) and DNase I were from Roche, Switzerland and nickel-nitrilotriacetic acid (Ni-NTA) resin from Qiagen, Hilden, Germany. 30% Acrylamide/Bis solution, 37.5:1, tetramethyl-ethylenediamine was purchased from BioRad, Lisbon, Portugal. All chemicals and reagents were of the highest purity available and ultrapure water (H_2O, 18.2 MΩ·cm at 25ºC, *Milli-Q*®) was used for the preparation of all solutions, unless stated otherwise.

6.2.2 Polystyrene chip fabrication

The fabrication of the PS chip was performed as described in section 5.2.3 of chapter 5.

6.2.3 Preparation of biological samples

6.2.3.1 Expression, purification of *Pf*HRP2

The expression and purification of the recombinant *Pf*HRP2 was performed according with the method described by Ndonwi *et al.* [9] with minor modifications. *E. coli* BL21 (DE3) was chosen as the host system, transformed with the *Pf*HRP2 sequence, followed by a 6-His tag in the pET 15b vector. This vector has an IPTG-induced T7 promoter, and was kindly provided by Professor Daniel E. Goldberg (Washington University, USA) [10] (see annex I for details on the pET 15b vector).

A sample of a vial with a seed bacterial starter culture solution stored in a cryoprotective medium with 50% (v/v) Glycerol (Sigma-Aldrich, St. Louis, MO, USA) at -80°C was collected and allowed to grow overnight in Luria-Bertani medium (Yeast extract 5 $g{\cdot}L^{-1}$, Tryptone 10 $g{\cdot}L^{-1}$ and NaCl 10 $g{\cdot}L^{-1}$) and ampicillin 50 $mg{\cdot}mL^{-1}$ for 16 h at 37°C, 220 rpm. Following the growth, the 20 mL from the overnight culture was divided and transferred to 2 L of Luria-Bertani medium. The Erlenmeyer flask was incubated at 37°C, 225 rpm to an optical density of 0.6 at 600 nm. Then, the temperature was lowered to 20°C and 0.5 mM of IPTG (NZYTech, Portugal) was added and incubated for 20 h at 180 rpm. This concentration ensures that the recombinant protein expression do not start at a high rate, which could be detrimental to protein folding [31].

Following the 20 h, bacteria were harvested by centrifugation for 15 min, 6000 rpm at 4°C, in 0.5 L centrifuge tubes (Beckman Coulter) in the Centrifuge Beckman Coulter Avanti J26-XPI with a JA-10 rotor. Pellets were resuspended in a wash buffer (50 mM potassium phosphate buffer pH 7.5, 30 mM NaCl, 30 mM imidazole, Alfa Aesar – Thermo

Fisher Scientific, Waltham, USA). One tablet per 10 mL of protease inhibitors (Mini EDTA-free, Roche, Switzerland), 50 µL of DNase I 5 $mg{\cdot}mL^{-1}$ (Roche, Switzerland), and 50 mM of magnesium sulphate (Sigma-Aldrich, St. Louis, MO, USA) were added to the suspension. The suspension was subjected to French pressure cell at 20000 psi (French pressure cell press, Thermo Electron Corporation – Thermo Fisher Scientific, Waltham, USA) three times and centrifuged at 45000 rpm for 1 h at 4°C in an ultra-centrifuge Optima LE-80K. The pellet was discarded, the supernatant collected and, then passed by gravity flow over an activated Ni-NTA resin (Ni-NTA Agarose, Qiagen, Hilden, Germany) pre-equilibrated with binding buffer (50 mM phosphate buffer pH 7.5, 500 mM NaCl, 30 mM imidazole - Alfa Aesar – Thermo Fisher Scientific, Waltham, USA), to provide favourable conditions for protein binding. The concentration of 500 mM NaCl was used to avoid weak electrostatic interactions of contaminant proteins with the column, and 30 mM of imidazole were used to remove proteins weakly bound to the column. The volume of 1 mL of Ni-NTA agarose was used for every 250 mL of supernatant and mixed via gentle shaking at room temperature for 1 h.

The soluble fraction from the cell lysate was loaded into the chromatography column, and the flow through was collected. The column was washed with wash buffer until an absorbance of less than 0.1 could be observed at 280 nm since amino acids with aromatic rings are responsible for the absorbance peak at 280 nm [31]. This step guaranteed that most of all proteins with nonspecific interactions had been washed from the resin.

Subsequently, the protein was eluted using the column elution buffer (50 mM phosphate buffer at pH 7.5, 30 mM NaCl, 500 mM imidazole), whereby the imidazole competes for the binding of Ni-NTA resin with the histidine residues of proteins [32]. Eluates were collected until the absorbance at 280 nm was less than 0.1. The eluates were concentrated by centrifugation (Amicon Ultra-4 Centrifugal Filter Units, 30k, 4 mL). The concentrated protein was aliquoted in cryovials with 200 µL each and stored in liquid nitrogen until further use. Each fraction, including flow-through, washes, and eluates were tested for purity and molecular weight estimation of the *Pf*HRP2 present using SDS-polyacrylamide gel electrophoresis (PAGE) and western blot (see section 6.2.4). Protein determination was by the BCA method (based on Smith *et al.* [33]) using a kit from Sigma-Aldrich, St. Louis, USA.

6.2.3.2 *Plasmodium falciparum* culture supernatant, infected RBCs, and parasite lysate

P. falciparum parasite strain NF54[34] had been previously cryopreserved in a 57% glycerol solution and was cultured in fresh RBCs at 5% haematocrit in RPMI medium (RPMI 1640, GIBCO) and supplemented with 5% albumax II, 5% Glucose, 1% (v/v) HEPES buffer (GIBCO), 5% Sodium bicarbonate (GIBCO), 5% Gentamycin, 5% Hypoxanthine and 5% L-glutamine with 3% O_2, 5% CO_2, and balance with N_2 gas and incubated at 37°C as previously described[35]. Growth media was replaced two days with fresh

complete malaria culture media. Parasitaemia values were obtained from thin blood smear readings using Giemsa stain on microscope slide.

To obtain the samples for the SERS-based immunoassay, 10 mL iRBCs cultures were centrifuged at 6000 *g* for 5 min. The supernatant was harvested and stored in a sterile centrifuge tube at -20°C or -80°C for later use. The pellet was resuspended in 10 mL PBS with 0.15% (w/v) saponin at 4°C, homogenised (by vortexing) for 15 s, incubated for 5 min on ice, and homogenised for additional 15 s. To induce parasite lysis, 40 µL cold lysis buffer (10 mM Tris-HCl pH 7.5, 0.5 mM EDTA, 1 mM dithiothreitol, 1 mM phenylmethylsulfonyl fluoride and 0.2% v/v Tween 20) was mixed with 10 µL of the lysed iRBCs and incubated for 15 min. These suspensions were centrifuged for 15 min at 6000 *g* at 4°C, and 1 mL of PBS was added to the pellet which was washed three times with PBS and stored at -20°C.

6.2.4 SDS-PAGE and Western blotting

All material used for the SDS-PAGE and Western blotting was cleaned with ethanol 70% (w/v) and ultrapure water before use.

Acrylamide resolving gels (30% Acrylamide/Bis Solution, 37.5:1, Biorad) at 12% (v/v) were chosen based on the molecular weight of *Pf*HRP2 (≈50 kDa) since this percentage offers a separation range of 20-120 kDa. The ratio between sample analysed and sample buffer was always 1:1. Molecular weight NZYTech markers were used, and the samples were incubated at 95°C for 5 min in a thermo-block (Biosan TS-100, Latvia) and subsequently centrifuged at 13000 *g* for 2 min. The electrophoresis was performed in Bio-Rad Mini-PROTEAN Tetra Vertical Electrophoresis Cell at constant voltage (90 V) for 120 min. After electrophoresis, the SDS-PAGE gel was stained with 0.1% (w/v) Coomassie Blue R-250, 5% (v/v) glacial acetic acid, Scharlau, Spain, and 30% (v/v) methanol. Afterwards, the staining solution was removed and added the destaining solution (5% (v/v) glacial acetic acid and 30% (v/v) methanol) until the bands could be discerned and the gel background was clear.

For the Western-blot protocol, after electrophoresis, the gels were transferred to a polyvinylidene fluoride membrane (Sigma-Aldrich, St. Louis, MO, USA). The blotting sandwich was prepared, and the inner module was placed into the electrophoresis chamber with transfer buffer pH 8.3 (Tris 25 mM, Glycine 192 mM, Methanol 20% (v/v)), a magnetic stir, and an ice pack. The transfer was run at 100 V for 60 min. Afterwards, the membrane was blocked for 60 min in 5% (w/v) skim milk in phosphate-buffered saline 1× and Tween 20 at 0.1% (w/v) (PBS-T, Sigma-Aldrich, St. Louis, MO, USA). The membrane was incubated for 60 min in anti-*Pf*HRP2 solution as the primary antibody (1:5000 dilution in 1% (w/v) skim milk in PBS-T) in a rocking shaker (mini-rocking shaker, Biosan, Latvia). Subsequently, the membrane was allowed to incubate for 60 min in the anti-mouse IgG–Peroxidase antibody solution as secondary antibody (1:10000 dilution in 1% (w/v) skim milk in PBS-T). Between each step, the membrane was washed

3 times with PBS-T for 5 min followed by washing with PBS at pH 7.4, 5 mM. A 3,3,5,5-tetramethylbenzidine solution (0.4 $g{\cdot}L^{-1}$) in citric acid buffer pH 5 at 25°C (Sigma-Aldrich, St. Louis, MO, USA) was allowed to react with the peroxidase linked to the membrane in the presence of 0.02% (v/v) hydrogen peroxide solution in the ratio 1:1 (Panreac AppliChem, Gatersleben, Germany). The gel images were further analysed using gel molecular weight analyser feature in the Origin Pro 2020 software.

6.2.5 SERS-based immunoassay of *Pf*HRP2 using the regenerated cellulose hydrogel

The SERS-based immunoassay of *Pf*HRP2 using the regenerated cellulose hydrogel was performed, as previously described in previous chapters 3 and 4. This includes the procedures executed in the preparation of gold nanostars, SERS immunotags (fully described in section 3.2.2), and regenerated cellulose hydrogel production (fully described in section 4.2.2).

For antibody immobilisation on TEMPO-oxidised-regenerated cellulose hydrogel (TO-RCH), volumes were modified as follows: the hydrogel (0.79 mm^2) was washed with ultrapure water and immersed in 32 µL of 10 mM 2-ethanesulfonic acid (MES) buffer pH 6.5. 1-ethyl-3-(3-(dimethylamino)propyl)carbodiimide/N-hydroxysulfosuccinimide (EDC/SNHS) activation was achieved through the protocol described by Dixit *et al.* [36]. Volumes of 32 µL of EDC and SNHS at 20.86 mM and 50.66 mM, respectively, were allowed to react with the hydrogel for 15 min in an orbital shaker at 250 rpm, at 25°C, and the volume was discarded. Afterwards, 32 µL of antibody (anti-*Pf*HRP2 or anti-IgG) at 3.5 $\mu g{\cdot}mL^{-1}$ in MES buffer 10 mM pH 6.5 were added. The solution was mixed with the pipette and incubated for 15 min in the orbital shaker. The sample was left incubating overnight at 4°C. The crosslinking reaction was stopped by washing three times the TO-RCH with 20 mM PBS buffer at pH 7.4 to remove electrostatically bound antibodies. A volume of 32 µL of skim milk as blocking agent at 0.5% (w/v) with Tween 20 at 0.05% (w/v) was added to the membrane and incubated in the orbital shaker for 30 min at 25°C. Therefore, 32 µL of 3.5 $\mu g \cdot mL^{-1}$ of *Pf*HRP2 were incubated for 30 min at 25°C. Between each step, the TO-RCH was washed with 20 mM PBS buffer at pH 7.4 three times, after which the washing solution was removed completely. The SERS-based sandwich immunoassay was finalised by incubation of 32 µL at 1 nM of SERS immunotags for 15 min at 25°C and washing with buffer three times.

6.2.6 SERS-based immunoassay inside the microfluidic device

The SERS-based immunoassay inside the microfluidic device using the TO-RCH was performed as previously described in previous chapter 5, section 5.2.4.

6.2.7 SERS-based microfluidic immunoassay characterisation

To characterise the biosensor, several features were examined, namely, sensitivity, reproducibility, selectivity towards the antigen, time and temperature stability, and multiplexing. The sensitivity was assessed by the parameters LOD and limit of quantification (LOQ) calculated according to IUPAC guidelines[37]. In terms of SERS-based immunoassay, the whole procedure was the same as previously described in section 6.2.6, with the following exceptions: for the selectivity assay, and as a negative control, non-infected RBCs culture was used and compared to an infected RBCs culture (presenting *Pf*HRP2 and *Pf*LDH). For time and temperature stability studies, SERS immunotags and the TO-RCH functionalised with the anti-*Pf*HRP2 were kept in phosphate buffer pH 7.4 and PBS 10 mM at 4°C during assays, respectively. A multiplex assay was performed by adding SERS immunotags with two different Raman reporters (MBA and 5,5-dithio-bis-(2-nitrobenzoic acid) - DTNB) that recognise different antigens, namely, SERS immunotags with MBA, were formed with monoclonal anti-*Pf*HRP2 that recognises *Pf*HRP2, and SERS immunotags with DTNB were formed with monoclonal anti-*Pf*LDH that recognises *Pf*LDH. The SERS immunotags at 1 nM were let to incubate with the TO-RCH immunoplatform loaded with equivalent amounts of anti-*Pf*LDH and anti-*Pf*HRP2 and incubated with the respective antigens as described before in section 6.2.6 to allow the formation of the sandwich immunoassay.

6.2.8 Raman and SERS Measurements

Raman measurements were performed in a Renishaw inVia Qontor micro-Raman spectrometer equipped with an air-cooled charge-coupled-device (CCD) as detector and a He–Ne laser delivering 32 mW of 632.81 nm laser radiation. The final immunoassay inside the microfluidic chip was performed on a microscope slide and the laser beam was focused with a 5× (n.a. 0.12) Leica objective lens (N Plan EPI). The laser was filtered by ≈10%, such that the power at the sample was ≈3.2 mW. Raman images of sandwich immunocomplexes on the TO-RCH were obtained using a Raman point mapping method (scan of 21×21 µm, step of 1 µm). Triplicates were taken of all spectra making a total of 1233 points (pixels) per sample. Between different Raman sessions, the spectrometer was calibrated using the Raman line at 520.7 cm^{-1} of an internal Si wafer. All SERS spectra were recorded at room temperature. All raw data were collected digitally with Wire 5.0 software. Noise reduction, available on the software, was used to estimate and remove the noise through principal components analysis (PCA). Baseline correction using a polynomial fitting (11^{th} order) was then performed, taking care to ensure minimal alteration of raw data. The DCLS analysis was then carried out with in-house scripts written in Python 3.8 (see section B.1 in appendix B). The method is described in section 4.2.7 in chapter 4.

6.2.9 Statistical analysis

For SERS-activity assays, results were presented as mean ± standard-deviation from at least three independent experiments run in triplicates. Normality of the data distribution was assessed firstly by the Kolmogorov-Smirnov [38] and then by Shapiro-Wilk [39] test for increased statistical power. The antigen detection in microfluidic assays were statistically compared using two-sample Student t-test, acquiring the $p-value$ accordingly with Welch correction [40]. To perform a statistical group comparison tests, one-way analysis of variance (ANOVA) [41] followed by the Tukey's multiple comparison test were applied [42]. Outliers were identified by Grubbs test [43]. Significance was considered when $p-values \leq 0.05$. Non-parametric analysis of variance (Kruskal-Wallis test [38]) was performed on the CLS score of individual immunoassay samples across all populations to test the statistical difference between groups.

6.3 Results and Discussion

6.3.1 Performance of capture platform towards *Pf*HRP2

Before testing the applicability in clinical diagnosis of the microfluidic SERS immunoassay, the detection of *Pf*HRP2 on the capture platform was evaluated. Firstly, the recombinant *Pf*HRP2 was spiked in the supernatant of RBCs, and LOD and LOQ were assessed. The native *Pf*HRP2 detection was also performed in the supernatant of iRBCs.

The purified recombinant *Pf*HRP2 produced by *E. coli* BL21 (DE3) culture was evaluated by SDS-PAGE and revealed mainly two bands of approximately 67 kDa and 22 kDa (Figure 6.1a). The 67 kDa is a higher apparent molecular weight than the predicted molecular weight of *Pf*HRP2 (≈35 kDa) [44, 45] but congruent with the ≈60 kDa from the purified native *Pf*HRP2 obtained herein from iRBCs culture (Figure 6.1c), and by other authors [10, 46]. The small increase in molecular weight (≈7 Da) has been also reported by other authors [9, 47] and might be a consequence of the amino acid substitutions during the rapid overexpression of *Pf*HRP2 in *E. coli* leading to protein heterogeneity. Western-Blot with anti-*Pf*HRP2 confirmed the 67 kDa band as *Pf*HRP2 and the reactivity of anti-*Pf*HRP2 monoclonal antibody towards its antigen (Figure 6.1b). Thus, the recombinant *Pf*HRP2 expressed and purified from *E. coli* was suitable for the spiking studies.

Using recombinant *Pf*HRP2 ensures that a known concentration is used while performing the assays. Notwithstanding this, only one sequence of *Pf*HRP2 is encoded by its expression plasmid, and since *Pf*HRP2 presents geographical variability, testing only this copy would limit the reactivity on the immunoassay. Thus, cultures of RBCs were used to identify native *Pf*HRP2 (Figure 6.1c and d). SDS-PAGE stained gel and Western-blot for the supernatants and lysed iRBCs allowed to assess the presence of native *Pf*HRP2 in both fractions which is in agreement with the observations reported by other authors [46].

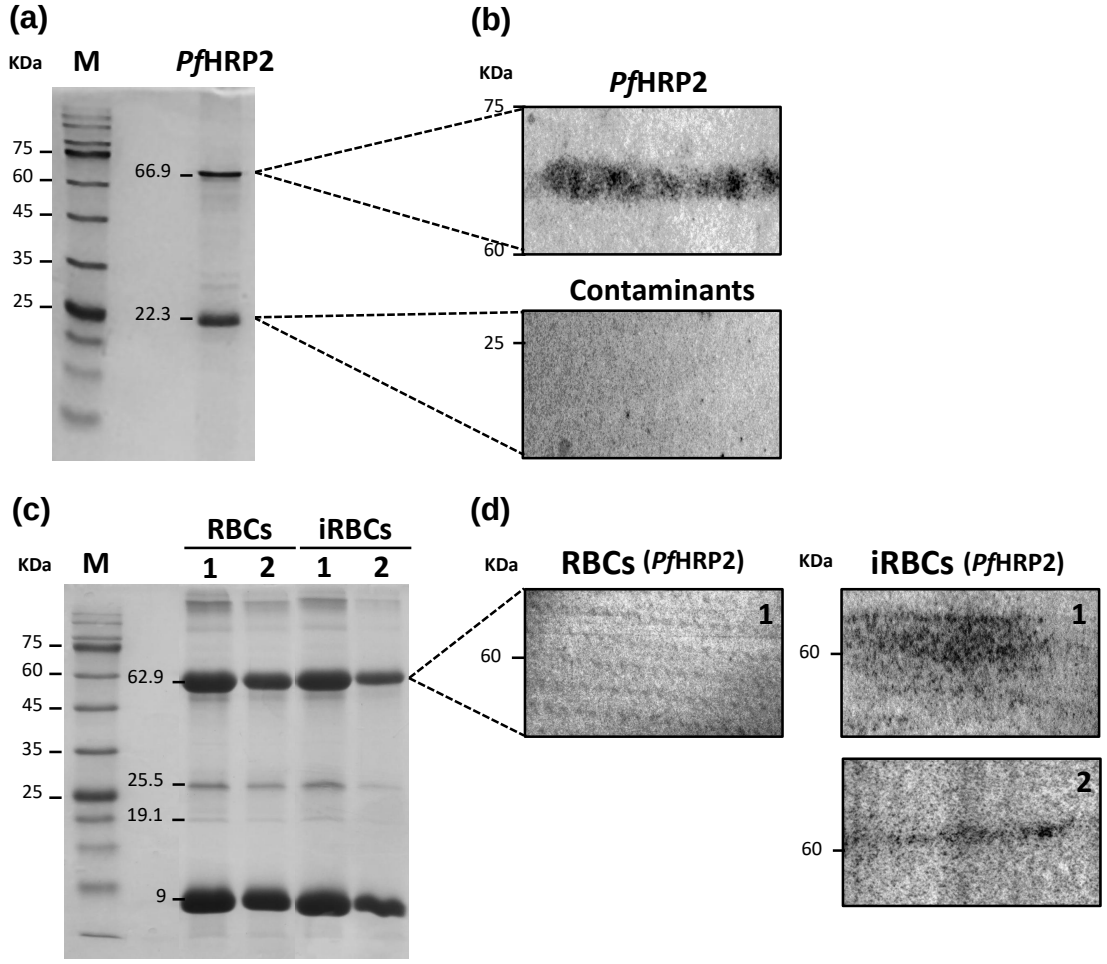

Figure 6.1: Biochemical characterisation of *Pf*HRP2 purified from *E. coli* BL21 (DE3) culture and from RBC and iRBC cultures. (a) SDS-PAGE gel of the purified *Pf*HRP2 by a Ni-NTA affinity column. A molecular weight maker is shown in lane "M" and the second lane is the eluted sample from column purification, *i.e*, *Pf*HRP2. (b) Western blot of the purified *Pf*HRP2 protein from the DE3 culture. (c) SDS-PAGE gel of the supernatant and lysed of infected and non-infected RBCs culture. A molecular weight maker is shown in lane "M". In the next four lanes, two correspond to non-infected RBCs culture and the last two to infected RBCs culture. The numbers "1" and "2" correspond to the lysed and supernatant samples, respectively. (d) Western blot of the iRBCs confirming the presence of *Pf*HRP2 in the lysed and supernatant samples. The same region was tested for non-infected RBCs culture as control.

To evaluate the recombinant *Pf*HRP2 sensitivity of detection by the capture platform, several concentrations in the range from 0.01 to 0.1 ng·L^{-1}, were spiked in diluted of the supernatant of RBCs and iRBCs cultures (Figure 6.2). The sensitivity of the capture platform was also determined using the supernatant of iRBCs culture with several percentages of parasitaemia obtained by dilution in RBCs supernatant (Figure 6.2).

As demonstrated in chapter 4, the DCLS method allows correlation of the SERS signal of MBA from the SERS immunotags to a positive detection of an antigen bound to the antibody immobilised on the capture platform and, consequently, the number of events corresponds to the concentration of the antigen. The supernatant of RBCs was used as the control sample to quantify the amount of non-specific binding of the SERS immunotags to the platform. A threshold value of 0.395 component coefficient was established for positive detection since, from all coefficient values obtained in the control sample, 95% were at or below 0.395. Table 6.1 summarises the LOD and LOQ of the capture platform for the different tested matrices. This SERS immunoassay in the capture platform demonstrated that the system is suitable to detect 1.5 ± 0.1 pg·mL^{-1} of *Pf*HRP2 which is comparable to other reported *Pf*HRP2 immunosensors[26, 48] while it uses a small amount of antibody (3.5 µg·mL^{-1}) and in a complex matrix.

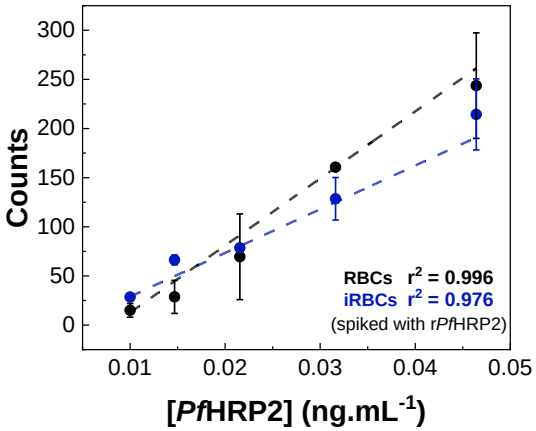

Figure 6.2: Sensitivity of the SERS immunoassay on the capture platform with the supernatant samples of RBCs and iRBCs – spiked and non-spiked with recombinant *Pf*HRP2. Linear fit and corresponding SERS counts from the immunoassay, obtained by the DCLS method. The black points and line with a coefficient of determination r^2 = 97% represent the supernatant samples of RBCs with recombinant *Pf*HRP2. The blue points and lines with a coefficient of determination r^2 = 94% represent the supernatant samples of iRBCs with recombinant *Pf*HRP2. Error bars indicate the standard deviation of three independent experiments.

6.3.2 Performance of the microfluidic device towards *Pf*HRP2

To confirm its applicability for clinical diagnosis, the capture platform performance integrated with the microfluidic device was evaluated using the same type of samples, *i.e*, the supernatant of RBCs and iRBCs cultures were spiked with increasing concentrations of recombinant *Pf*HRP2. The samples to test were inserted through the microfluidic

Table 6.1: Sensitivity of the SERS immunoassay on the capture platform on the supernatant samples of RBCs and iRBCs spiked with recombinant *Pf*HRP2. LOD and LOQ were calculated by the standard IUPAC method [37].

Type of sample	Spiking	LOD ($pg{\cdot}mL^{-1}$)	LOQ ($pg{\cdot}mL^{-1}$)
RBCs supernatant	recombinant *Pf*HRP2	1.5 ± 0.1	7.2 ± 0.5
iRBCs supernatant	recombinant *Pf*HRP2	2.3 ± 0.5	11.2 ± 0.2

device that captures *Pf*HRP2 inside the detection chamber due to the anti-*Pf*HRP2 antibodies immobilised onto the TO-RCH. The debris contained in the microchannels were then washed by PBS-T buffer before inserting the SERS immunotags to allow the formation of the SERS active immunocomplex. The final wash with PBS-T eliminates the excess of SERS immunotags leaving the sandwich complex to be detected by the micro-Raman spectrometer.

As stated in chapter 5, the operating mode of the microfluidic device is as simple as a lateral flow immunoassay with two detection chambers. Each detection chamber has a TO-RCH entrapped whereby the first detection chamber is functionalised with the antibody specific for *Pf*HRP2 (anti-*Pf*HRP2) and the second chamber is functionalised with anti-IgG to recognise the antibodies form the SERS immunotags. This second chamber is therefore a control for the SERS immunoassay.

Figure 6.3a shows the results of the recombinant *Pf*HRP2 detection using the microfluidic device and Table 6.2 shows the calculated LOD and LOQ. Figure 6.3a shows that recombinant *Pf*HRP2 could be detected up to 15 $pg{\cdot}mL^{-1}$ with high sensitivity and specificity which is well below the observed *Pf*HRP2 levels in cases of severe malaria (1000 $ng{\cdot}mL^{-1}$) [49]. It should be mentioned that the SERS signals obtained for the control of the SERS immunoassay, *i.e.* the capture of the SERS immunotags in the second chamber by the anti-IgG, remained constant over the several concentrations tested for *Pf*HRP2 detection (relative standard-deviation - RSD - of 0.72%), which validates the results of the assay.

The device was also tested to compare the performance between supernatants or lysates of the iRBCs cultures samples. For iRBCs supernatants, linearity was obtained for parasitaemias spanning 0.0001–0.0025%, equivalent to 6–1453 parasites·μL^{-1} (Figure 6.3b), whereas for the lysate samples, the parasiteamias tested ranged from 0.005-0.075%, equivalent to 291–4360 parasites·μL^{-1} (Figure 6.3c). The obtained LOD was of 0.0012 ± 0.0001% (equivalent to ≈69 parasites·μL^{-1}) which is a value much lower than the levels considered as low parasitaemia (0.2% of parasitaemia, equivalent to ≈10000 parasites·μL^{-1}) [7].

As shown in Table 6.2, a higher LOD was obtained for the lysate samples, which might be related to the high non-specific binding in the absence of the parasite antigens. Consequently, the threshold defined to consider a positive result must be higher than for the iRBCs supernatant, a matrix with a lower complexity as compared to iRBCs

lysates that contains the cell contents. This high background obtained for lysed RBCs was also reported by others which required an incorporation of a filtration unit (*i.e.* Fusion 5 strip™with 43.9 s·cm^{-1} of wicking rate) to surpass the background interference [50]. Nevertheless, the resultant LOD for the iRBCs samples is close or below the threshold recommended by the WHO, 200 parasites·µL^{-1}, and more sensitive than that provided by most of the commercial RDTs recommended by the WHO [4].

Thus, the microfluidic SERS immunoassay fabricated in this work shows a promising approach to bring a fast, easy, and cost-effective platform for malaria detection.

Table 6.2: Comparison of the sensitivity of analytical methods for SERS-based immunoassay detection towards malaria.

Type of sample	Spiking	LOD	LOQ
RBCs supernatant	recombinant *Pf*HRP2	15.3 ± 0.2 pg·mL^{-1}	73 ± 1 pg·mL^{-1}
iRBCs supernatant	recombinant *Pf*HRP2	14.2 ± 0.5 pg·mL^{-1}	68.0 ± 0.2 pg·mL^{-1}
iRBCs supernatant	-	0.0012 ± 0.0001 %	0.0058 ± 0.0006 %
iRBCs lysate	-	0.013 ± 0.005 %	0.06 ± 0.02 %

Table 6.3 summarises and compares studies on the detection of malaria. The combination of the capture platform developed in chapter 4 and the microfluidic device in chapter 5 allowed the production of a biosensor that it is superior to the ELISA [22], other microfluidic devices [26], and SERS immunoassays [51], and comparable to others [52]. Additionally, the microfluidic SERS immunoassay presented here is easier of fabricate than alternative designs [26, 52].

6.3.2.1 Reproducibility and selectivty

Besides the linearity and sensitivity, for a biosensor to be used in POCT sites, it must present other performance features such as reproducibility and selectivity. The ability of the device to discriminate the *Pf*HRP2 specifically in a complex sample can dictate the ability to avoid false positives results. Accordingly, the selectivity of the microfluidic SERS immunoassay was assessed by testing the responses to the RBCs and iRBCs with or without *Pf*HRP2. As can be seen in Figure 6.4a, when non-infected RBCs are tested, the absence of the target antigen leads to low coefficients (mean of 0.158 and 0.173 for the supernatant and lysate of RBCs, respectively) meaning a negative response. High DCLS scores from SERS signals are only obtained in the presence of the target antigen that allows the formation of the immunocomplex (Figure 6.4a). This behaviour was observed regardless of the type of sample (with or without a purified sample of *Pf*HRP2) which proves that the microfluidic device enables a selective response towards *Pf*HRP2. In fact, these results are congruent with PCR results reported by Jan *et al.* [54].

It should be mentioned that these samples also contains *Plasmodium falciparum* histidine rich protein 3 (*Pf*HRP3), a protein closely related with *Pf*HRP2 with 85-90% homology in the nucleotide sequence, and therefore, the possibility of some cross-reactions

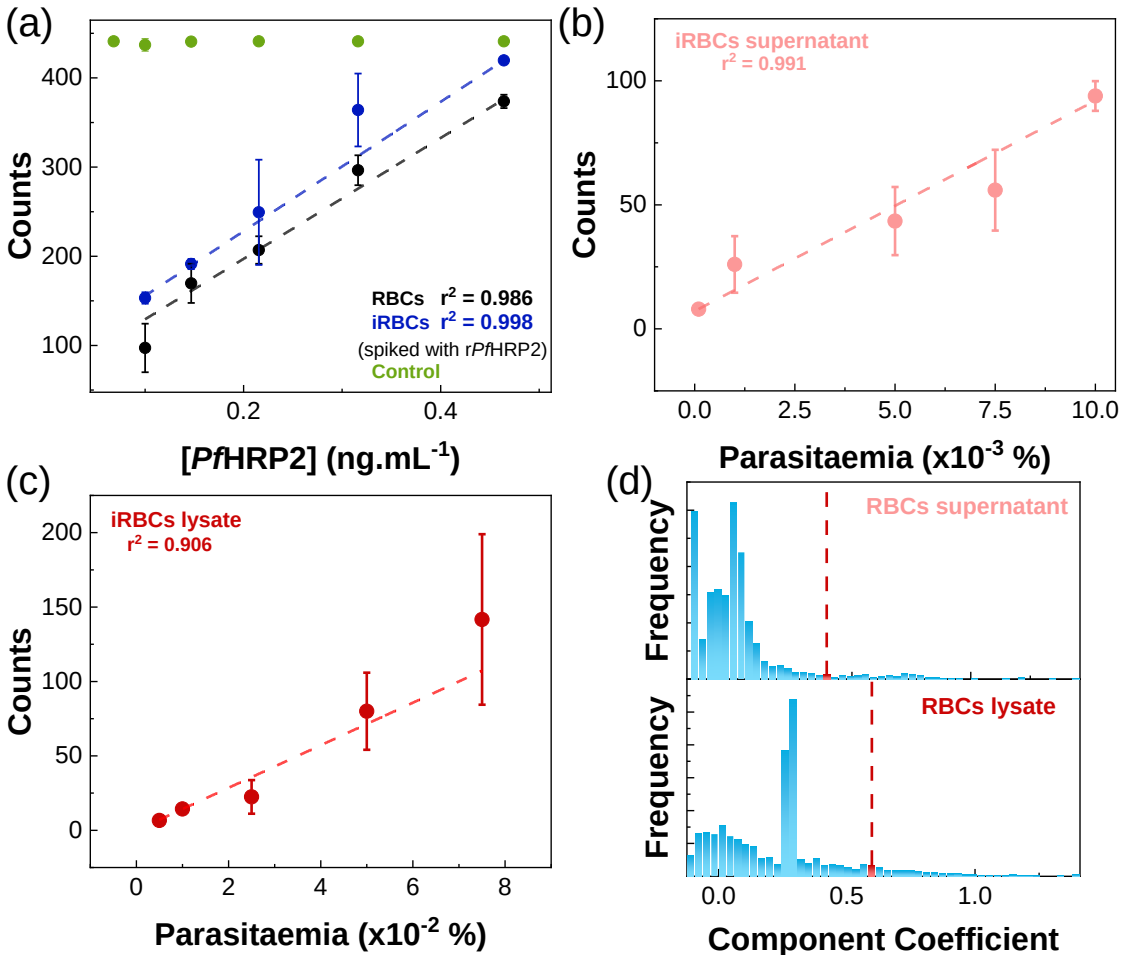

Figure 6.3: Sensitivity of the SERS immunoassay on the microfluidic device. (a) Linear fit and corresponding SERS counts from the immunoassay, obtained by the DCLS method. The black points and line with a coefficient of determination r^2 = 98.6% represent the supernatant samples of RBCs spiked with recombinant *Pf*HRP2. The blue points and lines with a coefficient of determination r^2 = 99.8% represent the supernatant samples of iRBCs spiked with recombinant *Pf*HRP2. The green points represent the SERS immunotags captured by the anti-IgG antibodies immobilised in the TO-RCH. (b) The pink points and line with a coefficient of determination r^2 = 99.0% represent the detection sensitivity of native *Pf*HRP2 in supernatant samples of iRBCs. (c) The red points and lines with a coefficient of determination r^2 = 90.6% represent the detection sensitivity of native *Pf*HRP2 in lysate samples of iRBCs. Error bars indicate the standard deviation of three independent experiments. (d) Histogram of component coefficient frequencies for blanks in the SERS immunoassay (top: RBCs supernatant and bottom: RBCs lysate). The red dashed line represents the 0.452 and 0.627 component coefficient that was considered as the threshold for the positive detection of a SERS immunoassay in RBCs supernatant and RBCs lysate, respectively.

Table 6.3: Comparison of the sensitivity of analytical methods for detection towards malaria.

Analytical method	Target	Type of sample	LOD	Ref.
Microchannel capillary flow assay	*Pf*HRP2	*Pf*HRP2 spiked serum	8.0×10^{3} pg·mL^{-1}	[24]
Droplet-based microfluidic device with antibody-immobilised magnetic beads	*Pf*HRP2	*Pf*HRP2 spiked serum	2.5×10^{3} pg·mL^{-1}	[26]
Gold screen-printed electrodes	*Pf*HRP2	*Pf*HRP2 spiked serum	4.0×10^{2} pg·mL^{-1}	[53]
Q-Plex™Human malaria array using dried blood spots	*Pf*HRP2	Patient blood	1.2×10^{2} pg·mL^{-1}	[54]
Carbon Nanofibers on Glass Microballoons Immunosensor	*Pf*HRP2	*Pf*HRP2 in PBS buffer	1.0×10^{2} pg·mL^{-1}	[55]
PS-based microfluidic SERS immunoassay (λ_{Laser}= 633 nm)	*Pf*HRP2	*Pf*HRP2 spiked in iRBC culture supernatant	1.5×10^{2} pg·mL^{-1}	This work
Silver nanospheres in SERS (mixed with blood lysate) (λ_{Laser}= 633 nm)	Hemozoin	iRBC culture lysate	5.0×10^{2} parasites·mL^{-1}	[30]
Silver nanospheres in SERS (synthetised within blood lysate) (λ_{Laser}= 633 nm)	Hemozoin	iRBC culture lysate	2.2×10^{2} parasites·mL^{-1}	[51]
Inductive sensor (impedance analysis)	Hemozoin	Hemozoin in PBS buffer	5.0×10^{1} parasites·mL^{-1}	[52]
Gold nano-structure substrate (λ_{Laser}= 532 nm)	Hemozoin	Patient blood lysate	1.0×10^{-1} parasites·mL^{-1}	[56]
Sandwich hybridisation-based LAMP	18S	Patient blood lysate	1.3×10^{-3} parasites·mL^{-1}	[57]
PS-based microfluidic SERS immunoassay (λ_{Laser}= 633 nm)	*Pf*HRP2	iRBC culture lysate iRBC culture supernatant	7.5×10^{2} parasites·mL^{-1} 6.9×10^{1} parasites·mL^{-1}	This work

during the immunoassay cannot be excluded [1]. Nevertheless, the microfluidic SERS immunoassay showed an outstanding and reliable selectivity response towards malaria detection.

The inter and intra-reproducibility of the SERS-based immunoassay were also evaluated by performing the immunoassay using three independent microfluidic devices. The RSD for the SERS signal between different devices was of 7.4% indicating similar responses across independent measurements and being ≤10% it can be considered as a good reproducibility (Figure 6.4b).

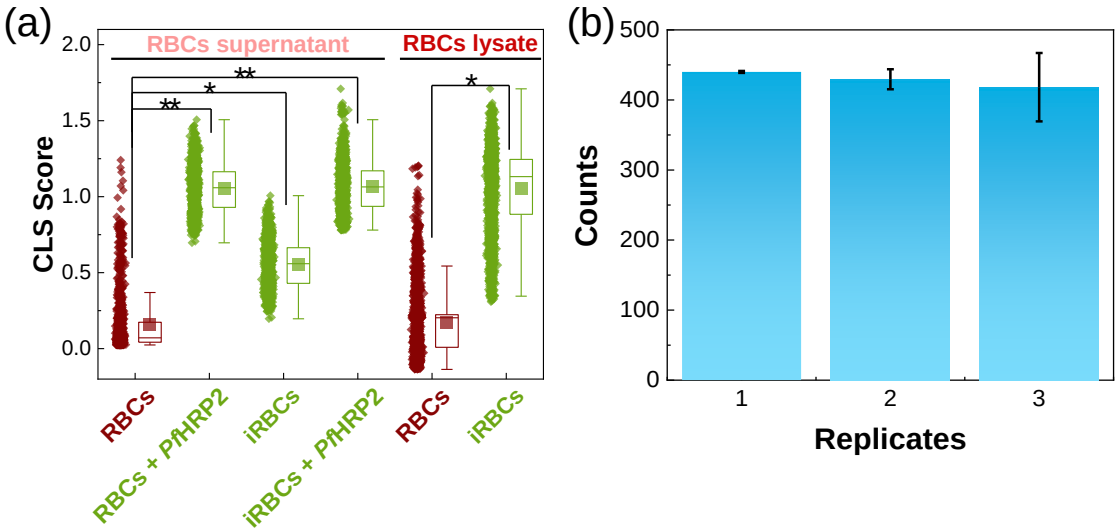

Figure 6.4: Selectivity and reproducibility response of the microfluidic SERS immunoassay based on DCLS results. (a) The DCLS technique was used to quantify the contributions of a negative result (red data), obtained when using the supernatant and lysate of non-infected RBCs ("RBCs"). The positive results (green data) were obtained for the target antigen, *Pf*HRP2. The following samples were analysed: Supernatant samples – "RBCs" is the supernatant of non-infected RBCs; "RBCs + *Pf*HRP2" refers to using the supernatant of non-infected RBCs spiked with *Pf*HRP2; " iRBCs" corresponds to the supernatant of infected RBCs and " iRBCs + *Pf*HRP2" is the same supernatant with *Pf*HRP2; Lysate samples – "RBCs" is the lysate of non-infected RBCs and " iRBCs" is the lysate of infected RBCs. In the box plots, squares are the mean value for each distribution, the middle line represents the median and the top and bottom lines of each box represent the 75 and 25 percentile values, respectively. Whiskers show upper and lower adjacent values which are 3× interquartile range. Non-parametric analysis of variance by Kruskal–Wallis test (ANOVA) was performed for statistical comparisons. $*p \leq 0.05$, $**p \leq 0.01$. (b) Immunoassay activity over three independent chips. Error bars correspond to the standard deviation from three independent measurements.

6.3.2.2 Duplex assay

Parasites that present gene deletions for *Pf*HRP2 (*pfhrp2*) and *Pf*HRP3 (*pfhrp3*) are completely undetectable by most RDTs. Unfortunately, the predominance of these parasites has been documented in several areas including South America, Asia, Middle East, and Africa [4]. This poses a serious threat to the efficacy of *Pf*HRP2-based RDTs and ultimately the patients. Additionally, the *Pf*HRP2 can persist in the bloodstream after the

disease has subsided [7]. Therefore, to improve the usefulness of the proposed microfluidic system, a duplexed SERS immunoassay was performed (see Figure 6.5). This study was performed as described in section 4.3.4 in chapter 4, whereby two different antibodies (anti-*Pf*HRP2 and anti-*Pf*LDH) were functionalised in the TO-RCH platform to capture the respective antigen. The immunocomplex for each antigen is accomplished by the same two antibodies conjugated in SERS immunotags with distinct Raman reporter (RR) molecules (MBA and DTNB). The DCLS method was able to distinguish the two specific RR reporters and the calculated DCLS coefficients for MBA and DTNB were correlated with the parasitaemia achieving a LOD of 0.002% for *Pf*HRP2 and 0.007% for *Pf*LDH. The obtained LODs represent a promising approach for multiplex detection that could avoid the false negative results due to genetic deletions or to non-*P. falciparum* malaria cases.

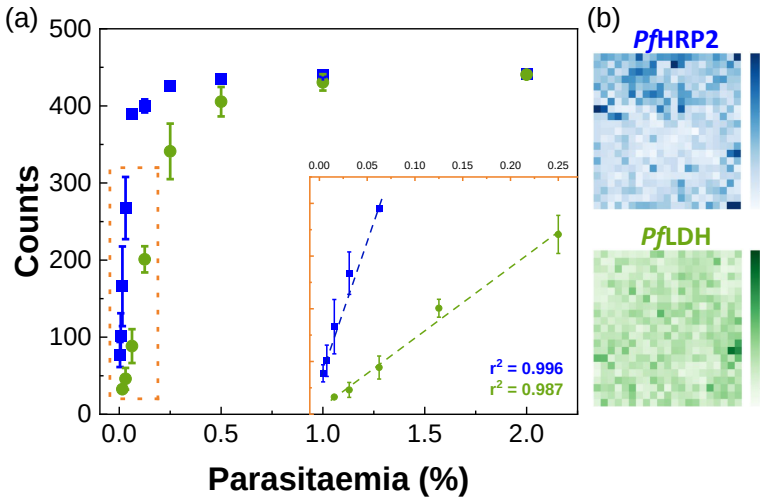

Figure 6.5: Duplex detection of *Pf*HRP2 and *Pf*LDH. (a) Linear fit and corresponding SERS counts from the microfluidic immunoassay, obtained by the DCLS method. Blue data with the coefficient of determination of r^2=99.6% corresponds to the data for *Pf*HRP2 and the green data with the coefficient of determination of r^2=98.7% corresponds to the data for *Pf*LDH. Error bars indicate the standard deviation of three independent experiments. (b) Pixelated SERS maps for duplexing detection. The DCLS method allowed data deconvolution generating the blue map (*Pf*HRP2 detection) and green (*Pf*LDH detection) components. The higher the CLS score, the more intense is the colour.

6.3.2.3 Long-term and temperature stability assay

Malaria, as other infectious diseases such as dengue fever and Zika virus, are typical from tropical and subtropical areas[58]. Thus, any biosensor aiming for application in POCT requires to be thermally stable. Accordingly, the thermal stability of the microfluidic device activity was tested for iRBCs in devices stored at 37°C and compared to the activities observed from devices stored at 4 and 25°C. The devices were evaluated 24 h after the antibody immobilisation was completed, and after 168 h (one week).

The capture platform with immobilised antibodies showed great stability after one

week of storage at 4°C (see chapter 4, section 4.3.5). This high stability was attributed in part to intermolecular cross-linking and to the high-water content environment provided by the TO-RCH. Similarly, as can be seen in Figure 6.6, the capture platform activity remained stable after one week at 4°C and 25°C. For the devices stored at 37°C, is possible to observe a decrease in the SERS activity of 3% after 24 h and only 10% after one week. The high stability provided by the microfluidic device might be related to the low gas permeability of PS used as material of the chip [59]. As a result, the PS encapsulates the capture platform allowing to minimise the evaporation of the buffer inside the microchannels. These results emphasise the importance of biomolecules stabilisation and that the thermal stability can determine if a microfluidic device is suitable for POCT.

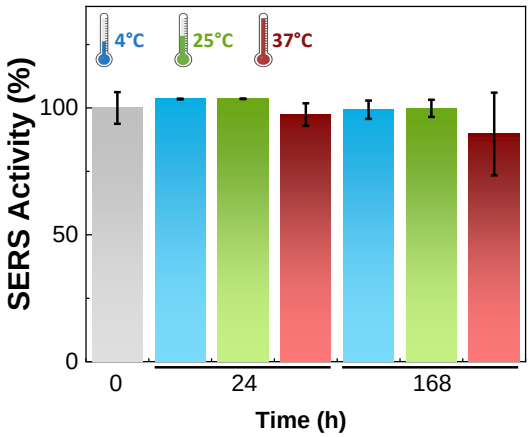

Figure 6.6: Time and thermal stability study. The SERS activity was measured in three independent microfluidic devices at different temperatures, namely, 4, 25 and 37°C after 24 h and 168 h. The grey bar represents the SERS activity measured after the antibody immobilisation (t_0) and the results obtained for the 24 h and 168 h for the 4°C (blue bars), 25°C (green bars) and 37°C (red bars) were compared to t_0.

6.4 Conclusions

Nowadays, the core of malaria diagnosis and management relies on microscopy and RDTs. Since October 2021, the world's first malaria vaccine recommended by WHO was introduced, which could save tens of thousands of children's life every year. Even so, new tools need to be develop in order to successfully implement prevention and treatment measures and hopefully, not limited to malaria.

A microfluidic SERS immunoassay was developed and its applicability to detect malaria, an infectious disease with a high global burden, was evaluated. The system detected the antigen *Pf*HRP2 in a RBC culture supernatant at concentrations as low as 15.3 ± 0.2 pg·mL^{-1}. The detection of plasma *Pf*HRP2 can then be used to correlate with severity of malaria cases. Although some discrepancy exists in the reported values among different works, is possible to connect *Pf*HRP2 concentrations of >1000 ng·mL to severe cases of malaria, whereas cases of severe febrile illness presented *Pf*HRP2 concentrations of

<200 ng·mL[12]. Though clinical samples should be tested in the future, these results suggest that the microfluidic SERS immunoassay developed could provide the means to the diagnosis of low-to-mid malaria parasitaemia levels with minimal user handling. Compared to commercial RDT-based lateral flow assays that detect *P. falciparum*, the microfluidic SERS prototype provided a similar level of operating process. Furthermore, a linearity range of 0.0001–0.0025% parasiteamia was obtained allowing a lower LOD of 0.0012±0.0001% parasiteamia which is the equivalent to ≈69 parasites·μL^{-1}, 7× lower than the maximum level usually obtained for most of RDTs. Thus, this device offered an objective quantification contrary to the qualitative detection provided by the RDTs. Moreover, the entire assay could be completed in less than 20 min. In terms of production, the PS-based microfluidic scalable fabrication makes it is more affordable than the PDMS-based microfluidic devices counterparts that require cleanroom facilities and more complex protocols.

An ever-greater concern is the ability of the assay to perform a differential diagnosis not only to distinguish between *falciparum* from non-*falciparum* malaria but also to respond to *pfhrp2* and *pfhrp3* deletions. The DCLS methods applied herein was able to distinguish between *Pf*HRP2 and *Pf*LDH suggesting the possibility of improving multiplexed systems to detect malaria but also other febrile illness that tend to mimic malaria clinical symptoms. Early diagnosis of these other febrile diseases, will avoid malaria-medication prescription, contributing to lower cases of drug resistance.

Finally, the time and temperature stability of the SERS microfluidic immunoassay were evaluated. This is a parameter that is required for a diagnostic test to be applied in POCT sites, but which is often overlooked. In terms of immunoassays, low temperatures are usually employed to ensure that antibodies are not denatured, which leads to a higher level of transport and storage proprieties. Besides the stability over time, this sensor also displayed thermal stability with capture efficiency remaining at 90% of the initial observed SERS activity. Similar to what was stated in chapter 4, the TO-RCH allows the retention of water and allied to the low gas permeability of PS might have helped to stabilise the antibodies. Thus, this work emphasises microfluidics as a promising solution to integrate new biosensors surpassing the impediments that are obstructing the application of biosensors in POCT.

References for chapter 6

[1] K. E. Poti et al. "HRP2: Transforming Malaria Diagnosis, but with Caveats". In: *Trends in Parasitology* 36.2 (2020), pp. 112–126.

[2] World Health Organization. *World Malaria Report 2021*. Tech. rep. Geneva: World Health Organization, 2021, pp. 1–322.

[3] World Health Organization. *World malaria report 2020: 20 years of global progress and challenges*. Tech. rep. Geneva: World Health Organization, 2020, pp. 1–300.

[4] World Health Organization. *Global Health Estimates 2019: Deaths by Cause, Age, Sex, by Country and by Region, 2000-2019*. Tech. rep. Geneva: World Health Organization, 2020, pp. 1–7.

[5] P. Reiter. "Global warming and malaria: knowing the horse before hitching the cart". In: *Malaria Journal* 7.SUPPL. 1 (2008), S3.

[6] R. W. Snow. "Global malaria eradication and the importance of *Plasmodium falciparum* epidemiology in Africa". In: *BMC Medicine* 13.1 (2015), pp. 23–26.

[7] F. D. Krampa et al. "Recent Advances in the Development of Biosensors for Malaria Diagnosis". In: *Sensors* 20.3 (2020), pp. 799–820.

[8] C. E. Benedetti et al. "*Plasmodium falciparum* histidine-rich protein II binds to actin, phosphatidylinositol 4,5-bisphosphate and erythrocyte ghosts in a pH-dependent manner and undergoes coil-to-helix transitions in anionic micelles". In: *Molecular and Biochemical Parasitology* 128.2 (2003), pp. 157–166.

[9] M. Ndonwi et al. "Inhibition of antithrombin by *Plasmodium falciparum* histidine-rich protein II". In: *Blood* 117.23 (2011), pp. 6347–6354.

[10] D. J. Sullivan, I. Y. Gluzman, and D. E. Goldberg. "Plasmodium Hemozoin Formation Mediated by Histidine-Rich Proteins". In: *Science* 271.5246 (1996), pp. 219–222.

[11] I. C. E. Hendriksen et al. "Diagnosing Severe Falciparum Malaria in Parasitaemic African Children: A Prospective Evaluation of Plasma PfHRP2 Measurement". In: *PLoS Medicine* 9.8 (2012), e1001297.

[12] I. C. E. Hendriksen et al. "Defining *falciparum*-Malaria Attributable Severe Febrile Illness in Moderate to High Transmission Settings on the Basis of Plasma *Pf*HRP2 Concentration". In: *The Journal of Infectious Diseases* 207.2 (2013), pp. 351–361.

[13] P. Pal et al. "*Plasmodium falciparum* histidine-rich protein II causes vascular leakage and exacerbates experimental cerebral malaria in mice". In: *PLOS ONE* 12.5 (2017), pp. e0177142.

[14] K. V. Ragavan et al. "Advances in biosensors and optical assays for diagnosis and detection of malaria". In: *Biosensors and Bioelectronics* 105.January (2018), pp. 188–210.

[15] O. G. Ajakaye and M. R. Ibukunoluwa. "Performance evaluation of a popular malaria RDT in Nigeria compared with microscopy". In: *Journal of Parasitic Diseases* 44.1 (2020), pp. 122–125.

[16] A. Mbanefo and N. Kumar. "Evaluation of Malaria Diagnostic Methods as a Key for Successful Control and Elimination Programs". In: *Tropical Medicine and Infectious Disease* 5.2 (2020), pp. 102–117.

[17] E. C. Oriero et al. "Novel techniques and future directions in molecular diagnosis of malaria in resource-limited settings". In: *Expert Review of Molecular Diagnostics* 15.11 (2015), pp. 1419–1426.

[18] N. M. Pham et al. "Malaria and the 'last' parasite: How can technology help?" In: *Malaria Journal* 17.1 (2018), pp. 1–16.

[19] D. G. Feleke, S. Tarko, and H. Hadush. "Performance comparison of CareStart™ HRP2/pLDH combo rapid malaria test with light microscopy in north-western Tigray, Ethiopia: A cross-sectional study". In: *BMC Infectious Diseases* 17.1 (2017), pp. 1–7.

[20] D. Selvarajah et al. "Loop-mediated isothermal amplification (LAMP) test for diagnosis of uncomplicated malaria in endemic areas: A meta-analysis of diagnostic test accuracy". In: *Malaria Journal* 19.1 (2020), pp. 1–10.

[21] H. Hopkins et al. "Highly Sensitive Detection of Malaria Parasitemia in a Malaria-Endemic Setting: Performance of a New Loop-Mediated Isothermal Amplification Kit in a Remote Clinic in Uganda". In: *The Journal of Infectious Diseases* 208.4 (2013), pp. 645–652.

[22] T. Lee et al. "Single Functionalized pRNA/Gold Nanoparticle for Ultrasensitive MicroRNA Detection Using Electrochemical Surface-Enhanced Raman Spectroscopy". In: *Advanced Science* 7.3 (2020), pp. 1902477–1902488.

[23] J. Kai et al. "A novel microfluidic microplate as the next generation assay platform for enzyme linked immunoassays (ELISA)". In: *Lab on a Chip* 12.21 (2012), pp. 4257–4262.

[24] S. Ghosh et al. "A new microchannel capillary flow assay (MCFA) platform with lyophilized chemiluminescence reagents for a smartphone-based POCT detecting malaria". In: *Microsystems and Nanoengineering* 6.1 (2020), pp. 1–15.

[25] K. Mitsakakis. *Labdisk: the portable lab bringing EU technology to Low- and Middle-Income Countries*. 2015. URL: https://wayback.archive-it.org/12090/20170401085548/ (visited on 04/05/2022).

[26] C. Kim, G. Hoffmann, and P. C. Searson. "Integrated Magnetic Bead–Quantum Dot Immunoassay for Malaria Detection". In: *ACS Sensors* 2.6 (2017), pp. 766–772.

[27] F. Milesi et al. "On-chip selective capture and detection of magnetic fingerprints of malaria". In: *Sensors (Switzerland)* 20.17 (2020), pp. 1–12.

[28] F. Chen et al. "Direct detection of malaria infected red blood cells by surface enhanced Raman spectroscopy". In: *Nanomedicine: Nanotechnology, Biology, and Medicine* 12.6 (2016), pp. 1445–1451.

[29] J. Langer et al. "Present and Future of Surface-Enhanced Raman Scattering". In: *ACS Nano* 14.1 (2020), pp. 28–117.

[30] K. Chen et al. "Towards ultrasensitive malaria diagnosis using surface enhanced Raman spectroscopy". In: *Scientific Reports* 6.1 (2016), pp. 20177–20187.

[31] N. A. Burgess-Brown. *Heterologous Gene Expression in E.coli*. Ed. by N. A. Burgess-Brown. Vol. 1586. Methods in Molecular Biology. New York, NY: Springer New York, 2017, pp. 11–31.

[32] A. Spriestersbach et al. "Purification of His-Tagged Proteins". In: *Methods in Enzymology*. Ed. by J. R. Lorsch. 1st ed. Vol. 559. New York, USA: Academic Press, 2015. Chap. 1, pp. 1–15.

[33] P. Smith et al. "Measurement of protein using bicinchoninic acid". In: *Analytical Biochemistry* 150.1 (1985), pp. 76–85.

[34] P. .-. P. I. Resources. *Gene PfNF54_130076100*. 2022. URL: https://plasmodb.org/plasmo/app/record/gene/PfNF54%7B%5C_%7D130076100 (visited on 07/03/2022).

[35] T. Ponnudurai, A. D. Leeuwenberg, and J. H. Meuwissen. "Chloroquine sensitivity of isolates of Plasmodium falciparum adapted to in vitro culture". In: *Tropical and geographical medicine* 33.1 (1981), pp. 50–54.

[36] C. K. Dixit et al. "Multisubstrate-compatible ELISA procedures for rapid and high-sensitivity immunoassays". In: *Nature Protocols* 6.4 (2011), pp. 439–445.

[37] M. Nič et al., eds. *IUPAC Compendium of Chemical Terminology*. Research Triagle Park, NC: IUPAC, 2009.

[38] D. Sheskin. *Handbook of Parametric and Nonparametric Statistical Procedures*. Ed. by Chapman & Hall/CRC. 5th ed. Boca Raton, Florida: Taylor & Francis, 2011.

[39] S. S. Shapiro and M. B. Wilk. "An Analysis of Variance Test for Normality (Complete Samples)". In: *Biometrika* 52.3/4 (1965), pp. 591–610.

[40] B. L. Welch. "The Generalization of 'Student's' Problem when Several Different Population Variances are Involved". In: *Biometrika* 34.1/2 (1947), pp. 28–35.

[41] P. T. Munroe. "ANOVA (Analysis of Variance)". In: *The Blackwell Encyclopedia of Sociology*. Ed. by P. T. Munroe. 1th ed. Oxford, UK: John Wiley & Sons, Ltd, 2015. Chap. 15.

[42] J. W. Tukey. "The Philosophy of Multiple Comparisons". In: *Statistical Science* 6.1 (1991), pp. 100–116.

[43] F. E. Grubbs. "Sample Criteria for Testing Outlying Observations". In: *The Annals of Mathematical Statistics* 21.1 (1950), pp. 27–58.

[44] N. Hall et al. "Sequence of *Plasmodium falciparum* chromosomes 1, 3-9 and 13". In: *Nature* 419.6906 (2002), pp. 527–531.

[45] *PF3D7_0831800 - Histidine-rich protein II - Plasmodium falciparum (isolate 3D7) - PF3D7_0831800 gene & protein*. 2016.

[46] B. Singh et al. "Purification of native histidine-rich protein 2 (nHRP2) from *Plasmodium falciparum* culture supernatant, infected RBCs, and parasite lysate". In: *Malaria Journal* 20.1 (2021), p. 405.

[47] E. L. Schneider and M. A. Marletta. "Heme binding to the histidine-rich protein II from *Plasmodium falciparum*". In: *Biochemistry* 44.3 (2005), pp. 979–986.

[48] W. Su et al. "Microfluidic platform towards point-of-care diagnostics in infectious diseases". In: *Journal of Chromatography A* 1377 (2015), pp. 13–26.

[49] L. M. Figueiredo et al. "A central role for *Plasmodium falciparum* subtelomeric regions in spatial positioning and telomere length regulation". In: *EMBO Journal* 21.4 (2002), pp. 815–824.

[50] G. Ruiz-Vega et al. "Electrochemical POC device for fast malaria quantitative diagnosis in whole blood by using magnetic beads, Poly-HRP and microfluidic paper electrodes". In: *Biosensors and Bioelectronics* 150.September 2019 (2020).

[51] K. Chen et al. "Review of surface enhanced Raman spectroscopy for malaria diagnosis and a new approach for the detection of single parasites in the ring stage". In: *IEEE Journal of Selected Topics in Quantum Electronics* 22.4 (2016), pp. 179–187.

[52] A. P. Hole and V. Pulijala. "An Inductive-Based Sensitive and Reusable Sensor for the Detection of Malaria". In: *IEEE Sensors Journal* 21.2 (2021), pp. 1609–1615.

[53] A. Hemben, J. Ashley, and I. Tothill. "Development of an Immunosensor for PfHRP 2 as a Biomarker for Malaria Detection". In: *Biosensors* 7.4 (2017), p. 28.

[54] I. K. Jang et al. "Assessment of Plasmodium antigens and CRP in dried blood spots with multiplex malaria array". In: *Journal of Parasitic Diseases* 45.2 (2021), pp. 479–489.

[55] E. Gikunoo, A. Abera, and E. Woldesenbet. "A Novel Carbon Nanofibers Grown on Glass Microballoons Immunosensor: A Tool for Early Diagnosis of Malaria". In: *Sensors* 14.8 (2014), pp. 14686–14699.

[56] W. Wang et al. "Antibody-free rapid diagnosis of malaria in whole blood with surface-enhanced Raman Spectroscopy using Nanostructured Gold Substrate". In: *Advances in Medical Sciences* 65.1 (2020), pp. 86–92.

[57] H. Pian et al. "Sandwich hybridization-based loop-mediated isothermal amplification (SHB-LAMP) for high-throughput detection of malaria RNA from asymptomatic infections". In: *Sensors and Actuators B: Chemical* 365.March (2022), pp. 1–7.

[58] W. Health Organization. *WHO Guidelines for malaria - 3 June 2022*. Tech. rep. Geneva: World Health Organization, 2022, pp. 1–396.

[59] K. Ren, J. Zhou, and H. Wu. "Materials for microfluidic chip fabrication". In: *Accounts of Chemical Research* 46.11 (2013), pp. 2396–2406.

Chapter

7 Conclusions and future perspectives

Part of the future challenges and perspectives presented in this chapter are under review to be published elsewhere:
***Maria João Oliveira**, Hugh J. Byrne, Ricardo Franco, and Hugo Águas. Microfluidic SERS devices: brightening the future of bioanalysis.*
Maria João was responsible for writing the article.

This chapter provides the general conclusions based on the results described in this PhD Thesis as well as an analysis of their significance. Inevitably, several questions remain unanswered and unexplored. Thus, a viewpoint on the future steps that might be taken to evolve the biosensor herein developed, are briefly described in this chapter. Also, a perspective of the challenges yet to be solved and the possible future developments of this research area is also explored.

7.1 Main achievements

Continuous technological evolution enables the development of more sensitive and precise techniques, improving the chance of early detection of disease biomarkers but also becoming the future gold-standard tool of prevention and surveillance. The work described in this PhD Thesis is a contribution to the current technological progress towards an inexpensive, disposable, and automated testing platform. Hence, the main achievements of this Thesis are based on the development of a microfluidic SERS immunoassay system capable of disease diagnosis by capturing the spectra of single SERS immunotags attached to analytes for a reliable identification. The work was guided by two main objectives: the development of the sandwich SERS-based immunoassay, and the fabrication of a microfluidic system capable of integrating the SERS immunoassay to use as a low-cost and simple platform suitable for translation into a working prototype.

The work started with the studies concentrated on creating a fully characterised SERS immunotag. To maximise the signal enhancement observed in SERS, highly branched gold nanostars were synthesised by the seed-mediated growth using gold nanospheres as seeds.

The gold nanostars (AuNSs) were synthesised using a surfactant-free method allowing a simple and effective functionalisation of the AuNSs with a Raman reporter (RR). The RR chosen was 4-mercaptobenzoic acid (MBA) due to its ability of working simultaneously as a capping agent for stabilising the AuNSs, as well as being a RR biocompatible for the subsequent antibody conjugation. The concentration of RRs is frequently confirmed by reaching an equilibrium concentration between colloidal stability and by noting that the SERS spectrum intensity is unchanged [1]. However, this work revealed that, despite using a concentration that is sufficient to exhibit a high SERS intensity and a red-shift of the localised surface plasmon resonance (LSPR), the formation of a RR monolayer should be attained by complementary techniques. Agarose gel electrophoresis (AGE) was used to verify the correct amount of the negatively charged MBA functionalisation agent necessary to fully cover the nanoparticles (NPs).

Two different approaches for bioconjugation were tested, namely, physisorption and chemisortion (covalent), with AGE being crucial on evaluating the conjugation efficiency and optimising the physical-chemical parameters that ensured a successful conjugation. The physical and chemical properties of the SERS immunotags including their morphology, stability, and concentration, were characterised using distinct and complementary techniques to understand the NP-RR-antibody immunotags behaviour. The functionality of these SERS immunotags to recognise an antigen was assessed through the peroxidase/anti-peroxidase model system. Although stable physisorbed SERS immunotags could be easily obtained, as the enzymatic assay proved, their ability to capture the antigen was highly improved by the covalent SERS immunotags. This difference can be explained by the antibody orientation strategy used during the incubation of the protein at the surface of the NPs. A pH lower than the isoelectric point (pI) value was used, promoting a rapid ionic adsorption of the antibody in the correct orientation, while the cross-linking reagents induce the covalent bond. Consequently, the bound antibodies are active and cannot be leached during the several steps of the SERS-based immunoassay and thus the higher enzymatic activity.

The approach developed herein allowed establishment of a method for the development of a fully functional SERS immunotag. Because the antibody used represents a generic immunoglobin (Ig), IgG, antibody, it opened the possibility to use a different antibody for other applications.

A sandwich immunoassay also needs a capture platform. Most of the capture platforms used consist of a biomolecular recognition ligand directly immobilised on a rigid support by covalent means. However, proteins tend to unfold when bound to this type of support [2]. Cellulose-based hydrogels can adsorb water, providing a protecting environment for immobilised proteins [3, 4]. Hence, a regenerated cellulose-based hydrogel was

used as a support for the antibody immobilisation. The regenerated cellulose hydrogel (RCH) is easily prepared from a renewable source, and has a low background fluorescence, allowing a very clean SERS signal, in contrast to other platforms. The same efficient approach that was used on SERS immunotags was also successful in bonding the antibodies to the RCH. Like the studies performed for SERS immunotags, the capture platform was characterised and modified to maximise antigen capture. The high-water content allowed the stabilisation of the antibodies, improving their time-stability and reusability. These two features have the potential to substantially reduce the biosensor's cost, making it more commercially attractive. The robust design presented herein promises the applicability of the sandwich SERS immunoassay in a microfluidic device for point-of-care testing (POCT) sites.

An important improvement made for these type of SERS assays was the inclusion of the direct classical least squares (DCLS) method for SERS analysis protocol. DCLS was demonstrated to be a simple, yet robust method to identify and quantify SERS signals from the SERS immunotags even in situations of partially overlapping key Raman bands derived from other components of the assay. As a result, quantitative mapping with DCLS treatment provide a more reliable method for limit of detection (LOD) and limit of quantification (LOQ) as compared to the traditional peak integral method.

The developed SERS immunoassay needs to be portable to be applied in POCT sites which can be accomplished by integrating the immunoassay into a microfluidic device. polystyrene (PS) belongs to a group of materials that have been exploited for microfluidics as an alternative for the polydimethylsiloxane (PDMS)-based microfluidics. Although PDMS has a rubber-like elasticity and a resolution limit useful for biological analyses, its low chemical resistance, the tendency to adsorb small molecules, and lack of scalability for mass-scale production, made PDMS until now unsustainable for applying it in commercial biosensing platforms worldwide. Shrinkable PS sheets allow to construct a 3D multilayer device by stacking each sheet providing a process simple to implement, which is also rapid and versatile. In particular, the transparency of the sheets makes these devices convenient for optical detection, either for colorimetric assays or, as in this work, for SERS-based assays.

Hence, pre-stressed PS sheets were used to develop a novel microfluidic SERS immunoassay device. Simulations of the microfluidic device design before its fabrication helped to elucidate what were the main features of the microfluidic system that influence the fluid behaviour at microscale, and what was the expected response time that the biosensor was going to operate. The simulation performed validated the proposed PS microfluidic chip.

The parameters at which the laser ablation occurs can greatly influence the microchannels obtained and need to be optimised to generate a good quality pattern with no degradation. One of the main advantages of using these shrinkable sheets has been demonstrated by this work whereby channels of width ≈230 µm and detection chambers with 1000 µm of diameter, obtained during the laser engraving, were shrunk to ≈130 µm and

≈500 μm, respectively. This process yields a reduction of dimensions by 58%, and more importantly, the whole procedure takes ≈30 min to complete and all the steps can be made in large-scale production.

Proteins tend to adsorb non-specifically to hydrophobic materials, and the higher the hydrophobicity, the higher the protein's affinity[5]. PDMS is naturally hydrophobic, and several surface treatments have been made to reduce the hydrophobicity including plasma and UV/ozone treatments [6], polymer coating [7, 8], among others [5]. None of these treatments are stable over time and imply extra steps [5]. An interesting finding in developing a PS-based chip was that the resolidification of PS during thermal bonding and shrinking process led to a decrease in surface roughness followed by an increase of hydrophilicity. This hydrophilicity portrays an improvement for microfluidics devices applied in biosensing.

The full transparency of the PS chip allowed the colour development in the enzymatic assay to be seen, which opens the possibility of using this type of devices for colorimetric applications. The SERS measurements performed on the PS-based chip demonstrated that SERS immunotags can be recognised inside the microfluidic device upon the sandwich immunocomplex.

Ultimately, all the previous work converged to a final and decisive step, of malaria antigen detection. Malaria was chosen as it is a life-threatening disease that is preventable and curable with early diagnosis and treatment. Hence, the fabricated microfluidic SERS immunoassay platform was tested for two different *P. falciparum* malaria antigens, namely, *Plasmodium falciparum* histidine rich protein 2 (*Pf*HRP2) and *Plasmodium falciparum* lactate dehydrogenase (*Pf*LDH). The duplex detection of the SERS sandwich assay formed in the detection chamber confirmed the presence of both malaria antigens. This type of duplex assay is highly desirable for regions where deletions of *Pf*HRP2 and/or *Pf*HRP3 are prevalent. The biosensor showed high specificity, and sensitivity while the complete assay can be done in less than 30 min. This proves that SERS biosensing presents competitive features to state-of-the-art diagnostic tools. Table 7.1 compares several important features required in a biosensor applied on a POCT site highlighting the advantages of each approach.

In summary, this dissertation results in a combination of life and material sciences and the biosensor developed in this work has the potential for scalability for massive biosensor platforms production. Hence, this biosensor represents a promising approach for the future of on-site analysis in health applications, but not limited to them, as it can be applied in different areas such as environment, food safety and industrial applications.

7.2 Advances beyond the State-of-the-Art

Accurate and timely detection of diseases, food contaminants and pollutants is crucial for effective response management. Currently, detection modalities rely on techniques used in high technology research laboratories. The massive advances of nanotechnology

Table 7.1: Comparison of SERS-based and clinical standard diagnostics for malaria infection [9–14].

Diagnostic tools	**PCR**[1]	**RDTs**[2]	**Microscopic Examination**	**This work**
Time	≈3 h	≈15 - 30 min	≈1 h	≈15 - 30 min
Volume (µL)	200	≈100	50	20
Cost (€/test)	30–95	≈5	≈12	ideally ≈5-15
LOD (parasites·µL^{-1})	0.5≤ 5	100-500	10-20[3]	69
Complexity	Moderate to high	Simple	Simple	Simple to moderate

[1] PCR: polymerase chain reaction.
[2] RDTs: rapid diagnostic tests.
[3] Expert personnel and good quality materials can achieve to <5 parasites·µL^{-1}, but under typical field conditions, the sensitivity is only ≈100 parasites·µL^{-1}.

have enabled the development of new and efficient systems with applications aimed at molecular detection and imaging, multifunctional therapeutics, and prevention and control of diseases[15–18].

Among the range of novel detection techniques, SERS has emerged as an ultrasensitive vibrational spectroscopic technique[19, 20]. Once seen as merely an extension of Raman spectroscopy, SERS has evolved as a new and vibrant multidisciplinary research field[19]. Although a field with a short history, since its accidental discovery[21], SERS has seen unbelievable advancements in many different areas and in several configurations. The use of SERS in bioanalysis is rapidly evolving as a suitable and powerful approach for disease detection and treatment[20]. This Thesis is a result of that growing interest.

During the development of the SERS immunotags, AGE, a well-established technique, proved to be decisive during the process of SERS tags formation allowing to verify the amount needed to form a monolayer around the NPs. This monolayer was essential to originate the strong signals observed in SERS measurements and more importantly, in a more reproducible way.

Regardless of the method, is important that the conjugation is specific enough to bind the biomolecule to the NP, while not interacting with its native structure, potentially altering its biological activity. Ideally, the conjugation strategy results in a stable colloidal system as a result of the attachment of biomolecules in a controlled manner, whereby the concentration is sufficient to cover the NP surface but also retain its activity. Parameters used during bioconjugation, such as pH, can even greatly influence the tertiary structure of proteins in the bioconjugates[22]. Analysing the bioconjugation process through AGE provided the means to assess how each parameter influences the microenvironment of the NP surface once biomolecules are conjugated to NPs.

Also, a RCH was developed and used as a capture platform for a SERS-based immunoassay. This hydrogel belongs to a class of materials that has recently attracted

interest as a support for protein immobilisation, specifically enzymes[23]. The motivation to use this type of materials is related to their biocompatibility, flexibility and particularly due to their high-water absorption capacity which increases the resistance of the proteins to temperature and pH variation[3]. This is notably the case when comparing the functionality of proteins immobilised onto rigid supports. These striking advantages are further supported by the fact that hydrogels have usually low production costs, and their synthesis and functionalisation can be carried out under mild conditions, as demonstrated in this Thesis.

Although several works report the use of hydrogels impregnated with NPs to produce a SERS-active substrate, none have been used as a capture platform for a SERS immunoassay. As demonstrated, RCH provided a robust capture platform with low background in Raman measurements, allowing a clean signal from the SERS tags.

The detection of SERS tags in the SERS-based immunoassay was even improved by implementing the DCLS method for identifying and quantifying the SERS tags. Several multivariate analysis (MVA) methods have been used in SERS field especially in label-free analysis but the current state-of-art in label detection is rapidly embracing more MVA methods which will certainly play an important role in the future of biosensors field[24].

Another important achievement beyond the state-of-art was the inclusion of a SERS-based immunoassay into a microfluidic device using shrinkable PS sheets. This low-cost, rapid, and simple to implement method enabled production of a 3D microfluidic chip as the basis of a novel microfluidic SERS-based immunoassay.

Finally, for the first time, this PS-based microfluidic SERS immunoassay device was employed for detection of malaria. Not only was it able to detect *Pf*HRP2, the ability of duplex detection of two malaria biomarkers (*Pf*HRP2 and *Pf*LDH) inside the same detection chamber was demonstrated. In addition, it should be possible to produce more detection chambers, without tremendously increasing the complexity of the device. As demonstrated by producing a second chamber, this microfluidic SERS immunoassay has the ability to use not only multiplex detection by differentiating different SERS tags, but also by localisation inside the device.

All these achievements led towards the development of a prototype of a device that is cost-efficient, robust, sensitive, and suitable for POCT through SERS analysis. Nevertheless, continuous improvements need to be made, and the next section focuses on some suggestions to improve this microfluidic SERS immunoassay.

7.3 Future challenges

An undeniable truth in science is that there is always room for improvement, and this work is no exception. The REASSURED framework[25] was used as a guide, but there are still several unmet challenges.

The pursuit for development of SERS tags with application in bioanalysis has contributed significantly to understanding the physicochemical properties of the NP-biomolecule system that determine the outcome of these tags. Still, several challenges remain unsolved, such as SERS tags reproducibility, quantification and calibration, expansion of multiplex labelling ability, reduction of the tag's size for high-spatial SERS imaging and *in vivo* tracking ability.

In parallel, the microfluidics field has seen as enormous growth over the years, with a broad range of applications. Notwithstanding this, microfluidics platforms can be greatly improved by increasing the amounts of laboratory protocols that can be included in one single device. Besides automation, the lifespan of the chip (*e.g.* possible channel blocking and clogging), the low throughput (*e.g.* single channel designs), the complex fabrication and limitations linked with material chosen, and the Raman signal of the material's device are among the questions needing answers.

The following section describes a few topics that can improve the microfluidic SERS immunoassay, applicable not only to malaria detection, but to several other biosensing applications.

7.3.1 Reproducible signal of SERS tags

Reproducibility has been a feature much criticised in SERS field. In the case of SERS tags, two factors must be considered: the hotspots and the RR molecules. Uniformity and distribution of both factors can have a tremendous impact in clinical diagnosis and biochemical detection and is one of the reasons why SERS has not yet made the translation into standard detection methods in clinical fields.

The precise control over hotspots plays an important role in designing SERS substrates since Fang and co-workers reported that the (*ipsis verbis*): "hottest sites ($h < 10^9$) account for just 63 in 1,000,000 of the total but contribute 24% to the overall SERS intensity" [26]. Random aggregation of metal NPs was one of the first approaches to increase Raman signal enhancement. However, irreproducible results together with lack of correlation of SERS signal with the exact nanostructure from which it originates, led to abandonment of this approach. A controlled aggregation mediated by a bifunctional linker (*e.g.* polymers [27], oligonucleotides [28, 29], or even the analyte [30]) connecting NPs together is one of the most used methods to form NPs clusters in a more reproducible way. These bifunctional linkers are placed in the hotspot, and some can also act as a RR. These approaches mean that, to profit from these hotspots, the molecules must be RRs or competing with the linking molecules for the vicinity of the hotspot. The molecular binding events triggered by small molecules can also be explored to act simultaneously as an aggregation and a detection binding event. Cholera toxin, for instance, binds to monosialoganglioside, and can be integrated in RR labelled AuNPs which assemble into cross-linked aggregates in response to cholera toxin. Nevertheless, only small molecules can be used as analytes, so this approach lacks universality.

Controlling hotspot formation by chemical processes increases the possibility for a RR molecule be in vicinity of these strong electromagnetic fields and subsequently a more reproducible SERS signal than simple aggregation of spheres [31]. Two main approaches can generate particles with several hotspots: anisotropic etching and anisotropic growth. Anisotropic nanocrystal growth methods provide several hotspots per particle and thus, were used in this work [32]. Nevertheless, not all geometries are possible and thus, anisotropic etching processes allows preparation of new NP shapes with high yields and purity [33]. However, these methods still present a higher complexity degree comparing with anisotropic growth and are usually achieved in the presence of a polymer which might impair RR adsorption to the NP when preparing SERS tags.

A reproducible signal is also dependent on the population of the produced SERS tags. Ensuring that all SERS tags yield the same SERS enhancement can be addressed via self-assembled monolayers (SAM)-coating or by purifying post-synthetic bioconjugates. Example of some techniques such as size-exclusion chromatography [34], diafiltration [35], centrifugation (in particular, density gradient centrifugation) [34, 36–39], have been used to separate metal NPs according to size and shape due to sedimentation-coefficient differences. These colloidal spatial isolation techniques can be extremely helpful to reduce the ambiguities in calculating and interpreting the respective SERS enhancement factors.

Crucial to improve reproducibility is the bioconjugate process by employing methods as based on click chemistry to assure that all the specific-target ligands exhibit the same orientation and consequently, the same specificity towards the analyte [40].

7.3.2 Improving multiplexing capability

The requirement for developing multiplex assays is related to the fact that many diseases cannot be diagnosed from a single biomarker detection. The parasite that causes malaria, for instance, has shown deletions in the genes that encode two of the main proteins used as antigens in RDTs (*pfhrp2* and *pfhrp3*). These strains with deleted genes have been reported in several countries, and although the global distribution of this phenomenon is not completely understood, these strains are undetectable by *Pf*HRP2-based RDTs [41]. Additionally, all the multiplex tests that can distinguish between *P. falciparum* and *P. vivax* require the detection of *Pf*HRP2 [42]. Furthermore, malaria is only one of the neglected tropical diseases and co-infection (*e.g.* with Epstein–Barr virus, Human immunodeficiency virus - HIV, *Trypanosoma cruzi*, among others) is not uncommon resulting in a synergistic epidemic [43].

Therefore, the ability of a mixed suspension of SERS tags to be used for simultaneous detection of multiple targets with high sensitivity and selectivity is the main motivation for the development of encoded SERS tags. The practically unlimited number of barcodes is due to the narrow and characteristic vibrational bands. Although several papers report two or three reporters with non-overlapping characteristic bands, the complexity that comes from using more reporters, can impair the peak integral method to validate the

SERS tags identification [19, 44–46]. To date, few papers have reported a library and systematic analysis of several SERS tags encoded with different reporters. In part, this due to the different chemical nature of the involved RRs (*e.g.* aromatic thiols versus fluorophore dyes) making difficult to design a collection of SERS tags feasible and scalable over a wide number of RRs. Some authors circumvented this problem by inserting an additional parameter to the number of RRs – the stoichiometric ratio (see Figure 7.1a). Mixing RRs to form a multicomponent SAM in different ratios, a bar code of only three reporters could generate seven different signals [47]. Notwithstanding this, these kinds of methods can only be applied if the RRs used have equivalent anchor groups. To achieve multiple active SERS tags, the design strategy must be independent to the chemical nature and size of the RR used, and few examples have been reported [48, 49]. Mir-Simon *et al.*, for instance, designed a synthetic strategy capable of testing 31 different codes [49]. Instead of using different codes, it is possible to divide them spatially. Fabrication of arrays provides the ability of using few SERS tags which are spatially addressable and thus enhancing the capability of multiplexing [50–52].

Combining sensing tags is another option to increase the multiplex ability. Dual modal nanoprobes, resulting from mixing two different RRs with two fluorophores, allows four codes suitable for cell imaging (see Figure 7.1b) [53]. If instead of fluorophores, quantum dots (QDs) are used, a larger encoded capacity is obtained. QDs have narrower emission bands and produce more colours that can be multiplexed. When combined with SERS tags, the number of available codes theoretically increases to $2^{m+n} - 1$, m being the number of QDs and n the number of SERS tags [46]. Multiplexing capacity of different type of reporters is shown in Table 2.1 in chapter 2.

However, using an increasing number of reporters will inevitably lead to overlapping bands making difficult to identify accurately individual tags. Multivariate curve resolution methods and machine learning can aid to overcome these pitfalls as described in section 7.3.4.

7.3.3 SERS tags quantification: Calibration of SERS intensities and enhancements

Improvements in SERS quantification, especially in a multiplex assay, are almost always followed by selecting a suitable calibration method for real sample analysis. Calibration of Raman signals in conventional Raman analysis is a typical procedure to minimise the variance of Raman instrumental and experimental factors including variation in the optical alignment, changes in excitation laser power or detector, and variation in the positioning of the sample. Measuring band intensities of the compound of interest against a standard might aid to achieve a more reliable quantitative analysis. In other words, adding a calibration method corrects the effects of changes in scattering from solutions due to turbidity, or inner filter effects from absorbing compounds and differences in focus due to non-uniform sample morphology from solids. Calibration methods can be external

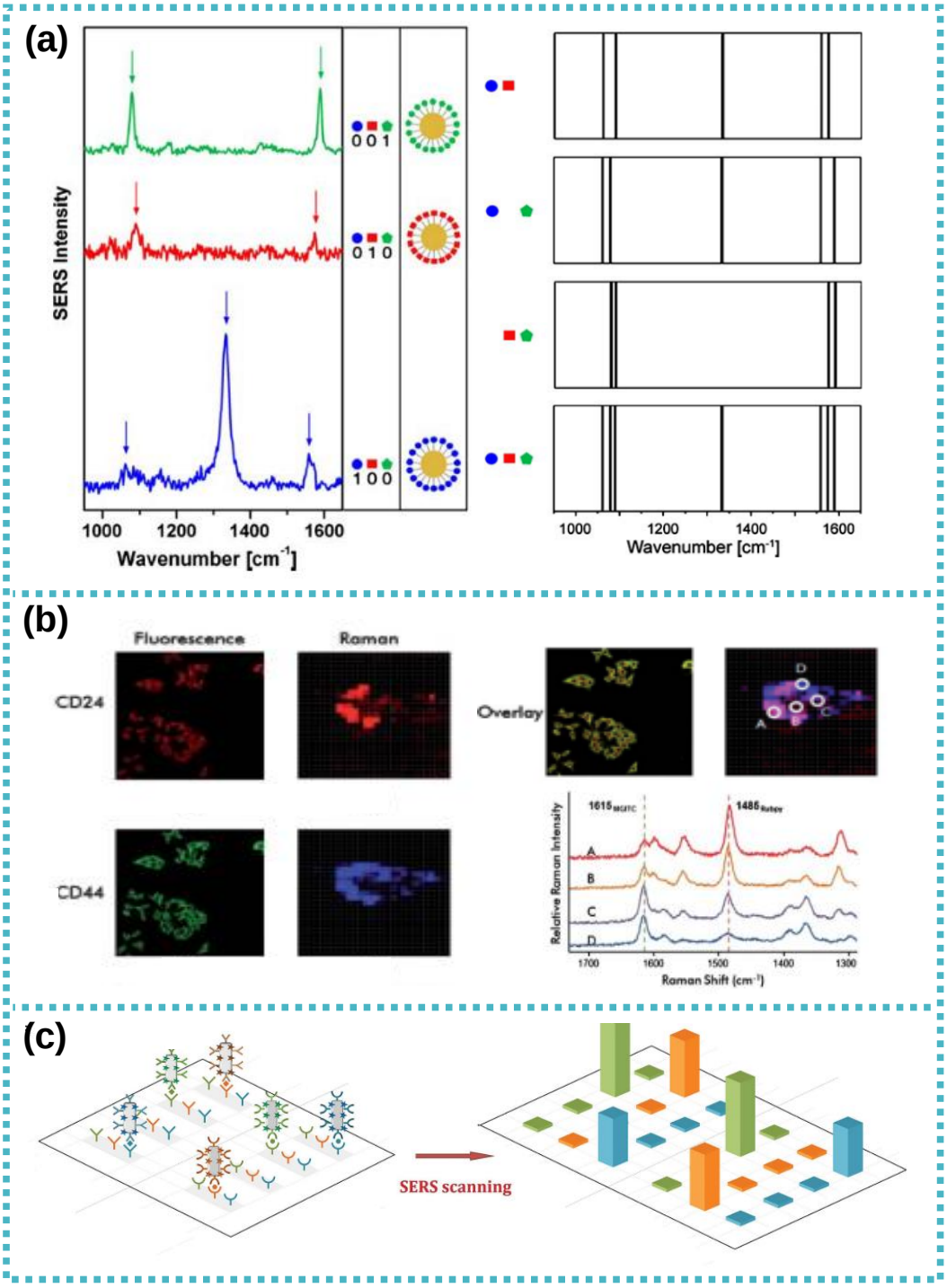

Figure 7.1: Examples of multiplex capability from SERS-based assays. (a) SERS spectra of one-component SAMs on AuNP: 5,5-dithio-bis-(2-nitrobenzoic acid) (DTNB) (blue), 2-bromo-4-mercaptobenzoic acid (red) and MBA (green). Bar code diagrams for SERS spectra of one-, two-, and three-component SAMs on AuNPs. Adopted from [54]. (b) Dual sensing through fluorescence-SERS duplex imaging of CD24 and CD44 markers expressed in MDA-MB-231 breast cancer cells. Raman spectra for four different spots (A, B, C and D). The 1485 cm^{-1} band of Rubpy and 1618 cm^{-1} band of malachite green isothiocyanate were used to identify localised distribution of CD24 and CD44 markers in the cell. Adopted from [55]. (c) Multiplex immunoassay using the 3D barcode chip. Different antigens can be identified according to the 2D spatial information and the characteristic Raman bands. Adopted from [52].

or internal [56]. External calibration provides high-throughput analysis with quantitative results in a short time, but is usually performed in different matrices of the testing solutions from real samples, which can decrease the calibration results accuracy [57]. Addition of internal standards into sample solutions can partly neutralise the influence of the sample matrix [58]. Internal standards provide SERS signal that can be correlated with a tag signal reducing the fluctuations of near-field enhancement among different hotspots and variations of instrument factors [59–61]. Therefore, internal standards should be sought in future works.

Although a universal standard detection method is lacking, the use of references always leads to an improvement in the linear fitting degree which indicates that the accuracy of quantitative SERS measurements has been significantly increased.

7.3.4 Robust spectral interpretation through multivariate curve resolution methods

Univariate quantification is based on taking a well-defined SERS vibrational band and calculating the area that is correlated to the concentration of the target analyte. Whilst caution is needed to apply the baseline and to subtract the background to give highly accurate results, this method usually works well when the SERS signal of the analyte is clean *i.e.* is unique and not crowded or overlapped with other spectral features. The situation changes when the analyte is within a complex matrix or when the goal is to perform quantitative multiplexed analysis. MVA techniques use the whole spectrum, or a subset of the spectral features as input and simplifies the multivariate data into a result with lower dimensions which is more readily interpretable. In other words, these methods simplify complex bio-spectroscopic information and consequently, one can draw conclusions about the sample. These MVA methods are included in the machine learning (ML) group and their role in spectral analysis has seen a prevalent increase in literature. MVA have been used in many analytical chemistry fields including Raman spectroscopy for many years [62–65], whereas their application within SERS, especially in SERS tags, for quantitative analysis is comparatively less well explored [24].

An important note to bear in mind while reading this section is that there is an overwhelming number of machine learning methods and their classification changes from report to report. A general scheme of the artificial intelligence universe is represented in Figure 7.2.

MVA may be exploratory analyses or multivariate regression based. Exploratory data analysis allows to extract a relationship between groups of samples with no prior information which means that they are unsupervised [63]. principal components analysis (PCA) is a very common, unsupervised chemometric approach that is used to visualise and explain the variance in data [66, 67].

More powerful methods of analysis belong to supervised learning methods. The goal of these methods is to ascertain whether measured SERS spectra can be correlated

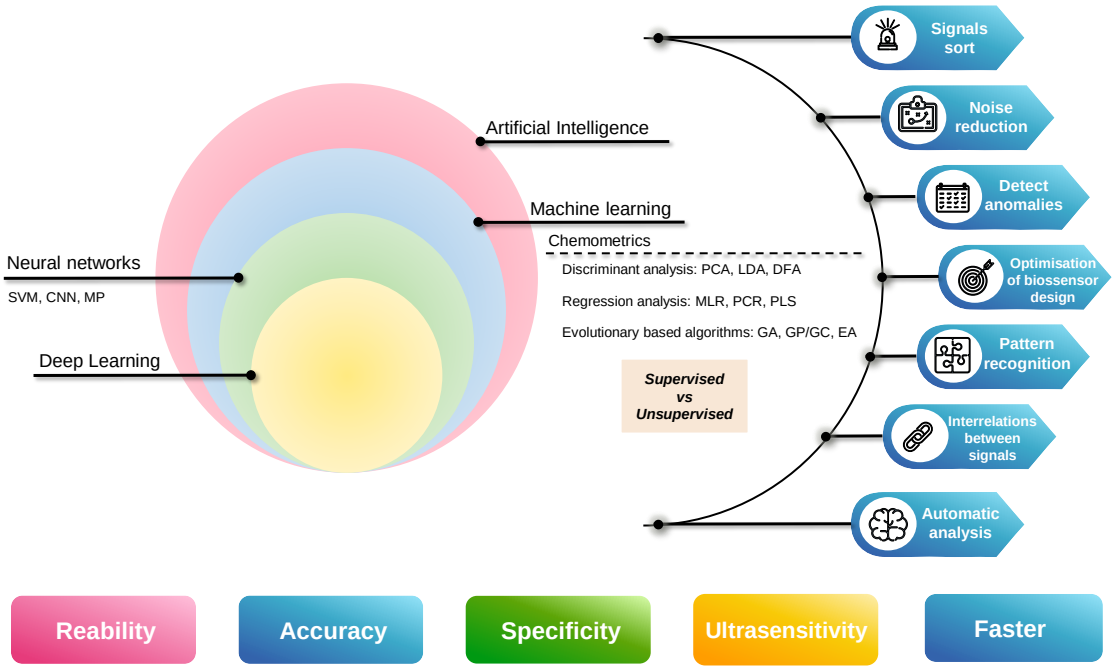

Figure 7.2: Relationship between artificial intelligence, machine learning, and deep learning, most used algorithms in literature and their function. Chemometrics: discriminant analysis: PCA (principal component analysis); LDA (linear discriminant analysis); DFA (discriminant function analysis); regression analysis: MLR: multiple linear regression; PCR (principal component regression); PLS (partial least-squares); evolutionary based algorithms: GA (genetic algorithm); GP/GC (genetic programming and computing); EA (evolutionary algorithm). Neural networks: SVM (support vector machine); CNN (convolutional neural network); MP (multilayer perceptron). Blue arrows underscore several benefits of machine learning techniques brought to the biosensors field. Adopted from [62–65].

with external variables or target classifiers and once calibrated, it is possible to predict the quantity of unseen samples accordingly with the targets. Partial least squares (PLS) regression has been one of the most applied chemometrics methods, able to quantify a wide range of analytes [65, 68, 69].

As discussed in section 7.3.2, the ability to perform multiplex SERS assays has been a constant motivation in SERS bioanalysis. Nevertheless, SERS tags signals still need to prevail over strong background Raman signals from containers for cell cultivation, tissue autofluorescence, or other sources. Moreover, although RRs have narrow linewidths, the higher the number of SERS tags, the higher the risk of overlapping. Multivariate curve resolution (MCR) methods permit resolution of mixtures to identify individual meaningful components within a sample and quantify each component [66, 67, 70]. Classical least squares is an algorithm that provides signal isolation with good reproducibility [70].

As demonstrated by this Thesis work, using the DCLS method to resolve the mixed spectra from each pixel of the Raman map, allows detection of SERS tags at low concentrations and to differentiate a positive from a negative response with high specificity and accuracy. This approach surpasses the conventional peak integral technique, in which

even small overlaps can be falsely recognised as the SERS signal. As a result, SERS quantification irreproducibility at ultralow concentrations (<1 nM) is also improved by MCR methods because this type of methods can embrace the stochastic characteristics of the SERS intensity fluctuations and generate a calibration curve by counting SERS events [71].

Algorithms in ML can acquire knowledge by extracting features from raw data. Then, the obtained knowledge is used to make informed decisions when dealing with a problem. Among ML methods, convolutional neural network is a popular method for spectral analysis due to its prediction accuracy with medium or large data sets that outperforms standard classification algorithms used in chemometrics [72–74]. In the future, ML methods can be used to train a multiplex assay to detect a particular condition, to discriminate between SERS tags and train the system to be able to associate different tags ratios [75]. Furthermore, the models generated by ML methods are generalisable to different analytes by transfer learning implementation [76]. This opens possibilities towards multiplexing SERS tags application even in a single-molecule detection system.

Deep learning applied to the SERS field has also shown promise, especially in healthcare applications [77]. Without the need for specific pre-processing or feature engineering, deep learning methods can automatically extract and transform the features into a higher-level representation. However, deep learning and ML-based SERS approaches depend on overcoming the irreproducibility in SERS data. Large variance in the data set increases the variance in predictions, which may have negative repercussions in semiquantitative or quantitative analysis. These problems may be mitigated by implementation of algorithms such as the multi-objective evolutionary algorithm [78]. Also, the application of these methods requires validation with traditional approaches to be acceptable in practical use. This poses a problem, considering that deep learning algorithms that tackle biosensing problems may require thousands of examples, which represents an enormous barrier for the development of SERS in a clinical setting.

Nevertheless, ML methods can interrogate appropriate nonlinear dependencies for complex data sets, offering the inimitable possibility of solving pressing challenges in the area of SERS bioanalysis and making it a promising methodology for use in clinical samples.

7.3.5 Automation through microfluidics

Automation is a requirement to bring the SERS immunoassay for POCT sites. Microfluidics can help to accomplish that need through the integration of several protocols into one single device. In terms of disease diagnosis, integrating the entire process, from blood collection to the detection, is highly desirable. Non-invasive specimens such as saliva and urine have been proposed as an alternative to blood samples in the case of malaria, but have yet to be validated [79]. Hence, the device would profit from providing a way to simplify the pre-treatment need to extract the analyte for end users.

Passive separation methods represent a valuable option, since they do not require

any cell labelling or sophisticated microfabrication process [80]. Hence, these systems are more cost-effective and adequate for separating blood cells from plasma. Examples of possible apparatus are illustrated in Figure 7.3. The separation mechanism can be based on the bifurcation law or the Dean coupled inertial migration effect. The first states that, within a laminar flow profile, the cells at a point of bifurcation will have a propensity to flow into the microchannel with a higher flow rate (Figure 7.3a) [80]. Consequently, the adjacent channel with a lower flow rate will contain a purified, cell-free fraction of plasma. The latter (Figure 7.3b) is achieved with particles flowing in a spiral microchannel with a rectangular cross-section [81]. The particles experience a combination of inertial lift and Dean drag forces. The magnitude and direction of these forces depend on the particle size. Once separated, the purified plasma can then flow into the side outlet channels. An evaluation for a better suited system should be performed and executed, taking advantage of the knowledge acquired from the rapid prototyping fabrication of PS-based microfluidics. Nevertheless, it is important to acknowledge that, for applications in which a precise control of microchannels is crucial, the shrinkage of this children's toy might not be ideal. More accurately pre-stressed thermoplastic sheets can somehow overcome this problem[82].

Another relevant development that could bring the biosensor closer to the POCT requirements, is the synthesis of SERS immunotags inside the microfluidic device, which would rely on the efficient storage of the reagents used for their design. This could also contribute to a more reproducible and standardised conjugation, as mentioned in section 7.3.1. A few examples of micro-reactors exist in the literature [83, 84], but significant efforts are still needed to develop an integrated high-throughput platform for synthesis of nanostructures, material evaluation, and biofunction screening. Only when these procedures are completely unified, can a full POCT biosensor be realised.

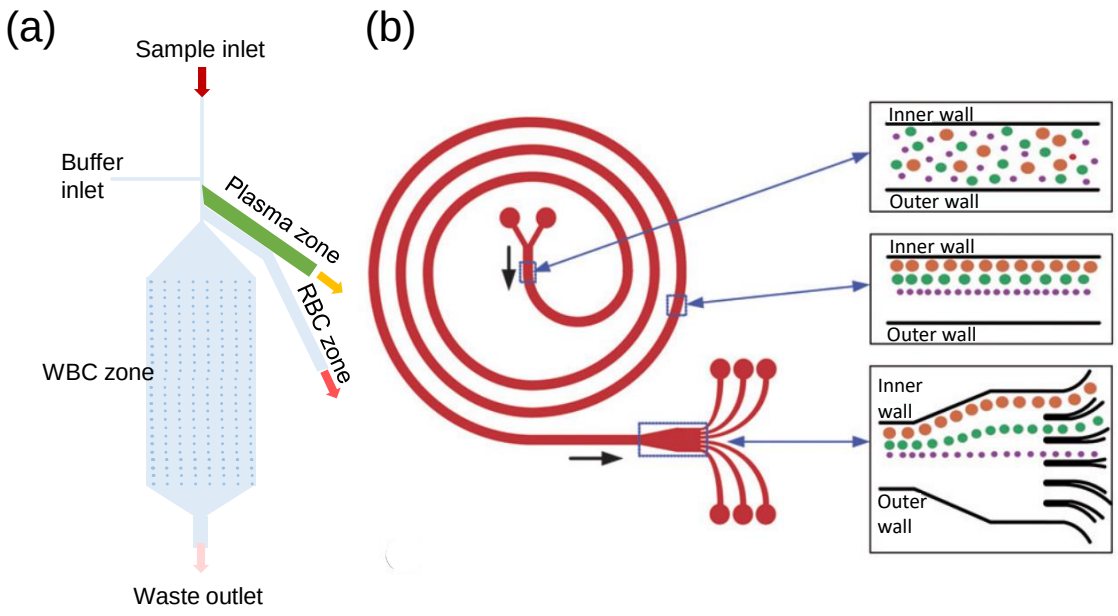

Figure 7.3: Passive separation method for automated microfluidic system. (a) Scheme of the microfluidic device for blood separation. The blood sample flows to the bifurcation region and plasma and red blood cell (RBC) were extracted to plasma and RBC zone, respectively. White blood cells (WBC) flows to the main channel and are trapped in the WBC zone. Adapted from [80]. (b) Scheme of the spiral microparticle separator. Randomly dispersed particles of different dimensions are introduced in the inlet and along the spiral microchannels will dispersed at different equilibrium positions along the inner wall due to a combination of inertial lift and Dean drag forces. Then the individual particle streams are extracted by a multiple outlet design. Adapted from [81].

7.4 Future perspectives

The design of nanosystems is already revolutionising the biosensors field and SERS has been established as a powerful and versatile discipline that offers higher sensitivity, signal specificity, and unparalleled multiplexing capabilities over traditional detection and imaging models. Thus, it has been exploited for applications from ultrasensitive and multiplex detection systems, to targeted controlled drug delivery and *in vivo* imaging systems.

Despite the increase in several applications in environmental, food safety, and medical healthcare areas, SERS has still not reached its full potential. Its widespread use in detection systems has been hindered due to batch-to-batch irreproducibility, the need for calibration and lack of large-scale synthetic procedures. Moreover, selecting the most suitable SERS tag production strategy is not trivial and, due to the wide variety of inorganic NPs and biomolecules available, no universal methodology exists. The striking features that make the nanomaterials so appealing and the tunability they offer in terms of size, shape, charge, surface area, colloidal stability, density, and others, makes difficult to transfer one protocol that works for a particular NP system to another, different, system. Similarly, RRs and biomolecules vary in size, chemical composition, 3D complexity,

among others, which increases the different possible combinations of functionalisation and bioconjugation protocols. Thus, each case needs optimisation, and a considerable amount of research has been dedicated to developing innovative SERS tags considering the intended application. Significant efforts have been devote to achieving nanostructures with high levels of uniformity and reproducibility, which would help to tackle the frequent problem of Raman intensity variations. Interestingly, this progress is somehow mitigated by the comparatively underdeveloped RRs field. Thus, although the functionality of these SERS tags is unquestionable, they are probably capable of far more. Moreover, the heterogeneity found within the NP materials and the resulting bioconjugates concerning orientation and attachment ratio remains a crucial concern. Hence, the need for non-heterogeneous and site-specific chemistries within the bioconjugation techniques is critical and the development of commercially available SERS tags together with standardised conjugation protocols will certainly play a role in the future.

Furthermore, performance comparison and cross reference the spectral analysis of SERS with existing well-established techniques is also important. While data reproducibility is crucial in research laboratories, clinical applications should confirm to more rigorous standards. Therefore, studies must be extended to clinically relevant scales for meaningful statistical analysis. To address this hurdle, machine learning approaches stands as a very promising tool. The advent of machine learning, beyond implementation of statistical data analysis, will surpass the quantification and identification of multiple analytes within complex mixtures, as to evolve into approaches able to make predictions or decisions without being explicitly programmed to do so.

Allied to nanosystems for biosensing tools, comes microfluidics devices to provide outstanding miniaturised analytical platforms. The world's growing and ageing population is causing a burden in the healthcare system. Consequently, the healthcare industry aims to replace the diagnostic tools that require a sophisticated infrastructure in to portable alternatives, practicable at healthcare centres and in home care, *i.e.* POCT sites. These alternatives will help to bring effective and quality primary care on a global scale.

The quest for accurate POCT diagnostics with microfluidic-based technologies has been somehow hindered by the use of PDMS, due to its ultra-high precision machining requirements that cannot translate these research prototypes to mass production in a cost-efficient manner. Therefore, microfluidics is mainly confined to the laboratory stage of scientific research with low maturity products in the market. Chemically compatible and optically transparent materials that allow simple and rapid fabrication while eliminating the need for PDMS will certainly help in the achievement of microfluidics in POCT. As stated throughout chapter 5, PS present several attractive features for the fabrication of a microfluidic device as demonstrated by this work. Nevertheless, the fabrication of multiple protocols integrated in a single microfluidic chip may be dependent on a thermoplastic with built-in actuators such as microvalves and micropumps which can pose some issues during its implementation, as their inherent high rigidity and Young's

modulus makes the fabrication of thin elastomeric membranes challenging. Recently, further efforts have been made with actuators based on styrene-ethylene/butylene-styrene, poly(tetrafluoroethene), PMMA combined with thermoplastic polyurethane or even using only PS, without complicated fabrication processes and increased cost[85].

Several examples of integration of biomolecular processes in microfluidic devices have been reported in literature[86]. Still, the integration of reagents in a consistent, low-cost, and precisely controlled device, while avoiding cross contamination, maintaining ease of operation, and with an appropriate shelf-life for commercial ends, is so far absent. Furthermore, whilst integration is fundamental for a portable device, the range of operating conditions has been largely overlooked by researchers. Temperature and humidity change considerably among the potential POCT sites and data on thermal stability of most developed biosensors has yet to be reported. When these hurdles are finally conquered, microfluidics devices will represent a sensitive, portable, and independent diagnostic tool and then, their commercialisation to an economy of scale can begin.

As a final thought, a through life cycle assessment should be undertaken to assess the possible impacts on the environment and human health from an exposure of the entire life cycle of a device. The development of novel nature-based materials that come from sustainable and economically efficient processes represents an ever more preeminent challenge as highlighted by the European Green Deal and the United Nation's Sustainable Development[87]. While the concepts of simplicity, sustainability, versatility, and low-power consumption were always present during this work, as the society evolves towards a more environmental conscious mindset, exciting sustainable technological advances are made and will unquestionably define our future.

In conclusion, SERS field is growing towards becoming an important tool for detection and personalised diagnosis. This forty-eight-years old technique still has some obstacles to conquer and although not replacing existing technologies, might become a standard tool working together with others and bringing novel and exciting developments.

References for chapter 7

[1] A. Pallaoro, G. B. Braun, and M. Moskovits. "Biotags Based on Surface-Enhanced Raman Can Be as Bright as Fluorescence Tags". In: *Nano Letters* 15.10 (2015), pp. 6745–6750.

[2] S. Arola et al. "Immobilization–Stabilization of Proteins on Nanofibrillated Cellulose Derivatives and Their Bioactive Film Formation". In: *Biomacromolecules* 13.3 (2012), pp. 594–603.

[3] L. H. Fu et al. "Multifunctional cellulose-based hydrogels for biomedical applications". In: *Journal of Materials Chemistry B* 7.10 (2019), pp. 1541–1562.

[4] P. Ball. "Water is an active matrix of life for cell and molecular biology". In: *Proceedings of the National Academy of Sciences of the United States of America* 114.51 (2017), pp. 13327–13335.

[5] I. Miranda et al. "Properties and applications of PDMS for biomedical engineering: A review". In: *Journal of Functional Biomaterials* 13.1 (2022), pp. 2–20.

[6] L. Xiong, P. Chen, and Q. Zhou. "Adhesion promotion between PDMS and glass by oxygen plasma pre-treatment". In: *Journal of Adhesion Science and Technology* 28.11 (2014), pp. 1046–1054.

[7] X. Zhao et al. "Cancer cell detection and imaging: MRI-SERS bimodal splat-shaped Fe3O4/Au nanocomposites". In: *Chinese Chemical Letters* 30.1 (2019), pp. 87–89.

[8] S. Shin, N. Kim, and J. W. Hong. "Comparison of Surface Modification Techniques on Polydimethylsiloxane to Prevent Protein Adsorption". In: *BioChip Journal* 12.2 (2018), pp. 123–127.

[9] K. V. Ragavan et al. "Advances in biosensors and optical assays for diagnosis and detection of malaria". In: *Biosensors and Bioelectronics* 105.January (2018), pp. 188–210.

[10] D. G. Feleke, S. Tarko, and H. Hadush. "Performance comparison of CareStart™ HRP2/pLDH combo rapid malaria test with light microscopy in north-western Tigray, Ethiopia: A cross-sectional study". In: *BMC Infectious Diseases* 17.1 (2017), pp. 1–7.

[11] A. Moody. "Rapid Diagnostic Tests for Malaria Parasites". In: *Clinical Microbiology Reviews* 15.1 (2002), pp. 66–78.

[12] C. K. Murray and J. W. Bennett. "Rapid Diagnosis of Malaria". In: *Interdisciplinary Perspectives on Infectious Diseases* 2009 (2009), pp. 1–7.

[13] H. Hopkins and J. Cunningham. "Point-of-care and near-point-of-care diagnostic tests for malaria: Light microscopy, rapid antigen-detecting tests and nucleic acid amplification assays". In: *Revolutionizing Tropical Medicine: Point-of-Care Tests, New Imaging Technologies and Digital Health* (2019), pp. 137–158.

[14] W. Health Organization. *WHO Guidelines for malaria - 3 June 2022*. Tech. rep. Geneva: World Health Organization, 2022, pp. 1–396.

[15] W. Hannah and P. B. Thompson. "Nanotechnology, risk and the environment: A review". In: *Journal of Environmental Monitoring* 10.3 (2008), pp. 291–300.

[16] P. D. Howes, R. Chandrawati, and M. M. Stevens. "Colloidal nanoparticles as advanced biological sensors". In: *Science* 346.6205 (2014), pp. 53–63.

[17] V. D. Krishna et al. "Nanotechnology: Review of concepts and potential application of sensing platforms in food safety". In: *Food Microbiology* 75 (2018), pp. 47–54.

[18] W. Zhou et al. "Gold Nanoparticles for in Vitro Diagnostics". In: *Chemical Reviews* 115.19 (2015), pp. 10575–10636.

[19] J. Langer et al. "Present and Future of Surface-Enhanced Raman Scattering". In: *ACS Nano* 14.1 (2020), pp. 28–117.

[20] S. Schlücker. "Surface-Enhanced Raman Spectroscopy: Concepts and Chemical Applications". In: *Angewandte Chemie International Edition* 53.19 (2014), pp. 4756–4795.

[21] A. J. McQuillan. "The discovery of surface-enhanced Raman scattering". In: *Notes and Records of the Royal Society* 63.1 (2009), pp. 105–109.

[22] L. Shang et al. "pH-Dependent Protein Conformational Changes in Albumin:Gold Nanoparticle Bioconjugates: A Spectroscopic Study". In: *Langmuir* 23.5 (2007), pp. 2714–2721.

[23] J. Meyer, L. E. Meyer, and S. Kara. "Enzyme immobilization in hydrogels: A perfect liaison for efficient and sustainable biocatalysis". In: *Engineering in Life Sciences* 22.3-4 (2022), pp. 165–177.

[24] F. Lussier et al. "Deep learning and artificial intelligence methods for Raman and surface-enhanced Raman scattering". In: *TrAC Trends in Analytical Chemistry* 124 (2020), pp. 115796–115811.

[25] K. J. Land et al. "REASSURED diagnostics to inform disease control strategies, strengthen health systems and improve patient outcomes". In: *Nature Microbiology* 4.1 (2019), pp. 46–54.

[26] Y. Fang, N.-H. Seong, and D. D. Dlott. "Measurement of the Distribution of Site Enhancements in Surface-Enhanced Raman Scattering". In: *Science* 321.5887 (2008), pp. 388–392.

[27] G. B. Braun et al. "Generalized Approach to SERS-Active Nanomaterials via Controlled Nanoparticle Linking, Polymer Encapsulation, and Small-Molecule Infusion". In: *The Journal of Physical Chemistry C* 113.31 (2009), pp. 13622–13629.

[28] D. Macdonald et al. "DNA detection by SERS: Hybridisation parameters and the potential for asymmetric PCR". In: *Analyst* 145.5 (2020), pp. 1871–1877.

[29] C. Sönnichsen et al. "A molecular ruler based on plasmon coupling of single gold and silver nanoparticles". In: *Nature Biotechnology* 23.6 (2005), pp. 741–745.

[30] Y. Zhang et al. "Stable Graphene-Isolated-Au-Nanocrystal for Accurate and Rapid Surface Enhancement Raman Scattering Analysis". In: *Analytical Chemistry* 88.21 (2016), pp. 10611–10616.

[31] M. J. Oliveira et al. "Office paper decorated with silver nanostars - an alternative cost effective platform for trace analyte detection by SERS". In: *Scientific Reports* 7.1 (2017), pp. 2480–2494.

[32] H. Yuan et al. "Gold nanostars: surfactant-free synthesis, 3D modelling, and two-photon photoluminescence imaging". In: *Nanotechnology* 23.7 (2012), p. 075102.

[33] M. J. Mulvihill et al. "Anisotropic etching of silver nanoparticles for plasmonic structures capable of single-particle SERS". In: *Journal of the American Chemical Society* 132.1 (2010), pp. 268–274.

[34] S. Li et al. "Separation of gold nanorods using density gradient ultracentrifugation". In: *Nano Research* 4.8 (2011), pp. 723–728.

[35] S. F. Sweeney, G. H. Woehrle, and J. E. Hutchison. "Rapid purification and size separation of gold nanoparticles via diafiltration". In: *Journal of the American Chemical Society* 128.10 (2006), pp. 3190–3197.

[36] O. Akbulut et al. "Separation of nanoparticles in aqueous multiphase systems through centrifugation". In: *Nano Letters* 12.8 (2012), pp. 4060–4064.

[37] S. Roy and A. Jaiswal. "SERS-Based Biosensors as Potential Next-Generation Point-of-Care Cancer Diagnostic Platforms". In: *Next Generation Point-of-care Biomedical Sensors Technologies for Cancer Diagnosis*. Ed. by P. Chandra, Y. N. Tan, and S. P. Singh. 1st ed. Singapore: Springer Nature Singapore Pte Ltd., 2017. Chap. 8, pp. 1–396.

[38] D. Rodoplu et al. "Development of a nanoparticle-based gradient method for simple and fast quantification of bacteria-nanoparticle conjugates". In: *Journal of Nanoparticle Research* 22.5 (2020), pp. 98–112.

[39] V. Sharma, K. Park, and M. Srinivasarao. "Shape separation of gold nanorods using centrifugation". In: *Proceedings of the National Academy of Sciences of the United States of America* 106.13 (2009), pp. 4981–4985.

[40] L. Yang et al. "Plasmonic Cu2- xSySe1- y Nanoparticles Catalyzed Click Chemistry Reaction for SERS Immunoassay of Cancer Biomarker". In: *Analytical Chemistry* 90.19 (2018), pp. 11728–11733.

[41] World Health Organization. *Response plan to pfhrp2 gene deletions*. Tech. rep. Geneva: World Health Organization, 2019, pp. 1–33.

[42] World Health Organization. *World Malaria Report 2021*. Tech. rep. Geneva: World Health Organization, 2021, pp. 1–322.

[43] J. R. Gutman et al. "Malaria and Parasitic Neglected Tropical Diseases: Potential Syndemics with COVID-19?" In: *The American Journal of Tropical Medicine and Hygiene* 103.2 (2020), pp. 572–577.

[44] L. Fabris. "SERS Tags: The Next Promising Tool for Personalized Cancer Detection?" In: *ChemNanoMat* 2.4 (2016), pp. 249–258.

[45] J. P. Nolan, E. Duggan, and D. Condello. "Optimization of SERS tag intensity, binding footprint, and emittance". In: *Bioconjugate Chemistry* 25.7 (2014), pp. 1233–1242.

[46] Y. Wang and S. Schlücker. "Rational design and synthesis of SERS labels". In: *Analyst* 138.8 (2013), pp. 2224–2238.

[47] B. Küstner et al. "SERS labels for red laser excitation: Silica-encapsulated SAMs on tunable gold/silver nanoshells". In: *Angewandte Chemie - International Edition* 48.11 (2009), pp. 1950–1953.

[48] Y. Li et al. "Microarray surface enhanced Raman scattering based immunosensor for multiplexing detection of mycotoxin in foodstuff". In: *Sensors and Actuators, B: Chemical* 266 (2018), pp. 115–123.

[49] B. Mir-Simon et al. "Universal One-Pot and Scalable Synthesis of SERS Encoded Nanoparticles". In: *Chemistry of Materials* 27.3 (2015), pp. 950–958.

[50] M. Lee et al. "Highly reproducible immunoassay of cancer markers on a gold-patterned microarray chip using surface-enhanced Raman scattering imaging". In: *Biosensors and Bioelectronics* 26.5 (2011), pp. 2135–2141.

[51] J. Li et al. "A universal strategy for the one-pot synthesis of SERS tags". In: *Nanoscale* 10.17 (2018), pp. 8292–8297.

[52] L. Wu and X. Qu. "Cancer biomarker detection: Recent achievements and challenges". In: *Chemical Society Reviews* 44.10 (2015), pp. 2963–2997.

[53] S. Lee et al. "Fabrication of SERS-fluorescence dual modal nanoprobes and application to multiplex cancer cell imaging". In: *Nanoscale* 4.1 (2012), pp. 124–129.

[54] M. Gellner, K. Kömpe, and S. Schlücker. "Multiplexing with SERS labels using mixed SAMs of Raman reporter molecules". In: *Analytical and Bioanalytical Chemistry* 394.7 (2009), pp. 1839–1844.

[55] S. Lee et al. "Fabrication of SERS-fluorescence dual modal nanoprobes and application to multiplex cancer cell imaging". In: *Nanoscale* 4.1 (2012), pp. 124–129.

[56] S. E. Bell and N. M. Sirimuthu. "Quantitative surface-enhanced Raman spectroscopy". In: *Chemical Society Reviews* 37.5 (2008), pp. 1012–1024.

[57] M. A. Woo et al. "Multiplex immunoassay using fluorescent-surface enhanced Raman spectroscopic dots for the detection of bronchioalveolar stem cells in murine lung". In: *Analytical Chemistry* 81.3 (2009), pp. 1008–1015.

[58] P. Šmejkal et al. "Characterization and surface-enhanced Raman spectral probing of silver hydrosols prepared by two-wavelength laser ablation and fragmentation". In: *Spectrochimica Acta - Part A: Molecular and Biomolecular Spectroscopy* 59.10 (2003), pp. 2321–2329.

[59] J. Gao et al. "An intrinsic internal standard substrate of Au@PS-: B -P4VP for rapid quantification by surface enhanced Raman scattering". In: *Analyst* 142.16 (2017), pp. 2936–2944.

[60] S. Lin et al. "Self-assembly of Au@Ag core-shell nanocubes embedded with an internal standard for reliable quantitative SERS measurements". In: *Analytical Methods* 10.34 (2018), pp. 4201–4208.

[61] R. Mei et al. "Gold Nanorod Array-Bridged Internal-Standard SERS Tags: From Ultrasensitivity to Multifunctionality". In: *ACS Applied Materials and Interfaces* 12.2 (2020), pp. 2059–2066.

[62] I. Behl et al. "Development of methodology for Raman microspectroscopic analysis of oral exfoliated cells". In: *Analytical Methods* 9.6 (2017), pp. 937–948.

[63] H. J. Byrne et al. "Spectral pre and post processing for infrared and Raman spectroscopy of biological tissues and cells". In: *Chemical Society Reviews* 45.7 (2016), pp. 1865–1878.

[64] Z. Farhane et al. "Differentiating responses of lung cancer cell lines to Doxorubicin exposure: in vitro Raman micro spectroscopy, oxidative stress and bcl-2 protein expression". In: *Journal of Biophotonics* 165.1 (2016), pp. 151–165.

[65] M. E. Keating et al. "Multivariate statistical methodologies applied in biomedical Raman spectroscopy: assessing the validity of partial least squares regression using simulated model datasets". In: *The Analyst* 140.7 (2015), pp. 2482–2492.

[66] G. P. Szekeres et al. "Fragmentation of Proteins in the Corona of Gold Nanoparticles As Observed in Live Cell Surface-Enhanced Raman Scattering". In: *Analytical Chemistry* 92.12 (2020), pp. 8553–8560.

[67] F. Zhao et al. "Robust quantitative SERS analysis with Relative Raman scattering intensities". In: *Talanta* 221.July 2020 (2021), p. 121465.

[68] K. Faulds et al. "Multiplexed detection of six labelled oligonucleotides using surface enhanced resonance Raman scattering (SERRS)". In: *Analyst* 133.11 (2008), pp. 1505–1512.

[69] K. Gracie et al. "Simultaneous detection and quantification of three bacterial meningitis pathogens by SERS". In: *Chem. Sci.* 5.3 (2014), pp. 1030–1040.

[70] Z. Tan et al. "Improvement of surface-enhanced Raman scattering detection and imaging by multivariate curve resolution methods". In: *Journal of Applied Physics* 125.17 (2019), pp. 173101–173113.

[71] C. D. L. de Albuquerque et al. "Digital Protocol for Chemical Analysis at Ultralow Concentrations by Surface-Enhanced Raman Scattering". In: *Analytical Chemistry* 90.2 (2018), pp. 1248–1254.

[72] J. Acquarelli et al. "Convolutional neural networks for vibrational spectroscopic data analysis". In: *Analytica Chimica Acta* 954 (2017), pp. 22–31.

[73] J. Dong et al. "A practical convolutional neural network model for discriminating Raman spectra of human and animal blood". In: *Journal of Chemometrics* 33.11 (2019), pp. 1–12.

[74] W. Liu et al. "Raman microspectroscopy of nucleus and cytoplasm for human colon cancer diagnosis". In: *Biosensors and Bioelectronics* 97.December (2017), pp. 70–74.

[75] M. Sánchez-Purrà et al. "Reporter Selection for Nanotags in Multiplexed Surface Enhanced Raman Spectroscopy Assays". In: *ACS Omega* 3.9 (2018), pp. 10733–10742.

[76] W. J. Thrift and R. Ragan. "Quantification of Analyte Concentration in the Single Molecule Regime Using Convolutional Neural Networks". In: *Analytical Chemistry* 91.21 (2019), pp. 13337–13342.

[77] H. Shin et al. "Early-Stage Lung Cancer Diagnosis by Deep Learning-Based Spectroscopic Analysis of Circulating Exosomes". In: *ACS Nano* 14.5 (2020), pp. 5435–5444.

[78] C. Levene et al. "Enhancing surface enhanced Raman scattering (SERS) detection of propranolol with multiobjective evolutionary optimization". In: *Analytical Chemistry* 84.18 (2012), pp. 7899–7905.

[79] J. Nyataya et al. "*Plasmodium falciparum* Histidine-Rich Protein 2 and 3 Gene Deletions and Their Implications in Malaria Control". In: *Diseases* 8.2 (2020), pp. 15–34.

[80] D.-H. Kuan et al. "A Microfluidic Device for Simultaneous Extraction of Plasma, Red Blood Cells, and On-Chip White Blood Cell Trapping". In: *Scientific Reports* 8.1 (2018), pp. 15345–15354.

[81] S. S. Kuntaegowdanahalli et al. "Inertial microfluidics for continuous particle separation in spiral microchannels". In: *Lab on a Chip* 9.20 (2009), pp. 2973–2980.

[82] C.-S. Chen et al. "Shrinky-Dink microfluidics: 3D polystyrene chips". In: *Lab on a Chip* 8.4 (2008), pp. 622–624.

[83] X. Y. Li et al. "High stability of gold nanoparticles towards DNA modification and efficient hybridization via a surfactant-free peptide route". In: *Chemical Communications* 53.87 (2017), pp. 11909–11912.

[84] L. P. Bressan et al. "3D-printed microfluidic device for the synthesis of silver and gold nanoparticles". In: *Microchemical Journal* 146.October 2018 (2019), pp. 1083–1089.

[85] S. A. M. Shaegh et al. "Rapid prototyping of whole-thermoplastic microfluidics with built-in microvalves using laser ablation and thermal fusion bonding". In: *Sensors and Actuators, B: Chemical* 255 (2018), pp. 100–109.

[86] R. Panneerselvam et al. "Microfluidics and surface-enhanced Raman spectroscopy, a win–win combination?" In: *Lab on a Chip* 22.4 (2022), pp. 665–682.

[87] United Nations Development Programme. *Sustainable Development Goals | United Nations Development Programme*. 2021. URL: https://www.undp.org/sustainable-development-goals (visited on 06/08/2022).

Appendix

A Supplementary tables

Table A.1: Components of SERS tags with some examples [1–14].

SERS nanotags components ***Function***	**Type**	**Examples**	**Linking mode**	**Advantages**	**Disadvantages**	**Features to consider**
Plasmonic nanoparticle *Plasmonic activity*				Signal generation due to LSPR Facile synthesis by bottom-up strategies	Lack of standardised protocols Lack of control over NP dispersity	LSPR band location Number of hotspots per particle Synthesis: easy, reproducibility and scalable
Metal Size Shape Number of NPs	Au, Ag 20-200 Spheres, rods, stars	Monomer vs cluster				
RR molecule *Provide characteristic spectral signature for sensitive and indirect identification of the selected target.*	Dyes: Nitrogen-containing cationic dye	Crystal Violet Rhodamine B/6G Nile blue	Electrostatic interaction N-Au(Ag) interaction	Plentiful fingerprint information (400-1800 cm^{-1}) Commercially-available Larger Raman scattering cross section for dyes	Emission in fingerprint region (400-1800 cm^{-1}) Spectral overlapping susceptibility in multiplexing assays Fluorescence for dyes Smaller Raman scattering cross section for thiol-small aromatic molecules	Raman scattering cross section Surface-seeking groups Metal affinity Ability to form SAM Water solubility Reactivity Simplicity and low-cost
	Sulphur-containing dye	Cyanine Malachite green	S-Au(Ag) interaction			
	Thiol-small aromatic molecules	Thiophenol aminohexanethiol, naphthalene dithiol, mercaptobenzoicacid, 1,4-biphenyltithiol	S-Au(Ag) interaction			
	Triple bond-containing RRs	4-Ethynylbenzenethiol derivatives 4-Mercaptobenzonitrile Metal carbonyl compounds	C≡C C≡N C≡O	Emission in silent region (1800-2800 cm^{-1}) Single narrow band High encoding capability Interference-free	Early-stage development Not commercially available: self-design and synthesis requirement	
Protective shell *Maintain the RR near the NP, stabilise the NPs and provide surface groups for bioconjugation*	Hydrophilic short spacers Biomolecules Polymers Silica	Ethylene glycol Bovine serum albumin PEG Tetraethoxyorthosilicate (TEOS)	Electrostatic interaction Covalent bond S-Au(Ag) interaction	Improves colloidal stability Terminal functional groups for bioconjugation Core physical and chemical protection Avoids loss of RR	Increases SERS tag size Time-consuming Labour-intensive	Coating synthesis Non-specific adsorption Toxicity Functional-end groups Colloidal stability
Bioconjugation *Molecular recognition of the target*	Proteins: enzymes and antibodies Aptamers Small molecules	via COOH, NH_2, SH click-chemistry	Covalent or non-covalent	Specificity towards the target analyte	Variable accordingly with chosen analyte	Target-specificity ligand Water solubility Bioconjugation reproducibility Price

Table A.2: Comparison of the covalent and non-covalent conjugation strategies in bioconjugation processes and possible interactions between biomolecules and nanoparticle's surface in bioconjugation process [15–19].

Non-covalent interactions	***Advantages***	***Disadvantages***
Spontaneous absorption of biomolecules onto the surface of stabilised NPs. Electrostatic interactions Positively charged groups in biomolecules are attracted by the negative charged surface of the metal NPs or *vice versa*. Hydrophobic interactions Attraction between hydrophobic parts of the biomolecule and the metal nanoparticle surface. Dative binding Donation of unshared electron pairs from free atoms of the biomolecule to the metal conducting electrons (e.g. sulphur-gold). Adaptive molecules Affinity-based receptor-ligand systems such as streptavidin and biotin.	Convenient and simple. Do not require any additional chemical components. Most useful in understanding physicochemical interactions at the nano–bio interface. Used to reduce non-specific reactions and aggregation. Affinity-based receptor-ligand systems provide strong bonds with high binding affinity to cells and resistance to: pH; Temperature variations; Denaturants.	Random orientation of proteins reducing its biomolecule activity Necessity of a high concentration of biomolecules for the preparation of biomolecule–gold particle conjugates. Difficult control over biological response due to the bioconjugate is mainly formed by electrostatic attractions. The binding is greatly influenced by changes in: pH; Ionic strength. More precisely, increasing the electrolyte concentration shields the attractive electrostatic interaction causing the desorption of biomolecules. Possible displacement by other molecules on the NPs surface specially in complex biological samples. Washing buffers can remove loosely bound proteins and reduce non-specific interactions.
Covalent interactions	***Advantages***	***Disadvantages***
Chemical bond between biomolecules and the surface of NPs. Conjugation chemistry Exploiting functional groups on both particles and biomolecules such as bifunctional linkers of mediator linkers. Maleimide coupling Diels–Alder cycloadditions with dienes; 1,3-dipolar cycloadditions with nitrones and azides; Michael-type additions with thiols and amines. Click chemistry Refers to a family of reactions that are modular, stereospecific, and high yielding.	Thermally stable (desirable in applications that require thermo cycling). Attaches more protein – 10-40% more protein via covalent. Prevents elution of bound protein increasing the stability. Correct spatial biomolecule orientation can be difficult via physical adsorption, whilst covalent attachment can orient the molecule properly, yielding increased activity and lower reagent consumption.	Effectiveness limitations when release is required as in drug release systems. Attachment of highly active antibodies can be impaired due to pH requirement for successful cross-linking reaction. Depending on the strategy, covalent binding can originate random orientation of proteins reducing its biomolecule activity. Covalent attachment can force the protein to have unfavourable interactions with the NP surface coating ligand, causing unfolding.

Table A.3: Main materials used for microfluidic chip fabrication [20, 21].

Materials/features	Silicon/glass	Polymers				Paper
		Elastomers	Thermosets	Thermoplastics	Hydrogels	
Examples	-	PDMS	SU-8	PMMA, polystyrene	Cellulose-based	Chromatographic
Microfabrication technique[a]	Wet and dry etching	Casting	Photolithography	Thermomoulding	Casting, printing	Photolitography, printing
Resolution limit	<100 nm	<1μm	<100 nm	≈100 nm	≈10 μm	≈200 mm
Mechanical stability	Very high	Low	High	Medium	Low	Very low
Chemical stability	Very high	Low	High	Low	Low	Low
Solvent compatibility	Very high	Low	High	Medium to high	Low	Medium
Thermostability	Very high	Medium	High	Medium to high	Low	Medium
Hydrophobicity	Hydrophilic	Hydrophobic	Hydrophobic	Hydrophobic	Hydrophilic	Amphiphilic
Optical transparency	No/High	High	High	Medium to high	Medium to low	low
Oxygen permeability[b]	0.01	≈500	0.03-1	0.05-5	1	1
Scalability	Medium	Low[c]	Low	High	N/A	High
Cost	High	Medium	Medium to high	Medium to low	Low	Low
Main advantages	Excellent chemical, mechanical and thermal resistance; High thermal-conductivity	*Once the high-resolution mould is made, multiple devices can be fabricated outside the clean room.*			Moldability	Low cost
		Rubber-like elasticity (useful to form pumps and valves); Low investment cost	High aspect ratio features; High optical transparency	Low cost in mass production		
Main disadvantages	Expensive; Laborious and time-consuming fabrication	*Low melting point; Tendency to adsorb reagents*			Fragile	Sample evaporation; Low sensitivity
		Only suitable for research prototyping	High cost	High investment cost; Insufficient gas permeability		
Applicability	Capillary electrophoresis; Analytical and micro-reaction devices	Cell-based studies; Clinical and veterinary diagnostics and POC devices or 'organs-on-chips' devices	Platforms requiring high chemical/ thermal stability; Moulds for elastomers	Mass-scale production of conventional microfluidic devices	Clinical and veterinary diagnostics and POC devices or 'organs-on-chips' devices	Colorimetric analysis; Mass-scale production

[a] Photosensitive glass can be considered as thermoset.
[b] Oxygen permeability is beneficial to long-term living cells studies, but the loss of water may lead to a shift in pH and disturb the chemical analysis.
[c] Only suitable for research prototyping because is difficult to scale up (cost per unit does not decrease).

Table A.4: SERS strategies for different types of malaria biomarkers.

Biomarker	Target	Detection scheme	Sample		Capture strategy	Sensitivity (LOD)	Multiplex (RR used)	Microfluidics	References
			Origin	Patient /Spiked					
iRBCs	Lysate	Direct	Blood	Patient (25)	Centrifugation	100 parasites/mL	-	-	[22]
Protein	*Pf*LDH	Indirect	Blood	Patient	AuGlass/ AgNP/Au substrate	1 parasite/μL	MBA[b]	-	[23]
	*Pf*HRP2	Indirect	Blood lysate	Patient (163)	Silica coated SERS tags	99.5% sensitivity[a]	Tag 493[b] Tag 421[b] Tag 420[b]	-	[24]
Acid nucleic	*PF3D7_-1343700* gene[c]	Indirect	Synthetic	-	Magnetic enrichment	3 pM	DSNB[b]	-	[25]
	Ribosomal RNA	Indirect	Synthetic iRCBs[b] culture lysates	Culture	Magnetic enrichment	200 fM	IR780	Lab-on-a-stick chip	[26]
Small molecules	Haemozoin	Direct	iRCBs culture			$1.5 \times 10^7 mL^{-1}$	-	-	[27]
	Haemozoin	Direct	Synthetic	Spiked	Magnetic enrichment	5 nM (30 parasites/μL)	-	-	[28]
	Haemozoin	Direct	iRCBs culture lysates			2.5 parasites/μL	-	-	
	Haemozoin	Direct	iRCBs culture lysates			0.0005% and 0.005% parasitaemia	-	-	

[a] Sensitivity based on known samples.
[b] Abbreviations: infected red blood cells (iRBCs); 4-mercaptobenzoic acid (MBA); 4,4'-dipyridyl-d8 (Tag 421); 4,4'-dipyridyl (Tag 420); 2,5-bis(4-pyridyl)-1,3,4-thiadiazole (Tag 493); 5,5-dithiobis(succinimidyl-2-nitrobenzoate) (DSNB).
[c] Confers resistance to artemisinin drugs.

References for appendix A

[1] W. E. Doering and S. Nie. "Spectroscopic Tags Using Dye-Embedded Nanoparticles and Surface-Enhanced Raman Scattering". In: *Analytical Chemistry* 75.22 (2003), pp. 6171–6176.

[2] L. Fabris. "SERS Tags: The Next Promising Tool for Personalized Cancer Detection?" In: *ChemNanoMat* 2.4 (2016), pp. 249–258.

[3] X. Gu et al. "SERS Sensors: Recent Developments and a Generalized Classification Scheme Based on the Signal Origin". In: *Annual Review of Analytical Chemistry* 11 (2018), pp. 147–169.

[4] J. Kneipp, H. Kneipp, and K. Kneipp. "SERS—a single-molecule and nanoscale tool for bioanalytics". In: *Chemical Society Reviews* 37.5 (2008), pp. 1052–1060.

[5] L. A. Lane, X. Qian, and S. Nie. "SERS Nanoparticles in Medicine: From Label-Free Detection to Spectroscopic Tagging". In: *Chemical Reviews* 115.19 (2015), pp. 10489–10529.

[6] J. Langer et al. "Present and Future of Surface-Enhanced Raman Scattering". In: *ACS Nano* 14.1 (2020), pp. 28–117.

[7] M. Moskovits. "Persistent misconceptions regarding SERS". In: *Physical Chemistry Chemical Physics* 15.15 (2013), pp. 5301–5311.

[8] M. Muhammad and Q. Huang. "A review of aptamer-based surface-enhanced Raman scattering biosensors: Design strategies and applications". In: *Talanta* 227.December 2020 (2021), p. 122188.

[9] L. Rodriguez-Lorenzo, L. Fabris, and R. A. Alvarez-Puebla. "Multiplex optical sensing with surface-enhanced Raman scattering: A critical review". In: *Analytica Chimica Acta* 745 (2012), pp. 10–23.

[10] B. Shan et al. "Novel SERS labels: Rational design, functional integration and biomedical applications". In: *Coordination Chemistry Reviews* 371 (2018), pp. 11–37.

[11] Y. Wang et al. "Microspectroscopic SERS detection of interleukin-6 with rationally designed gold/silver nanoshells". In: *Analyst* 138.6 (2013), pp. 1764–1771.

[12] Y. Wang and S. Schlücker. "Rational design and synthesis of SERS labels". In: *Analyst* 138.8 (2013), pp. 2224–2238.

[13] Z. Wang et al. "SERS-Activated Platforms for Immunoassay: Probes, Encoding Methods, and Applications". In: *Chemical Reviews* 117.12 (2017), pp. 7910–7963.

[14] Y. Zeng et al. "Watching SERS glow for multiplex biomolecular analysis in the clinic: A review". In: *Applied Materials Today* 15 (2019), pp. 431–444.

[15] M.-E. Aubin-Tam and K. Hamad-Schifferli. "Gold Nanoparticle-Cytochrome c Complexes: The Effect of Nanoparticle Ligand Charge on Protein Structure". In: *Langmuir* 21.26 (2005), pp. 12080–12084.

[16] S. Bucak et al. "Protein separations using colloidal magnetic nanoparticles". In: *Biotechnology Progress* 19.2 (2003), pp. 477–484.

[17] M. H. Jazayeri et al. "Various methods of gold nanoparticles (GNPs) conjugation to antibodies". In: *Sensing and Bio-Sensing Research* 9 (2016), pp. 17–22.

[18] J. H. Oh et al. "Recent advances in chemical functionalization of nanoparticles with biomolecules for analytical applications". In: *Analytical and Bioanalytical Chemistry* 407.29 (2015), pp. 8627–8645.

[19] R. A. Sperling and W. J. Parak. "Surface modification, functionalization and bioconjugation of colloidal Inorganic nanoparticles". In: *Philosophical Transactions of the Royal Society A: Mathematical, Physical and Engineering Sciences* 368.1915 (2010), pp. 1333–1383.

[20] K. Ren, J. Zhou, and H. Wu. "Materials for microfluidic chip fabrication". In: *Accounts of Chemical Research* 46.11 (2013), pp. 2396–2406.

[21] S. M. Yang et al. "Microfluidic Point-of-Care (POC) Devices in Early Diagnosis: A Review of Opportunities and Challenges". In: 22.4 (2022), p. 1620.

[22] W. Wang et al. "Antibody-free rapid diagnosis of malaria in whole blood with surface-enhanced Raman Spectroscopy using Nanostructured Gold Substrate". In: *Advances in Medical Sciences* 65.1 (2020), pp. 86–92.

[23] N. Mhlanga et al. "Sandwich-based surface-enhanced Raman scattering probes for detection and quantification of malaria". In: *Journal of Raman Spectroscopy* 51.12 (2020), pp. 2416–2424.

[24] D. Sebba et al. "A point-of-care diagnostic for differentiating Ebola from endemic febrile diseases". In: *Science Translational Medicine* 10.471 (2018), eaat0944.

[25] H. T. Ngo et al. "Sensitive DNA detection and SNP discrimination using ultrabright SERS nanorattles and magnetic beads for malaria diagnostics". In: *Biosensors and Bioelectronics* 81 (2016), pp. 8–14.

[26] H. T. Ngo et al. "Direct Detection of Unamplified Pathogen RNA in Blood Lysate using an Integrated Lab-in-a-Stick Device and Ultrabright SERS Nanorattles". In: *Scientific Reports* 8.1 (2018), pp. 4075–4088.

[27] K. Chen et al. "Review of surface enhanced Raman spectroscopy for malaria diagnosis and a new approach for the detection of single parasites in the ring stage". In: *IEEE Journal of Selected Topics in Quantum Electronics* 22.4 (2016), pp. 179–187.

[28] C. Yuen. "Magnetic field enriched surface enhanced resonance Raman spectroscopy for early malaria diagnosis". In: *Journal of Biomedical Optics* 17.1 (2012), pp. 017005–1–7.

Appendix

B Proof-of-concept SERS assay

B.1 Python script for DCLS analysis

```
import pandas as pd
import numpy as np
from sklearn.preprocessing import minmax_scale

def references_spectra(controls_files, folder_selected, ref_labels):
    """Returns the spectra to use as control for the components
    """
    c_spectra = []
    controls_labels = []

    for spectrum in range(len(controls_files)):
        control      = pd.read_csv(folder_selected+"//"+controls_files[
    spectrum])
        control      = pd.DataFrame.to_numpy(control)
        control      = minmax_scale(control[22:,1], feature_range=(0,1))
        c_spectra.append(control)
    c_spectra = np.array(c_spectra)

    for label in range(len(ref_labels)):
        label = ref_labels[label]
        controls_labels.append(label)

    return c_spectra, controls_labels

def least_sq(sample_spectrum, c_spectra):
    """Returns the component resulted for each control spectrum
    """
    # sample_spectrum (unknown spectrum): array of w values.
    # components (known spectra): array of n (number of components) columns
    with w values.
```

```
    # This def returns an array of n values. Each value is the similarity
    score for the sample_spectrum and a component spectrum.
    similarity = np.dot(inv(np.dot(c_spectra, c_spectra.T)) ,
                        np.dot(c_spectra, sample_spectrum))

    return similarity
```

Listing B.1: The two main functions written in Python that perform DCLS analysis for each spectrum according to the references given.

B.2 Cellulose oxidation mediated by TEMPO

The cellulose oxidation was mediated by TEMPO to introduce carboxyl groups on its surface (Figure B.1). TEMPO is responsible for catalysing the conversion of C6 primary hydroxyls of cellulose to carboxyl groups by TEMPO/NaBr/NaClO oxidation in water at pH 10–11 [1, 2]. This is an efficient and selective conversion chemistry which can be further utilised in immunoassays by activation with EDC/SNHS cross-linking.

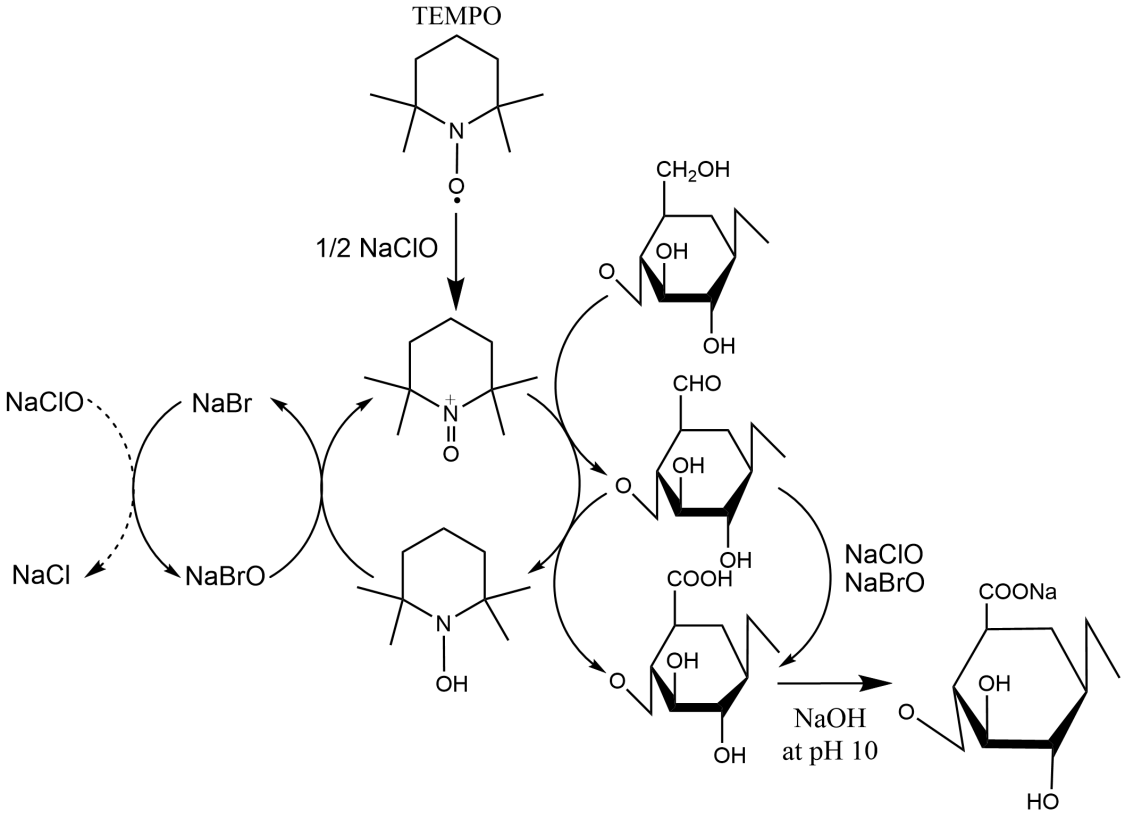

Figure B.1: Oxidation of C6 primary hydroxyls of cellulose to C6 carboxylate groups by TEMPO /NaBr/NaClO oxidation in water at pH 10-11 [2].

B.3 Functionalisation and bioconjugation of gold nanostars with DTNB

UV-Vis spectroscopy and AGE were used to verify the functionalisation process *i.e.* the presence of DTNB after its addition to the AuNSs at a ratio of 1:50,000, as previously optimised (Figure B.2). Considering the UV-Vis spectra, a 18 nm red-shift of the LSPR is observed for DTNB. This phenomenon occurs due to an increase in the local refractive index at the AuNS surface [3]. Since AuNSs are anisotropic, they show a large change in the refractive index due to the presence of hotspots (especially at tips or edges) responsible for enhanced electromagnetic fields [3–5]. Regarding AGE, as synthesised, non-functionalised AuNSs did not migrate in AGE, probably due to the loss of the weakly bound citrate ions or the presence of specific interactions between the gel and the NPs [6]. Conversely, functionalised AuNSs present an electrophoretic mobility, corresponding to a full layer of DTNB covering the AuNSs (Figure B.2). The electrophoretic mobility decreases even more when the covalent conjugation process is completed to formed the SERS immunotags (physiosorption conjugation was used as control).

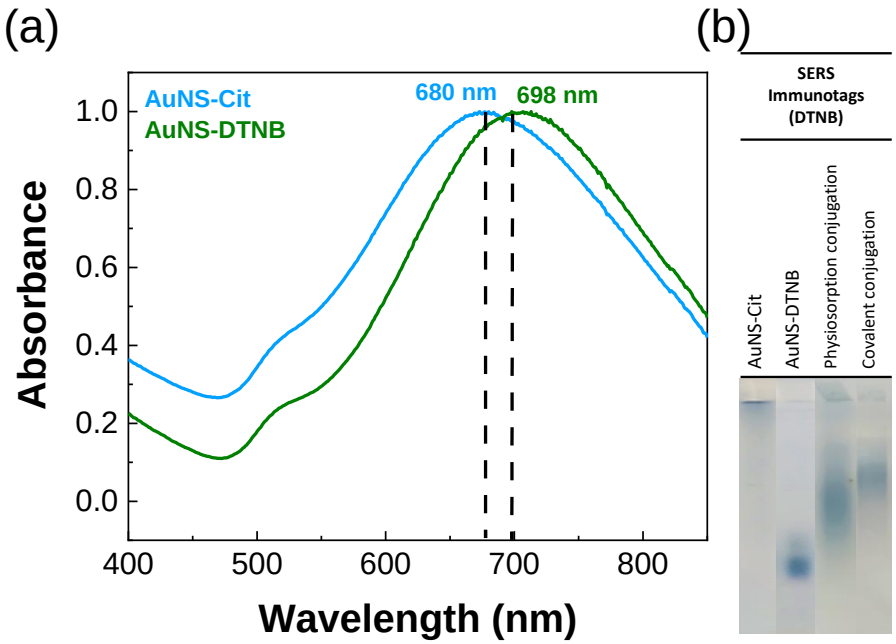

Figure B.2: Functionalisation and bioconjugation of AuNSs with DTNB. (a) UV-Vis spectra of non-functionalised AuNSs *i.e.* with citrate ions from the synthesis (blue line) and DTNB-functionalised AuNSs (green line). The AuNSs present a LSPR band centred approximately at 680 nm and a large broadening due to their multiple resonances caused by the tips and edges. This LSPR is red-shifted to 698 nm when DTNB is added to replace the citrate ions due to its thiol group which has a higher affinity for gold. (b) Photograph of an agarose gel where a difference in electrophoretic mobility can be readily distinguish SERS immunotags with DTNB by physiosorption (third lane) and covalent (fourth lane) conjugations, as RR from the DTNB-functionalised AuNSs (second lane), and, from the non-functionalised AuNSs (first lane).

References for appendix B

[1] A. Isogai and Y. Kato. "Preparation of polyuronic acid from cellulose by TEMPO-mediated oxidation". In: *Cellulose* 5.1 (1998), pp. 153–164.

[2] A. Isogai, T. Saito, and H. Fukuzumi. "TEMPO-oxidized cellulose nanofibers". In: *Nanoscale* 3.1 (2011), pp. 71–85.

[3] S. Barbosa et al. "Tuning size and sensing properties in colloidal gold nanostars". In: *Langmuir* 26.18 (2010), pp. 14943–14950.

[4] V. Giannini, R. Rodríguez-Oliveros, and J. A. Sánchez-Gil. "Surface Plasmon Resonances of Metallic Nanostars/Nanoflowers for Surface-Enhanced Raman Scattering". In: *Plasmonics* 5.1 (2010), pp. 99–104.

[5] C. L. Nehl, H. Liao, and J. H. Hafner. "Optical Properties of Star-Shaped Gold Nanoparticles". In: *Nano Letters* 6.4 (2006), pp. 683–688.

[6] M. S. Jimenez et al. "Evaluation of agarose gel electrophoresis for characterization of silver nanoparticles in industrial products". In: *Electrophoresis* 37.10 (2016), pp. 1376–1383.

Annex

I pET-15b vector in *E.coli* BL21 (DE3)

*Pf*HRP2 was cloned in the pET 15b vector that uses *Escherichia coli* BL21 (DE3) as the host system [1]. The target gene cloned in this type of plasmids is under control of the strong bacteriophage T7 transcription signals. The expression is driven by the chromosomally encoded bacteriophage T7 RNA polymerase, which is under the promoter *lac*UV5 control (a strong variant of the wild-type *lac* promoter), and thus, its expression is induced by the addition of IPTG [2]. Upon IPTG addition, the T7 RNA polymerase is produced and recognises the T7 promoter from pET-15b vector transcribing the target gene eight times faster than *E. coli* RNA polymerase and consequently, allows *Pf*HRP2 overexpression.

To be mentioned that the $P_{lac\text{UV5}}$ mutant is leakier than P_{lac} due to be cyclic adenosine monophosphate receptor protein independent [3]. Consequently, the T7 polymerase can be produced in the non-inducing period, and the cells will begin *Pf*HRP2 production before they reached a desirable biomass. If the expression levels are high, it can lead to toxicity levels and ultimately to the loss of the expression plasmid or the occurrence of mutations in the expressed gene. To reduce the basic leakage expression of $P_{lac\text{UV5}}$, the *lacI* mutant was developed, which only can bind to the *lacO* (lac operator) [3]. An illustration of the molecular mechanism is represented in Figure I.1.

The pET-15b vector map is shown in Figure I.2 [4]. This vector contains a selective marker for ampicillin resistance (amp^R); an origin of replication (*ori*, pBR322) that allows plasmid replication in *E. coli*; *rop* gene encodes a small protein acting as primer repressor and in combination with origin of replication on the plasmid, results in low copy numbers of the plasmid (15-20 copies) [4]. The *E. coli* also has a natural promoter and coding sequence for the lac repressor. In absence of IPTG, LacI represses the transcription of the gene *PfHRP2* as well as the transcription of T7 RNA polymerase from the LacUV5 promoter in *E.coli* BL21 (DE3) [4].

The target gene (in this case, *Pf*HRP2) is recognised by T7 promoter by T7 RNA

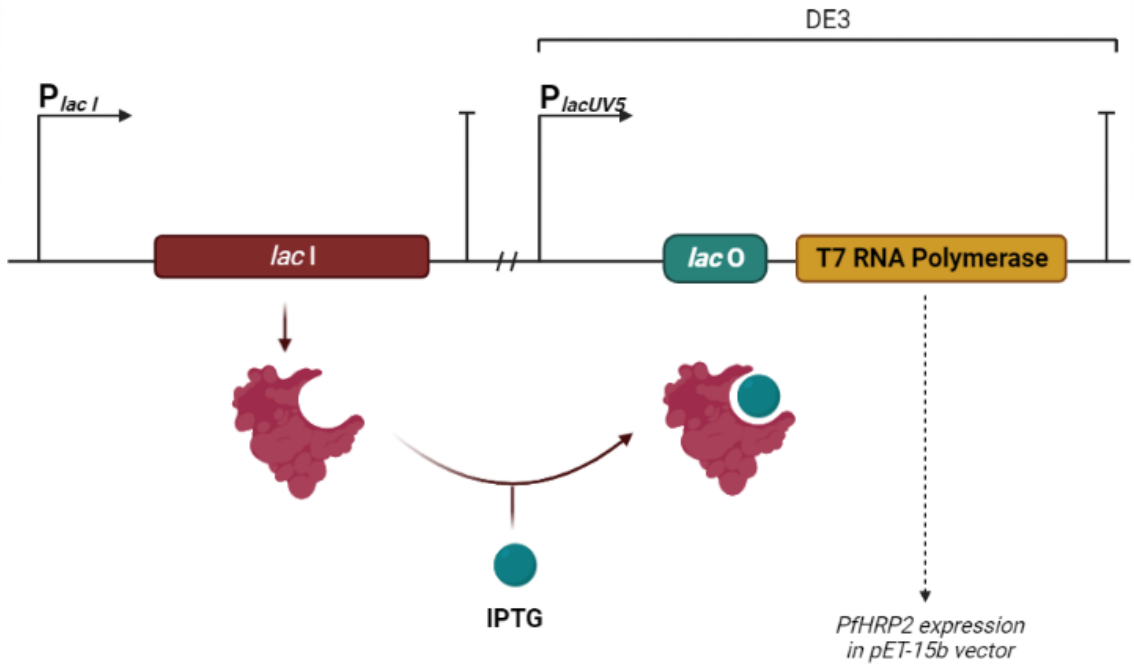

Figure I.1: *E. coli* BL21 DE3 strain for the T7 expression system. Image created in Biorender.

polymerase and is controlled by LacI through the *lac* operator [4]. The recombinant clone in pET-15b begins with twentieth amino acid of *Pf*HRP2 to avoid the hydrophobic leader peptide [1]. The gene is transcripted including a sequence of six histidines located in the N-terminal of the *Pf*HRP2. This tag of histidines (0.8 kDa) allows to perform immobilised metal affinity chromatography purifying the protein, and due to being of very small size, it does not affects the function of the protein [4]. A thrombin site is also included in this plasmid adding the possibility of deleting the six histidine tag [4].

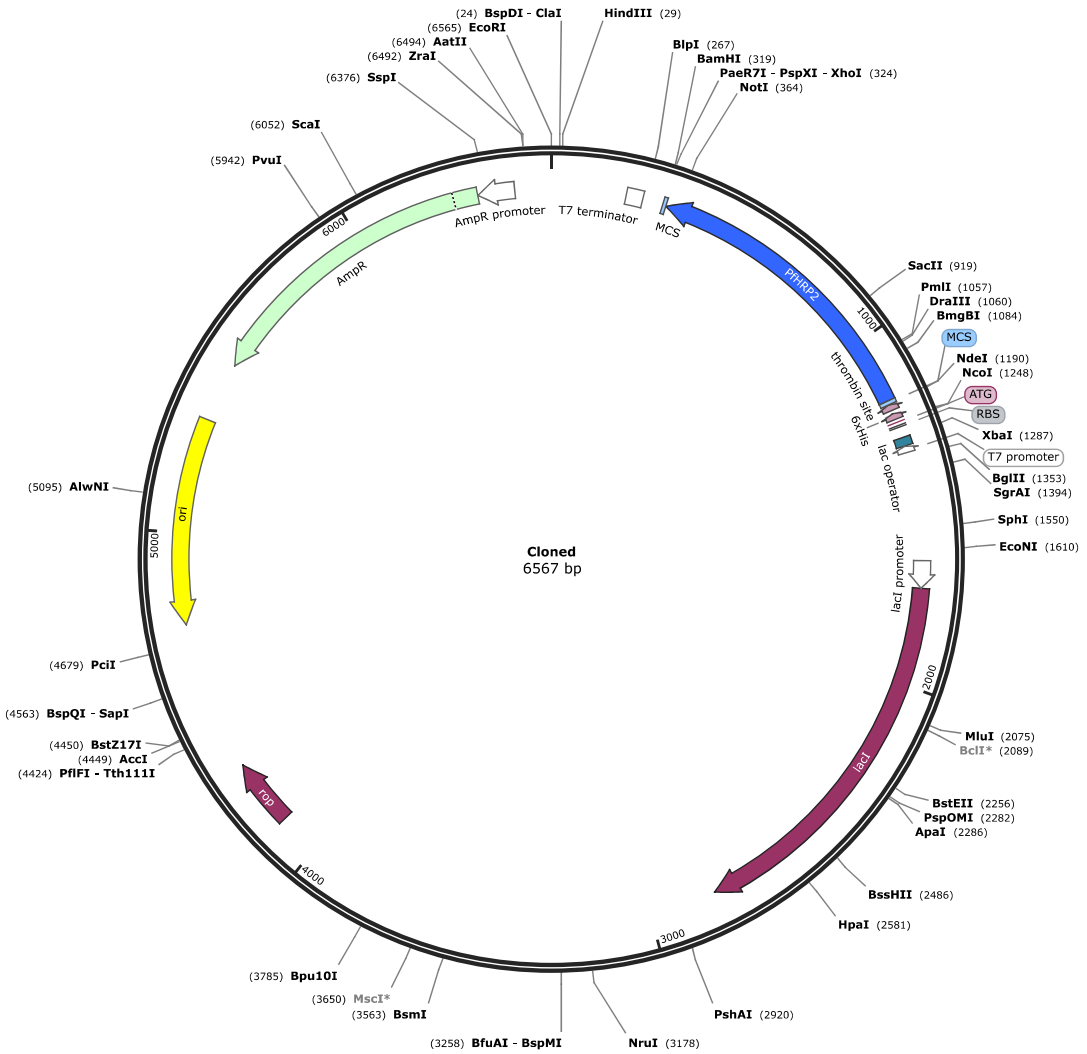

Figure I.2: pET-15b vector map with *PfHRP2* gene inserted.

References for annex I

[1] D. J. Sullivan, I. Y. Gluzman, and D. E. Goldberg. "Plasmodium Hemozoin Formation Mediated by Histidine-Rich Proteins". In: *Science* 271.5246 (1996), pp. 219–222.

[2] F. William Studier et al. "Use of T7 RNA polymerase to direct expression of cloned genes". In: *Methods in enzymology*. Vol. 185. 1. 1990, pp. 60–89.

[3] F. Du et al. "Regulating the T7 RNA polymerase expression in E. coli BL21 (DE3) to provide more host options for recombinant protein production". In: *Microbial Cell Factories* 20.1 (2021), p. 189.

[4] L. Vinet and A. Zhedanov. "pET System Manual". In: *Novagen* 172.10 (2010), pp. 1–50.

2022

NANOSERS MICROFLUIDICS PLATFORM FOR RAPID SCREENING FOR INFECTIOUS DISEASES

Maria João Oliveira